UNIVERSITY OF CATANIA

DEPARTMENT OF CIVIL ENGINEERING AND ARCHITECTURE (DICAR)

PH.D. COURSE IN "EVALUATION AND MITIGATION OF URBAN AND LAND RISKS"

XXXIV CYCLE

DYNAMIC SOIL–STRUCTURE INTERACTION ANALYSIS ON LIQUEFIABLE SOILS BY NUMERICAL MODELLING AND DESIGN OF A BIAXIAL LAMINAR SHEAR BOX

Tutor
Prof. Salvatore Grasso

Co-Tutor
Prof. Valentina Lentini

Coordinator of the Ph.D. course
Prof. Antonino Cancelliere

<div align="right">

Ph.D Student
Dr. Maria Stella Vanessa Sammito

</div>

Academic Year: 2020/2021

LIST OF CONTENTS

Whether it is a tsunami,
whether it is a hurricane,
whether it is an earthquake,
when we see these great fatal and natural acts,
men and women of every ethnic persuasion
come together and they just want to help.

Martin Luther King III

ACKNOWLEDGEMENTS

1. Introduction

The present study aims to analyse the dynamic soil-structure interaction (DSSI) on liquefiable soils by means of numerical modelling. Moreover, a new laminar shear box has been designed at the Laboratory of Earthquake Engineering and Dynamic Analysis (L.E.D.A.) of the University of Enna "Kore" (Sicily, Italy).

Seismic-induced soil liquefaction is a major cause of damage and loss of human lives during earthquakes. Thus, the evaluation of the susceptibility of a site to liquefaction and the assessment of its effect on structures are important topics in seismic geotechnical engineering.

Several studies have been carried out in the last decades to assess soil liquefaction. However, it is still a challenging task. The main issues are the uncertainties associated to soil behavior and the large number of variables related to the interaction between the soil, water, foundation and structure.

The numerical simulations and the use of constitutive models for liquefaible soil are a valuable help in this complex problems. However, the liquefaction phenomenon is difficult to achieve in the constitutive models and it requires a large number of input parameters. Reduced-scale model tests are advantageous for seismic studies thanks to the ability to provide economic and realistic information about the ground amplification, change in water pressure and soil non-linearity.

In order to understand the liquefaction phenomenon, it has been useful to proceed in steps starting from free field conditions and considering gradually more complex configurations.

This work has been divided into 6 chapters, including the introduction (Chapter 1).

In Chapter 2, a theoretical background on the research topic is given. In paragraph 2.1, finite element modelling has been presented as a valuable method for the soil-structure interaction problems thanks to advances in computational technology. The UBC3D-PLM model, implemented in PLAXIS3D

software, has been described as a powerful and advanced constitutive model for simulating liquefaction phenomenon.

An overview of the liquefaction phenomena has been presented in paragraph 2.2, highlighting several criteria by which liquefaction susceptibility can be judged. Case history examples have been also reported in order to underline some critical aspects of the liquefaction phenomenon. Historical date of past earthquakes are important to support the development and updating of CRR curves in the Simplified Procedure, described in detail in paragraph 2.3. This framework includes an important function that takes into account fundamental aspects of dynamic site response, i.e. the shear stress reduction coefficient, r_d, which depends on several factors (depth, earthquake and ground motion characteristics, dynamic soil properties).

Chapter 3 presents several soil containers that have been used in the last three decades. Particular attention has been paid to the laminar shear box and liquefaction studies. Six types of soil container have been identified: rigid container, rigid container with flexible boundaries, rigid container with hinged end-wall, Equivalent Shear Beam (EBS) container, laminar container and active boundary container.

In Chapter 4, new variations of r_d with depth have been obtained using different deterministic earthquake scenarios as input motion. The relationships are based on large numbers of site response analyses for different site conditions. Relationships are proposed for the eastern coastal plain of Catania area (Italy). The city of Catania, in South-Eastern Sicily, was affected by several destructive earthquakes of about magnitude 7.0 in past times. Extensive liquefaction effects occurred following the 1693 and 1818 strong earthquakes.

Chapter 5 deals with 3D FEM full-coupled structure analyses for a strategic building located in the city of Messina (Sicily, Italy). The structure was built after the strong earthquake of 1908, also

known as Messina-Reggio Calabria earthquake, that caused severe ground shaking. A parametric study with three different seismograms of the 1908 earthquake has been carried out. The seismicity, the geological and geotechnical properties of the subsoil and the description of the building are reported in paragraphs 5.1 and 5.2. Deep site and laboratory investigations, undertaken in the area in which the Regional Department of Civil Defence (DRPC) is located, have allowed the definition of the geometric and geotechnical model of the subsoil (paragraph 5.3). The validation of the three-dimensional finite element model, including the definition of the dynamic boundary conditions, is reported in paragraph 5.4. The non-linear soil behaviour has been investigated in paragraph 5.5, while paragraph 5.6 covers the stress-based simplified procedure for evaluating soil liquefaction potential in the area in which the DRPC is located.

The dynamic response of the soil-structure system in terms of accelerations, response spectra, amplification functions and displacements has been investigated in paragraph 5.7.

In paragraph 5.8, the UBC3D-PLM model has been calibrated by means of the simulation of cyclic direct simple shear tests (CDSS) using PLAXIS3D software. The seismic behaviour of the soil-structure system on liquefiable soil has been analysed in terms of liquefaction potential, excess pore pressures (EPPs), accelerations, response spectra and displacements under the three seismograms of the 1908 earthquake.

Chapter 6 covers the design of a new laminar shear box at the Laboratory of Earthquake Engineering and Dynamic Analysis (L.E.D.A.) of the University of Enna "Kore" (Sicily, Italy). The laminar box has been developed and assembled for the liquefaction studies.

2. Theoretical background

2.1 Numerical modelling (DSSI)

Many aspects have to be considered for the retrofitting and/or improving of an existing structure. One important aspect is an accurate investigation of the soil. Knowing the specific conditions of the subsoil, it is possible to investigate its filtering effects in terms of acceleration and frequency. The main factors responsible for seismic motion amplification are the impedance contrast between the layers, and the resonance effects due to the closeness between the predominant frequencies of the input motions and the resonance frequencies of the soil.

However, due to the kinematic and inertial interaction between the soil and the structure, the dynamic response deviates from the FF condition. This interaction is mutual and known as Dynamic Soil-Structure Interaction (DSSI). A comparison between the alignment under the structure and the free field condition usually shows that the presence of the structure generates a beneficial effect. However, it is important to investigate and understand the DSSI effects because the interaction can sometimes be detrimental. In addition, the DSSI takes on an even more decisive role when sliding and uplift occur at the soil-foundation interface (Massimino et al. 2019).

Another important aspect is the knowledge of the frequency of the structure. For the period of the structure under consideration, the dynamic soil-structure interaction can led to a designed acceleration greater than that required for the free field condition. Moreover, the double resonance phenomenon, that is the matching of the resonance frequencies of the soil with the fundamental frequency of the building resting on the soil, can occur.

In recent years numerical methods, such as the Finite Element Method (FEM), have increasingly been used to model static and dynamic response of soils and rocks thanks to advances in computational technology. In FEM, the mechanical behaviour of soil is described by means of

8

constitutive models, in which model parameters are used to quantify particular features and properties of the soil.

One of the widely used constitutive models is the equivalent visco-elastic constitutive model. Seylabi et al. (2018) explored the capabilities of calibrated equivalent linear soil models in capturing the seismic response of buried box structures. Massimino et al. (2018) evaluated the seismic response of a soil-building system by means of the ADINA code using the equivalent viscoelastic constitutive model.

Castelli et al. (2021) adopted a linear elastic-plastic model (Mohr-Coulomb model) in order to investigate the dynamic soil-foundation-interaction of a cooling tower founded on piles. An advanced model for the simulation of soil behavior is the Hardening Soil model (Schanz et al. 1999). It describes the soil stiffness more accurately by using three different input parameters at the reference pressure p^{ref}: the secant stiffness in standard drained triaxial test, E_{50}^{ref}, the unloading/reloading stiffness, E_{ur}^{ref}, and the tangent stiffness for primary oedometer loading, E_{oed}^{ref}. In contrast to the Mohr-Coulomb model, the Hardening Soil Model also accounts for stress-dependency of stiffness moduli. Moreover, the yield surface is not fixed in principal stress space, but it can expand due to plastic strain (Vakili et al., 2013; Surarak et al., 2012). The Hardening Soil model assumes an elastic material behaviour during unloading and reloading. However, the strain range in which soils can be considered truly elastic is very small. With increasing strain amplitude, soil stiffness decays nonlinearly. In addition to all features of the Hardening Soil Model, the advanced Hardening Soil Model with small-strain stiffness takes into account an increased soil stiffness for small strains (Benz, 2006; Benz et al., 2009). Amorosi et al. (2016) carried out a non-linear finite element study to back-interpret the free field seismic response recorded at the Lotung Large Scale Seismic Test site using the Hardening Soil Model with small-strain stiffness. Deghoul et al. (2020) studied the behavior of

pile-supported wharf embedded in rock dike using PLAXIS2D code and three different soil constitutive models.

The numerical modelling of the soil becomes more complex when it is susceptible to liquefaction and therefore the interaction between soil, structure and water must be considered.

In order to simulate the seismic response of liquefiable soil, it is needed an appropriate constitutive model which has the ability to describe this phenomenon. According to Kramer and Elgamal (2001), constitutive models need to simulate:

a) undrained pore-pressure generation as a function of the amplitude of shear loading and the material state (effective stress and density);

b) the effect of initial shear stress (anisotropic initial loading);

c) transformation of the soil from a solid to a liquefied state and its effects on stiffness;

d) the effects of various soil fabrics and fabric degradation on stiffness;

e) stiffness and dilatancy evolution under cyclic loading;

f) the onset of instabilities (diffuse and localized);

g) the transition to the steady state.

However, capturing all of these features is beyond the capability of existing constitutive models (Kavazanjian et al., 2016).

The importance of various features depends on the situation and modelling goals. For example, the bearing capacity failure is sensitive to residual strength, while foundation settlements on deep liquefaction deposits are more sensitive to consolidation and permeability. Finally, one of the most important requirements of all constitutive models is the simplicity in which the model parameters can be obtained from field or laboratory test (Da Fonseca et al., 2017).

In the presence of buildings, the behaviour of liquefiable deposit is even more complex and it is altered in comparison to the free-field. A building modifies the initial stress field in the soil and alters its potential to develop excess pore pressure and its dynamic response.

The assessment of the liquefaction effects on buildings requires:

1)   an appropriate simulation of the soil behaviour and of the soil-structure interaction in order to reflect the modification of the global dynamic response;

2)   a definition of damage levels accounting for the loss of functionality related to rigid-body movements: global settlements and tilting.

From experimental and numerical studies, there are some repeating aspects (Da Fonseca et al., 2017). Lower degree of liquefaction is expected below buildings rather than in the free field. Higher settlement is expected below buildings rather than in the free field, and can occur during and after shaking.

The foundation tilting is caused by dynamic inertial forces in the building or deformations in the soil. This phenomenon can produce flexural and shear-induced damage to building. The damage may increase when differential settlements occur. However if the foundation and the structure are relatively rigid compared to the soil stiffness rigid-body tilt can occur without structural damage.

For the simulation of soil liquefaction and soil-structure interaction the following software can be used: OpenSees, FLAC and PLAXIS. OpenSees (2017) is an open-source software developed at the Pacific Earthquake Engineering Research (PEER) Center. The software is capable of modelling the coupling response between the soil skeleton and pore fluid by means of the *PressureDependMultiYield* (PDMY02) material model. Karimi and Dashti (2016) used the PDMY02 for the validation of the liquefaction-induced settlements of a single degree of freedom (SDOF) structure founded on a rigid mat.

FLAC (Fast Lagrangian Analysis of Continua) is a finite difference software for advanced geotechnical analysis of soil, rock, groundwater and ground support. The PM4SAND model is a sand plasticity model implemented in FLAC specially developed for geotechnical earthquake engineering applications (Boulanger and Ziotopoulou, 2013). Ziotopoulou and Montgomery (2017) employed this model in order to investigate the effects of post-liquefaction reconsolidation settlements on shallow foundations. Moreover, the UBCSAND Model is available in FLAC as a User-Defined constitutive Model (UDM). It is an effective stress plasticity model for the use in advanced stress-deformation analyses of geotechnical structures (Itasca, 2017). Dashti and Bray (2003) performed fully-coupled numerical simulations with the UBCSAND model capturing building settlements measured in centrifuge experiments of structures with shallow foundations on liquefiable sand.

In this study, the Dynamic Soil–Structure Interaction analysis on liquefiable soil has been investigated by means of PLAXIS3D software (Bentley Systems). PLAXIS is a two- or three-dimensional finite element program used to perform deformation, stability and flow analysis for various type of geotechnical applications. The basic soil elements of the 3D finite element mesh are the 10-node tetrahedral elements (Figure 2.1) (PLAXIS 3D, 2020).
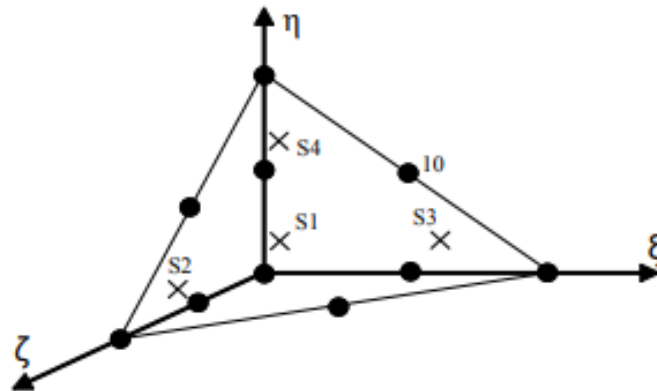

Figure 2.1 3D soil element (10-node tetrahedron) (From PLAXIS 3D, 2020).

The constitutive model for simulation of soil liquefaction in PLAXIS3D is the UBC3D-PLM model which is a 3D generalization of the UBCSAND model developed at University of British Colombia (Puebla et al. 1997; Beaty and Byrne 1998). The initial 3D implementation in PLAXIS was presented by Tsegaye (2010) and an improved version was developed by Petalas and Galavi (2013). Galavi et al. (2013) studied the numerical aspects of seismic liquefaction in soil as implemented in PLAXIS and displayed how most of the model parameters can be found from the corrected SPT blow count.

2.1.1 Hardening Soil Model with small-strain stiffness

In the Hardening Soil model (HS model), the yield surface can expand due to plastic straining. There are two types of hardening, shear hardening and compression hardening. Shear hardening is used to model irreversible strains due to primary deviatoric loading. Compression hardening is used to model irreversible plastic strains due to primary compression in oedometer loading and isotropic loading. Both types of hardening are considered in the formulation of the HS model.

A basic idea for the formulation of the HS model is the hyperbolic relationship between the vertical strain, ε_1, and the deviatoric stress, q, in primary loading for standard drained triaxial test (Figure 2.2).
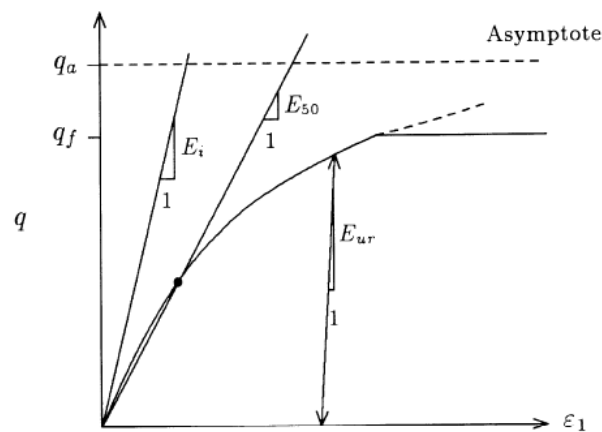

Figure 2.2 Hyperbolic stress-strain relation in primary loading for a standard triaxial test (From Schanz et al., 1999).

13

This relationship was fist formulated by Kondner and Zelasko (1963) and after used in the hyperbolic model (Duncan and Chang, 1970). However, the HS model supersedes the hyperbolic model by using the theory of plasticity than the theory of elasticity. The model also includes the soil dilatancy and a yield cap. Figure 2.3 shows the yield surface of the HS model in the principal stress space.
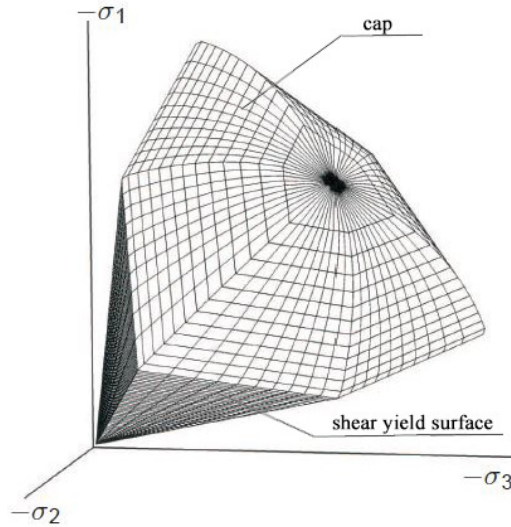

Figure 2.3 Total yield contour of the Hardening Soil Model in the principal stress space for cohesionless soil (From PLAXIS3D, 2018a; modified).

The main characteristics of the model are the following:

- stress dependent stiffness according to a power law;

- plastic straining due to primary deviatoric loading;

- plastic straining due to primary compression;

- elastic unloading/reloading;

- failure according to the Mohr Coulomb failure criterion.

For oedometer conditions of stress and strain, the model implies for example:

$$E_{oed} = E_{oed}{}^{ref} \left(\frac{\sigma'_1}{p^{ref}} \right)^m \qquad (2.1)$$

where E_{oed}^{ref} is the tangent stiffness for primary oedometer loading corresponding to the reference pressure p_{ref} (Figure 2.4), σ'_1 is the major principal effective stress and *m* is the power for stress-level dependency of stiffness.
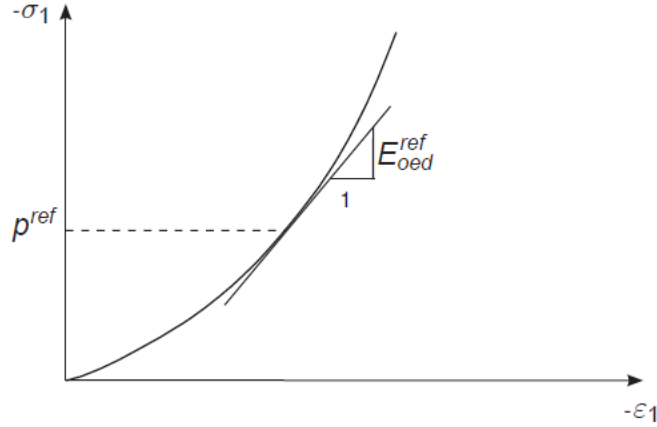

Figure 2.4 Definition of E_{oed}^{ref} in oedometer test results (From PLAXIS3D, 2018a).

The standard drained tests tend to yield curves that can be described by:

$$-\varepsilon_1 = \frac{1}{E_i}\frac{q}{1 - \dfrac{q}{q_a}} \quad for\ q < q_f \tag{2.2}$$

where q_a is the asymptotic value of the shear strength, E_i is the initial stiffness, q_f is the ultimate deviatoric stress. When $q=q_f$ the failure criterion is satisfied and perfectly plastic yielding occurs as described by the MC model. E_i is related to the secant modulus E_{50} by:

$$E_i = \frac{2E_{50}}{2 - R_f} \tag{2.3}$$

where R_f is the failure ratio given by the ratio between q_f and q_a. The parameter E_{50} is given by:

$$E_{50} = E_{50}^{ref}\left(\frac{c'cos\varphi' - \sigma_3'sen\varphi'}{c'cos\varphi' + p^{ref}sen\varphi'}\right)^m \tag{2.4}$$

where E_{50}^{ref} is the secant stiffness at 50 % of the maximum deviatoric stress at the cell pressure equal to the reference stress p_{ref}, c' is the effective cohesion, φ' is the effective angle of internal friction and $\sigma_3'\ is$ the minor principal effective stress.

The triaxial modulus largely controls the shear yield surface and the oedometer modulus controls the cap yield surface.

For unloading and reloading stress path, another stress-dependent modulus E_{ur} is used:

$$E_{ur} = E_{ur}^{ref} \left(\frac{c' \cos\varphi' - \sigma_3' \operatorname{sen}\varphi'}{c' \cos\varphi' + p^{ref} \operatorname{sen}\varphi'} \right)^m \tag{2.5}$$

in which E_{ur}^{ref} is the reference Young's modulus for unloading and reloading.

The MC failure criterion is used in the HS model. However, the yield locus varies with the strain hardening parameter γ_p (Figure 2.5).
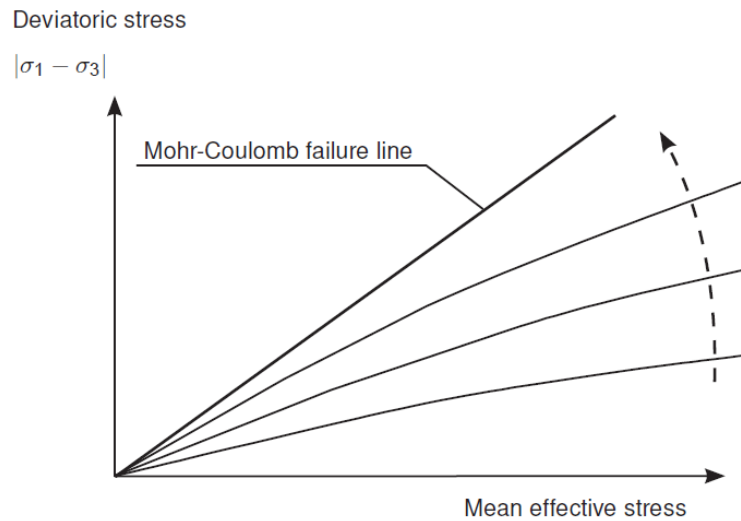

Figure 2.5 Variation of the yield locus with various values of the hardening parameter γ_p in p'-q space. (From PLAXIS3D, 2018a).

The plastic hardening parameter is equal to:

$$\gamma_p = -(2\varepsilon_1{}^p - \varepsilon_v{}^p) \tag{2.6}$$

where $\varepsilon_1{}^p$ and $\varepsilon_v{}^p$ are the axial and volumetric strains respectively.

The shear hardening flow rule in the HS model is linear and involves the mobilized dilatancy angle ψ_m and γ_p as follows:

$$\dot{\varepsilon_v{}^p} = \operatorname{sen}\psi_m \dot{\gamma_p} \tag{2.7}$$

16

The mobilized dilatancy angle depends on the mobilized shear angle φ_m (Figure 2.6) according to the following equations:

for $sen\varphi_m < \dfrac{3}{4}sen\varphi$ $\qquad\qquad\qquad\qquad \psi_m = 0$

for $sen\varphi_m \geq \dfrac{3}{4}sen\varphi$ and $\psi > 0$ $\qquad sen\psi_m = max\left(\dfrac{sen\varphi_m - sen\varphi_{cv}}{1 - sen\varphi_m sen\varphi_{cv}}, 0\right)$ $\qquad\qquad$ (2.8)

for $sen\varphi_m \geq \dfrac{3}{4}sen\varphi$ and $\psi \leq 0$ $\qquad \psi_m = \psi$

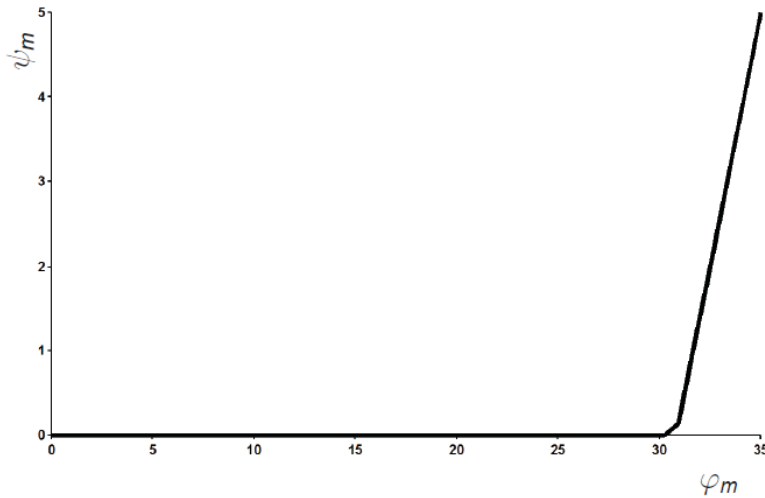If $\varphi = 0$ $\qquad\qquad\qquad\qquad\qquad\qquad \psi_m = 0$

Figure 2.6 Plot of mobilized dilatancy angle ψ_m and mobilized friction angle φ_m (From PLAXIS3D, 2018a).

The equations are an adaptation from the stress-dilatancy theory by Rowe (1962) as explained by Shanz and Vermeer (1997). The essential property of the theory is that the material contracts for small stress ratio ($\varphi_m < \varphi_{cv}$), while dilatancy occurs for high stress ratio ($\varphi_m > \varphi_{cv}$).

The critical state friction angle, φ_{cv}, can be computed from the friction angle φ and the peak dilatancy angle using the Equation (2.9).

$$sen\varphi_{cv} = \dfrac{sen\varphi - sen\psi}{1 - sen\varphi sen\psi}$$ $\qquad\qquad$ (2.9)

17

The parameters required to use the HS model are c', φ, ψ, which are parameters for the MC failure criteria. Additionally, the soil stiffness parameters are required: E_{50}^{ref}, E_{ur}^{ref}, and E_{oed}^{ref} (PLAXIS3D, 2018a; Schanz et al., 1999).

However, it is important to state that the HS model assumes an elastic behaviour during the unloading and reloading. The model does not generate the hysteretic damping, the accumulation of pore pressure and the liquefaction. Therefore, it is not appropriate to simulate dynamic problems.

The strain range in which the soil is truly elastic is very small. With the increasing strain amplitude, soil stiffness decays nonlinearly. The Hardening Soil model with small strain stiffness (HS small) takes into account this aspect by introducing two additional parameters:

- the initial or very small-strain shear modulus, G_0;

- the shear strain level $\gamma_{0.7}$ at which the secant shear modulus, G_S, is reduced to about 70% of G_0.

The stress dependency of the shear modulus G_0 is taken into account with the power law:

$$G_0 = G_0^{ref} \left(\frac{c'cos\varphi' - \sigma_3'sen\varphi'}{c'cos\varphi' + p^{ref}sen\varphi'} \right)^m \tag{2.10}$$

Where G_0^{ref} is the reference shear modulus at very small strain ($\varepsilon < 10^{-6}$).

The most used relationship in soil dynamic is that one proposed by Hardin - Drnevich (1972):

$$\frac{G_s}{G_0} = \frac{1}{1 + \left| \frac{\gamma}{\gamma_r} \right|} \tag{2.11}$$

where γ_r is the threshold given by:

$$\gamma_r = \frac{\tau_{max}}{G_0} \tag{2.12}$$

with τ_{max} is the shear stress at failure. Santos and Correia (2001) suggest to use the shear strain at which the secant modulus is reduced to about 70% of its value. Therefore the Equation (2.11) becomes:

18

$$\frac{G_s}{G_0} = \frac{1}{1 + a \left| \frac{\gamma}{\gamma_{0.7}} \right|} \tag{2.13}$$

Using a=0.385 and $\gamma = \gamma_{0.7}$ the equation gives G_S/G_0=0.772.

In the HS small, the stress-strain relationship can be formulated from the secant shear modulus as:

$$\tau = G_s \gamma = \frac{G_0 \gamma}{1 + 0.385 \dfrac{\gamma}{\gamma_{0.7}}} \tag{2.14}$$

Taking the derivative with respect to the shear strain gives the tangent shear modulus:

$$G_t = \frac{G_0}{\left(1 + 0.385 \dfrac{\gamma}{\gamma_{0.7}} \right)^2} \tag{2.15}$$

The small-strain stiffness reduction curve is bound by the lower cut-off of the tangent shear modulus G_S that is the unloading and reloading stiffness G_{ur} (Figure 2.7):

$$G_{ur} = \frac{E_{ur}}{2(1 + v_{ur})} \quad \text{with } G_t \geq G_{ur} \tag{2.16}$$

where E_{ur} is the elastic stiffness and v_{ur} is the Poisson's ratio for unloading-reloading.
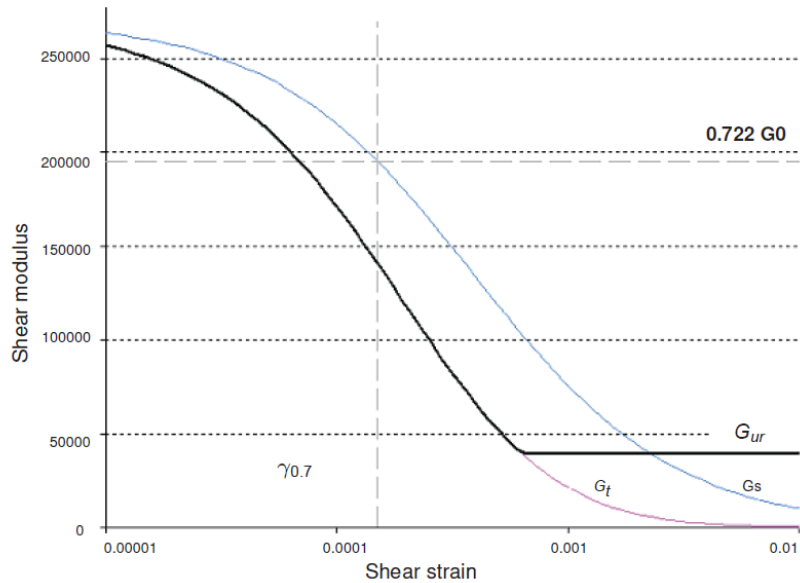

Figure 2.7 Secant and tangent shear modulus curves (From PLAXIS3D, 2018a).

19

The HS small model uses the Masing's rules in order to describe the hysteretic behaviour of materials in unloading/reloading cycles (Figure 2.8) (Masing, 1926):

- the shear modulus in unloading is equal to the initial tangent modulus for the initial loading curve;

-the shape of the unloading and reloading curves is equal to the initial loading curve, but twice in size:

$$\gamma_{0.7,reloadiing} = 2\gamma_{0.7,virgin-loadiing} \tag{2.17}$$
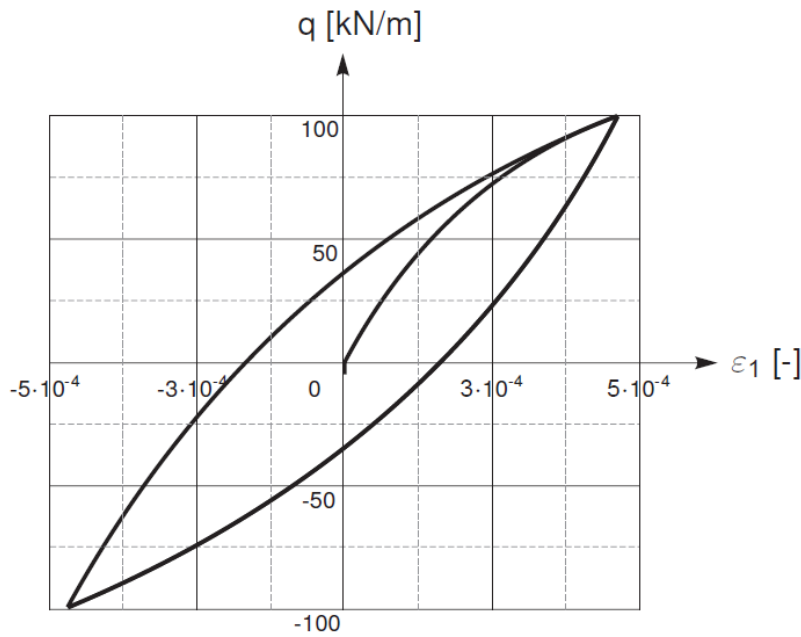

Figure 2.8 Hysteretic material behaviour (From PLAXIS3D, 2018a).

The hysteretic behaviour of the HS small model leads to damping. The amount of damping depends on the applied load amplitude. However, the model does not generate the accumulated pore pressure (PLAXIS3D, 2018a).

2.1.2 UBC3D-PLM model

The UBC3D-PLM model is an effective stress elasto-plastic model which is capable of simulating the liquefaction behaviour of sands or silty sands under seismic loading (Tsegaye, 2010; Petalas and Galavi, 2013). The UBC3D-PLM model uses two yield surface to model the cyclic behaviour of soils, namely primary and secondary yield surface (Figure 2.9).
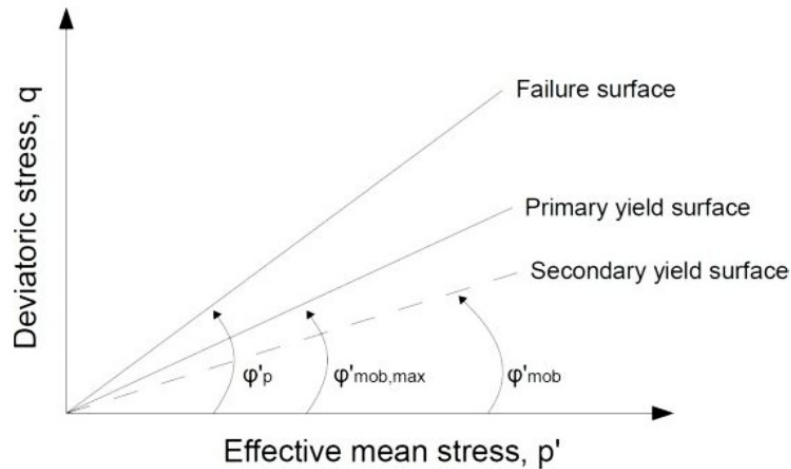

Figure 2.9 Yield surfaces in p'-q space (From Galavi et al. 2013).

The primary surface is based on isotropic hardening and becomes active when the mobilised friction angle is equal to the maximum mobilised friction angle that the soil has ever reached. In this case, the current stress ratio is the highest stress ratio in the loading history.

A simplified kinematic hardening rule is utilised for the secondary yield surface, which becomes active when the mobilised friction angle is less than the maximum mobilised friction angle. This is the case when the current stress ratio is lower than the maximum stress ratio in the loading history.

To explain the effect of both yield surfaces, a stress state is considered on the isotropic axis and both yield surfaces are at the same position. By loading from isotropic stress state, both primary and secondary yield surfaces expand according to the same hardening rule. If the soil is unloaded, the secondary yield surface shrinks and the behaviour of the soil is elastic. By reloading the soil, the

secondary yield surface becomes activate and the behaviour will be elasto-plastic again. As soon as the mobilised friction angle reaches the maximum mobilised friction angle, the primary yield surface becomes active again and the behaviour becomes softer.

The distinction between these two yield surface is made in order to ensure a smooth transition into the liquefied state of the soil, to enable the distinction between primary and secondary loading and to have a densification rule (higher rate of hardening) in the secondary yield surface.

The Mohr-Coulomb yield function is used to define both yield surface. The formulation is given by:

$$f_m = \frac{\sigma'_{max} - \sigma'_{min}}{2} - \left(\frac{\sigma'_{max} + \sigma'_{min}}{2} + cot\varphi'_p\right)sin\varphi'_m \tag{2.18}$$

where σ'_{max} is the maximum principal effective stress, σ'_{min} is the minimum principal effective stress, c′ is the cohesion of the soil, φ'_p is the peak effective friction angle of the soil and φ'_m is the mobilised friction angle during hardening. The intermediate stress does not influence the yield surface in three dimensional stress space.

The elastic behaviour, which occurs within the secondary yield surface, is governed by a stress dependent non-linear rule. The elastic bulk modulus, K, and the elastic shear modulus, G, are stress dependent and are given by the following equations:

$$K = k_B^e p_{ref} \left(\frac{p'}{p_{ref}}\right)^{me} \tag{2.19}$$

$$G = k_G^e p_{ref} \left(\frac{p'}{p_{ref}}\right)^{ne} \tag{2.20}$$

where k_B^e and k_G^e are the bulk and the shear modulus factors at a reference stress level, respectively; p′ is the mean effective stress; me and ne are two parameters to define the rate of stress dependency of stiffness; p_{ref} is the reference stress level commonly taken as the atmospheric pressure (i.e.100kPa). Pure elastic behaviour is predicted by the model during unloading.

According to the theory of plasticity, the direction of the plastic strain increment is specified by the gradient of the plastic potential function. In the proposed model, a non-associated flow rule based on the Drucker-Prager model is used. The plastic potential function g is formulated as:

$$g = q - \frac{6 sin\psi_m}{3 - sin\psi_m}\left(p' + c'cot\varphi'_p\right) \tag{2.21}$$

where ψ_m is the mobilised dilation angle; q is the deviatoric stress and p′ is the mean effective stress. It follows that the direction of the plastic strain increment is perpendicular to the Drucker-Prager surface.

Similar to the Hardening Soil model, the flow rule in the UBC3D-PLM model is based on three observations (Figure 2.10):

- there is a unique stress ratio, defined by the constant volume friction angle, φ'_{cv}, for which plastic shear strains do not cause plastic volumetric strains;

-stress ratios below $sen\varphi'_{cv}$ exhibit contractive behavior, while stress ratios above $sen\varphi'_{cv}$ lead to a dilative behavior. Therefore, the constant volume friction angle works as the phase transformation angle;

- the amount of contraction or dilatancy depends on the difference between the current stress ratio and the stress ratio at $sen\varphi'_{cv}$.
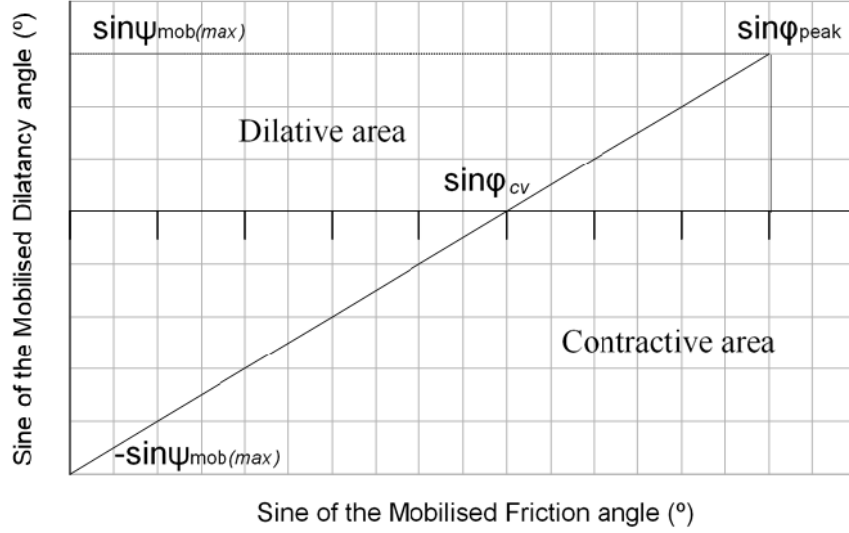
Figure 2.10 Modified Rowe's flow rule as used in UBC3D-PLM model (From PLAXIS3D, 2018a).

The increment of plastic volumetric strain $d\varepsilon_v^p$ is given by Equation (2.22), where the mobilised dilatancy angle ψ_m is computed using the flow rule derived from stress-dilatancy theory developed by Rowe (1962):

$$d\varepsilon_v^p = sen\psi_m d\gamma^p \tag{2.22}$$

$$sin\psi_m = sin\varphi_m' - sin\varphi_{cv}' \tag{2.23}$$

where $d\gamma^p$ is the plastic shear strain increment.

The primary yield function has an isotropic hardening rule. It governs the amount of plastic strain as a result of mobilisation of the shear strength. The hyperbolic hardening rule, as formulated by Tsegaye (2010) in UBC3D-PLM model, is defined by the following relation:

$$dsin\varphi_m' = 1.5k_G^P \left(\frac{p'}{p_{ref}}\right)^{np} \frac{p_{ref}}{p'} \left(1 - \frac{sin\varphi_m'}{sin\varphi_{ult}'}\right)^2 d\lambda \tag{2.24}$$

where k_G^P is the plastic shear modulus factor; np is the plastic shear modulus exponent; $d\lambda$ is the plastic strain increment multiplier and φ_{ult}' is the ultimate mobilised friction angle to limit the hyperbolic curve and is obtain from the failure ratio, R_f, according to:

24

$$R_f = \frac{\sin\varphi'_p}{\sin\varphi'_{ult}} \tag{2.25}$$

The failure ratio, R_f, is always less than 1.

A kinematic hardening rule is used for the secondary surface. It allows for modelling the gradual generation of pore-water pressures under lower rate in the cyclic just before liquefaction onset, phenomenon known as soil densification. Therefore, this relationship is called as Densification rule. The secondary yield surface generates less plastic strain compared to the primary yield surface. The plastic shear modulus number, k_G^P, during secondary loading increases as a function of the number of cycles in order to capture the effect of soil densification as follows:

$$k_{G,secondary}^P = k_G^P \left(4 + \frac{n_{rev}}{2}\right) hard f_{dens} \tag{2.26}$$

where k_G^P is the initial value entered for the primary yield surface; $k_{G,secondary}^P$ is the secondary plastic shear modulus factor; n_{rev} is the number of shear stress reversals from loading to underloading or vice versa (two reversals count for one full cycle); $hard$ is a factor which is correcting the densification rule for loose sand and f_{dens} is a user input parameter to calibrate the densification rule.

Once the stress path reaches the yield surface defined by peak friction angles, volumetric strain becomes constant (volumetric locking) owing the formation of the flow rule, i.e. $sen\varphi'_m$ becomes $sen\varphi'_p$ and remains constant meaning that $sen\psi_m$ is also constant. Therefore, stiffness degradation of soil due post-liquefaction behaviour of loose sands and cyclic mobility of dense sands cannot be modelled. To solve this problem, a new parameter is defined at this stage. Plastic shear modulus k_G^P is decreased gradually as a function of generated plastic-deviatoric strain during dilatation of the soil element. Stiffness degradation is given as:

$$k_{G,post-liquefaction}^{P} = k_G^P E_{dil} \tag{2.27}$$

$$E_{dil} = max(e^{-110\varepsilon_{dil}}; f_{Epost}) \tag{2.28}$$

where k_G^P is the input plastic shear modulus; $k_{G,post-liquefaction}^{P}$ is the plastic shear modulus factor during liquefaction; ε_{dil} is the accumulation of plastic-deviatoric strain that is generated during dilatation of the soil element and f_{Epost} is the input parameter that is used to limit the value of E_{dil}. Finally, the increment of the pore water pressure is computed by:

$$dp_w = \frac{k_w}{n} d\varepsilon_v \tag{2.29}$$

where k_w is the bulk modulus of the pore fluid; n is the porosity and $d\varepsilon_v$ is the volumetric strain increment (Galavi et al., 2013; Bhatnagar et al. 2016; Petalas and Galavi, 2013; PLAXIS, 2018b).

2.2 Liquefaction

Liquefaction is defined as the transformation of a granular material from solid to a liquefact state as a consequence of increase pore-pressure and reduced effective stress (Marcuson, 1978).

The build-up pore pressure is often expressed as excess pore water pressure ratio defined by the following equation:

$$r_u = \frac{\Delta u}{\sigma_{v0}'} \tag{2.30}$$

where Δu is the excess pore pressure and σ_{v0}' is the initial vertical effective stress of the soil (Amini et al., 2019).

The pore-pressure ratio is an index of how close a soil is to liquefaction. Prior to cyclic loading, $r_u =$ 0. As excess pore pressure is generated, r_u increases and it is near to 1 when the liquefaction occurs (Kavazanjian et al., 2016).

The evaluation of the susceptibility of a site to seismic-induced liquefaction is an important step in many geotechnical investigations. Kramer (1996) defined several criteria by which liquefaction susceptibility can be judged. These include historical, geological, compositional and state criteria.

Liquefaction case histories can be used to identify specific sites that may be susceptible to liquefaction in future earthquakes. Moreover, post-earthquake field investigations have shown that liquefaction effects have been confined to an area within a particular distance of the seismic source. This distance increases with increasing magnitude.

Geologic processes that arrange soils into uniform grain size distributions and loose states, such as fluvial deposits, produce soil deposits with high liquefaction susceptibility. Liquefaction can be also observed in alluvial plains, beaches or terraces. The susceptibility of older deposits to liquefaction is lower than that of newer deposits. Therefore, soils of Holocene age are more susceptible than soils of Pleistocene age.

Liquefaction occurs only in saturated soils. In particular, liquefaction susceptibility decreases with increasing of the groundwater depth: effects of liquefaction are commonly observed at sites where the groundwater table is at the depth of few meters from the ground surface.

Liquefaction susceptibility is also affected by compositional characteristics of the soil that include particle size, shape and gradation. For many years, liquefaction phenomena were thought to be limited to sands. However, coarse and nonplastic silts with bulky particle shape can be susceptible to liquefaction as observed in the laboratory and in the field. Clays are nonsusceptible to liquefaction. Coarser-grained soils were considered too permeable to generate pore pressure long enough for

liquefaction onset. However, when pore pressure dissipation is impeded by the presence of impermeable layers, gravelly soil can be susceptible to liquefaction.

Liquefaction susceptibility is influenced by gradation and particle shape. Well-graded soils are less susceptible to liquefaction that poorly graded soils. Soils with rounded particle shapes (fluvial and alluvial environments) densify more easily than soils with angular grains, therefore they are more susceptible to liquefaction. Finally, liquefaction susceptibility also depends on the initial state of the soil, i.e. its stress and density characteristics at the time of the earthquake. In this respect, looser soils are more susceptible to liquefaction than dense soils.

The interest in these topic arises in 1964 when Good Friday earthquake (M_w=9.2) in Alaska was followed by the Niigata earthquake (M_S=7.5) in Japan. Both earthquakes produced extensive liquefaction-induced damages, including slope failures, bridge and building foundation failures (Figure 2.11) (Kramer, 1996).

Figure 2.11 Liquefaction-induced bearing capacity failures of the Kawagishi-cho apartment buildings following the 1964 Niigata earthquake (From Kramer, 1996).

Another strong earthquake (M_W=7.8) occurred on 16th July 1990, in the north-central region of Luzon Island, Philippines. Numerous damages due to liquefaction, such as settlements and tilt of the

28

buildings (Figure 2.12), falling down of the bridges and lateral spreading along the river, occurred specially in the central district of Dagupan City (Adachi et al., 1992).

Figure 2.12 Settlements and tilting of buildings following the 1990 Luzon earthquake (From Orense, 2011).

Extensive soil liquefaction was also observed during the 1995 Kobe earthquake (M_W=7.2), creating damage to harbour facilities in Port Kobe and large economic losses for the city. The effects were seen in ground settlements, deformation and tilting of structures, lateral spreads, sand boils and pavement fissures (Soga, 1998).

During the August 17, the 1999 Kocaeli earthquake of Turkey (M_w = 7.4) caused great destruction to buildings, bridges and other facilities. During this earthquake, severe damages due to soil liquefaction and associated ground deformations also occurred in the eastern Marmara Region of Turkey. Soil liquefaction was commonly observed along the shorelines (Kanibir, 2006).

On February 27, 2010, a large earthquake of Magnitude 8.8 hit the Central-South region of Chile. Field observations showed that the earthquake triggered liquefaction in more than 170 different sites, covering a north-south distance of about 950 km. Liquefaction phenomenon induced damages to the road infrastructure, railroads system, buildings and houses (Figure 2.13) (Verdugo, 2015).

Figure 2.13 Damages to the road infrastructure and railroads system after the 1999 Kocaeli earthquake (From Verdugo and González, 2015).

A series of strong local earthquakes hit the city of Christchurch (New Zealand) in the period between September 2010 and December 2011. The 22 February 2011 earthquake (Mw=6.2) was particularly devastating. The earthquake caused widespread and severe liquefaction over approximately one third of the city area (Figure 2.14). In areas close to waterways, the liquefaction was often accompanied by lateral spreading (Cubrinovski, 2014).

Figure 2.14 Differential settlement of a 6 storey reinforced concrete building in the city of Christchurch (From Cubrinovski, 2014).

Recently, on the 16th of April 2016, the Kumamoto earthquake (Mw 7.0) hit the Central Kyushu Region, Japan, following a Mw 6.2 event on the 14th of April. The earthquake sequences caused

severe damage in Kumamoto Prefecture. In southern Kumamoto City, evidences of liquefaction were found at many locations, and some buildings and river levees suffered from significant settlement and deformation (Figure 2.15) (Kiyota et al., 2017).

Figure 2.15 Liquefaction-induced damage to levee along Akitsukawa-River (From Kiyota et al., 2017).

Significant liquefaction phenomena occurred also in the territory of Italy. The city of Catania, in South-Eastern Sicily (Italy), was affected by several destructive earthquakes of about magnitude 7.0 in past times. Extensive liquefaction effects occurred following the 1693 and 1818 strong earthquakes (Grasso and Maugeri, 2008; Maugeri and Grasso, 2013).

The December 28, 1908, Southern Calabria - Messina earthquake (Intensity MCS XI, Mw 7.24) was the strongest seismic event of the 20th century in Italy. The effects have been categorized as slope movement, ground settlement, ground vertical movement, liquefaction, ground crack and hydrological anomaly (Comerci et al., 2015).

Recently, significant and widespread liquefaction effects were observed in various areas of Emilia-Romagna region during the seismic events of May 20 and 29, 2012, with magnitude respectively of Ml 5.9 and Ml. 5.8 (Figure 2.16) (Vannucchi et al., 2012).

Figure 2.16 Liquefaction evidences observed immediately after the earthquake (From Vannucchi et al., 2012).

Historical date of past earthquake are important to develop methods for assessment of liquefaction and of its consequence. At least since 1971, case history date have been published to support the development and updating of CRR curves in the Simplified Procedure (Da Fonseca, 2015).

2.3 Simplified procedure

The stress-based simplified procedure for evaluating soil liquefaction potential, originally developed by Seed and Idriss (1971), consists in the computation of the liquefaction resistance factor (F_{SL}) profile given by the ratio of the cyclic resistance ratio CRR(z) to cyclic shear stress ratio CSR(z), where z is the depth of the deposit.

The cyclic stress ratio CSR can be calculated by the following equation (Boulanger and Idriss, 2014):

$$CSR = \frac{\tau_{av}}{\sigma'_{v0}} = 0.65 \left(\frac{a_{max}}{g}\right)\left(\frac{\sigma_{v0}}{\sigma'_{v0}}\right) r_d \tag{2.31}$$

where τ_{av}=average cyclic shear stress, a_{max}=peak horizontal acceleration at the ground surface generated by the earthquake, g=acceleration of gravity, σ_{v0} and σ_{v0}'=total and effective overburden stresses, and r_d=stress reduction coefficient depending on depth.

Moreover, the stress-based analysis framework includes a magnitude scaling factor (MSF). It allows to adjust the induced CSR during earthquake magnitude M to an equivalent CSR for an earthquake magnitude M = 7.5. According to Youd et al. (2001), the MSF is given by the following expression:

$$MSF = \frac{10^{2.24}}{M^{2.56}} \qquad (2.32)$$

Central to this method is the evaluation of the stress reduction coefficient r_d. It is added to adjust for the flexibility of the soil profile because the soil does not respond as a rigid body (Idriss and Boulanger, 2004). For routine practice the values of r_d are estimated from the chart by Seed and Idriss (1971) as shown in Figure 2.17.
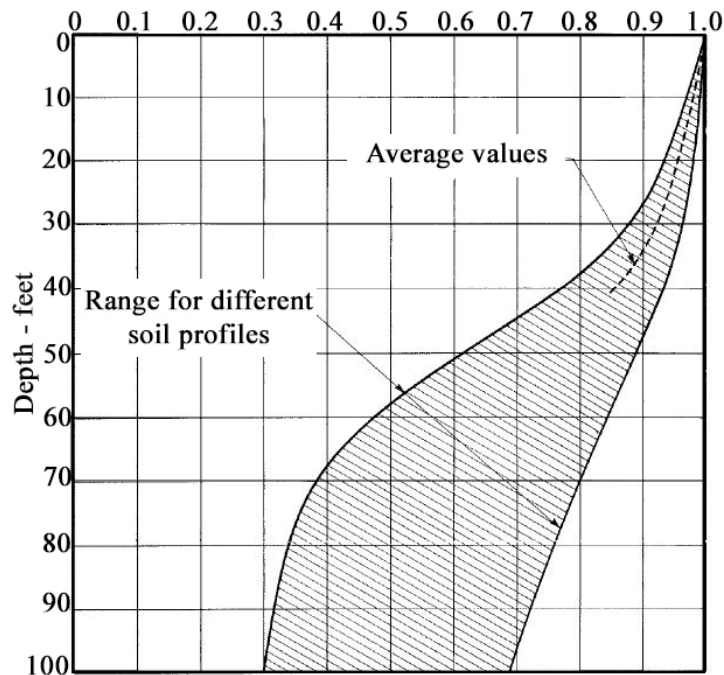
Figure 2.17 Range of values of r_d for different soil profiles (From Seed and Idriss, 1971; modified).

This chart was determined using a limited number of input strong motion and soil profiles having sand in the upper ±15 m. The dashed line labeled "Average values" represents the recommended values of r_d from the surface to a depth of 12 m (~40 ft) (Cetin and Seed, 2004). The value of r_d decreases from a value of 1 at the ground surface to lower value at large depths.

The following equations can be used to estimate the average r_d value given in the chart from the surface to a depth 30 m (~100 ft):

$$r_d = 1.0 - 0.00765z \quad for \; z \leq 9.15m \tag{2.33}$$

$$r_d = 1.174 - 0.0267z \quad for \; 9.15m < z \leq 23m \tag{2.34}$$

$$r_d = 0.744 - 0.008z \quad for \; 23m < z \leq 30m \tag{2.35}$$

where z = depth below ground surface in meters.

The Equations (2.33) and (2.34) were proposed by Liao and Whitman (1986) and the Equation (2.35) was proposed by Robertson and Wride (1997). Youd et al. (2001) suggested the Equations (2.33) and (2.34) for noncritical projects and did not recommend values of r_d below a depth of 23 m. Indeed, the uncertainty of r_d increases with depth and the simplified procedure is not well verified for depths greater than 15 m (Robertson and Wride, 1997). Moreover, the r_d proposal of Seed and Idriss (1971) understates the variance and provides biased (generally high) estimation of r_d between 3 and 15 m. Unfortunately, it is the critical soil strata for evaluating soil liquefaction potential (Seed et al., 2001). Several other relationships have been proposed because of the importance of assessment of CSR. Ishihara (1977) performed a series of analyses using uniform soil profile and sinusoidal input motions and concluded that the parameter r_d can be expressed as:

$$r_d = \frac{V_S}{wz} sin\left(\frac{wz}{V_S}\right) \tag{2.36}$$

where V_S = uniform soil shear wave velocity, w = frequency of excitation, z = depth. This relationship is plotted in Figure 2.18.
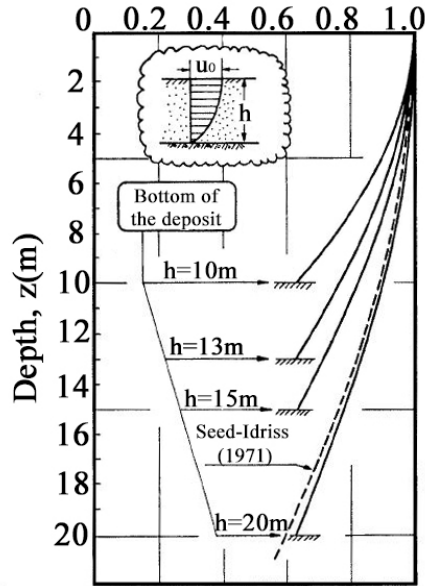
Figure 2.18 Stress reduction coefficient versus depth (From Ishihara, 1977; modified).

Another simple and widely used relationship is the one proposed by Iwasaki (1986) in which the parameter r_d is expressed through a linearly decreasing function with depth as:

$$r_d = 1 - 0.015z \tag{2.37}$$

This function was obtained applying six earthquake motions to two alluvial deposits.

Idriss (1999), based on studies carried out by Golesorkhi (1989), performed several hundred parametric site response analyses and proposed a r_d relationship that takes into account the effects of earthquake magnitude and depth in the evaluation of r_d.

For $z \leq 34$ m the following equation was obtained:

$$ln(r_d) = \alpha(z) + \beta(z)M \tag{2.38}$$

where:

$$\alpha(z) = -1.012 - 1.126 \, sin\left(\frac{z}{11.73} + 5.133\right) \tag{2.39}$$

$$\beta(z) = 0.106 + 0.118 \, sin\left(\frac{z}{11.28} + 5.142\right) \tag{2.40}$$

35

For z > 34 m the following expression is more appropriate:

$$r_d = 0.12\exp(0.22M) \qquad (2.41)$$

in which z = depth in meters and M = moment magnitude.

Plots of r_d calculated using previous equation for M = 5½, 6½, 7½, and 8 are presented in Figure 2.19. Also shown is the average of the range published by Seed and Idriss (1971).
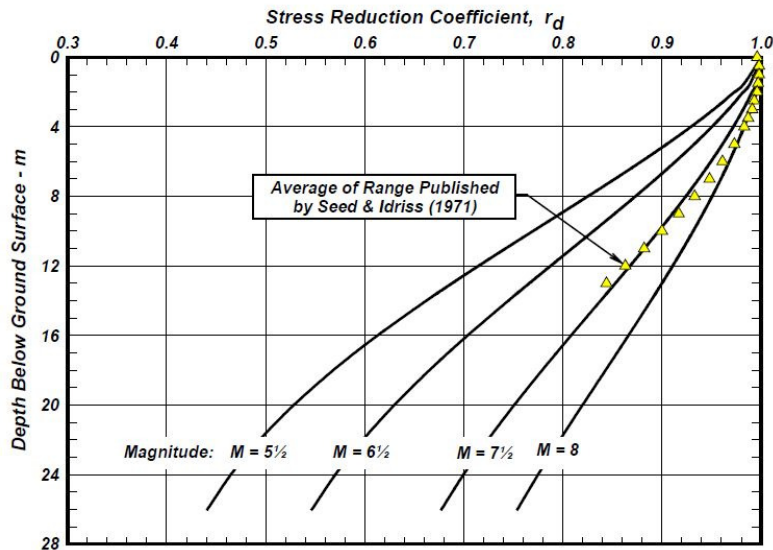
Figure 2.19 Variation of the stress reduction coefficient with depth and earthquake magnitude (From Idriss and Boulanger, 2004).

Cetin and Seed (2004), using the Bayesian updating method, suggested new r_d correlations as a function of depth, earthquake magnitude, intensity of shaking, and site stiffness. They performed a total of 2153 site response analyses by the equivalent linear method. The r_d recommendations proposed by Seed and Idriss (1971) are conservatively biased compared to over 80,000 point estimations of r_d from 2153 cases as shown in Figure 2.20.
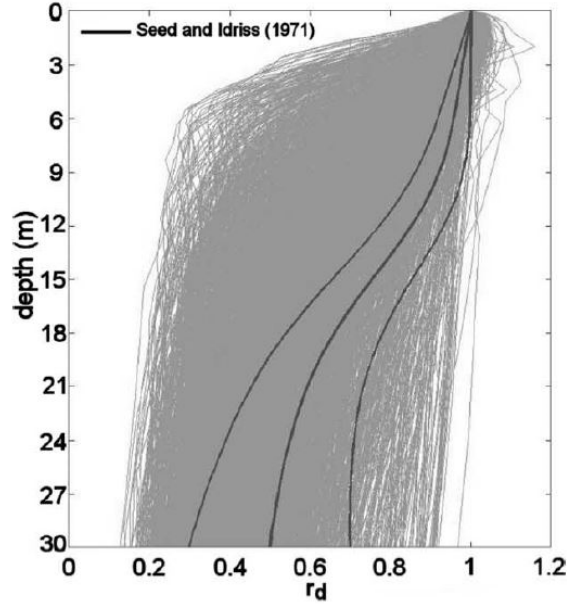
Figure 2.20 r_d results of the site response analyses. Also shown for comparison is the proposed r_d range and recommendations of Seed and Idriss (1971) (From Cetin and Seed, 2004).

Another probabilistic relationship was developed by Kishida et al. (2009a, 2009b) using Monte Carlo simulations. The relationship was based on about 23,000 analyses. The input parameters were the PGA, the average shear wave velocity, and the spectral ratio parameter.

A recent study was performed by Lasley et al. (2016). They suggested a new r_d relationship from equivalent-linear site response analyses. Several forms for r_d were examined and the following form was selected for its simplicity and shape:

$$r_d = (1 - \alpha)\exp\left(\frac{-z}{\beta}\right) + \alpha \tag{2.42}$$

where α = limiting value of r_d at large depths, β = variable that controls the curvature of the function at shallow depths, z = depth in meters and $(1-\alpha)$ = term that scales the exponential.

Two different sets of expression for α and β were proposed, one being a function of magnitude (M_w) and average shear-wave velocity in the upper 12 m of the profile (V_{S12}) and the other solely being a function of M_W. The first set of expressions for α and β is:

37

$$\alpha_1 = \exp(b_1 + b_2 M_w + b_3 V_{S12}) \tag{2.43}$$

$$\beta_1 = \exp(b_4 + b_5 M_w + b_6 V_{S12}) \tag{2.44}$$

and the second set is:

$$\alpha_2 = \exp(b_1 + b_2 M_w) \tag{2.45}$$

$$\beta_2 = b_3 + b_4 M_w \tag{2.46}$$

where b_1-b_6 are regression coefficients.

The cyclic resistance ratio CRR is commonly evaluated using empirical correlations with SPT and CPT (Idriss and Boulanger, 2010; Boulanger and Idriss, 2014). However, Marchetti (1982) and later studies suggested that the horizontal stress index from DMT is a suitable parameter to evaluate the liquefaction resistance of sands (Grasso and Maugeri, 2008; Monaco et al., 2005).

Then, it is possible to evaluate the liquefaction potential index (LPI). The LPI, proposed by Iwasaki et al. (1978), provides a depth-weighted index of the potential for triggering of liquefaction at a site (NASEM, 2016). It is computed as:

$$LPI = \int_0^{20} F(z)w(z)dz \tag{2.47}$$

where:

$$F(z) = 0 \text{ for } F_{SL} \geq 1 \tag{2.48}$$

$$F(z) = 1 - F_{SL} \text{ for } F_{SL} < 1 \tag{2.49}$$

$$w(z) = 10 - 0.5z \tag{2.50}$$

According to Iwasaki et al. (1982), the level of liquefaction severity with respect to LPI is given in

Table 2.1. The LPI framework has been used in many recent studies (Dixit et al. 2012; Maurer et al.

2014; Kim et al. 2020).

Table 2.1 Level of liquefaction severity Iwasaki et al. (1982).

LPI	Level of Liquefaction Severity
0	Very low
$0 < LPI \leq 5$	Low
$5 < LPI \leq 15$	High
$LPI > 15$	Very high

3. Soil containers

Geotechnical scaled seismic model tests can be divided into two categories: shaking table test at 1-g and centrifuge test at n-g (Bojadjieva et al., 2015; Ecemis, 2013; Prasad et al., 2004; Turan et al., 2008; Zayed et al., 2017). Shaking table tests have the advantages of well controlled large amplitude, and easier experimental measurements than centrifuge tests. However, high gravitational stresses cannot be produced (Alaie and Chenari, 2018; Bhattacharya et al., 2012; Bojadjieva et al., 2015; Ecemis, 2013; Jafarzadeh, 2004; Prasad et al. 2004, Mohsan et al., 2018).

Most studies of seismic soil behaviour were for one-dimensional shaking (Carvalho et al., 2010; Gibson et al., 1997; Pamuk et al., 2007; Prasad et al. 2004; Sarlak et al., 2017; Takahashi et al., 2001; Turan et al. 2008; Zayed et al. 2017). However, real earthquake excitations are multiaxial (Zeghal et al. 2018). Ng et al. (2004) performed biaxial shaking centrifuge tests to investigate the response of saturated embankments. Ueng et al. (2006) developed a large flexible laminar shear box for the study of the behaviour of saturated sand under two-dimensional earthquake shaking. Zeghal et al. (2018) investigated the dynamic response and liquefaction of saturated sand deposits subjected to biaxial shaking.

A variety of model container configurations have been used in the last three decades. Six type of soil container could be identified: rigid container, rigid container with flexible boundaries, rigid container with hinged end-wall, Equivalent Shear Beam (EBS) container, laminar container, and active boundary container (Bhattacharya et al., 2012).

3.1 Rigid containers

The simplest way for geotechnical modelling is to use a rigid box. In this design, the shear stiffness of the end wall is much higher that the stiffness of the layers of soil contained in it (Bhattacharya et al., 2012). Sadrekarimi and Ghalandarzadeh (2005) performed 1g shaking table tests using a transparent Plexiglas container to study liquefaction mitigation methods. Motamed and Towhata (2010) used a rigid container with transparent side walls to study the seismic performance of pile groups behind quay walls subjected to liquefaction (Figure 3.1). Özener et al. (2008) investigated the liquefaction behaviour of layered sands using a cylindrical Plexiglas container (Figure 3.2).

(a)

(b)
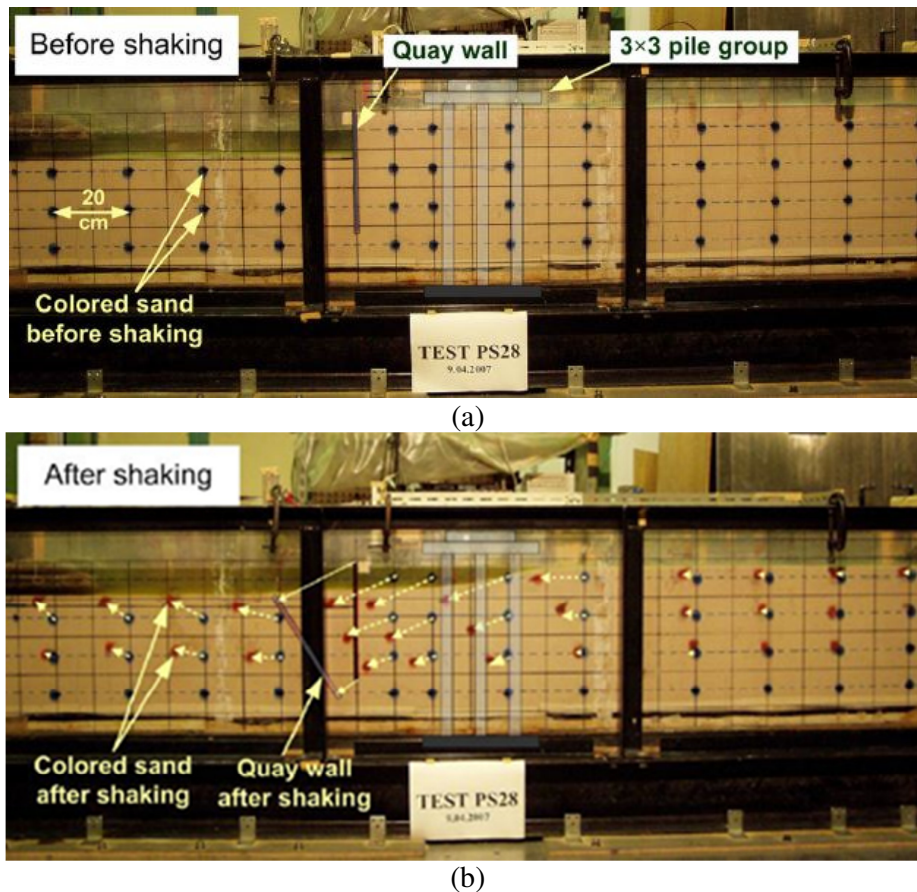
Figure 3.1 View of the model: (a) before shaking, (b) after shaking (From Motamed and Towhata, 2010).
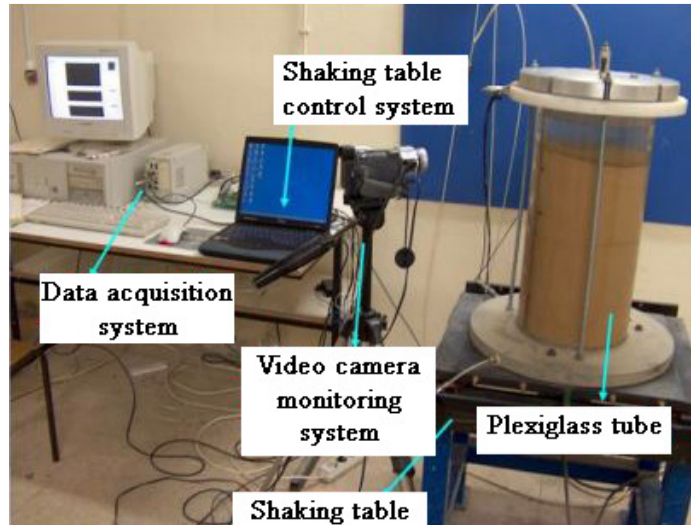
Figure 3.2 General view of the experimental test (From Özener et al., 2008).

However, the rigid box is often not suitable because the waves reach the rigid walls and reflect back to the soil. To reduce the reflection of the waves and the lateral stiffness of the walls, boundary conditions can be modified by the use of soft materials, i.e. duxseal or sponge (Bhattacharya et al. 2012). Madabhushi et al. (1992) performed centrifuge tests using a rigid box with absorbent boundaries constituted of a 5 inch thick duxseal layer with a thin sand sheet. Saha et al. (2015) studied the effect of soil-structure interaction using a rigid box with absorbent boundaries. They were created by fixing up 50 mm thickness of sponge at both end walls (Figure 3.3).
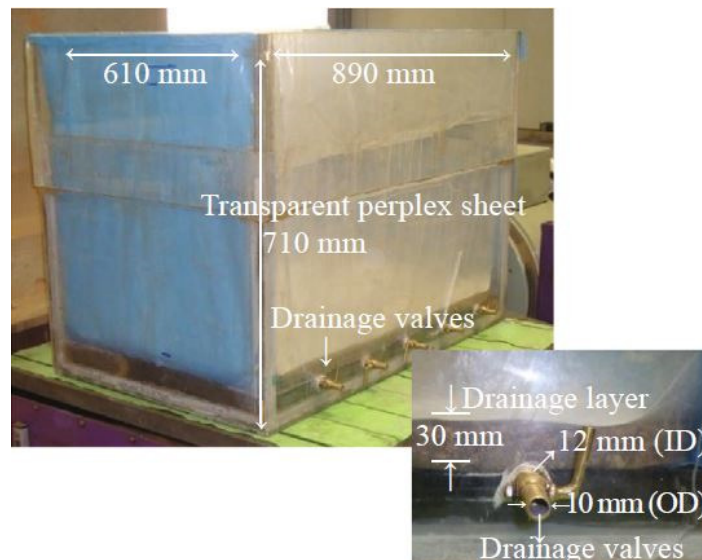
Figure 3.3 Rigid box with absorbent boundaries (From Saha et al., 2015).

In a rigid container with hinged end-wall, the walls can rotate about the base due to the hinged connection (Bhattacharya et al. 2012) (Figure 3.4). Fishman et al. (1995) designed a rigid container with hinged end-wall to replicate the free-field seismic response of a soil layer overlying a rigid base.
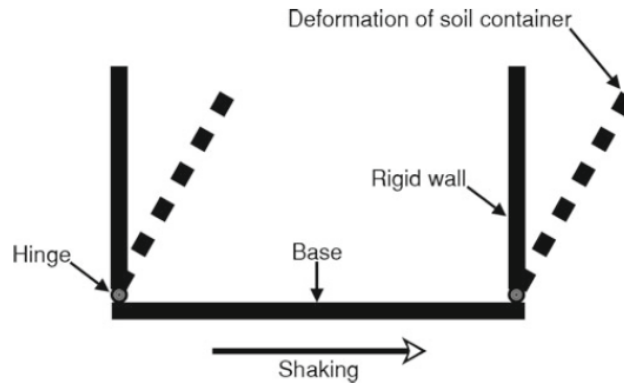
Figure 3.4 Schematic diagram of rigid container with hinged end-walls (From Bhattacharya et al. 2012).

3.2 Equivalent Shear Beam (EBS) container

For increasing the flexibility of the box wall, Equivalent Shear Beam (ESB) containers (Zeng and Schofield, 1996) or laminar box soil containers (Hushmand et al., 1988) can be used.

The ESB container consists of an alternating stack of aluminium alloy and rubber rings for flexibility (Carvalho et al. 2010; Dar, 1993; Madabhushi et al., 1998; Teymur and Madabhushi, 2003; Zeng and Schofield, 1996). In this design, the stiffness of the end walls of the container is designed to match the shear stiffness of the soil contained in it at a particular strain level (Bhattacharya et al. 2012).

Abate and Massimino (2016), Massimo et al. (2019) and Biondi et al. (2015) carried out shaking table tests at the Earthquake Engineering Research Centre (EERC-University of Bristol) in order to investigate some aspects of the dynamic soil-structure interaction (DSSI).

The Bristol University ESB (5.0m x 1.0 m x 1.2 m) was designed by Crewe et al. (1995). It is formed of a series of rectangular aluminium rings, each of which is linked to the upper and lower rings with neoprene blocks (Figure 3.5).

Figure 3.5 General view of the shear stack (From Biondi et al. 2015).

3.3 Laminar container

Laminar box soil container consists of a stack of stiff rings (or layers) supported by ball bearing, linear bearing or rollers. Moreover, during shaking, an internal rubber membrane is placed inside the container to protect the layers from soil penetration. The design principle of a laminar box is to minimize the lateral stiffness of the container in order to ensure that the soil governs the response of the soil-box system (Bhattacharya et al. 2012). The active boundaries container is very similar to the laminar container but external actuators are connected to each lamina (Figure 3.6) (Bhattacharya et al. 2012).
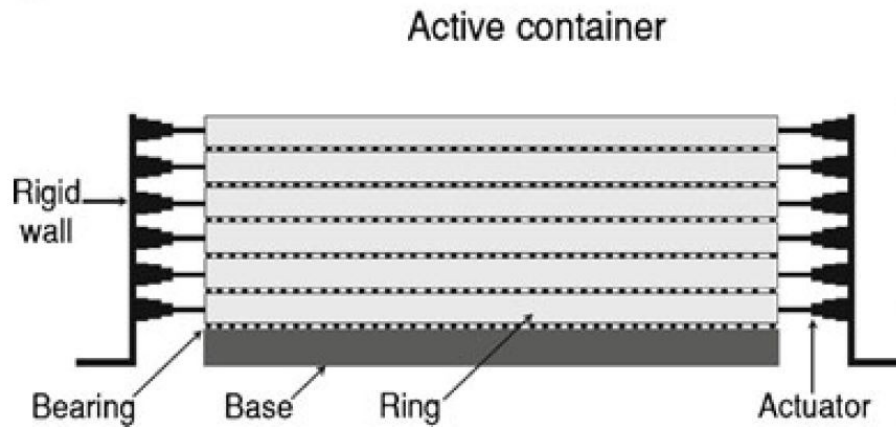
Figure 3.6 Active boundaries container (From Bhattacharya et al. 2012).

Laminar box soil container is often used to model liquefaction (Bojadjieva et al., 2015; Chen and Ueng, 2011; Ecemis, 2013; Mohsan et al., 2018; Thevanayagam et al., 2009; Ueng et al., 2006; Ueng et al., 2010; Yao et al., 2004; Zeghal et al., 2018).

Alaie and Chenari (2018) designed a laminar shear box at the University of Guilan. It consisted of fifteen rectangular layers separated by ball bearings. Four roller columns were installed to prevent the frames from the shaking direction (Figure 3.7).

Ecemis (2013) carried out 1D shaking table tests in order to simulate the liquefaction of loose to medium dense saturated sands. The laminar box was composed of 24 rings made of aluminium I-beams. In order to reduce the friction between the layer, rings were separated and supported by eight rollers (Figure 3.8).

Figure 3.7 General view of the laminar box (From Alaie and Chenari, 2018).
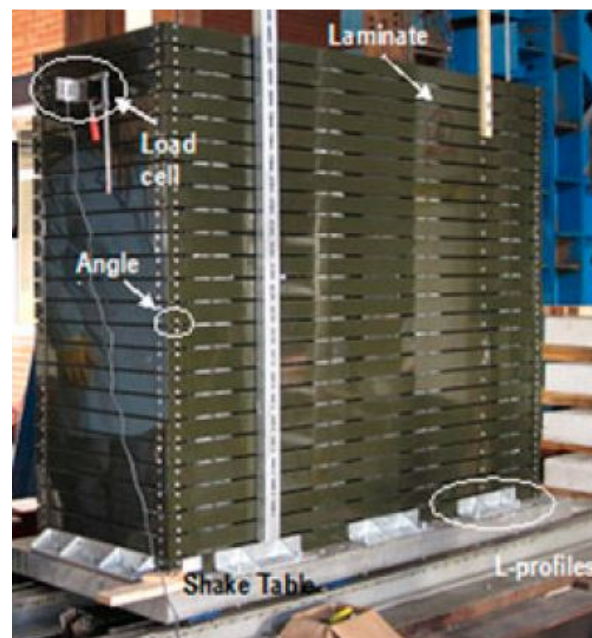
Figure 3.8 General view of the laminar box (From Ecemis, 2013).

Zayed et al. (2017) designed a laminar container at the University of California, San Diego. The container consisted of laminates supported by cantilevered bearings connected to external frames (Figure 3.9). This design has the advantage of avoiding a cumulative vertical load.

Mohsan et al. (2018) designed a laminar soil box for studying the behaviour of saturated soils, especially liquefaction. A set of seventeen laminae were placed on each other in a skeleton by linear bearing (Figure 3.10). The movement is allowed in one direction.
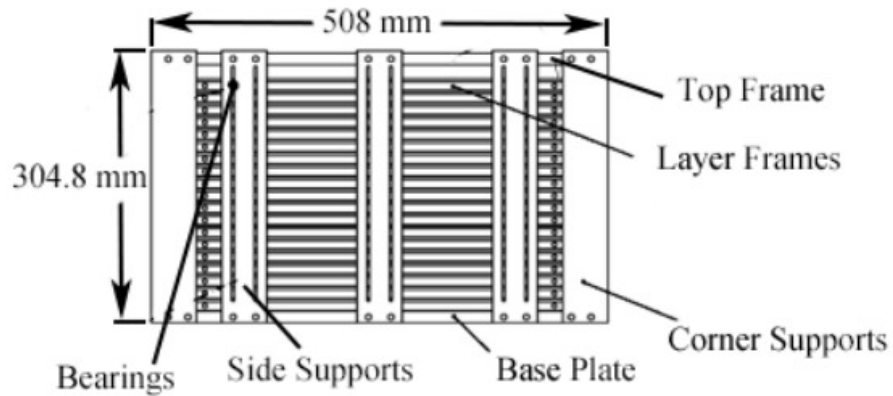
Figure 3.9 General view of the laminar box (From Zayed et al. 2017).

| (a) | (b) |
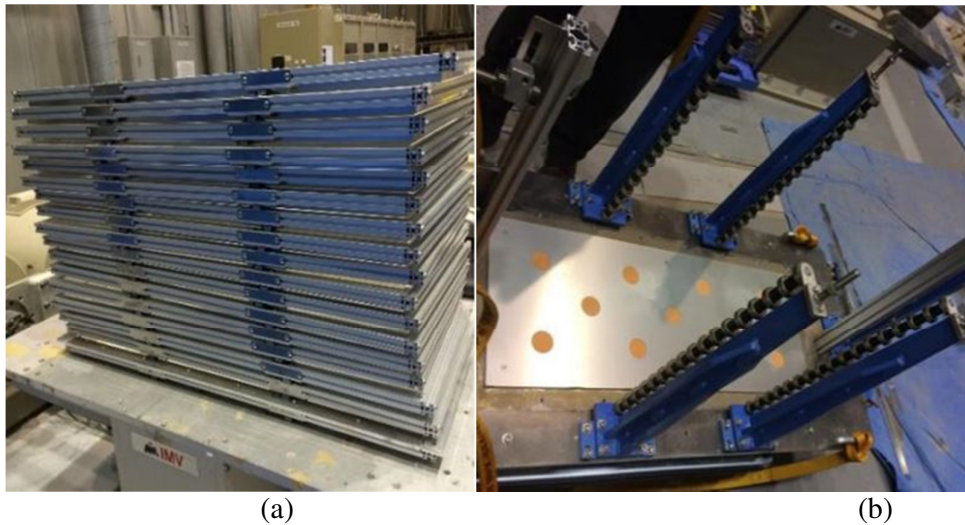
Figure 3.10 (a) Laminae (b) skeleton for laminae (From Mohsan et al. 2018).

Thevanayagam et al. (2009) studied the effects of liquefaction and lateral spreading using 2D laminar box system. The laminar box consisted of 24 octagon-shaped aluminium laminates made of I-beams. The rings were separated by high capacity ball bearings placed between the laminates. Figure 3.11 shows the laminar box system.

Zeghal et al. (2018) performed a number of centrifuge model tests using a 2D laminar container. It consisted of twelve-sided rings separated from the ones above and below by roller bearings. A general view of the laminar container is reported in Figure 3.12.

Figure 3.11. Laminar box system (From Thevanayagam et al., 2009).
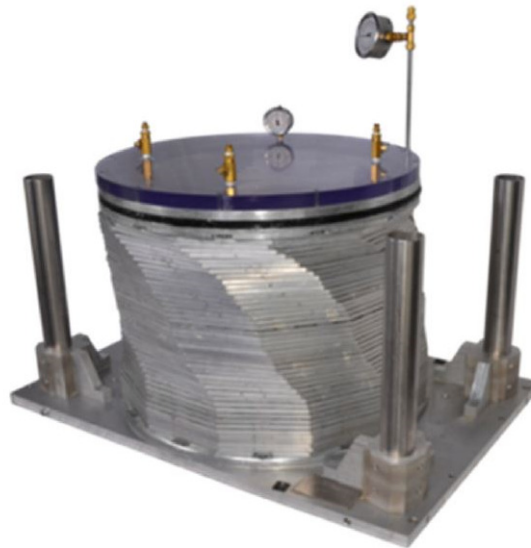
Figure 3.12 General view of the laminar container (From Zenghal et al., 2018).

Jafaradeh (2004) designed a 2D laminar for the shaking table of the Earthquake Research Center of Sharif University of Technology (SUT). The system was composed of 24 layers separated by transfer ball bearings. In the four sides of the box, 4 steel columns were installed to prevent oversize deformations (Figure 3.13).

Figure 3.13 General view of the laminar container (From Jafaradeh, 2004).

A 2D laminar shear box was designed by Ueng et al. (2006) at the National Center for Research on Earthquake Engineering (NCREE) in Taiwan for the study of liquefaction and soil-structure interaction. To allow biaxial motion and to ensure non-torsional motion, a special mechanism design was adopted.

The laminar box was composed of 15 layers supported on the surrounding rigid steel walls. Each layer consisted of two nested frames, an inner frame with inside dimensions of 1880 mm by 1880 mm and an outer frame with inside dimensions of 1940 mm by 2340 mm.

Schematic drawings of the biaxial laminar box are reported in Figure 3.14.
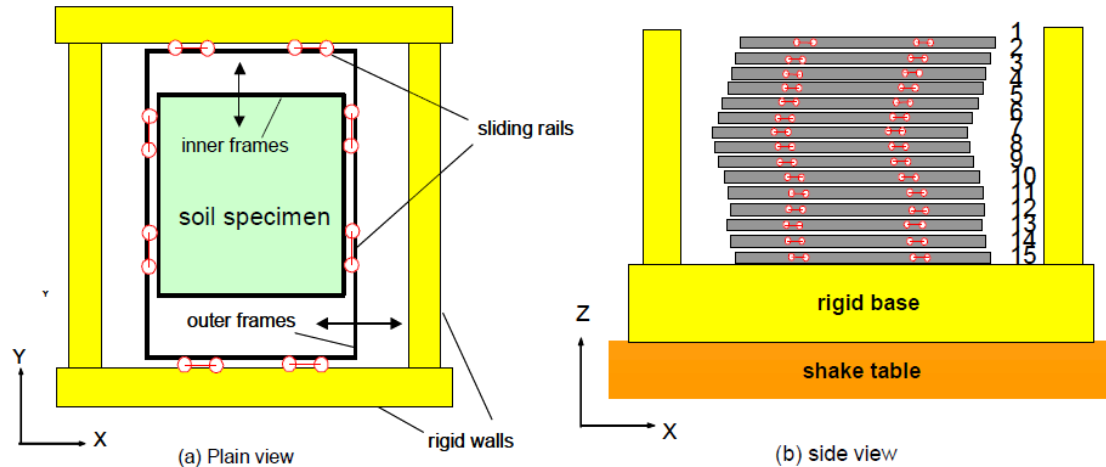
Figure 3.14 Schematic drawings of the biaxial laminar box (From Ueng et al., 2007).

Table 3.1 summarizes several examples of laminar shear boxes.

Table 3.1. Examples of laminar shear boxes

Reference	1-g/N-g	1D/2D	Design
Alaie and Chenari (2018)	1-g	1D	Layers supported by ball bearings
Ecemis (2013)	1-g	1D	Layers supported by rollers
Zayed et al. (2017)	N-g	1D	Layers supported by bearings connected to an external frame
Mohsan et al. (2018)	1-g	1D	Layers placed in a skeleton supported by linear bearing
Thevanayagam et al. (2009)	1-g	2D	Layers supported by ball bearings
Zenghal et al. (2018)	N-g	2D	Layers supported by roller bearings
Jafaradeh (2004)	1-g	2D	Layers supported by ball bearings
Ueng et al. (2006)	1-g	2D	Layers of frames supported on the surrounding rigid steel walls

Before shaking the soil is in a k_0 condition, while during shaking, the normal stresses remain constant and shear stresses increases (Bhattacharya et al. 2012). The soil at different depths could move differently in the horizontal plane (Ueng et al. 2006). For this reason, the design principle of a laminar box is to minimize the lateral stiffness of the container in order to ensure that the soil governs the response of the soil-box system (Bhattacharya et al. 2012).

Important factors that affect the performance of the laminar box are the wall effect, the membrane effect, the effect of friction between the layers and the effect of inertia induced by the mass of the box walls (Ecemis, 2013; Jafarzadeh, 2004; Ueng et al. 2006, Prasad et al. 2004).

In a laminar box the stiffness of the walls is limited to the friction between the layers and the influence of the rubber membrane (Fiegel et al. 1994; Ecemis, 2013). Prasad et al. (2004) performed

several tests, with membrane and without membrane, demonstrating that the membrane effect was localized near the edge and did not affect the performance of the soil.

To reduce the friction between layers ball bearings, linear bearings or roller bearings are placed between the layers. The remaining friction force can be measured by static pull out tests (Ecemis, 2013; Jafarzadeh, 2004; Prasad et al. 2004).

Due to the inertia effect, the measured acceleration in the model is less than the real value. To eliminate this effect, the measured acceleration needs to be corrected by the following equation:

$$a_s = \left(\frac{m_1 + m_2}{m_1}\right) a \tag{3.1}$$

being a_s = acceleration of the soil without the influence of the box; a = measured acceleration; m_1 = mass of soil within the layer; m_2 = mass of the corresponding layer (Ecemis, 2013; Jafarzadeh, 2004; Prasad et al. 2004).

Moreover, Bhattacharya et al. (2012) defined the following criteria that a model container has to satisfy:

a) Maintain stress similarity in the model as in the prototype - The stress field is not affected by the boundaries at a considerably distance from the end-walls. It has to be adequately evaluated by experimental or numerical analysis;

b) Maintain stain similarity in the model as in the prototype - The displacement at a particular depth has to be constant. In other words, the horizontal cross section must remain horizontal;

c) Reduce the wave reflections from the sidewalls;

d) Propagation of the shaking to the soil layer-this criterion can be accomplished by the use of a rough base;

e) Water tightness for saturated soil tests.

4. New Stress Reduction Factor for Evaluating Soil Liquefaction

The procedure for computing the factor of safety against liquefaction is termed "simplified procedure." One of the parameters to be evaluated is the stress reduction coefficient, r_d, as a parameter describing the ratio of cyclic stress for a flexible soil column to the cyclic stress for a rigid soil column (Cetin and Seed, 2004) (Figure 4.1):

$$r_d = \frac{(\tau_{max})_{deformable\ soil}}{(\tau_{max})_{rigid\ body}} \tag{4.1}$$
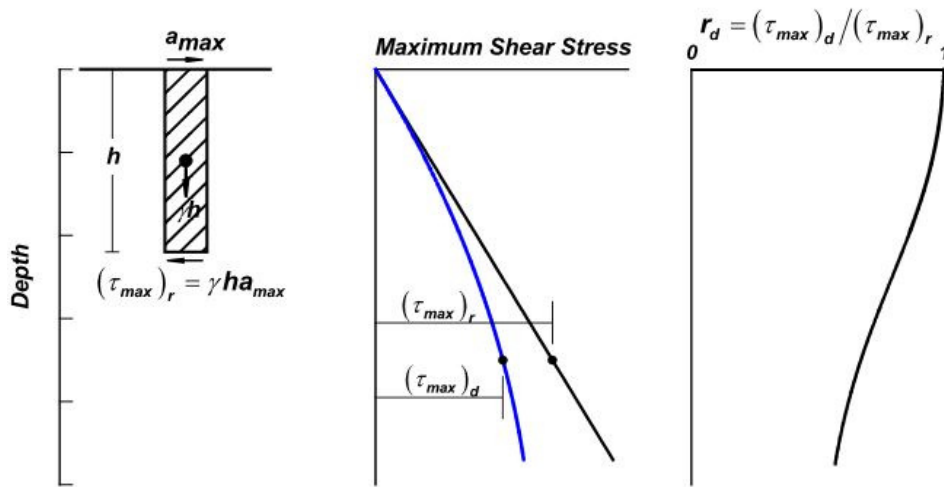
Figure 4.1 Scheme for determining maximum shear stress, τ_{max}, and the stress reduction coefficient, r_d (From Idriss and Boulanger, 2004).

New stress reduction coefficient r_d relationships are proposed for the Catania area (Italy). They have been developed from equivalent-linear site response analyses.

The city of Catania, in South-Eastern Sicily (Italy), is subjected to high seismic hazards. It was shaken by a number of strong earthquakes. In particular the events of February 1169, December 1542, January 1693, February 1818 and January 1848 produced relevant damages (Bonaccorso et al., 2005).

Seismic liquefaction phenomena were reported by historical sources (Baratta, 1901; Del Giudice, 1858; Mercalli, 1883) following the 1693 (M_S = 7.0–7.3, I_o = X–XI MCS) and 1818 (M_S = 6.2, I_o =

IX MCS) strong earthquakes (Galli and Meloni, 1993). The most significant liquefaction features seem to have occurred in the Catania area, near Saint Giuseppe La Rena site, situated in the meisoseismal region of both events. These effects are significant for the implications on hazard assessment mainly for the alluvial flood plain just south of the city, where most industry and facilities are located (Castelli et al., 2016b). The seismic events that occurred in January 1693 and February 1818 have been chosen as scenario earthquakes.

4.1 Site Response Analyses

Local site response analyses have been performed in Catania area, which is recognized as a typical Mediterranean city at high seismic risk (Caruso et al. 2016; Castelli et al., 2018a; Ferraro et al. 2018). A database of about 1200 boreholes and water-wells is available in the data-bank of the Research Project: *Detailed Scenarios and Actions for Seismic Prevention of Damage in the Urban Area of Catania* (Maugeri, 2005). The creation of the database provided the basis for the geotechnical zonation and seismic microzonation of the city of Catania (Grasso and Maugeri, 2009; 2012). Based on the geotechnical zonation, the eastern coastal plain of Catania is susceptible to liquefaction because of the presence of saturated sand deposits in the uppermost 20 meters. Table 4.1 shows experimental sites and tests used to obtain new r_d relationships. The locations of experimental sites are reported in Figure 4.2.

Table 4.1 Experimental sites and tests used to obtain new r_d relationships in Catania area.

Experimental Sites	Tests
Saint Giuseppe La Rena	SPT 1 (borehole 418)
Saint Giuseppe La Rena	SPT 2 (borehole 419)
Saint Giuseppe La Rena	SPT 3 (borehole 420)
Saint Giuseppe La Rena	SPT 4 (borehole 421)
Saint Giuseppe La Rena	SPT 5 (borehole 422)
Saint Giuseppe La Rena	SPT 6 (borehole 423)
Saint Giuseppe La Rena	SPT 7 (borehole 424)
Saint Giuseppe La Rena	SPT 8 (borehole 425)

53

Saint Giuseppe La Rena	SDMT 1
Catania Harbour	SDMT 2
Catania Harbour	SDMT 3
Catania Harbour	SDMT 4
Catania Harbour	SDMT 5
Catania Harbour	SDMT 6
Nazario Sauro school	SDMT 7
Nazario Sauro school	SDMT 8
INGV building	SDMT 9
Madre Teresa di Calcutta School	SDMT 10
STM M6	SDMT 11
Bellini Garden	SDMT 12
Monte Po	SDMT 13
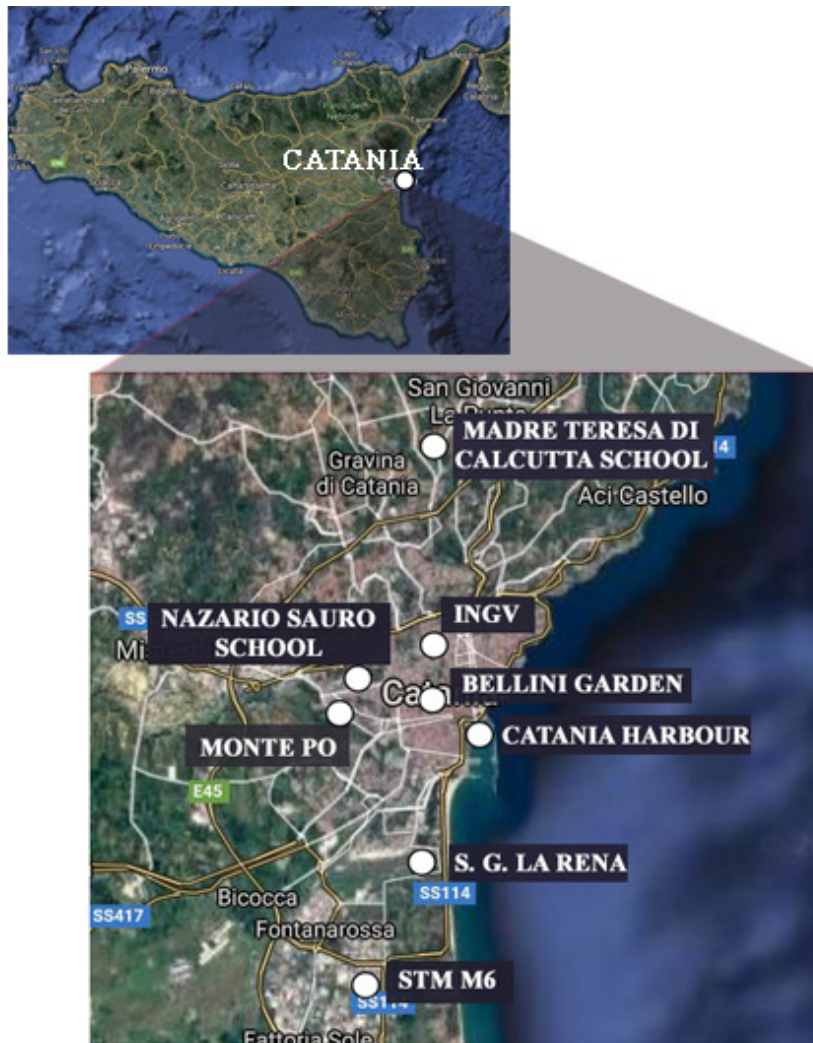
Figure 4.2 Map of experimental sites in Catania area (Italy).

In the Saint Giuseppe La Rena site, eight boreholes (No. 418–425 of the database) were made. The depth of the boreholes varies from 8 to 30 meters, the water table lies around 2 m below the ground

surface and, for all of them, standard penetration tests (SPTs) date are available. Near the borings, eleven cone penetration tests (CPTs) were also made. More recently, at the same site, a seismic dilatometer Marchetti test (SDMT1) was performed. The SDMT1 has an effective depth of 23 m. The subsoil exploration revealed the presence of sand with a content of fine particles less than 30% for a depth of about 10 meters.

The locations of the SPTs, CPTs, and SDMT1 are reported in Figure 4.3 (Grasso and Maugeri, 2008). Figure 4.4 shows an example of SPT profile.
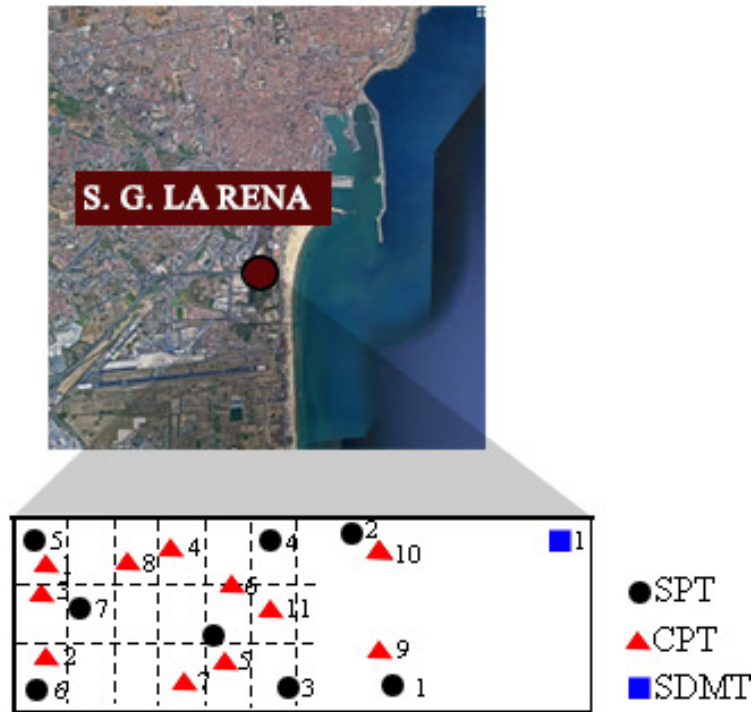
Figure 4.3 Location of standard penetration test (SPT), cone penetration tests (CPT), and seismic dilatometer Marchetti tests (SDMT) in the Saint Giuseppe La Rena site (Eastern coast of Catania, Sicily).
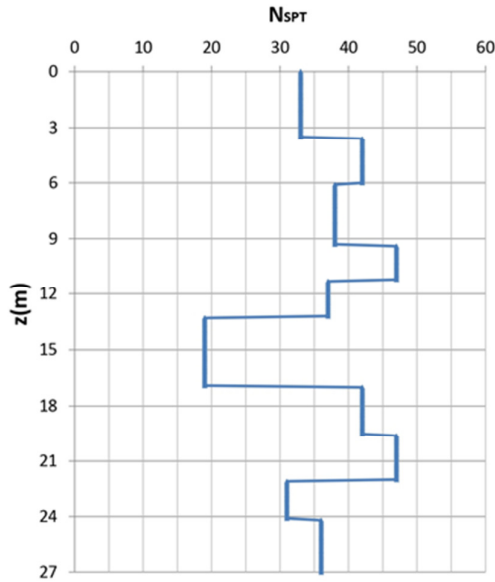
Figure 4.4 N_{SPT} test results versus depth (borehole 421-SPT4).

In the Catania Harbour area five seismic dilatometer Marchetti tests (SDMT2-6) were performed.

They have an effective depth of 30.50 m, 32.00 m, 31.00 m, 30.00 m, and 32.00 m.

Two seismic dilatometer tests, indicated as SDMT 7 and SDMT 8, were conducted from ground level

to depths of 17.5 m and 29.5 m, respectively, in the Nazario Sauro school site. In addition, in the

INGV (National Institute of Geophysics and Volcanology) site, a seismic dilatometer test (SDMT 9)

was performed. It has an effective depth of 34.50 m. Other SDMT tests (SDMT 10-13) were carried

out in Madre Teresa di Calcutta School (SDMT 10, depth of 29.50 m), STM M6 (SDMT 11, depth of

39.94 m), Bellini Garden (SDMT 12, depth of 30.44 m), and Monte Po (SDMT 13, depth of 12.50 m)

sites. Figure 4.5 shows the location of the SDMTs in each experimental sites.

(a)

(b)

Figure 4.5 Layout of SDMT tests: a) Catania Harbour area; b) Nazario Sauro School; c) National Institute of Geophysics and Volcanology (INGV); d) Madre Teresa di Calcutta School; e) STM M6; f) Bellini Garden; g) Monte Po.

The SDMTs have been carried out with the aim to evaluate the soil profile of shear wave velocity for the site response analyses. V_S measurements have been incorporated within a Marchetti flat dilatometer (DMT) by placing a velocity transducer in a connecting rod just above the blade. The seismic modulus is an instrumented tube housing two receivers at a distance of 0.50 m (Castelli et al., 2016a; Grasso and Maugeri, 2008) (Figure 4.6).

(a)	(b)
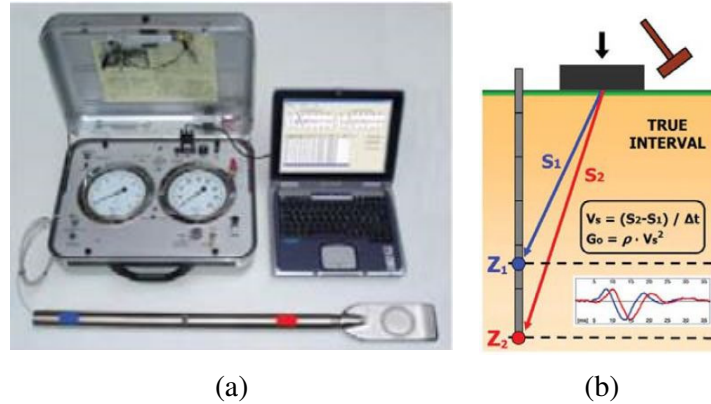
Figure 4.6 Seismic dilatometer test: (a) SDMT equipment (blade and seismic module); (b) schematic test layout (From Castelli et al., 2016a).

The test configuration "two receivers"/"true interval" avoids the problem connected with the possible inaccurate determination of the "first arrival" time sometimes met with the "pseudo interval" configuration (one receiver) (Grasso and Maugeri, 2008; Castelli et al., 2016a). The energization is obtained by a swinging hammer, hitting horizontally a steel parallelepipedal base. The shear wave velocity Vs is the ratio between the difference of distance between the energy source and the two receivers and the measured delay time of the pulse from the upper to the lower receiver (Grasso and Maugeri, 2008)

SDMT obtained parameters by the equipment shown in Figure 4.7 at the sites are: the material index, I_d; the vertical drained constrained modulus, M; the angle of shear resistance, ϕ; the horizontal stress index, K_D; the shear waves velocity, V_S; the small strain shear modulus, $G_0 = \delta V_S^2$.

(a)	(b)

Figure 4.7 SDMT equipment (a) at the Saint Giuseppe La Rena site; (b) at the Catania Harbour site; (c) at STM M6 site; (d) at Bellini Garden site; (e) at Monte Po site; (f) at INGV site.

Shear wave velocity plays a fundamental role in seismic analyses. It is widely recognized that N_{SPT}-value and S-wave velocity of sands are variables dependent on several parameters such as combinations of effective stress, void ratio, soil fabric, etc., (Kokusho et al. 1999).

The possibility of using the standard penetration test blowcounts, in order to determine the V_S, is based on the presence in the literature of several empirical correlations that relate V_S and N_{SPT}-values.

The following empirical correlations have been used to obtain the shear wave velocity profiles, as a function of depth, for each of the eight boreholes.

a)   Ohta and Goto (1978):

$$V_S = 54.33(N_{SPT})^{0.173}\alpha\,\beta\,\left(\frac{z}{0.303}\right)^{0.193} \tag{4.2}$$

where V_S = shear wave velocity (m/s), N_{SPT} = number of blows from SPT, z = depth in meters, α= age factor (Holocene = 1.000, Pleistocene = 1.303), β = geological factor (clays = 1.000, sands = 1.086).

b)   Yoshida and Motonori (1988):

$$V_S = \beta(N_{SPT})^{0.25}\sigma_{V0}'^{0.14}$$
(4.3)

where V_S = shear wave velocity (m/s), N_{SPT} = number of blows from SPT, β= geological factor (any soil 55, fine sand 49), σ_{v0}' = effective vertical stress.

In Figure 4.8, the shear wave velocities are shown against depth for borehole 421, as an example, by Equations (4.2) and (4.3). Also shown is the shear wave velocity from SDMT1. It is possible to notice that the values obtained with the correlation of Yoshida and Motonori are slightly higher than values determined with the correlation of Ohta and Goto and closer than the values measured from the SDMT1. Thus, it was decided to choose for the seismic response analysis, the values of Vs calculated with the Equation (4.3), because they are more likely to adhere to the real values. Moreover, Equation (4.3) better captures the soil variability because it includes the unit weight of soil.
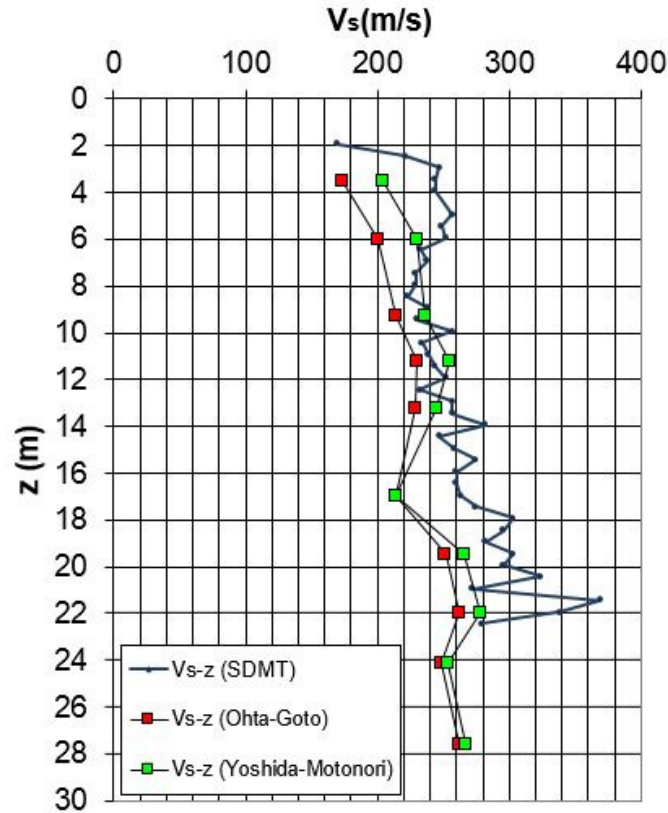
Figure 4.8 Comparison of V_S determined from empirical correlations, Equations (4.2) and (4.3), and SDMT1.

In addition to situ investigations, the following laboratory tests were carried out on undisturbed samples: n. 6 Resonant Column tests, n. 3 Direct shear tests, and n. 3 Triaxial tests.

Local site response analyses have been performed using 1-D linear equivalent code STRATA (Kottke et al., 2008) assuming the geometric and geological models of substrate as 1-D physical models.

The shear wave velocity profiles used for soil response analyses are obtained from SPTs date, available for all the eight boreholes (N°418–425), and from the seismic dilatometer tests (SDMT1-13). The values of the other parameters were taken from the geotechnical characterization obtained through in situ and laboratory tests performed.

The dynamic response model requires the knowledge of the depth of bedrock. The conventionally adopted depth of the bedrock corresponds to a V_S value of 800 m/s (soil type A according to Italian technical regulations, NTC (2018)). The criterion of choice adopted to evaluate the depth of bedrock

consists in the linear interpolation of the shear waves profiles. The depth obtained is approximately 80 m which corresponds to a V_S value of about 800 m/s. During strong earthquakes the soil tends to behave as non-linear material. To take into account the soil non linearity, laws of shear modulus and damping ratio against strain have been inserted in the code.

The fourteen 1-D columns have been excited at the base using four seismograms. The chosen input motions are: three seismograms, called B3R3RAD, PT1R3, and PT6R3, evaluated assuming the source to be along the Hyblean-Maltese fault and generating the 1693 seismic ground motion scenario (Grasso et al., 2005; Laurenzano et al. 2004); a seismogram evaluated assuming the source to be along the Hyblean-Maltese fault and generating the 1818 seismic ground motion scenario (Grasso et al., 2005). The seismograms have been scaled to the maximum PGA of 0.3 g and to the maximum PGA of 0.5 g. Figures 4.9 and 4.10 show the results of seismic site response analyses for the seismic dilatometer tests (SDMT1-13) and for n. 418–425 boreholes to evaluate the variation of r_d over a range of soil profiles.
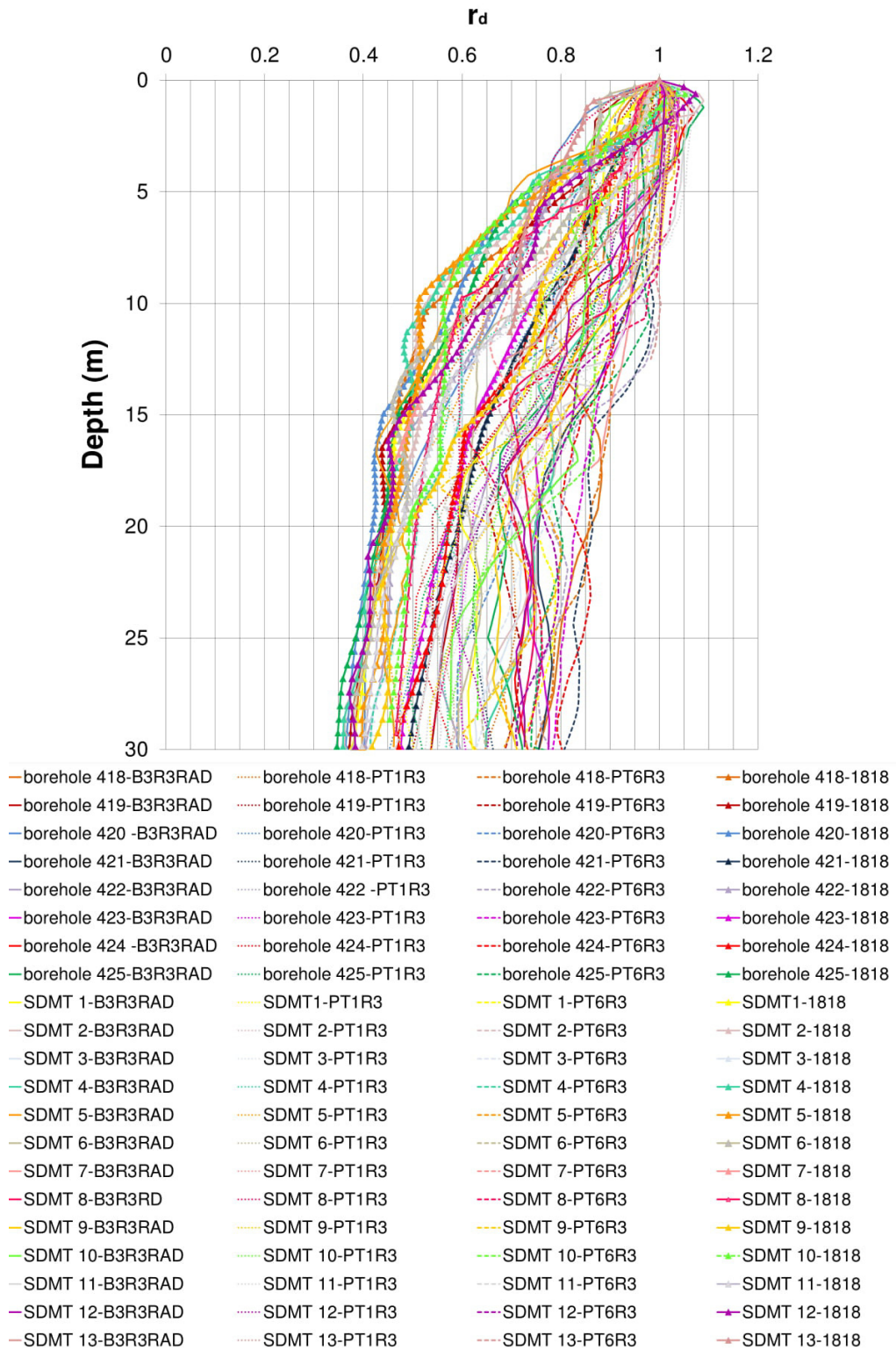
Figure 4.9 r_d results from response analyses for different soil profiles (SPT1-8 and SDMT1-13) using as input 1693 and 1818 scaled synthetic seismograms to the maximum PGA of 0.3 g.
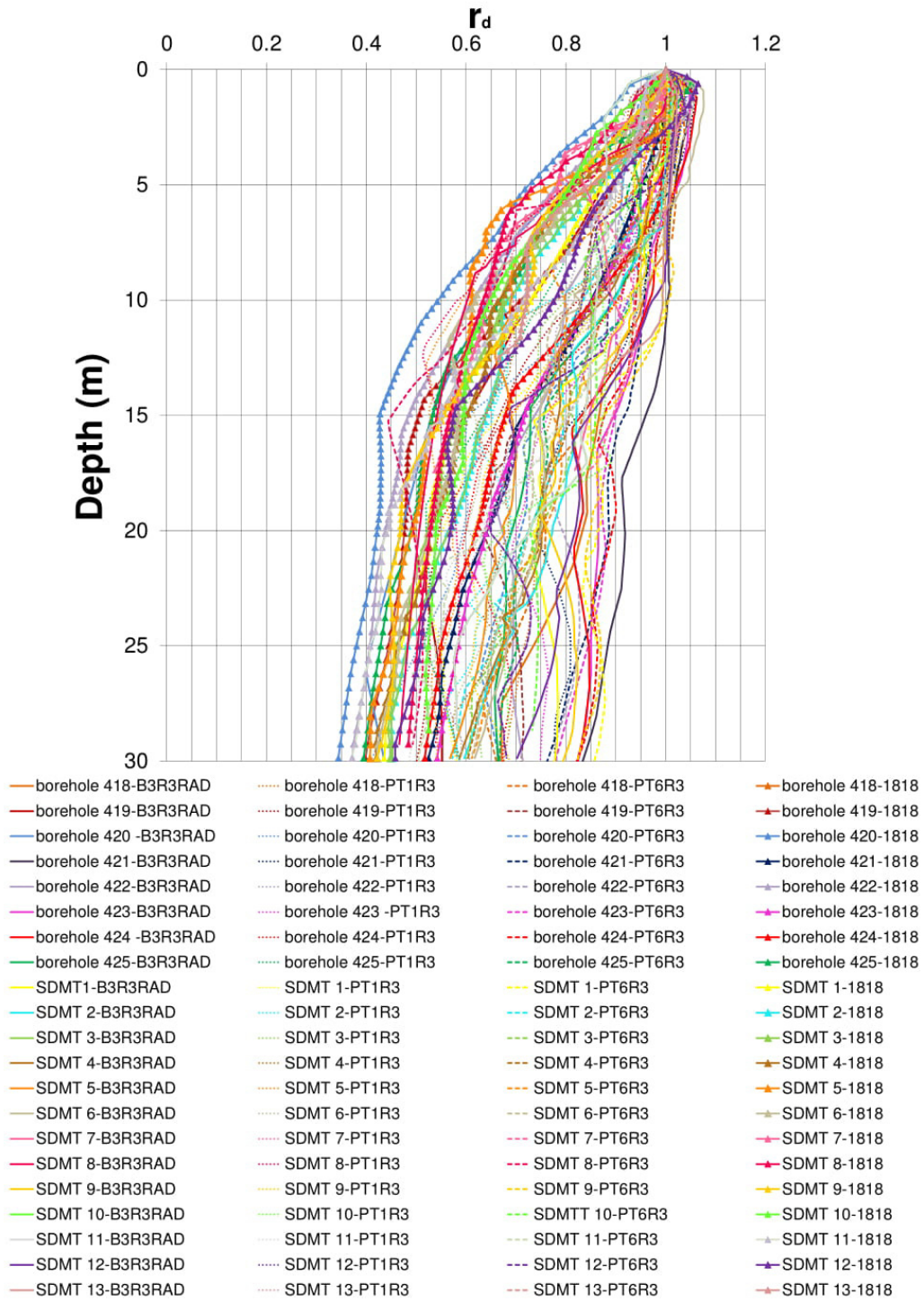
Figure 4.10 r_d results from response analyses for different soil profiles (SPT1-8 and SDMT1-13) using as input the 1693 and 1818 scaled synthetic seismograms to the maximum PGA of 0.5 g.

4.2 Evaluation of the Shear Stress Reduction Factor

According to the approach originally proposed by Seed and Idriss (1971), the ranges of values of r_d for sandy saturated soil profiles of Catania area have been determined. They are shown in the Figures 4.11 and 4.12.
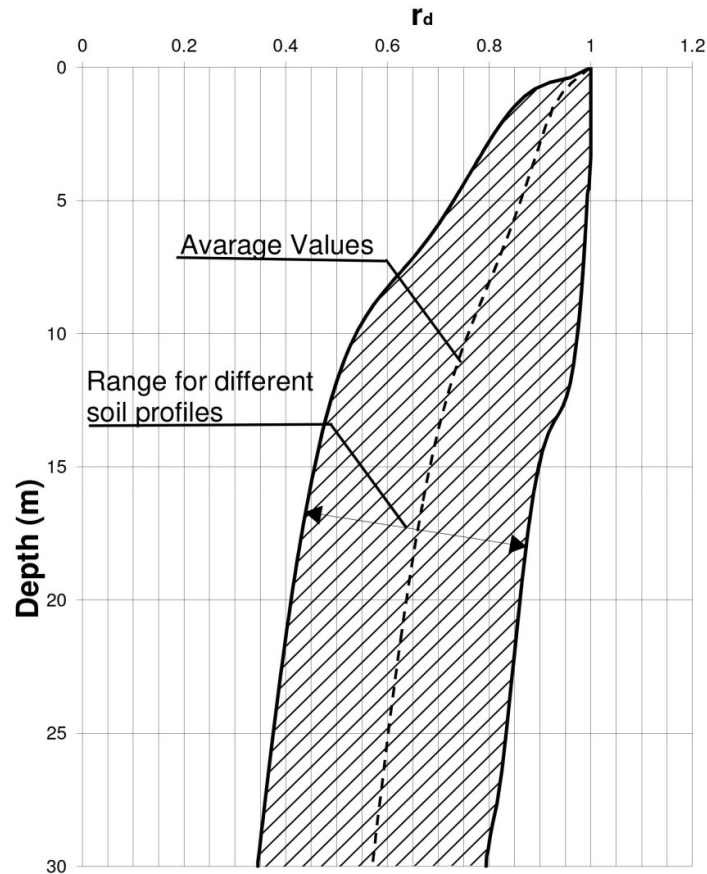
Figure 4.11 Range of values of r_d for different soil profiles (SPT1-8 and SDMT1-13) using 1693 and 1818 scaled synthetic seismograms to the maximum PGA of 0.3 g.
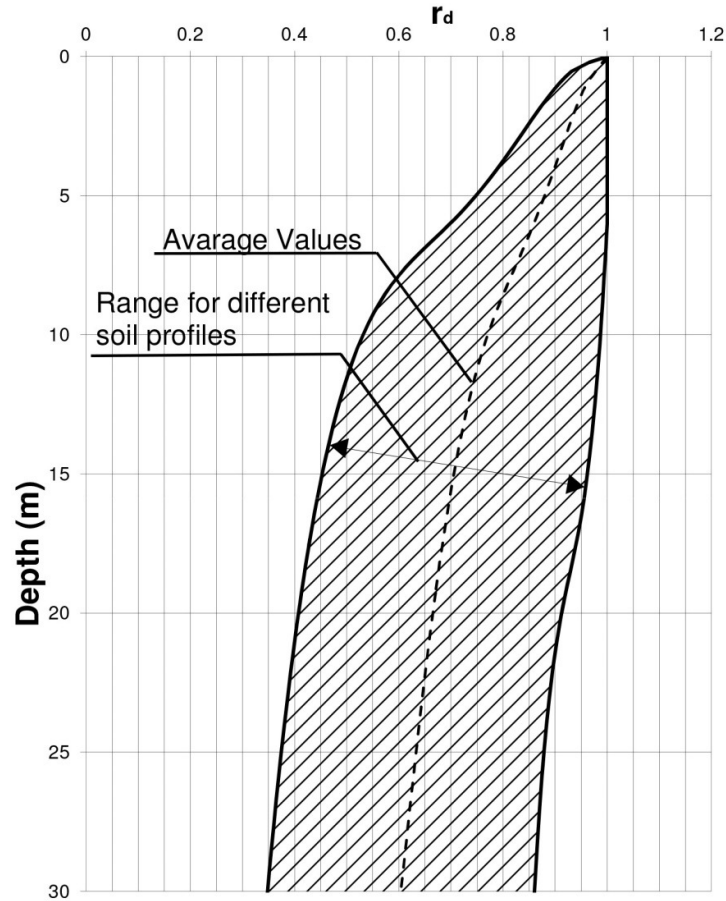
Figure 4.12 Range of values of r_d for different soil profiles (SPT1-8 and SDMT1-13) using 1693 and 1818 scaled synthetic seismograms to the maximum PGA of 0.5 g.

The dashed lines labelled "Average values" represent the recommended values of r_d from the surface to a depth of 30 m. They can be approximated by Equations (4.4) and (4.5).

$$r_d = 1 - 0.018\,z \qquad PGA = 0.3g \tag{4.4}$$

$$r_d = 1 - 0.017\,z \qquad PGA = 0.5g \tag{4.5}$$

In the Figure 4.13, the r_d relationships obtained for soil profiles of the Catania area are compared to the relationship previously proposed by Iwasaki (1986). As can be seen from the chart, the latter provides slightly higher estimates of r_d.
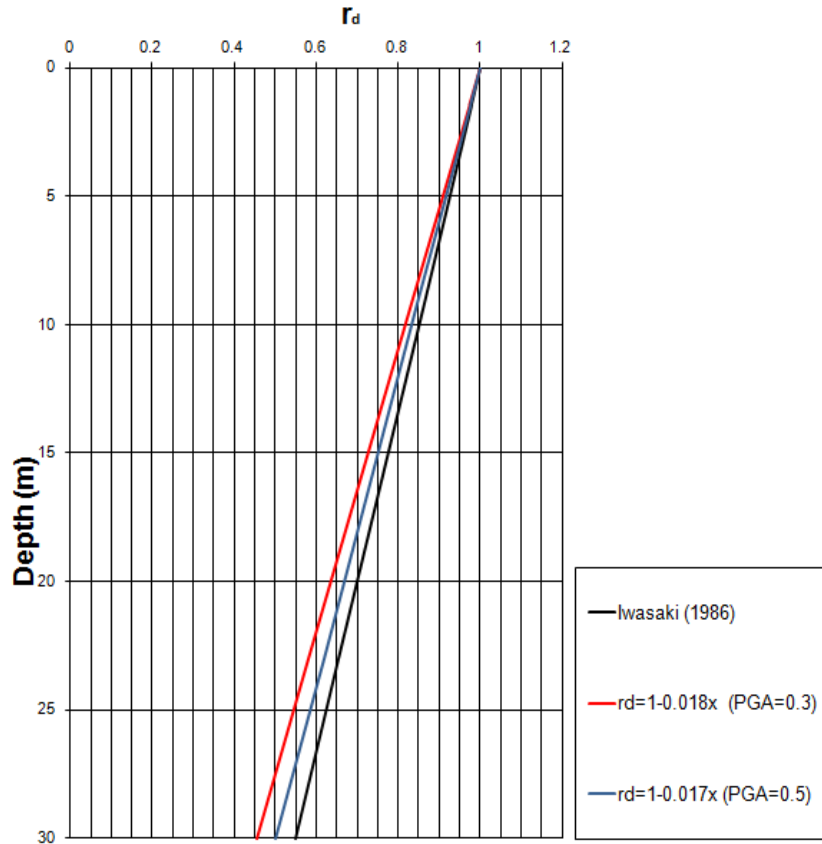
Figure 4.13 Comparison of r_d relationship obtained by Iwasaki (1986) and relationships proposed in this study.

Moreover, the following two sets of equations can be used to estimate the average r_d values, given in the Figures 4.11 and 4.12, from the surface to a depth 30 m:

$$r_d = 1.0 - 0.028z \quad for \ z \leq 9.15m \quad (PGA = 0.3g) \tag{4.6.1}$$

$$r_d = 0.840 - 0.010z \quad for \ 9.15m < z \leq 23m \quad (PGA = 0.3g) \tag{4.6.2}$$

$$r_d = 0.723 - 0.005z \quad for \ 23m < z \leq 30m \quad (PGA = 0.3g) \tag{4.6.3}$$

$$r_d = 1.0 - 0.024z \quad for \ z \leq 9.15m \quad (PGA = 0.5g) \tag{4.7.1}$$

$$r_d = 0.889 - 0.011z \quad for \ 9.15m < z \leq 23m \quad (PGA = 0.5g) \tag{4.7.2}$$

$$r_d = 0.677 - 0.002z \quad for \ 23m < z \leq 30m \quad (PGA = 0.5g) \tag{4.7.3}$$

67

In the Figure 4.14, the suggested r_d relationships are compared to relationships previously proposed by Liao and Whitman (1986), and Robertson and Wride (1997) from the chart of Seed and Idriss (1971). It is possible to observe that the r_d proposal of Seed and Idriss (1971) provides higher estimation of r_d between 0 and 19 m.
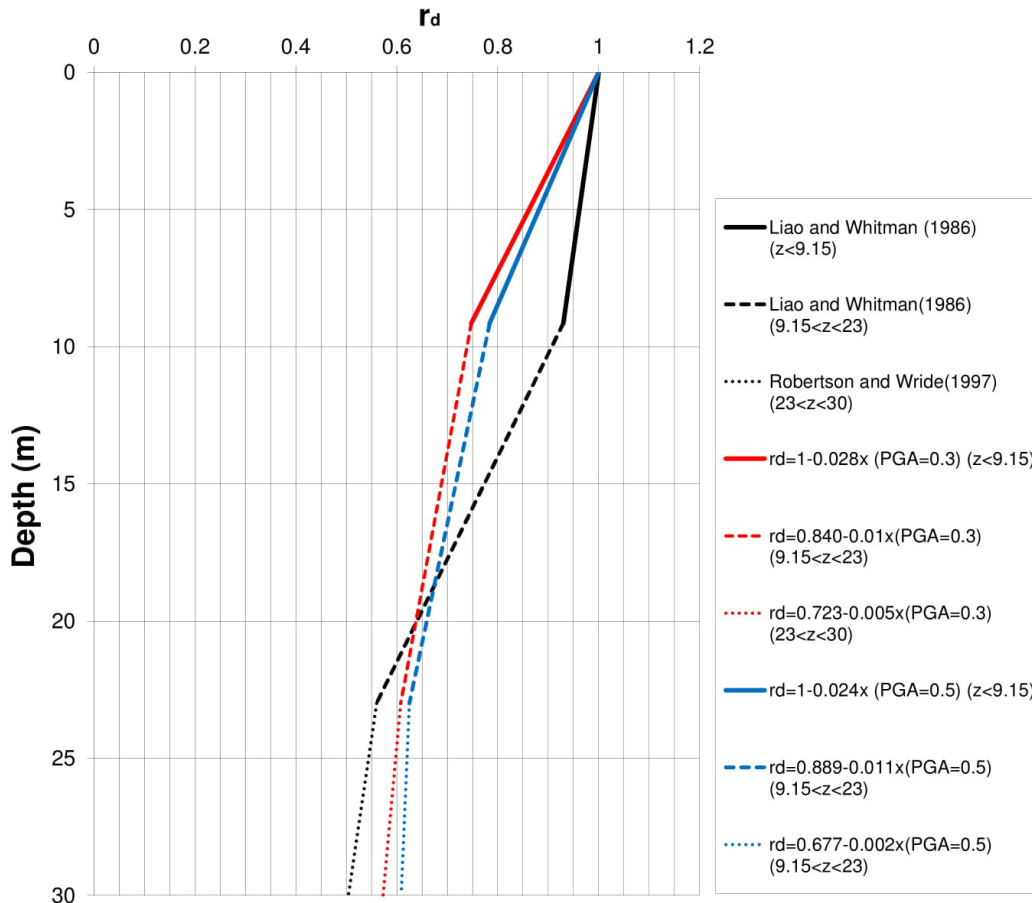
Figure 4.14 Comparison of r_d relationships obtained by Liao and Whitman (1986) and Robertson and Wride (1997), and relationships proposed in this study.

Lastly, it is possible to notice that the Equations (4.4), (4.6.1), (4.6.2), and (4.6.3) provide slopes of the straight lines slightly lower than that given by Equations (4.5), (4.7.1), (4.7.2), and (4.7.3), respectively. This is due to the fact that during strong motion the soil tends to behave as non-linear.

5. Numerical application to a strategic building in the city of Messina

The study deals with 3D FEM full-coupled structure analyses for a strategic building located in the city of Messina (Sicily, Italy). The structure was built after the strong earthquake of 1908, also known as Messina-Reggio Calabria earthquake, that caused severe ground shaking. A parametric study with three different seismograms of the 1908 earthquake has been carried out. Deep site and laboratory investigations, undertaken in the zone of the Regional Department of Civil Defence (DRPC), have allowed the definition of the geometric and geotechnical model of the subsoil. Numerical analyses have been conducted with the finite element code PLAXIS 3D. The Free-Field and Compliant Base dynamic boundary conditions have been considered.

5.1. Geology and Seismicity of the Area

Sicily is one of the Italian regions with high seismic risk. It was shaken in the past by large destructive events (1169, 1542, 1693, 1783, 1818, 1848 and 1990) (Grasso and Maugeri, 2002, 2009, 2014). A repetition of events with similar characteristics would provide the additional risk of a damaging tsunami, as well as, liquefaction phenomena around the coastal areas (Castelli et al., 2016b; Grasso et al., 2021; Maugeri and Grasso, 2013).

The Regional Department of Civil Defence (DRPC) in Messina (eastern tip of Sicily) is located in a flat area weakly inclined eastward. It falls in a wide coastal plain characterized by alluvial deposits of Holocene age (Figure 5.1), with average width around 700 meters and long coastline in direction NNE-SSW (Pino et al., 2018).
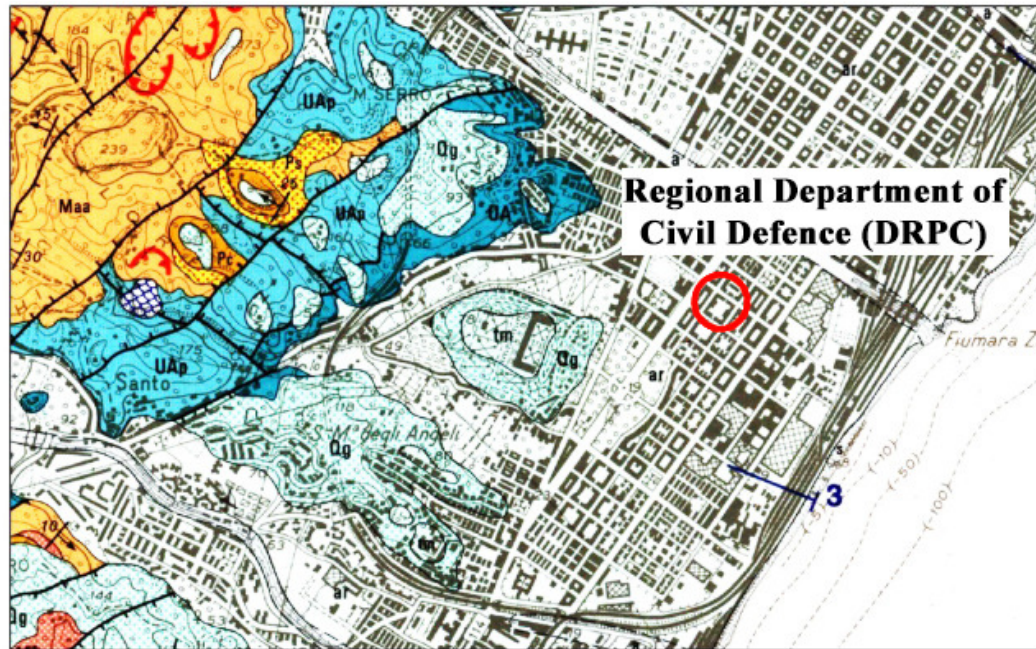
Figure 5.1 Geological sketch of the city of Messina (scale 1:25.000) (Gargano, 1994; modified).

In the North-eastern part of the Sicily-Messina Strait, there is a transition between a residual subduction process (located in the Southern part of the Calabria Region) and the collisional Europe-Africa process established in the western part of the North-Eastern Sicily (Castelli et al., 2018b).

Due to the residual subduction process (from the Messina Strait to the Lamezia Plain), superficial crustal structures are subjected to a regime of detachment stress. It is at the origin of violent earthquakes in normal fault mechanism of the Arco Calabro-Peloritano (Pappalardo et al., 2016), especially with the earthquakes of February 5 and 7, 1783 (Gioia Tauro plain and Mesima Valley) and with the December 28, 1908 earthquake (Strait of Messina) (Pino et al., 2018). In fact, the Strait of Messina lies between the Calabrian region of southern Italy and Sicily, forming a part of the Calabrian Arc, where the African Plate is thrust beneath Calabria, Sicily and the Tyrrhenian Sea. The Strait is bounded on either side by a series of normal faults which approximately follow the north-south and the northeast-southwest trending Sicilian and Calabrian coastlines (Figure 5.2) (Castelli et al., 2018b).

70
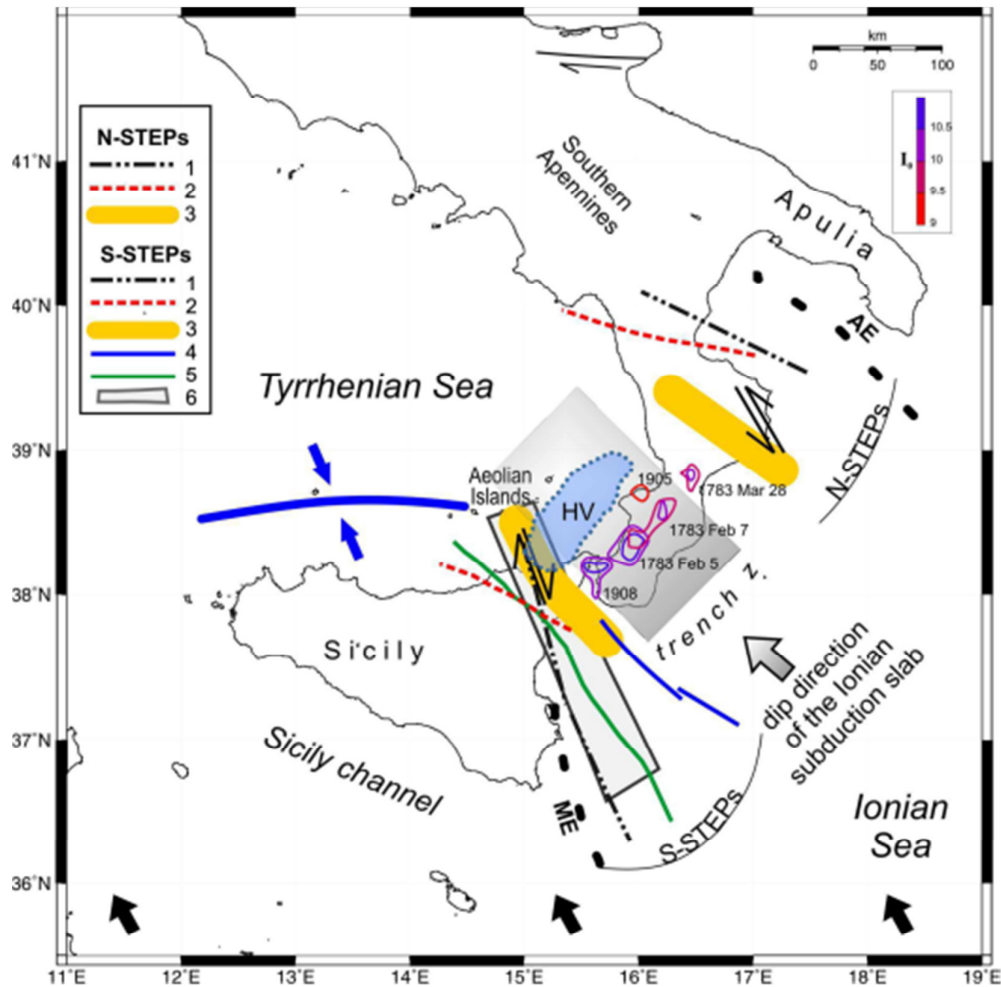
Figure 5.2 Structural sketch of Calabrian Arc Region with localization of historical earthquakes and STEP fault systems (after Pino et al., 2008).

The February 5–March 28, 1783 earthquake sequence in Calabria (M 5.7 and M 7.0), with up to 50,000 casualties, was an event that caused severe damage to both Messina and Reggio Calabria areas (RMS, 2008).

On December 1908, a devastating earthquake occurred along the Strait of Messina between eastern tip of Sicily and the western tip of Calabria in the south of Italy. The Southern Calabria-Messina earthquake (Intensity MSC XI, Mw 7.24) was the strongest seismic event of the 20th century in Italy with the most ruinous in term of casualties (at least 80,000) (Castelli et al., 2018b). Moreover, liquefaction phenomena occurred in the Messina and Reggio Calabria areas (Castelli et al., 2019).

The 1908 seismic event has been chosen as the scenario earthquake in this study. Figure 5.3 shows the intensity map for 1908 earthquake.
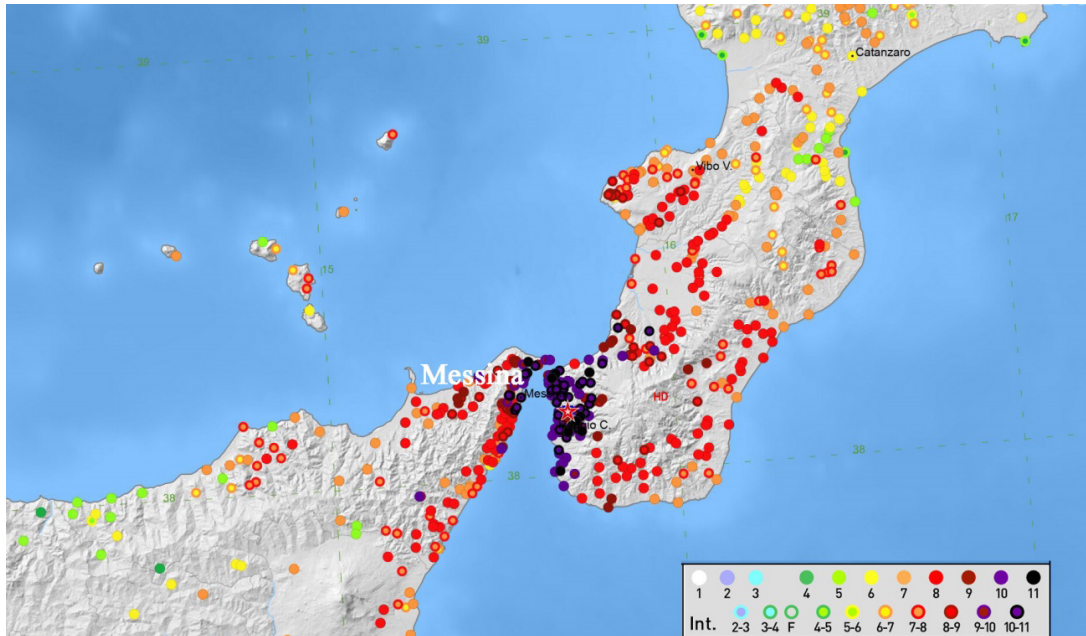
Figure 5.3 Intensity map. Earthquake of December 28, 1908 (Guidoboni et al., 2018, 2019; modified).

Moreover, the area around the Strait of Messina has experienced the January 11, 1693 earthquake. The event, known as "Val di Noto earthquake," struck a vast territory of Southeastern Sicily. It had an estimated magnitude of 7.4 on the moment magnitude scale and caused the partial, and, in many cases, total, destruction of 57 cities and 60,000 casualties (Bonaccorso et al., 2015; Castelli et al., 2016a).

5.2. *The DRPC building and geotechnical properties of the subsoil*

The Regional Civil Defence Department (DRPC) in the city of Messina has been chosen as study case. The building is located in an urbanized area and it rises about 700 meters from the coast. The structure is composed of four floors: an underground floor (at 1.6 m below the ground surface), a

raised floor, a first floor and a second floor. The building has a rectangular plan and it was built after the strong earthquake of 1908. In plan, it is possible to identify two compartments: a main compartment (I) composed of perimeter and spine walls and a second compartment (II) composed of masonry columns and reinforced concrete beams (Figure 5.4). The building foundation is made up of concrete beams (I Compartment) and plinths (II Compartment). They were embedded for a depth equal to 2.9 m.
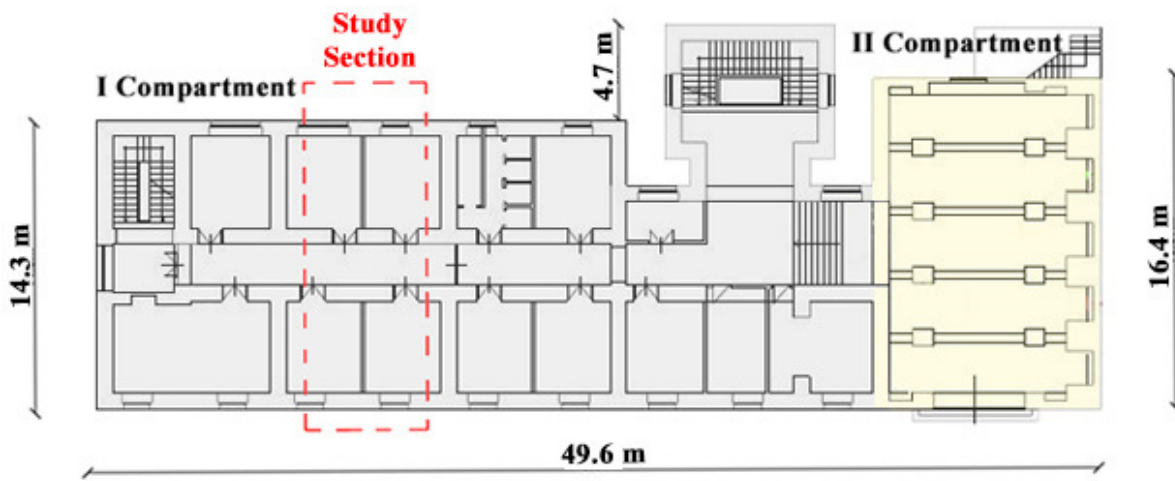
Figure 5.4 Plan view of the raised floor of the DRPC building.

To evaluate the geotechnical characteristics of the subsoil, in situ and laboratory tests have been performed in the zone of the Regional Department of Civil Defence (DRPC) in Messina. Three boreholes (S1, S2 and S3) have been carried out and, for all of them, Standard Penetration Tests (SPTs) are available. The locations of the boreholes are reported in Figure 5.5.

Figure 5.5 Boreholes location in the zone of the Regional Department of Civil Defence (DRPC) in Messina (Sicily, Italy).

The results of boreholes, driven to the depths of 60 meters (S1 and S2) and 80 meters (S3), show the

presence of silty sand and gravel interspaced from horizons of clay and sandy silt (Figure 5.6).
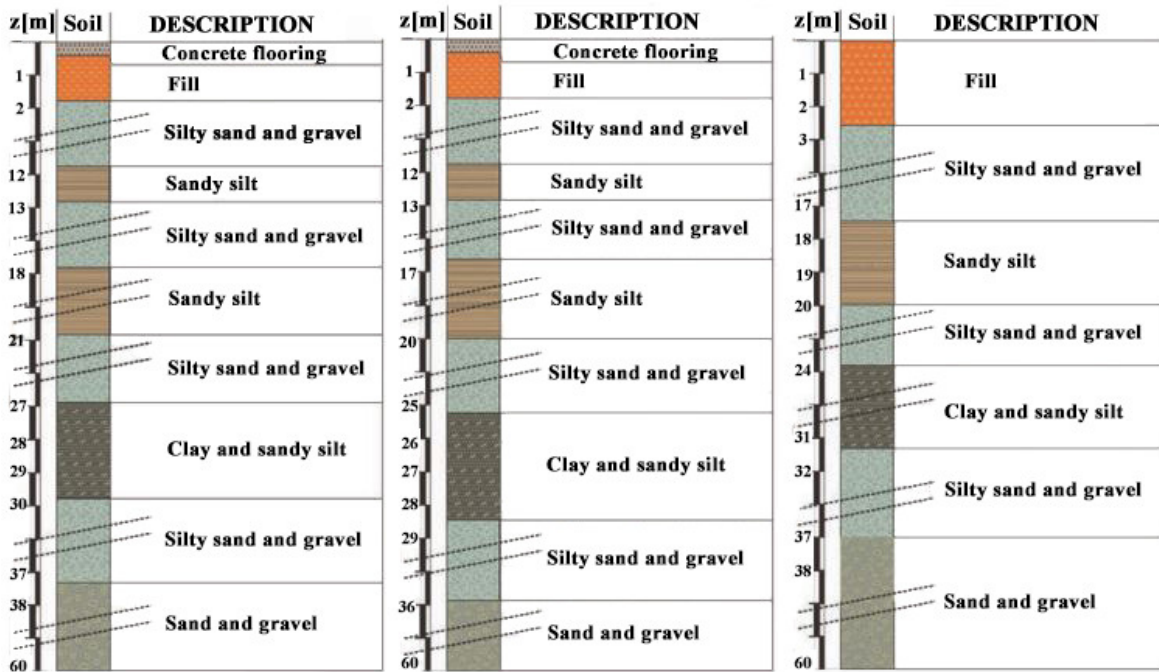
Figure 5.6 Soil profiles of S1, S2 and S3 boreholes.

The S1 and S2 boreholes have been equipped for the execution of a Cross Hole test and S3 has been equipped for the execution of a Down Hole test. A Seismic Dilatometer Marchetti Test (SDMT) has been also performed with the aim to evaluate the soil profile of the shear wave velocity.

In Figure 5.7 the shear wave velocities, obtained by D-H, C-H and SDMT tests, are shown against depth.
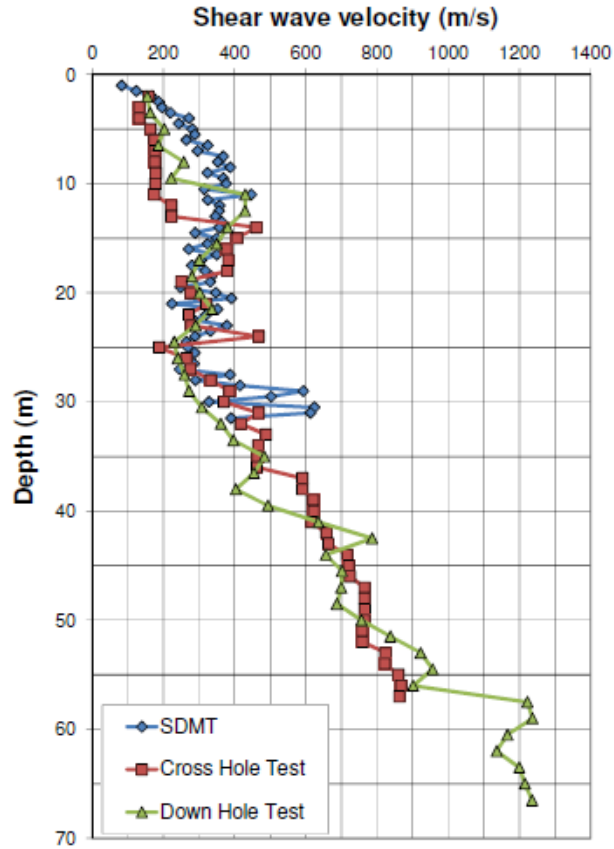
Figure 5.7. V_S profiles obtained by D-H, C-H and SDMT tests.

In addition to in situ investigations, the following laboratory tests have been carried out on undisturbed samples: n. 6 Direct Shear Tests (DST), n. 2 Consolidated Undrained Triaxial Tests (CUTxT), n. 4 Cyclic Loading Torsional Shear Tests (CLTST), n. 4 Resonant Column Tests (RCT). Based on the laboratory tests, index properties and strength parameters mainly encountered in this area are reported in Tables 5.1 and 5.2, respectively.

Table 5.1 Index properties for the study area.

Sample	H [m]	γ [kN/m^3]	w_n [%]	G_s	e	n	S_r [%]
S1C1	7.00 - 7.40	18.34	11.93	2.79	0.67	0.40	49.95
S2C1	3.00 - 3.50	18.63	18.90	2.75	0.72	0.42	72.03
S2C2	6.00 - 6.40	19.81	13.19	2.74	0.54	0.35	67.15
S3C1	5.50 - 6.00	19.12	15.08	2.79	0.65	0.39	64.87
S3C2	14.60 - 15.00	19.91	12.51	2.74	0.52	0.34	65.57
S3C3	21.00 - 21.40	16.18	33.61	-	-	-	-
S3C4	27.00 - 27.50	17.95	39.78	2.76	1.11	0.53	99.11

where: z=depth, γ=unit weight per volume; w_n=natural water content, G_s=specific gravity, e= void index, n=porosity, S_r=degree of saturation.

76

Table 5.2 Strength parameters for the study area.

Sample	H [m]	DST c' [kPa]	DST φ' [°]	DST c_r [kPa]	DST φ_r [°]	CUT_XT c_u [kPa]	CUT_XT φ_u [°]	CUT_XT c' [kPa]	CUT_XT φ' [°]
S1C1	7.00 - 7.40	12	34	-	-	-	-	-	-
S2C1	3.00 - 3.50	15	32	-	-	-	-	-	-
S2C2	6.00 - 6.40	30	41	-	-	-	-	-	-
S3C1	5.50 - 6.00	16	23	-	-	96	17	85	22
S3C2	14.60 - 15.00	9	33	-	-	-	-	-	-
S3C3	21.00 - 21.40	-	-	-	-	-	-	-	-
S3C4	27.00 - 27.50	15	21	0	11	82	14	38	20

where: c' = Cohesion and φ' = Angle of Shear Resistance; Direct Shear Test (DST), CU Triaxial Tests (CUT$_X$T).

Shear modulus G and damping ratio ξ have been obtained in the laboratory from Resonant Column Tests (RCT) and Cyclic Loading Torsional Shear Tests (CLTST) performed by means of a Resonant Column/Cyclic Loading Torsional Shear Apparatus.

Values of shear modulus G [MPa] and damping ratio ξ [%] versus γ [%], for S2C3 sample, as an example, are reported in Figure 5.8.
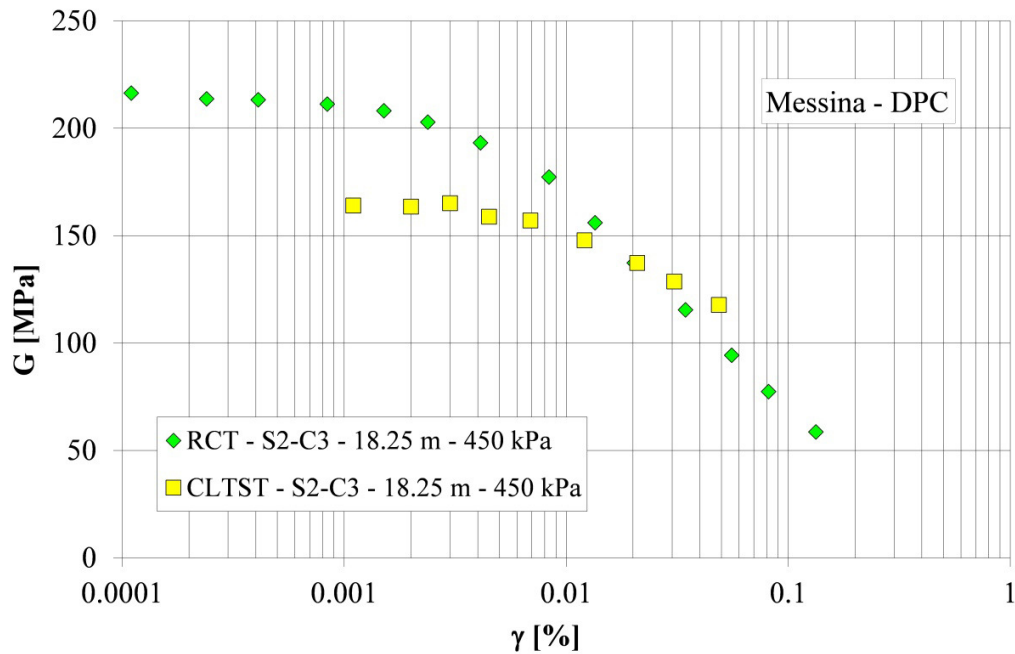
(a)
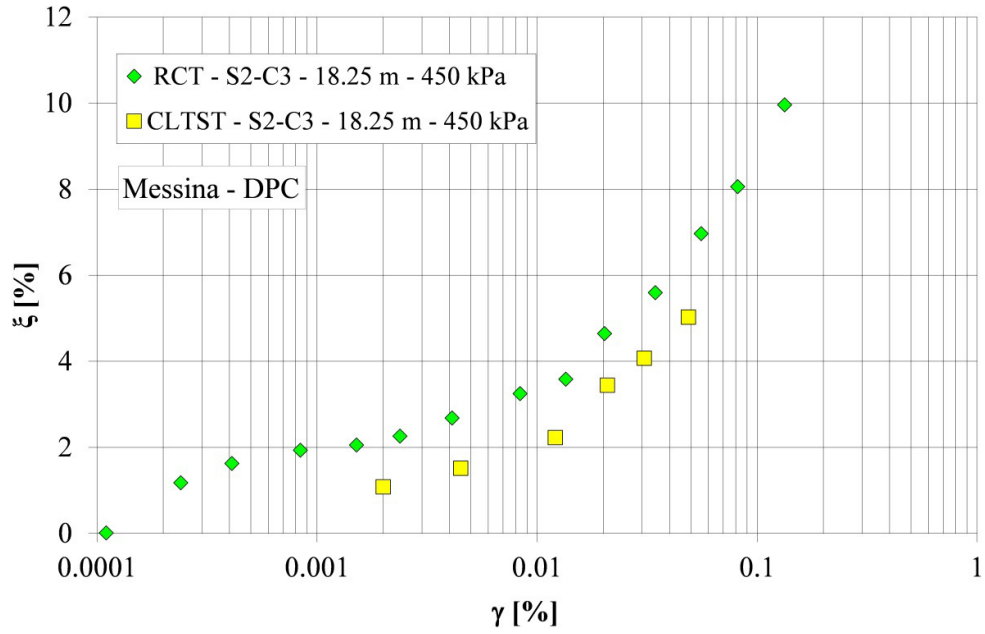
(b)

Figure 5.8 (a) G [MPa] versus γ [%] curves; (b) ξ [%] versus γ [%] curves from RCT and CLTST tests.

The experimental results have been used to determine the empirical parameters of the Equation (5.1) proposed by Yokota et al. (1981) to describe the shear modulus decay with shear strain level:

$$\frac{G(\gamma)}{G_0} = \frac{1}{1 + \alpha\gamma(\%)^\beta} \tag{5.1}$$

in which: G(γ) = strain dependent shear modulus; γ = shear strain; α,β= soil constants. The values of α = 20 and β = 0.87 have been obtained.

As suggested by Yokota et al. (1981), the inverse variation of damping ratio with respect to the normalised shear modulus has an exponential form:

$$\xi(\gamma)(\%) = \eta exp\left[-\lambda\frac{G(\gamma)}{G_0}\right] \tag{5.2}$$

in which: ξ (γ) = strain dependent damping ratio; γ= shear strain; η, λ = soil constants. The values of η = 19 and λ = 2.3 have been obtained.

5.3. Model geometry and dynamic boundary conditions

The following soil stratigraphy has been defined by means the boreholes S1, S2 and S3 to be used in the numerical model: fill (from 0 to 2 m), silty sand and gravel 1a (from 2 to 9 m), silty sand and gravel 1b (from 9.0 to 17.5 m), sandy silt (from 17.5 to 20.5 m), silty sand and gravel 2a (from 20.5 to 27.0 m), sandy silt & clay (from 27 to 30 m), silty sand and gravel 2b (from 30 to 37 m), silty sand and gravel 3a (from 37 to 50 m), silty sand and gravel 3b (from 50 to 60 m). The soil profile is shown in Figure 5.9.
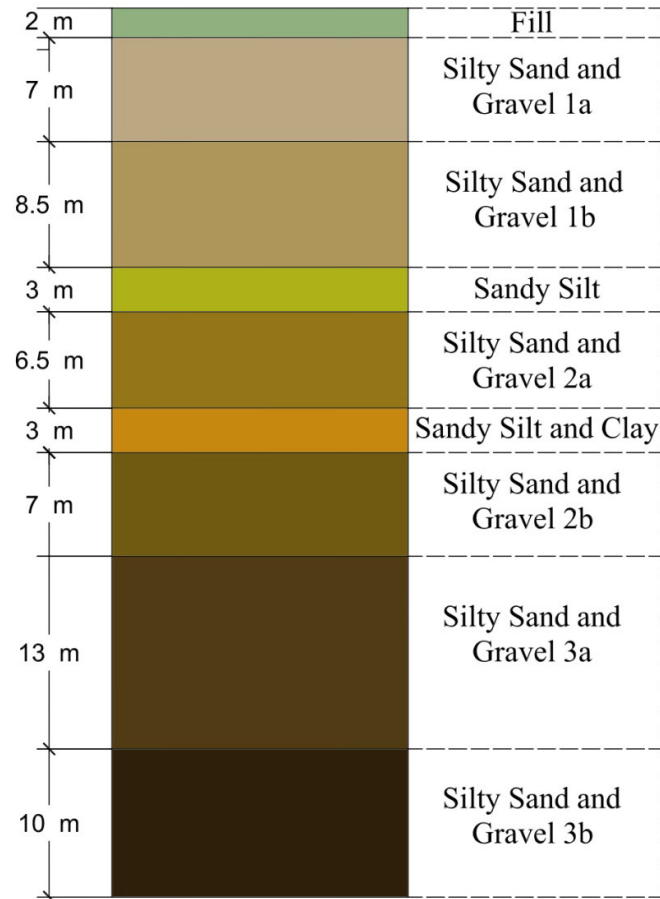
Figure 5.9 Soil stratigraphy obtained by in situ characterization.

In the numerical analyses, the dynamic inputs have been applied along the x-direction by imposing a given displacement at the bottom boundary. Therefore, in order to minimize boundary effects as

much as possible, the length of the model L (along the x-direction) has been chosen equal to six times

the depth of the bedrock (conventional bedrock, $V_S > 800$ m/s).

$$L = 6 \, z_{bedrock} = 6 \cdot 60 \, m = 360 \, m \tag{5.3}$$

Instead, the width of the model has been fixed equal to 6 m. The basic soil elements of the 3D finite

element mesh are the 10-node tetrahedral elements. The Average Element Size (AES) respects the

following equation (Kuhlemeyer and Lysmer, 1973):

$$AES \leq \frac{V_{s,min}}{6 \div 8 f_{max}} \tag{5.4}$$

where $V_{S,min}$ is the lowest wave velocity and f_{max} is the maximum frequency component of the input

waves. Based on C-H, D-H and SDMT tests, $V_{S,min}$ is equal to 146 m/s (fill layer). From the Fourier

spectrum, it can be found that the maximum frequency component is 3.37 Hz, which leads to a length

of 5.4 m÷7.2 m. The total number of elements is 32,328. The finite element mesh is shown in Figure

5.10.
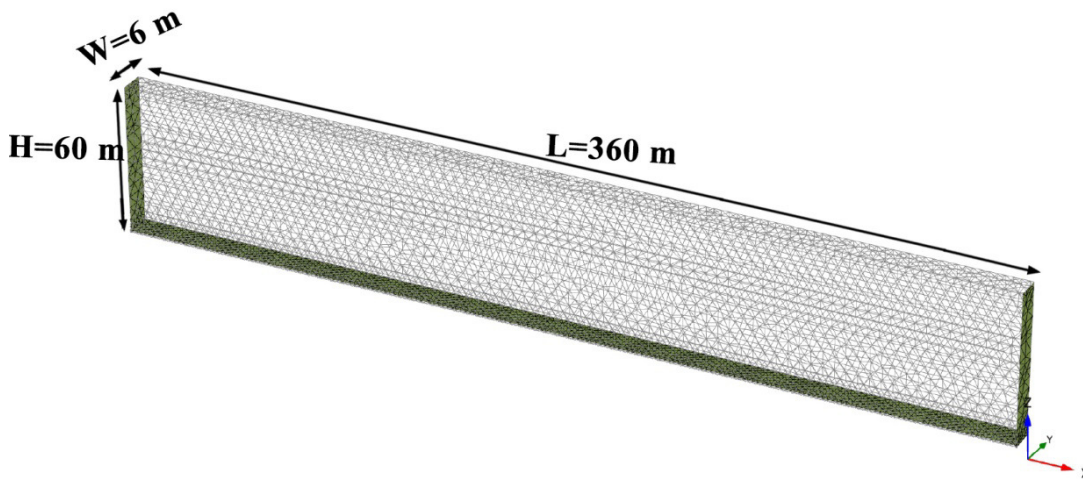
Figure 5.10 3D Finite element mesh.

With regard to the boundary conditions, to generate the initial stresses due to gravity loading, default

fixities have been applied, corresponding to normally fixed vertical boundaries and a fully fixed base.

For the dynamic phase, the Free-Field and Compliant Base boundary conditions have been considered (Figure 5.11).
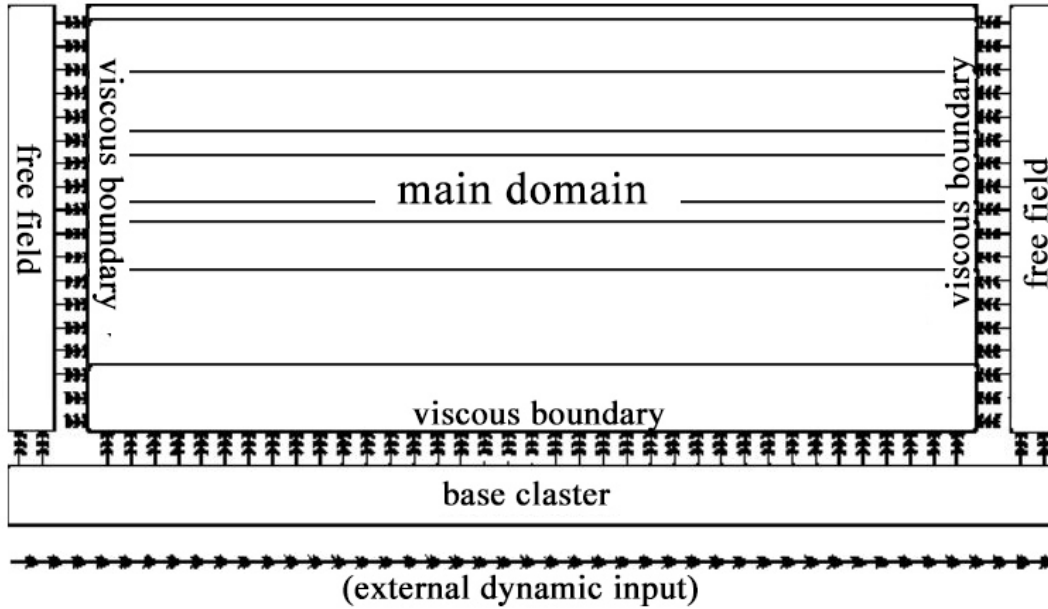
Figure 5.11 Free Field boundary condition with Compliant Base (Galavi et al. 2013; PLAXIS3D, 2018b; modified).

The Free Field condition simulates the propagation of waves into the far field with a minimum reflection at the boundary. The domain is reduced to the area of interest and the free field motion is applied to the boundaries employing free-field elements. The motion is transferred from the free field elements to the main domain by applying equivalent normal and shear forces. Two dashpots are added in the normal and shear direction at each node of the model boundary (Figure 5.12) (Galavi et al., 2013; PLAXIS3D, 2018b).
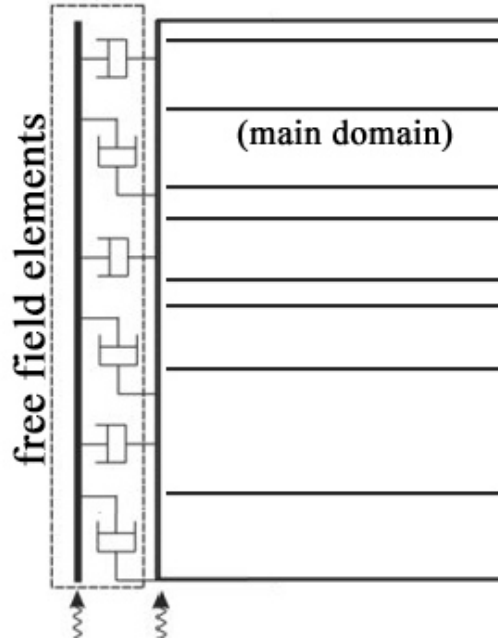
Figure 5.12 Free field elements (Galavi et al., 2013; PLAXIS3D, 2018; modified).

The Compliant Base boundary (Joyner and Chen, 1975) simulates the continuation of waves into the deep soil with a minimum reflection at the bottom boundary. Free field elements can be also attached to the bottom of the main domain (Galavi et al., 2013; PLAXIS3D, 2018b). The water head has been imposed at the depth of 3 m. Model geometry and boundary conditions are shown in Figure 5.13.
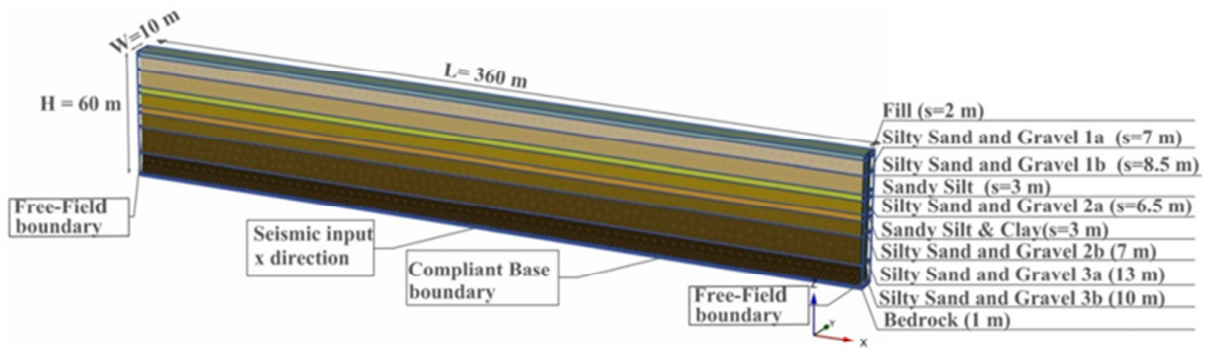
Figure 5.13. Model geometry and boundary conditions.

5.4 Soil dynamic response and validation of the model

In order to evaluate the soil dynamic response and to validate the finite element model, the numerical analyses have been carried out in two steps. In the first step, local site response analyses have been performed using 1-D equivalent codes taking into account a soil column. In the second step, results obtained by 1-D equivalent linear method have been compared with those derived by means of PLAXIS three-dimensional finite element software, assuming a linear visco-elastic soil behavior.

5.4.1 Equivalent Linear Analyses

Local site response analyses have been performed using 1-D linear equivalent codes EERA (Bardet et al., 2000) and STRATA (Kottke et al., 2008). The V_S profile used for soil response analyses is obtained from D-H, C-H and SDMT tests performed in the zone of Regional Department of Civil Defence (DRPC) of Messina (Italy) and reported in Figure 5.7. The value of the other parameters have been derived from the geotechnical characterization by means of in situ and laboratory tests.

The dynamic response model requires the knowledge of the depth of the bedrock that has been fixed at 60 m (conventional bedrock, V_S>800 m/s). Moreover, during strong earthquake, such as that of 1908 assumed as the scenario event in this study, the soil tends to behave as a non-linear material. To take into account the soil non linearity, laws of shear modulus and damping ratio against strain have been considered in the analyses. Resonant Column Test (RCT) and Cyclic Loading Torsional Shear Test (CLTST), carried out on specimens S1C1 (retrieved at 7.0-7.4 m in S1 borehole) and S3C4 (retrieved at 27.0-27.5 m in S3 borehole), respectively, have been used. The soil model is shown in Table 5.3.

Table 5.3 Soil model for site response analyses.

Layers	from [m]	to [m]	Thickness [m]	V_S [m/s]	G/γ- D/γ	γ [kN/m3]
Fill	0	2	2	146	S1C1- RCT	16.0
Silty Sand and Gravel 1a	2	9	7	218	S1C1- RCT	20.7
Silty Sand and Gravel 1b	9	17.5	8.5	335	S1C1- RCT	21.4
Sandy Silt	17.5	20.5	3	318	S1C1- RCT	18.3
Silty Sand and Gravel 2a	20.5	27	6.5	288	S1C1- RCT	21.4
Sandy Silt & Clay	27	30	3	347	S3C4- CLTST	18.3
Silty Sand and Gravel 2b	30	37	7	457	S1C1- RCT	21.4
Silty Sand and Gravel 3a	37	50	13	665	S1C1- RCT	21.4
Silty Sand and Gravel 3b	50	60	10	911	S1C1- RCT	21.4
Bedrock				1300		24.0

A parametric study with three different seismograms of the 1908 earthquake has been carried out. The model has been excited at the base using three seismograms of 1908, called Amoruso, Tortorici and DISS Messina Straits. The first seismogram (Amoruso et al., 2002) has a PGA of 0.456 g. The second one (Tortorici et al., 1995) has been scaled to the value of 0.337 g corresponding to a return period of 950 years (Class IV, public buildings of strategic importance) in the current Italian seismic code NTC(2018). The third seismogram, DISS Messina Straits, has a PGA of 0.293 g. Figure 5.14 shows the synthetic seismograms used in this study and the values of the first and second predominant frequencies of the input motions, f_p.
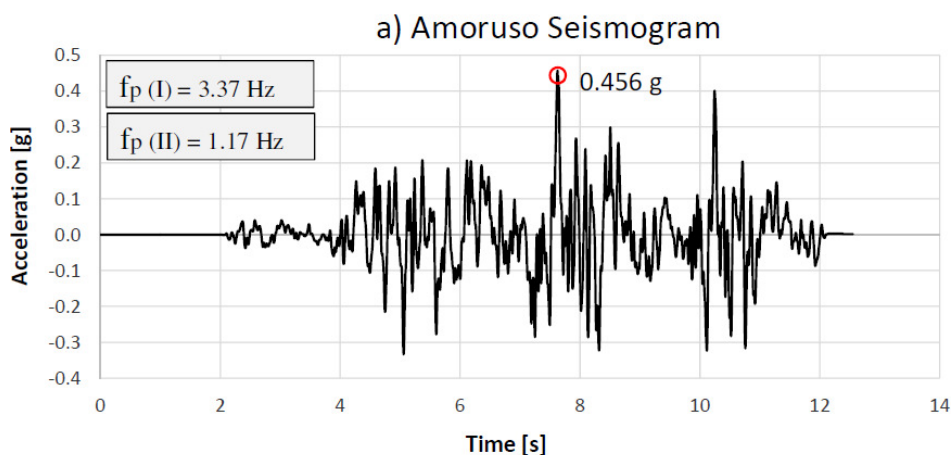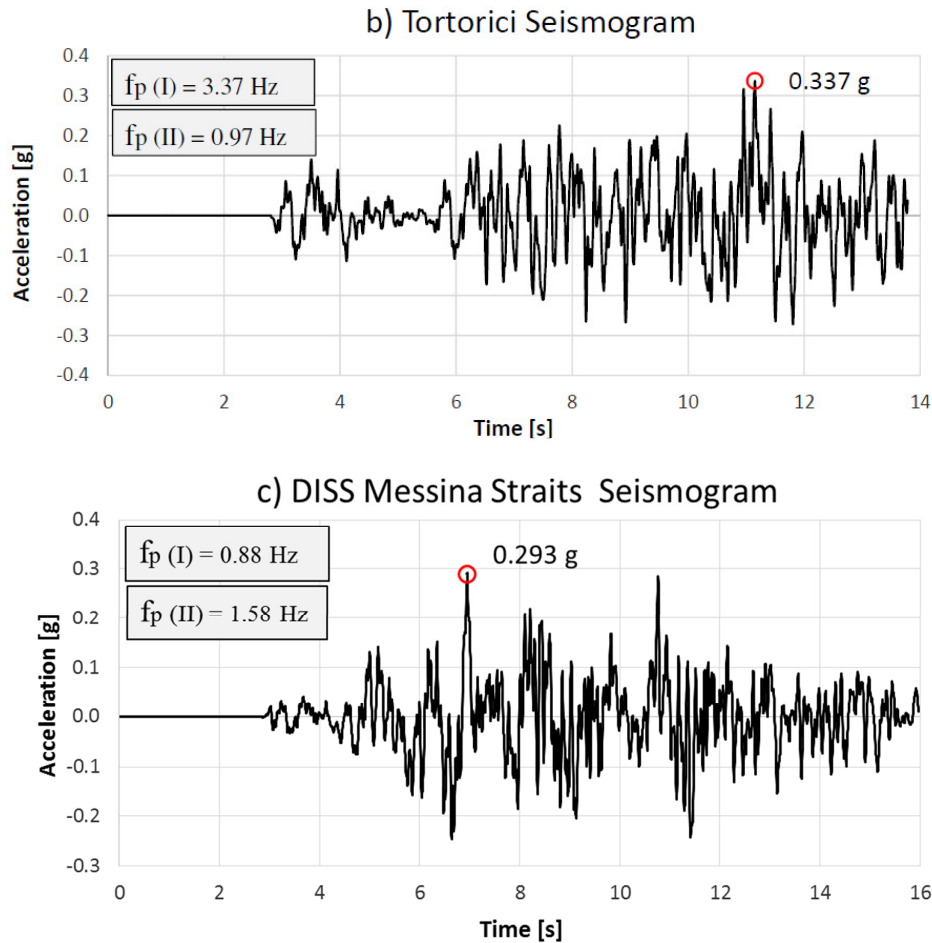
Figure 5.14 Adopted seismic inputs for numerical analyses: a) Amoruso seismogram (PGA=0.456 g) ; b) Tortorici seismogram scaled to the value of 0.337 g; c) DISS Messina Straits seismogram (PGA=0.293 g).

Results obtained by 1D equivalent linear codes have been reported in the following paragraph and compared with those derived by means of PLAXIS3D using a linear visco-elastic soil behavior.

5.4.2 FEM modelling and linear visco-elastic soil behavior

Numerical FEM analyses have been performed by PLAXIS3D software using a linear visco-elastic (LE) constitutive model. The values of the shear modulus, G, and the damping ratio, ξ, evaluated by 1-D linear equivalent codes using as input the three 1908 seismograms, have been inserted in the

software. The values of G and ξ, assigned to each layers for the three 1908 synthetic seismograms, are reported in Table 5.4.

Table 5.4 Values of the shear modulus, G, and the damping ratio, ξ, assigned to each layers using as input the three 1908 seismograms.

Layers	Amoruso		Tortorici		DISS Messina Straits	
	G [kN/m2]	ξ [%]	G [kN/m2]	ξ [%]	G [kN/m2]	ξ [%]
Fill	17485	5.27	21461	6.36	25975	5.52
Silty Sand and Gravel 1a	15926	9.58	18872	8.94	20258	8.71
Silty Sand and Gravel 1b	44279	8.07	44405	9.06	49683	8.90
Sandy Silt	24944	9.58	25401	9.59	24944	9.586
Silty Sand and Gravel 2a	45954	9.58	20834	9.59	20834	9.586
Sandy Silt & Clay	126724	7.11	47635	13.98	78593	12.06
Silty Sand and Gravel 2b	172050	7.71	52460	9.59	110956	8.53
Silty Sand and Gravel 3a	539833	5.47	412516	6.27	483048	5.82
Silty Sand and Gravel 3b	1337757	4.31	1076163	5.01	1194968	4.23

In PLAXIS3D, the damping ratio ξ is introduced through the Rayleigh damping formulation in which the damping matrix [C] is given by a portion of the mass matrix [M] and a portion of the stiffness matrix [K]:

$$[C] = \alpha[M] + \beta[K] \tag{5.5}$$

where the parameters α and β are the Rayleigh coefficients. The damping ratio ξ and the Rayleigh coefficients are related by the following equation:

$$\alpha + \beta\omega^2 = 2\omega\,\xi \qquad \text{with } \omega = 2\pi f \tag{5.6}$$

in which ω is the angular frequency in rad/s and f is the frequency in Hz.

Solving the equation for two different target frequencies and the corresponding target damping ratio gives the Rayleigh coefficients:

$$\alpha = 2\omega_1\omega_2 \frac{\omega_1\xi_2 - \omega_2\xi_1}{\omega_1{}^2 - \omega_2{}^2} \tag{5.7}$$

$$\beta = 2\frac{\omega_1\xi_1 - \omega_2\xi_2}{\omega_1{}^2 - \omega_2{}^2} \tag{5.8}$$

Hashash and Park (2002) suggest to select the first frequency as the fundamental natural frequency of the soil deposit f_1 according to the following formula:

$$f_1 = \frac{Vs}{4H} \qquad (5.9)$$

where V_S is the shear wave velocity in the soil deposit of thickness H. The fundamental natural frequency of the soil deposit is equal to 1.76 Hz. While, the second target frequency is given by the closest odd integer larger than the ratio f_p/f_1.

The values of the Rayleigh coefficients, assigned to each layers for the three 1908 synthetic seismograms, are reported in Table 5.5.

Table 5.5 Values of the Rayleigh coefficients assigned to each layers using as input the three 1908 seismograms.

Layers	Amoruso α	Amoruso β	Tortorici α	Tortorici β	DISS Messina Straits α	DISS Messina Straits β
Fill	0.7763	0.0032	0.9369	0.0038	0.6101	0.0050
Silty Sand and Gravel 1a	1.4112	0.0058	1.3169	0.0054	0.9627	0.0079
Silty Sand and Gravel 1b	1.1888	0.0049	1.3346	0.0055	0.9837	0.0081
Sandy Silt	1.4112	0.0058	1.4127	0.0058	1.0596	0.0087
Silty Sand and Gravel 2a	1.4112	0.0058	1.4127	0.0058	1.0596	0.0087
Sandy Silt & Clay	1.0473	0.0043	2.0593	0.0084	1.3330	0.0109
Silty Sand and Gravel 2b	1.1357	0.0046	1.4127	0.0058	0.9428	0.0077
Silty Sand and Gravel 3a	0.8058	0.0033	0.9236	0.0038	0.6433	0.0053
Silty Sand and Gravel 3b	0.6349	0.0026	0.7373	0.0030	0.4675	0.0038

Figure 5.15 shows the results obtained by means of EERA, STRATA and PLAXIS3D, in terms of maximum accelerations with depth, using as input the three 1908 synthetic seismograms.
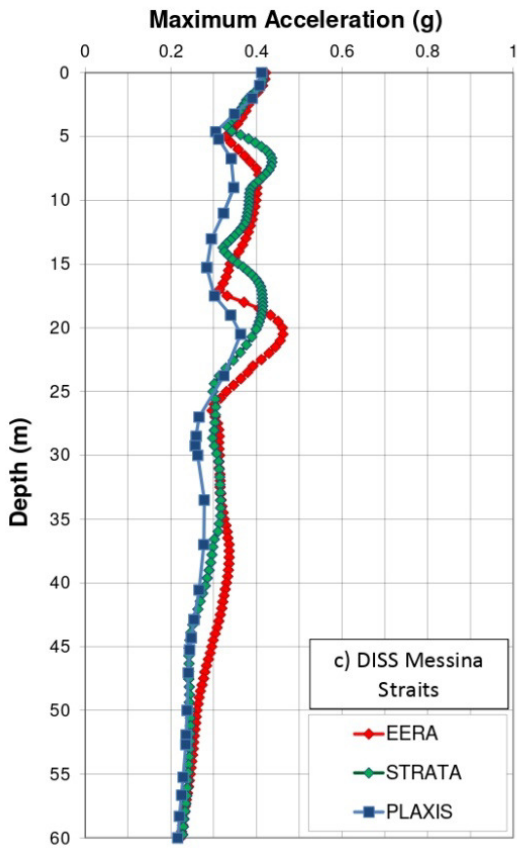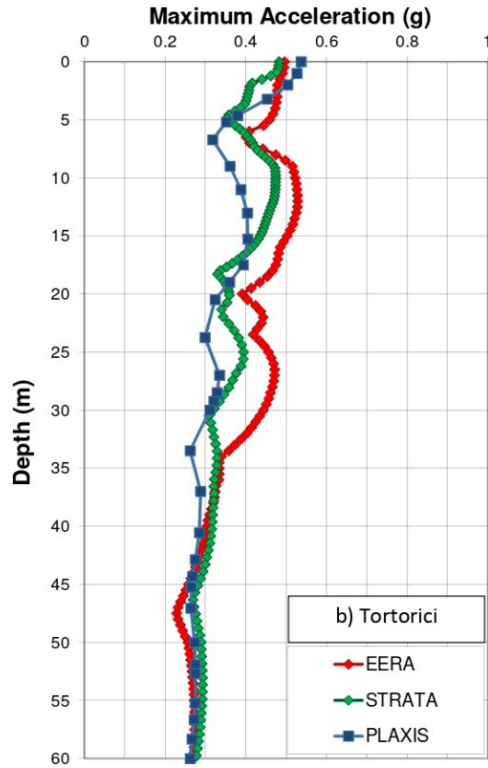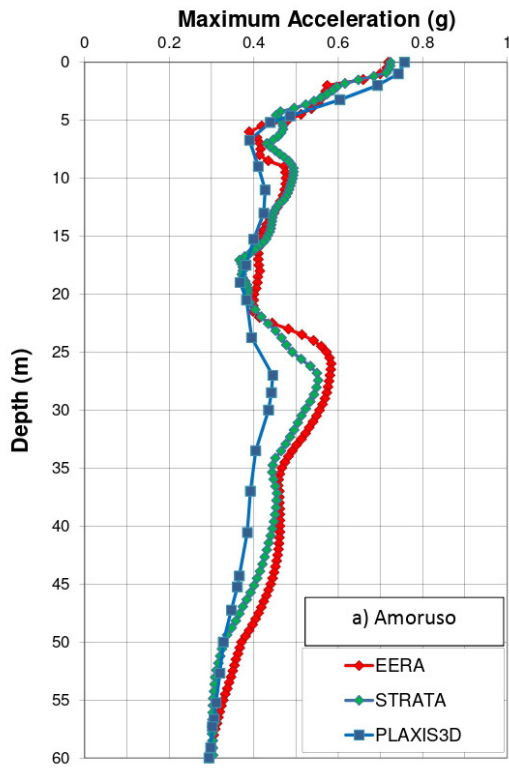
Figure 5.15 Comparison of maximum accelerations with depth obtained by EERA, STRATA and PLAXIS3D using as input: a) the Amoruso seismogram; b) the Tortorici seismogram; c) the DISS Messina Straits seismogram.

Values of surface maximum accelerations and soil amplification factors R for the three 1908 synthetic seismograms, obtained by EERA, STRATA and PLAXIS3D, are reported in Table 5.6.

Table 5.6 Values of the surface maximum accelerations and soil amplification factors R obtained by EERA, STRATA and PLAXIS3D.

	Amoruso	Tortorici	DISS Messina Straits
PGA_{input}	0.456 g	0.337 g	0.293 g
$PGA_{output, EERA}$	0.719 g	0.496 g	0.421 g
$PGA_{output, STRATA}$	0.724 g	0.482 g	0.416 g
$PGA_{output, PLAXIS3D}$	0.757 g	0.537 g	0.412 g
$R_1= PGA_{output, EERA}/ PGA_{input}$	1.577	1.471	1.437
$R_2= PGA_{output, STRATA}/PGA_{input}$	1.588	1.430	1.420
$R_3= PGA_{output, PLAXIS3D}/PGA_{input}$	1.660	1.691	1.406

Results of the site response analyses show high values in soil amplification effects. Furthermore, the soil amplification factors R obtained using the 1908 input motions are greater than the amplification value provided by Italian technical code NTC (2018), equal to 1.206 for a return period of 950 years and for soil type C (180 m/s $<V_{S,eq}= 268$ m/s < 360 m/s). The smallest values of R were found for the DISS Messina Straits seismogram.

In Figure 5.16, results are presented in term of response spectra at the surface, obtained by setting a structural damping of 5%. In particular, Tortorici seismogram has been scaled to the value of 0.337 g corresponding to a return period of 950 years in the current Italian seismic code NTC (2018). Therefore, for comparison, the elastic response spectrum provided by the Italian seismic code is also shown in Figure 5.16 b).
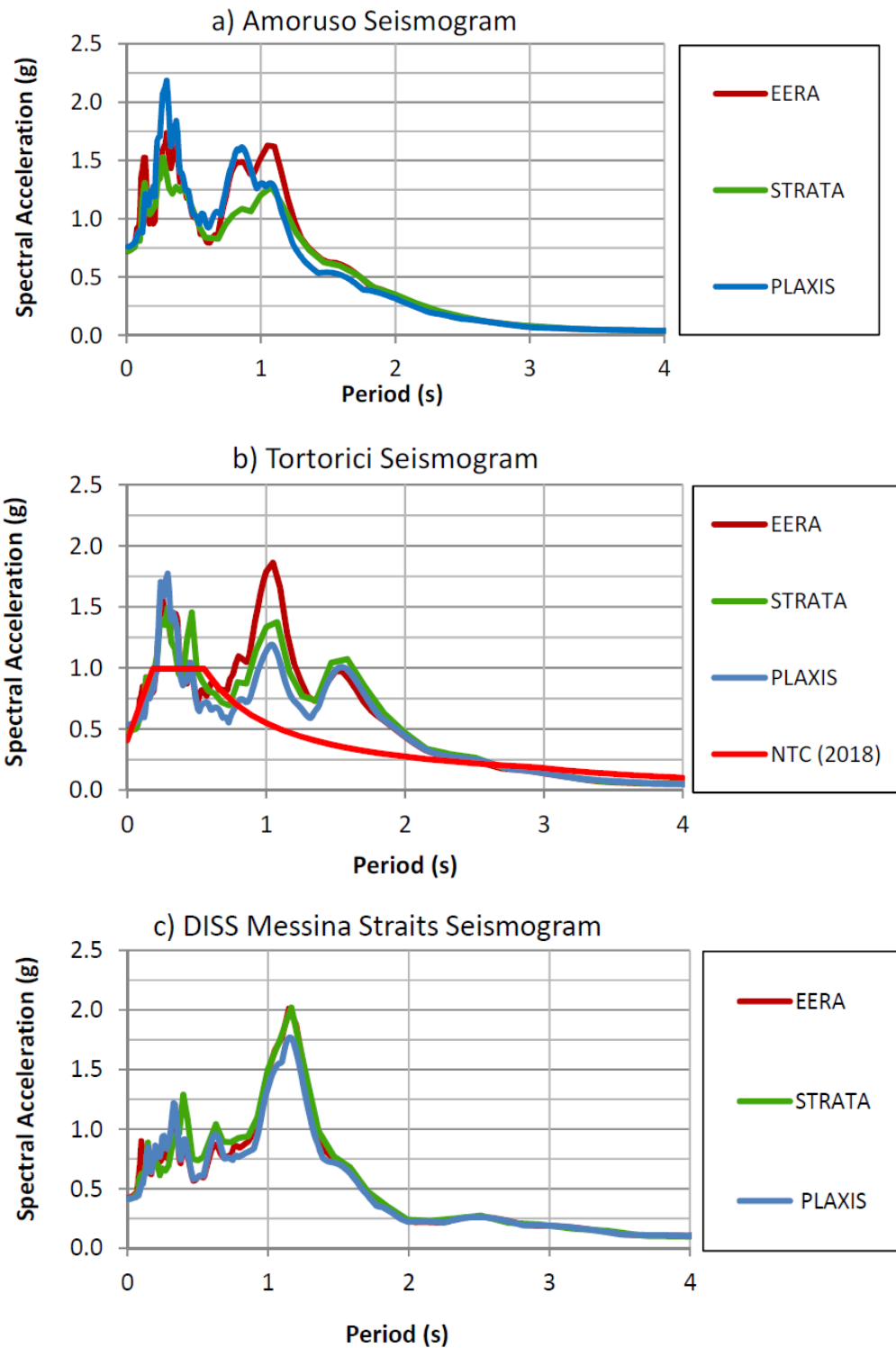
Figure 5.16. Elastic response spectra obtained by EERA, STRATA and PLAXIS3D using as inputs: a) the Amoruso seismogram; b) the Tortorici seismogram; c) the DISS Messina Straits seismogram.

Considering the results obtained using the 1908 Amoruso seismogram (Figure 5.16 a)), the maximum

spectral acceleration $S_{e,max}$ = 2.1 g at T = 0.3 s is obtained. A second less important period T = 1.1 s

can be observed. The results obtained using the 1908 Tortorici seismogram (Figure 5.16 b)) show that the maximum spectral acceleration $S_{e,max} = 1.9$ g at T = 1.1 s is found. A second and a third less important periods T = 0.3 s and T=1.6 s can be observed. Finally, considering the DISS Messina Straits seismogram (Figure 5.16 c)), the maximum spectral acceleration $S_{e,max} = 2.0$ g at T = 1.2 s is obtained.

Figure 5.17 shows the amplification functions, A(f), evaluated as the ratio between the Fourier spectrum at the surface level and the Fourier spectrum of the input motions applied at the base of the model.

a) Amoruso Seismogram

b) Tortorici Seismogram
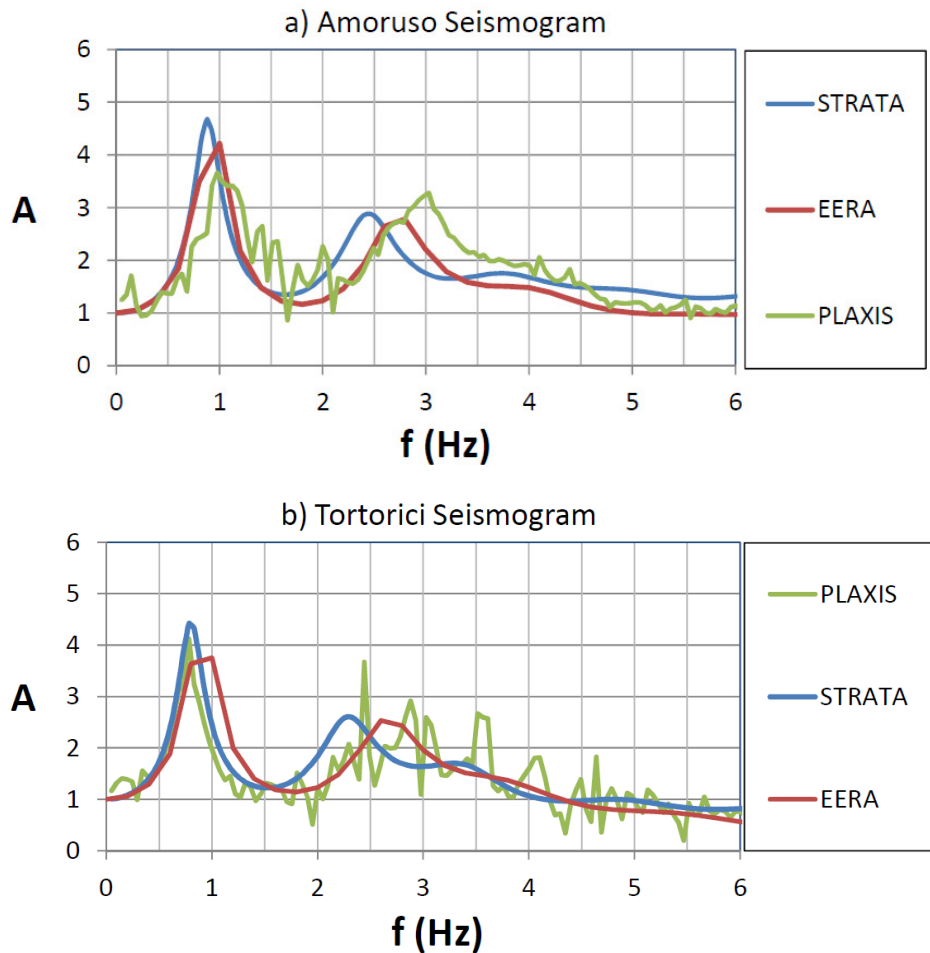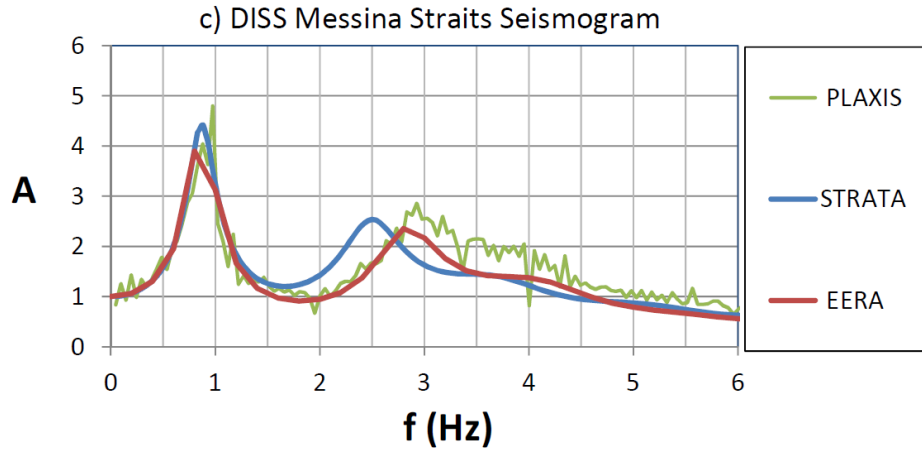
Figure 5.17 Amplification functions obtained by EERA, STRATA and PLAXIS3D using as inputs: a) the Amoruso seismogram; b) the Tortorici seismogram; c) the DISS Messina Straits seismogram.

Figures 5.15-5.17 and Table 5.6 show that results of the site response analyses obtained by EERA, STRATA and PLAXIS3D are in good agreement. Therefore, the three-dimensional finite element model, including the definition of the dynamic boundary conditions, defined in PLAXIS3D, have been validated. From this model, it is possible to study even more complex problems as well as soil-structure interaction analysis.

5.5 Non-Linear Finite Element Analysis

The non-linear soil behaviour has been simulated using the Hardening Soil model with small-strain stiffness (HSsmall). The HSsmall model, implemented in PLAXIS3D, is based on the Hardening soil model (HS) with the addition of two parameters that describe the variation of stiffness with strain. The HS model requires three stiffness moduli at the reference pressure, p^{ref}, of 100 kPa: E_{50}^{ref}, E_{ur}^{ref} and E_{oed}^{ref}. All moduli are stress-level dependent, according to the following expressions:

$$E_{oed} = E_{oed}^{ref} \left(\frac{\sigma'_1}{p^{ref}} \right)^m \qquad (5.10)$$

$$E_{50} = E_{50}{}^{ref} \left(\frac{\sigma'_3}{p^{ref}} \right)^m \tag{5.11}$$

$$E_{ur} = E_{ur}{}^{ref} \left(\frac{\sigma'_3}{p^{ref}} \right)^m \tag{5.12}$$

where σ'_1 and σ'_3 are the major and minor principal effective stresses, and m is the power for stress-level dependency of stiffness.

Surarak et al. (2012), in order to determine the stiffness and strength parameters of the Hardening Soil Model, used the oedometer tests and drained triaxial tests. However, the latter are not available for the area under consideration. Monaco and Marchetti (2004) explained how the seismic dilatometer test (SDMT) can be used to determine the stiffness parameters. Based on an intensive literature survey carried out by Schanz and Vermeer (1997), they assumed E_{oed} equal to the dilatometer modulus M_{DMT}. This approach was also used by Arroyo et al. (2008) and Cox and Mayne (2015).

In this study, the parameters for soil stiffness have been obtained from the Seismic Dilatometer Marchetti Test (SDMT) performed in the zone of Regional Department of Civil Defence (DPC) of Messina. The tangent stiffness modulus, E_{oed}, has been imposed equal to dilatometer modulus, M_{DMT}. Moreover, according to Vermeer (2001), the following ratios have been adopted:

$$E_{50}{}^{ref} = E_{oed}{}^{ref} \tag{5.13}$$

$$E_{ur}{}^{ref} = 4 \, E_{oed}{}^{ref} \tag{5.14}$$

For the all soil layers, the exponent, m, and the Poisson's ratio for unloading-reloading, ν_{ur}, have been assumed equal to 0.5 and 0.2, respectively.

The depth of the geometric model is equal to 60 m, as defined in paragraph 5.3, but the SDMT has an effective depth of 31.50 m. The dilatometer modulus M_{DMT} shows a slightly increasing trend with depth. Therefore, in order to obtain the parameters for depths greater than 31.5 m, a linear interpolation of the values has been performed (Figure 5.18).
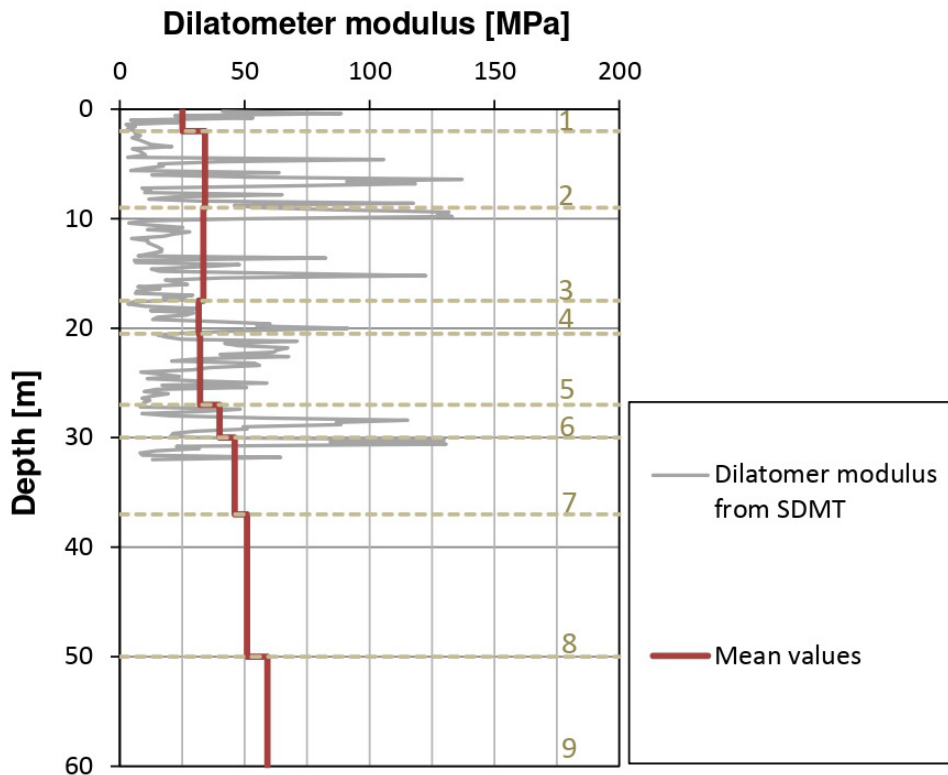
Figure 5.18 Dilatometer modulus M_{DMT} obtained from the SDMT test and mean value for each layer.

To describe the variation of stiffness with strain, two additional parameters have been added: the reference shear modulus at very small strain, G_0^{ref}, and shear strain level $\gamma_{0.7}$ at which the secant shear modulus G_S is reduced to 72.2 % of G_0. The stress dependency of the shear modulus G_0 is taken into account with the power law:

$$G_0 = G_0^{ref} \left(\frac{\sigma'_3}{p^{ref}} \right)^m \tag{5.15}$$

Values of G_0 are given by:

$$G_0 = \rho V_S^2 \tag{5.16}$$

in which V_S is the shear wave velocity of the layer. It has been obtained from D-H, C-H and SDMT tests. The values of $\gamma_{0.7}$ have been taken from Resonant Column Test (RCT) and Cyclic Loading Torsional Shear Test (CLTST), carried out on specimens S1C1 (retrieved at 7-7.4 m in S1 borehole) and S3C4 (retrieved at 27-27.5 m in S3 borehole) (Figure 5.19). The strength parameters have been derived directly from Direct Shear Tests.
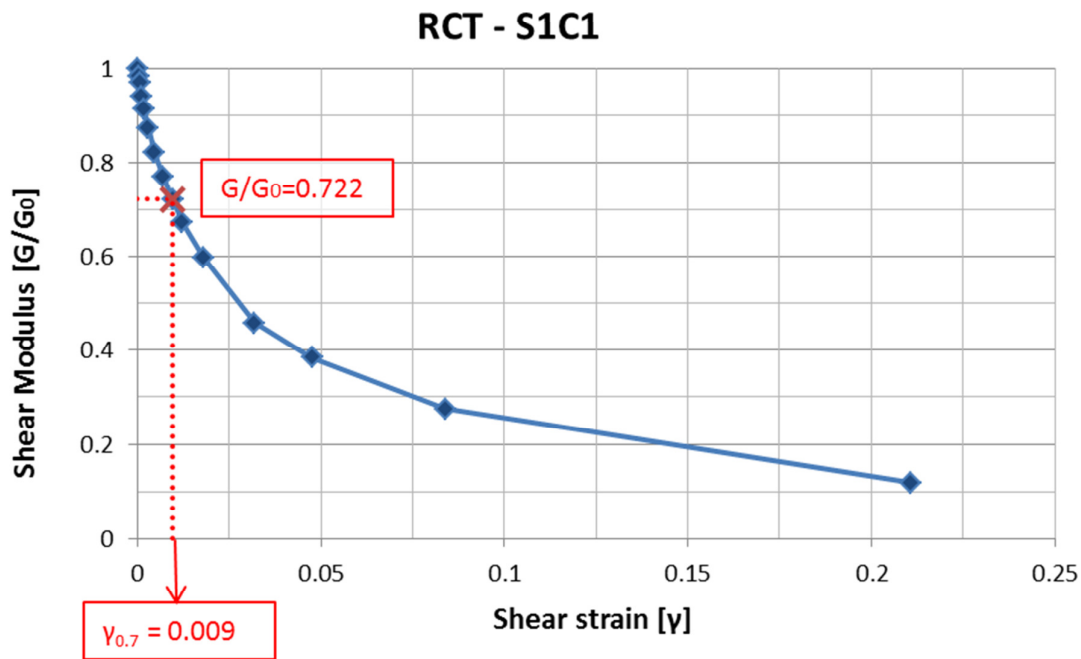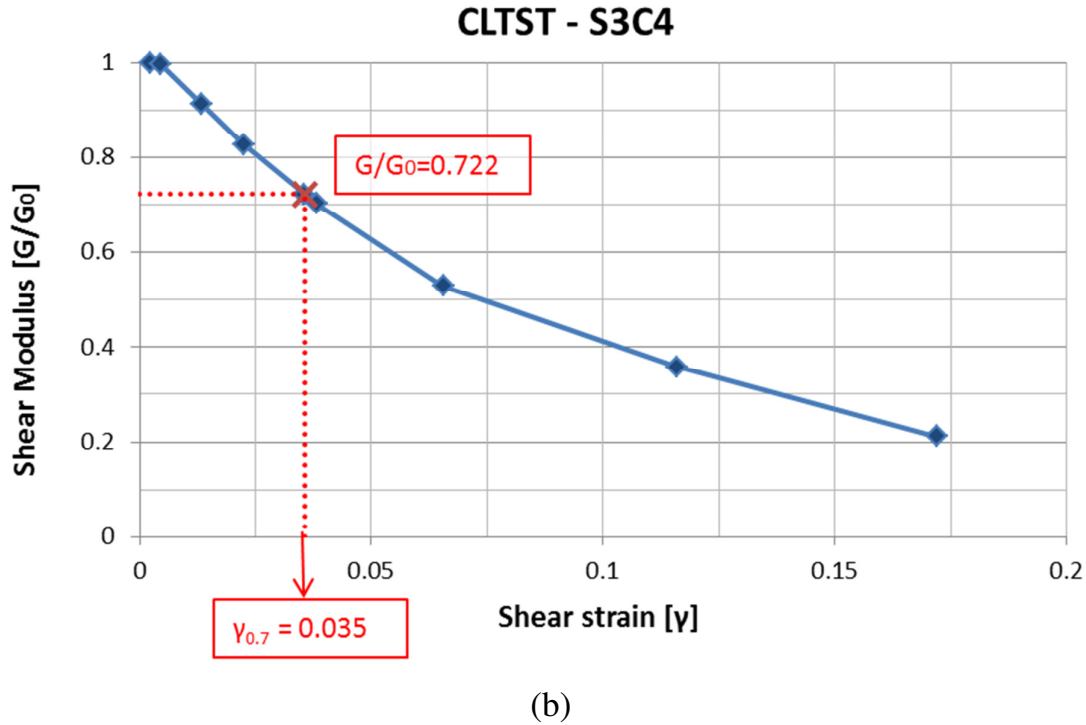
(a)

(b)

Figure 5.19. Values of $\gamma_{0.7}$ obtained from RCT and CLTST carried out on (a) sample S1C1 (retrieved at 7-7.4 m in S1 borehole) and (b) S3C4 (retrieved at 27-27.5 m in S3 borehole), respectively.

Table 5.7 reports the input parameters of the model, i.e. for the Silty Sand and Gravel 1a and Sandy Silt and Clay layers.

Table 5.7 Input parameters for the Silty Sand and Gravel 1a and Sandy Silt and Clay layers.

Parameter		Silty Sand and Gravel 1a	Sandy Silt and Clay layer	Unit
General				
Material model	-	HSsmall	HSsmall	-
Total unsaturated unit weight of soil	γ_{unsat}	16.7	13.1	kN/m^3
Total saturated unit weight of soil	γ_{sat}	20.7	18.3	kN/m^3
Stiffness parameters				
Secant stiffness in standard drained triaxial test	E_{50}^{ref}	36527	24412	kN/m^2
Tangent stiffness for primary oedometer loading	E_{oed}^{ref}	36527	24412	kN/m^2
Unloading/reloading stiffness	E_{ur}^{ref}	146107	97649	kN/m^2
Power for stress-level dependency of stiffness	m	0.5	0.5	-
Additional stiffness parameters				
Reference shear modulus at very small strains	G_0^{ref}	129156	118903	kN/m^2
Threshold shear strain at which GS=0.722 G0	$\gamma_{0.7}$	0.009	0.035	-
Strength parameters				
Cohesion	c'	0	15	kN/m^2
Friction Angle	φ'	34	21	°

The non-linear site response analysis has been performed using as excitation at the base of the model the 1908 Amoruso seismogram (PGA=0.456 g). Figures 5.20 and 5.21 show the results in terms of maximum accelerations with depth and response spectrum at the surface obtained by means of

96

PLAXIS3D using the HS small model. For comparison also shown are the results of FEM modeling with linear visco-elastic soil behavior.
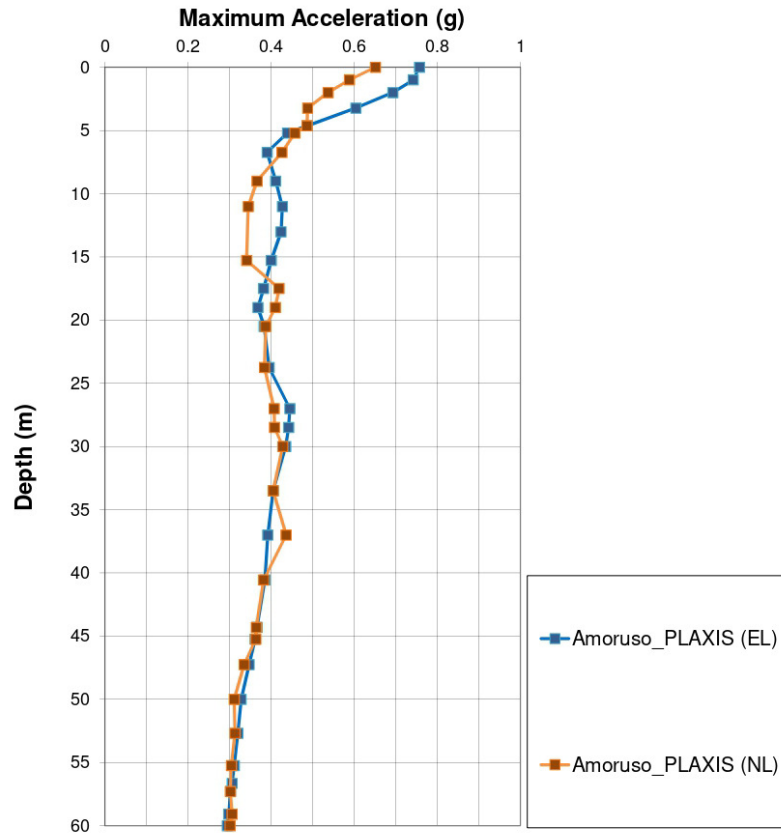
Figure 5.20. Comparison of maximum accelerations with depth obtained by means of PLAXIS3D using the HSsmall and linear visco-elastic constitutive models
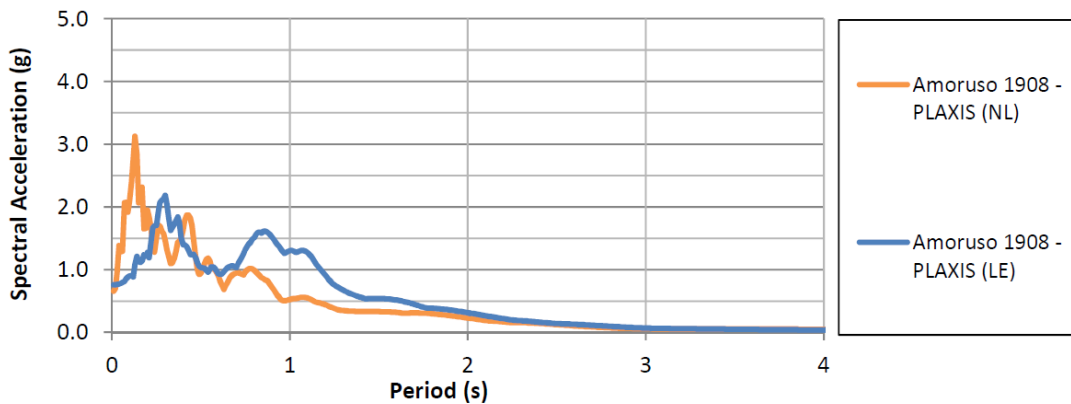
Figure 5.21. Comparison of the response spectrum at the surface obtained by means of PLAXIS3D using the HSsmall and linear visco-elastic constitutive models.

Results show that the values of the maximum accelerations with the depth obtained using the HSsmall model are very similar to those obtained using the linear visco-elastic soil model between

about 60 m and 5 m of depth. While greater differences are obtained in the first 5 meters of depth. The observed differences can be attributed to the plasticization of the soil that occurs in the seismic response analysis conducted with HSsmall. Indeed, it is possible to observe that the soil amplification factor R, obtained using the visco-elastic constitutive model, is equal to 1.66. While, R is equal to 1.43 using the HSsmall model.

An important aspect to consider is related to damping. The equivalent linear analysis consists in the execution of a sequence of complete linear analysis with subsequent update of the parameters of stiffness and damping, derived in the laboratory from Resonant Column Tests (RCT) and Cyclic Loading Torsional Shear Tests (CLTST). In PLAXIS3D, the HSsmall model shows hysteresis in cyclic loading (Figure 2.8) that leads to damping. Therefore, no additional damping has been added. The maximum amount of hysteretic damping obtained with the HSsmall model depends on the ratio of G_0 and $G_{ur} = E_{ur}/2(1 + \nu_{ur})$. A larger ratio leads to a larger maximum amount of hysteretic damping. However, there are some uncertainties in the choice of the three stiffness moduli: E_{50}^{ref}, E_{ur}^{ref} and E_{oed}^{ref}. The main uncertainty is linked to the great variability of the dilatometer modulus values (from 4 MPa to 130 MPa) obtained from the SDMT tests. Moreover, the latter only reaches a depth of 31.5 m.

On the basis of the above considerations, for the study of the soil-structure interaction, it has been preferred to use the viscoelastic constitutive model, that has been validated in paragraph 5.4.2.

5.6 Simplified Procedure Analysis

The stress-based simplified procedure for evaluating soil liquefaction potential requires the estimation of two variables: the seismic demand on a soil layer, expressed in terms of cyclic stress

ratio (CSR), and the capacity of the soil to resist liquefaction, expressed in terms of cyclic resistant ratio (CRR) (Youd et al., 2001). Therefore, the evaluation of the susceptibility of a site to seismic-induced liquefaction can be assessed comparing the CSR to the CRR (Grasso and Maugeri, 2008). Estimates of the in situ CSR can be developed directly, using the dynamic response analysis. The CSR has been evaluated by the Equation (2.31) from the site response analysis using as input the Amoruso seismogram (paragraph 5.4.1). Thus, the value of 0.72 g has been chosen for the peak horizontal acceleration at the ground surface a_{max} and the r_d profile, showed in Figure 5.22, has been taken to adjust for the flexibility of the soil profile. Moreover, for comparison, the r_d values have been also obtained by the Equations (2.33) and (2.34) (Liao and Whitman, 1986).
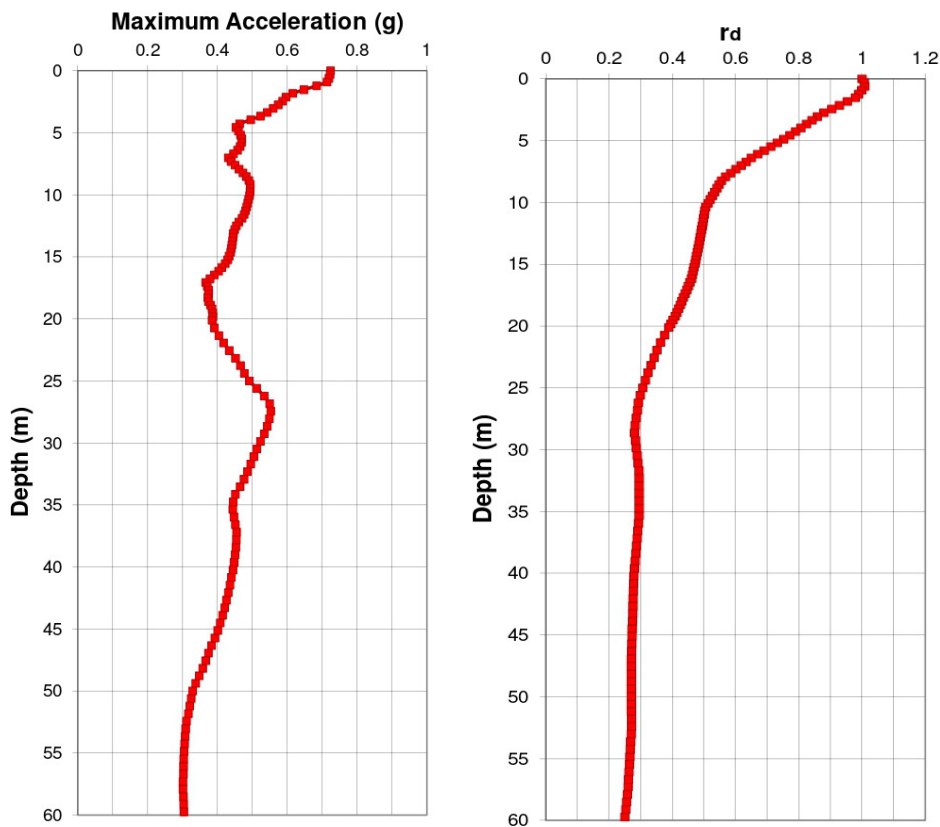
Figure 5.22 Maximum accelerations and stress reduction factor with depth obtained from site response analysis using as input the Amoruso seismogram (PGA=0.456g).

CRR has been evaluated from the SPT date according to Robertson and Wride (1997) by the following expression:

$$CRR_{7.5} = \frac{a + cx + ex^2 + gx^3}{1 + bx + dx^2 + fx^3 + hx^4}$$ (5.17)

where $CRR_{7.5}$ is the cyclic resistance ratio for earthquakes of magnitude 7.5; x=$(N_1)_{60}$; a=0.048; b=0.1248; c=-0.004721; d=0.009578; e=0.0006136; f=-0.0003285; g=-0.00001673 and h=0.000003714.

The values of $CRR_{7.5}$ have been scaled to a magnitude of M=7.24 of the 1908 scenario earthquake by means of the magnitude scaling factor (MSF) (Equation 2.32).

The N values obtained from the SPT tests, have been corrected to determine $(N_1)_{60}$ values by Equation (5.18) (Robertson and Wride,1997).

$$(N_1)_{60} = N\ C_N C_E C_B C_R C_S$$ (5.18)

in which N is the measured SPT value, C_N is the correction for overburden pressure; C_E is the correction for hammer energy ratio (ER), C_B is the correction factor for borehole diameter, C_R is the correction factor for rod length and C_S is the correction for samplers.

The corrected N values $(N_1)_{60}$ are reported in Figure 5.23 (a) and the values of $CRR_{7.24}$ from SPT tests are shown in Figure 5.23 (b).
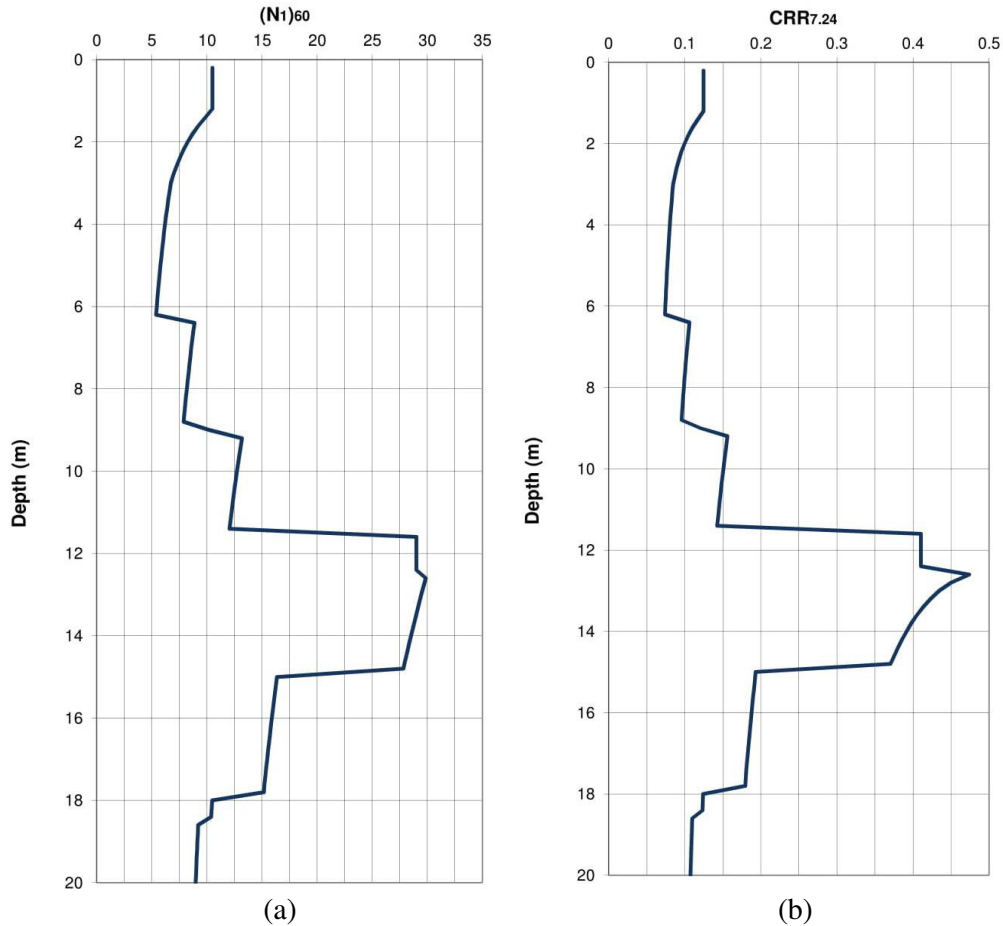
Figure 5.23 (a) $(N_1)_{60}$ test results versus depth; (b) $CRR_{7.24}$ from SPT date.

The ratio of the cyclic resistance ratio CRR(z) to cyclic stress ratio CSR(z) provides the liquefaction resistance factor F_{SL} profile:

$$F_{SL}(z) = \frac{CRR(z)}{CSR(z)} \tag{5.19}$$

The liquefaction potential index LPI (Iwasaki et al. 1978) has been computed by Equation (2.47) and the associate level of liquefaction severity is reported in Table 2.1.

Figure 5.24 shows the Liquefaction Potential values obtained from SPT date using the results of the site response analysis to evaluate the CSR. Also shown are the Liquefaction Potential values obtained using the Equations (2.33) and (2.34) proposed by Liao and Whitman (1986) to evaluate the stress reduction factor r_d.
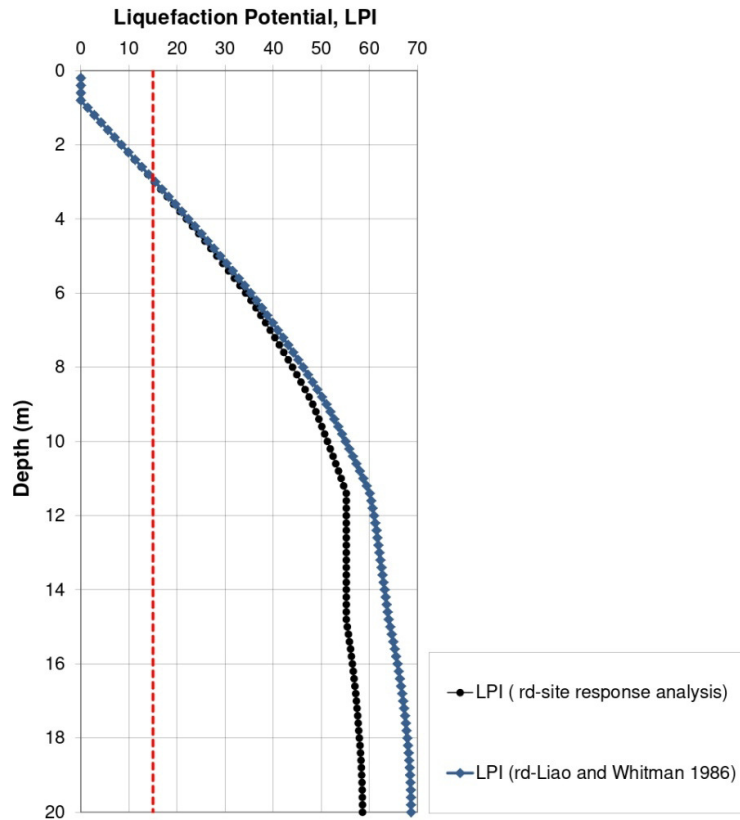
Figure 5.24 Liquefaction potential values obtained from SPT date.

It is possible to observe that the two profiles are in good agreement. However, higher LPI values are obtained using the equation proposed by Liao and Whitman (1986). Furthermore, results demonstrate that the level of liquefaction severity is very high already at the depth of about 3 meters and the profiles become almost constant from the depth of about 11 m. In light of this, it has been decided to further study the soil liquefaction by means of PLAXIS three-dimensional finite element software (paragraph 5.8).

5.7 Coupled Soil-Structure System

The dynamic response of the fully-coupled soil-structure system has been performed by means of PLAXIS 3D software. The free field (FF) condition has been compared with the alignment under the

structure (SSI) in order to investigate how the Dynamic Soil Structure Interaction (DSSI) phenomena can modify the free-field motion.

Structural objects are composed of 6-node triangular plate elements with six degrees of freedom per node. Structural elements have been simulated by means of an elastic constitutive model. For a proper modelling of the soil-structure interaction, interfaces have been added to the foundational plates allowing frictional sliding and uplift at the soil-foundation interface. In PLAXIS3D, interfaces are composed of 12-node interface elements that consist of pairs of nodes compatible with the 6-noded triangular side of the soil element and the plate element.

An elastic-plastic model is used to describe the behavior of the interfaces. For the elastic and plastic behavior, the shear stress τ can be obtained by the Equations (5.20) and (5.21), respectively:

$$\tau < \sigma_n' tan\varphi'_i + c'_i \tag{5.20}$$

$$\tau = \sigma_n' tan\varphi'_i + c'_i \tag{5.21}$$

where σ_n' is the effective normal stress, φ'_i and c'_i are the friction angle and the cohesion of the interface. The main interface parameter is the strength reduction factor, R_{inter}. A value of R_{inter} less than 1 reduces the interface strength and the interface stiffness according to the following equations:

$$c'_i = R_{inter} c'_{soil} \tag{5.22}$$

$$tan\varphi'_i = R_{inter} tan\varphi'_{soil} \leq tan\varphi'_{soil} \tag{5.23}$$

$$G_i = R_{inter}^2 G_{soil} \leq G_{soil} \tag{5.24}$$

where G_i is the shear modulus of the interface. The interaction has been modelled by choosing a suitable value for the strength reduction factor in the interface. R_{inter} has been assumed to be 2/3.

In order to reduce the model size and the calculation time, a representative section of 6 meters has been considered (Figure 5.4). The coupled soil-structure system is shown in Figure 5.25.
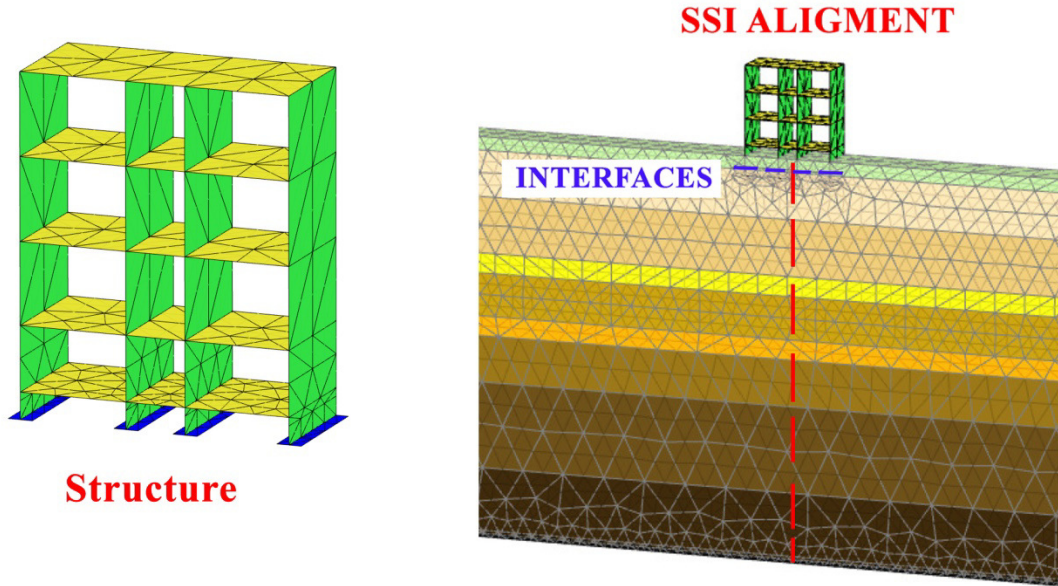
Figure 5.25 Coupled soil-structure system.

The free field (FF) condition has been compared with the alignment under the structure (SSI) in order to study how the DSSI modifies the dynamic response, including its accelerations, response spectra and amplification functions.

The maximum accelerations with depth are shown in Figure 5.26 for each seismogram of the 1908 earthquake. Surface maximum accelerations and soil amplification factors, R, for FF and SSI conditions, are summarize in Table 5.8.
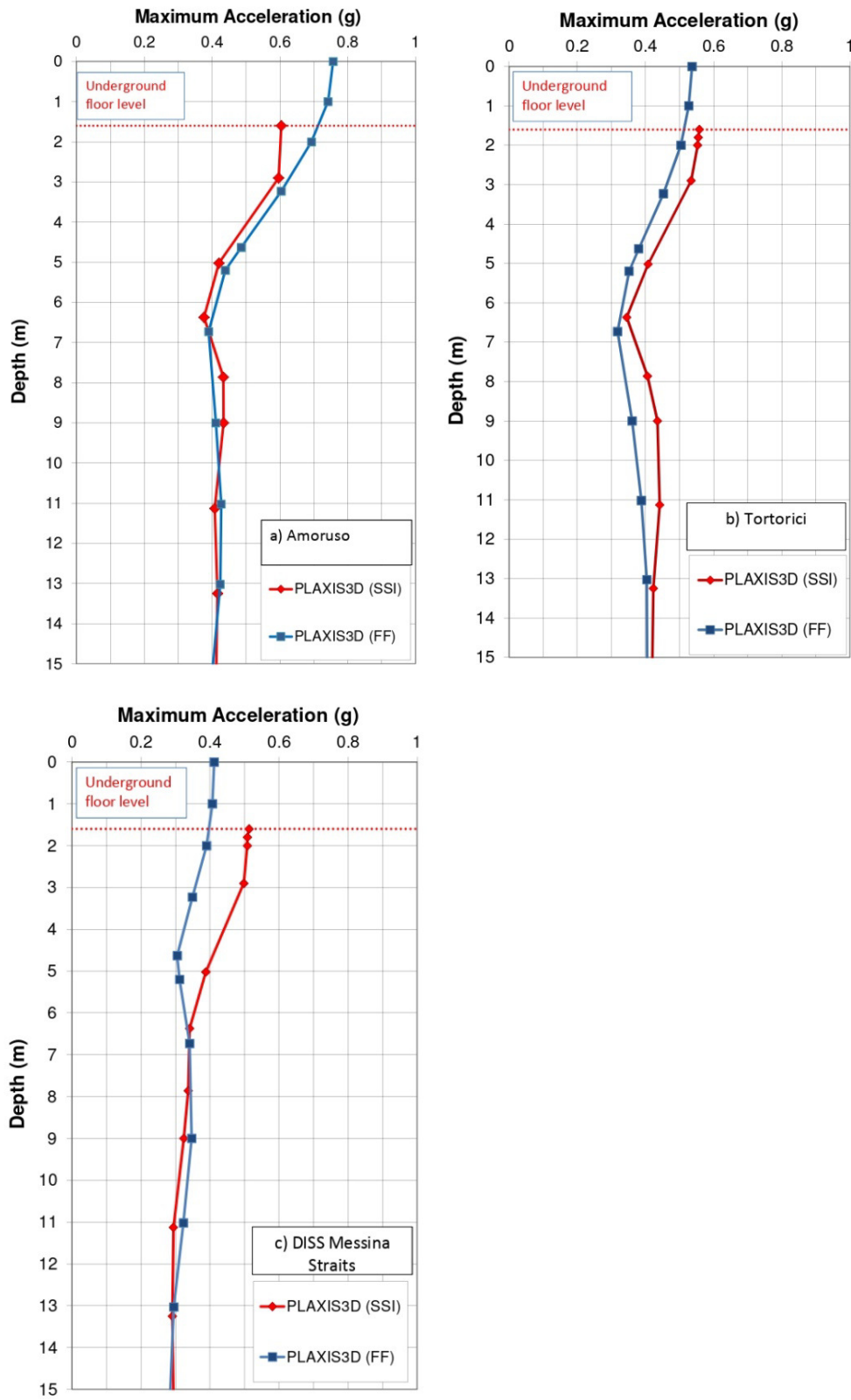
Figure 5.26 Maximum accelerations with depth along SSI and FF alignments using: a) the Amoruso seismogram; b) the Tortorici seismogram; c) the DISS Messina Straits seismogram.

Table 5.8 Values of surface maximum accelerations and soil amplification factors for FF and SSI conditions using: a) the Amoruso seismogram; b) the Tortorici seismogram; c) the DISS Messina Straits seismogram.

	FF, a)	SSI, a)	FF, b)	SSI, b)	FF, c)	SSI, c)
PGA_{input}	0.456 g	0.456 g	0.337 g	0.337 g	0.293 g	0.293 g
PGA_{output}	0.757 g	0.604 g	0.537 g	0.558 g	0.421 g	0.513 g
$R= PGA_{output} / PGA_{input}$	1.660	1.324	1.691	1.656	1.406	1.751

Results show that the SSI has beneficial effects using as input the Amoruso seismogram and there are no substantial differences between the SSI and FF conditions considering the Tortorici seismogram. Instead, the soil amplification factor for the SSI alignment (R=1.751) is much greater than that achieved for the FF alignment (R=1.406) using the DISS Messina Straits seismogram. In this case, the presence of the structure generates a higher amplification and detrimental effects.

Figure 5.27 reports the results at the surface in term of spectral accelerations. Moreover, the period of the structure (T_{STRU}=0.44 s; f_{STRU}=2.25 Hz) has been determined by the amplification functions obtained as the ratio between the fourier spectra at the top and at the bottom of the structure (Figure 5.28) (Massimino et al., 2019).
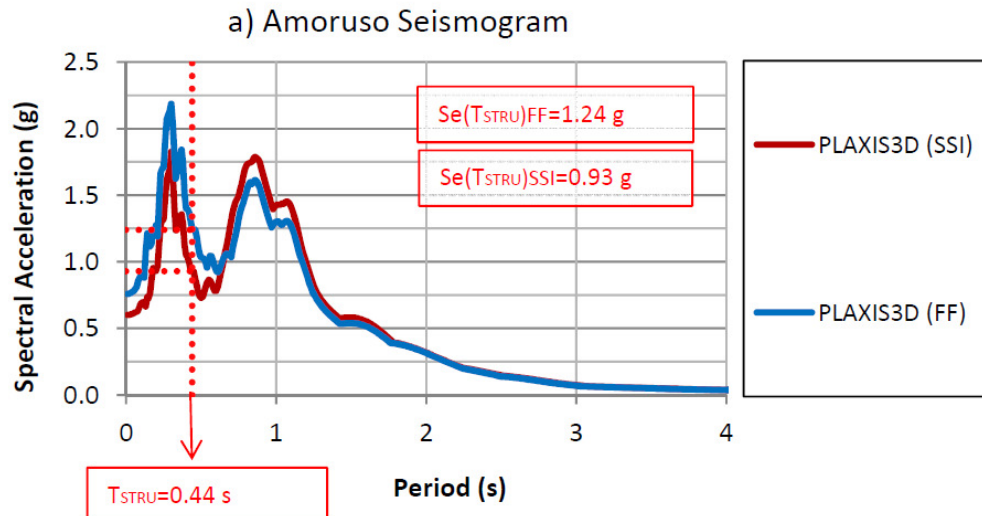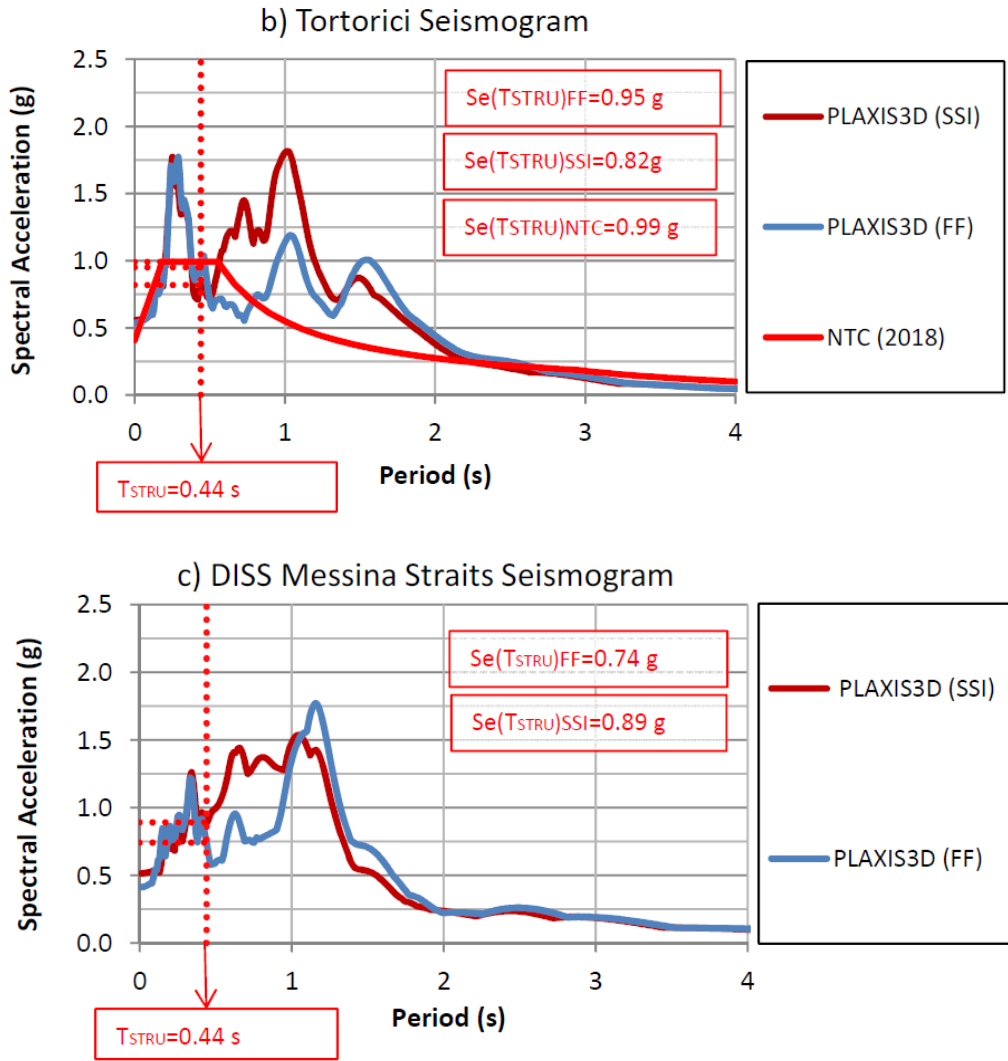
Figure 5.27 Results at the surface in term of spectral accelerations using: a) the Amoruso seismogram; b) the Tortorici seismogram; c) the DISS Messina Straits seismogram.
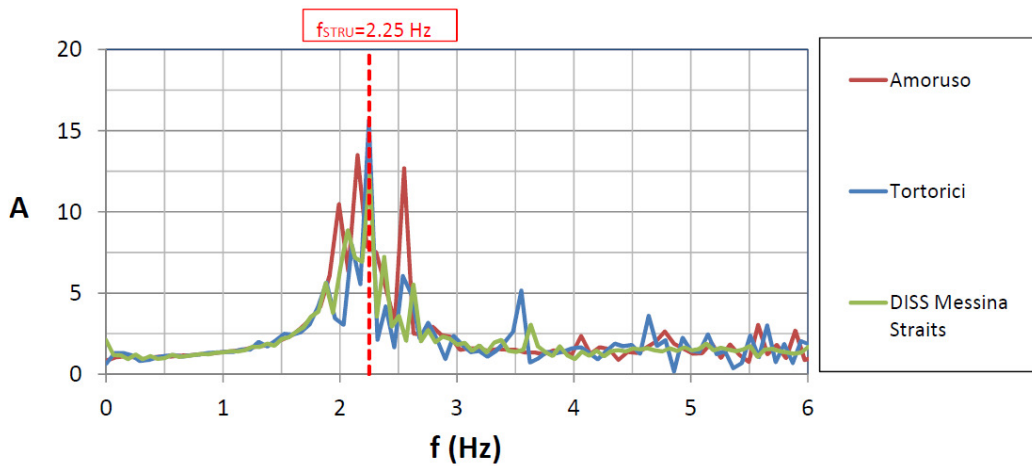
Figure 5.28 Amplification functions obtained as the ratio between the Fourier Spectra at the top and at the bottom of the structure.

Considering the Amoruso seismogram (Figure 5.27 a)), for the period of the structure, a spectral acceleration of 1.24 g has been obtained for the free field condition, while a lower value of 0.93 g has been found for the SSI alignment. Therefore, in this case, taking into account the DSSI has a beneficial effect.

Based on the response spectrum obtained using the Tortorici seismogram (Figure 5.27 b)), spectral accelerations of 0.95 g (FF condition) and 0.82 g (SSI condition) have been found for T_{STRU}=0.44 s, while according to Italian seismic code, a greater value of 0.99 g has been achieved. Thus, the NTC(2018) spectrum is more conservative for the period under consideration. In both cases (Figure 5.27 a) and Figure 5.27 b)) the spectral acceleration is lower considering the full-coupled analyses.

The results obtained adopting the DISS Messina Straits seismogram (Figure 5.27 c)) show a spectral acceleration $S_e(T_{STRU})$=0.74 g for FF condition and $S_e(T_{STRU})$=0.89 g for SSI condition. The SSI leads to a designed acceleration greater than that required in the FF condition due to the second less important period T= 0.65 s in the SSI alignment.

Amplification functions, A(f), for FF and SSI conditions are presented in Figure 5.29. The main resulting frequencies for SSI and FF conditions are compared with the first and the second predominant frequencies of the input motions, and with the frequency of the structure.
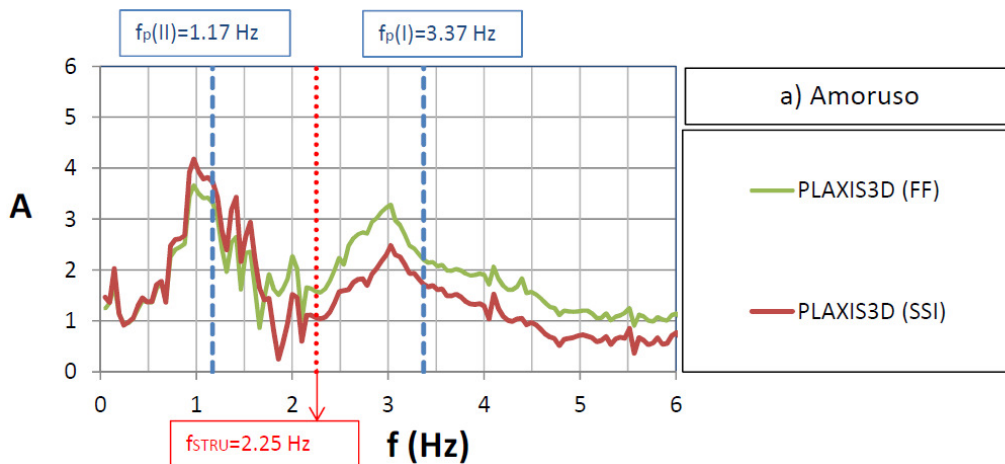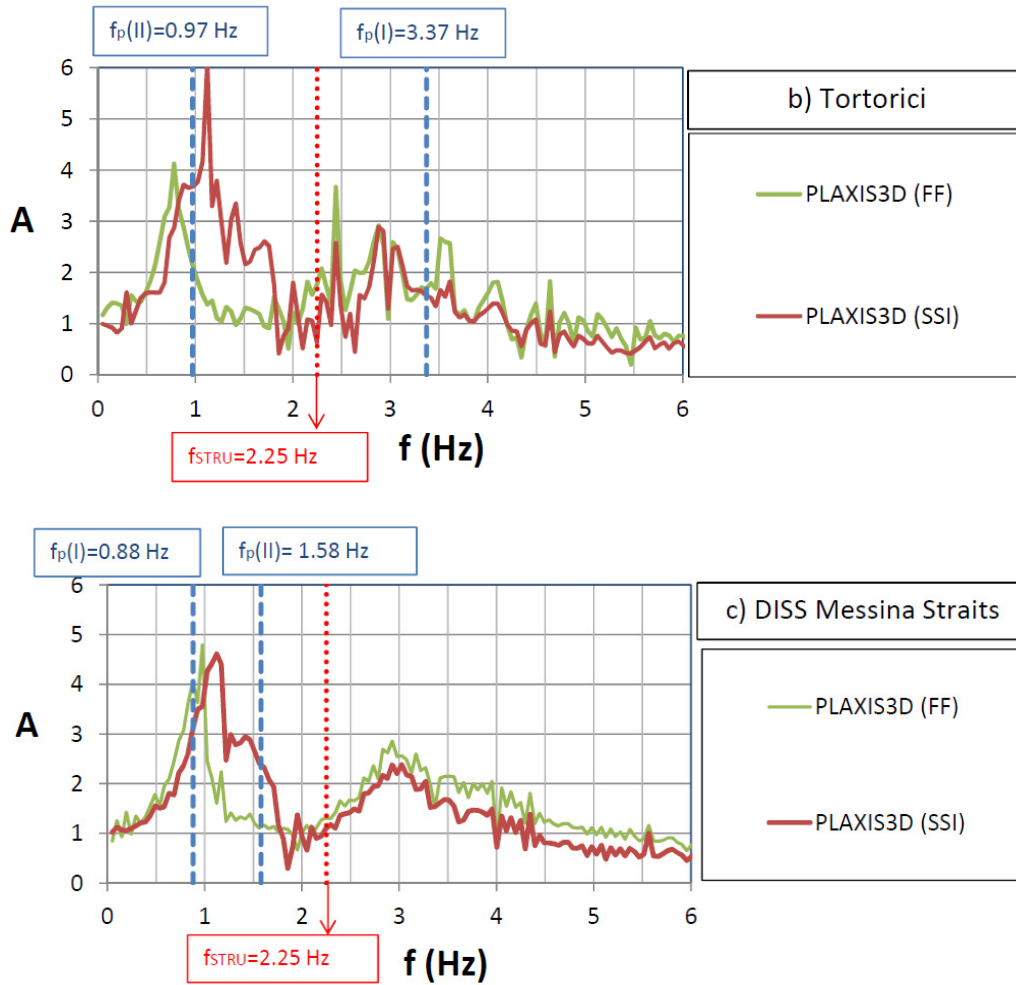
Figure 5.29 Amplification functions for FF and SSI conditions using: a) the Amoruso seismogram; b) the Tortorici seismogram; c) the DISS Messina Straits seismogram.

Figure 5.29 a) shows that, between the amplification function achieved for SSI and FF conditions adopting the Amoruso seismogram, there are no substantial differences. The main resulting frequencies are equal to $f_{FF}(I)=f_{SSI}(I)=0.97$ Hz and $f_{FF}(II)=f_{SSI}(II)=3.02$ Hz. They are far from the frequency of the structure ($f_{STRU}=2.25$ Hz).

Considering the Tortorici seismogram (Figure 5.29 b)), it is possible to observe that A(f) peaks move towards greater frequencies considering the full-coupled analysis: $f_{FF}(I)=0.78$ Hz and $f_{SSI}(I)=1.12$ Hz; $f_{FF}(II)=2.44$ Hz and $f_{SSI}(II)=2.88$ Hz. In this case, taking into account the SSI has a positive effect

because the first resulting frequency for FF condition is closer to the frequency of the structure (f_{STRU}=2.25 Hz).

In both cases (Figure 5.29 a) and b)) the second predominant frequencies of the input motions (1.17 Hz and 0.97 Hz, respectively) are very near to the first resulting frequencies.

The results obtained using the DISS Messina Straits seismogram (Figure 5.29 c)) show a different trend mainly due to the predominant frequencies of the input motion. In this case, the first fundamental input frequency ($f_p(I)$=0.88 Hz) is close to $f_{FF}(I)$=0.98 Hz and $f_{SSI}(I)$=1.12 Hz. However, the presence of the structure causes also a shift and an increase of the amplification values toward the second predominant frequency of the input ($f_p(II)$=1.58 Hz). In fact, in this case, the presence of the structure has generated a higher amplification compared to the FF condition.

Finally, the deformed mesh (scaled up 50 times) and the total displacements, u_z, at the end of the dynamic phase using DISS Messina Straits seismic input are displayed in Figures 5.30 and 5.31. It is possible to observe that the highest values of settlements of about 11 mm are underneath the central part of the building.
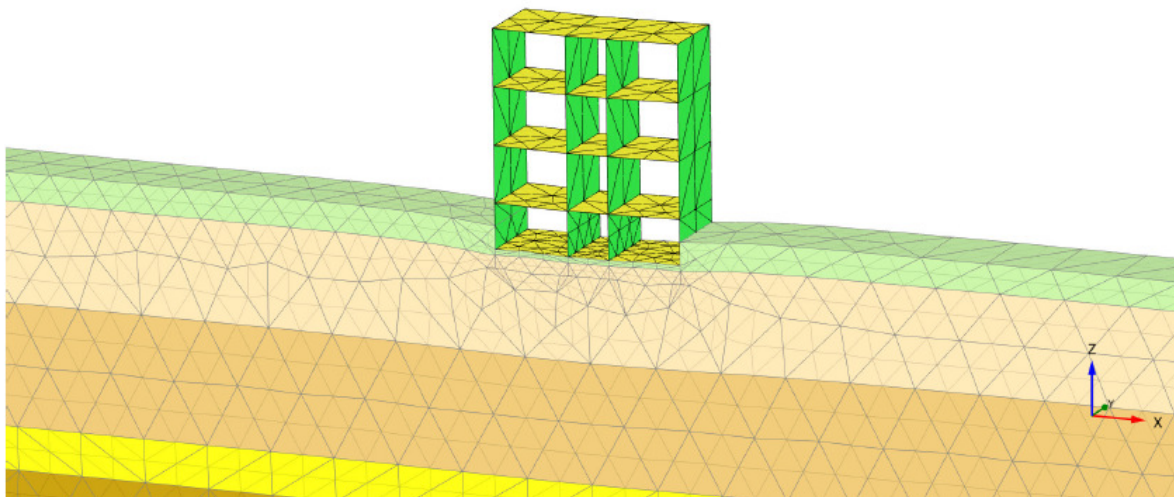
Figure 5.30 Deformed mesh (scaled up 50 times) at the end of the dynamic phase using DISS Messina Straits seismic input.

110
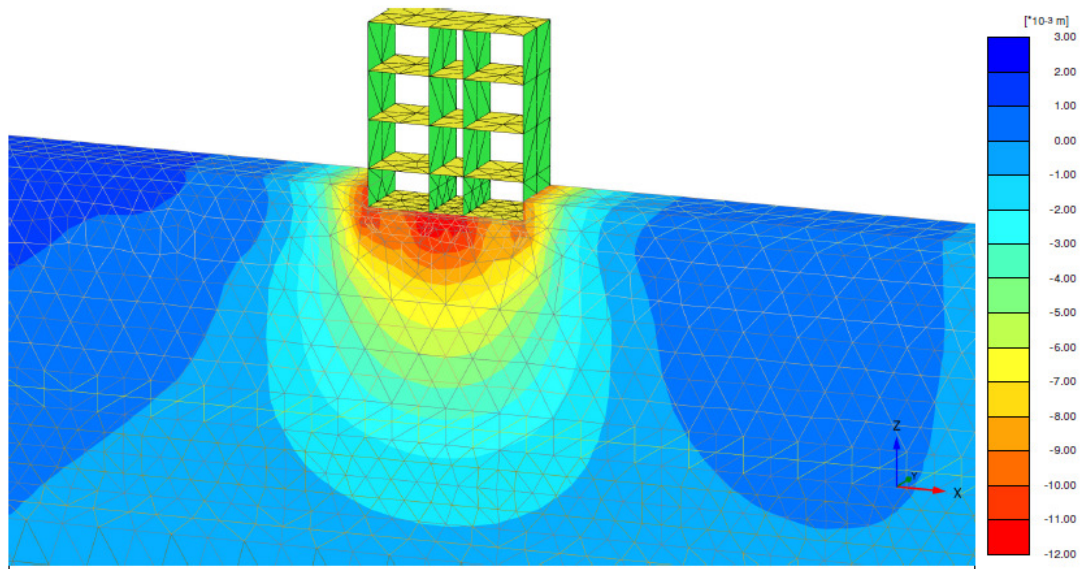
Figure 5.31 Total displacements at the end of the dynamic phase using DISS Messina Straits seismic input.

5.8 Full-coupled FEM model with liquefaction

The total stress analysis is the simplest and commonly way of modelling liquefaction. In this type of analysis, generation and dissipation of excess pore pressures are totally ignored inducing an oversimplification of the problem.

A second type of calculation is based on the effective stress analysis in which liquefaction is occurred as a result of excess pore pressure generation under undrained conditions. All input parameters are effective parameters and the total stress is summation of effective stress and excess pore pressure. Due to the complex behaviour of soil, it needs more information about the mechanical behaviour of soil and a proper constitutive model (Galavi et al., 2013).

In this work, the full-coupled FEM analysis with liquefaction has been performed by means of PLAXIS three-dimensional finite element software and the UBC3D-PLM model has been used to model the behavior of the liquefiable soil layer. An effective stress analysis has been considered in which the parameters are effective and the generation of excess pore water pressure is carried out

111

under undrained conditions (Galavi et al. 2013). The model uses an isotropic hardening rule and a kinematic hardening rule for primary and secondary yield surfaces, respectively, in order to take into account the effect of soil densification and predict a smooth transition into the liquefied state during undrained cyclic loading (Petalas and Galavi, 2013).

For the potentially liquefiable layer (silty sand and gravel 1a), the visco-elastic constitutive model has been assigned to generate the initial stresses due to gravity loading and the UBC3D-PLM model has been used to calculate the undrained dynamic response. Indeed, the UBC3D-PLM model is not appropriate to generate the initial stresses (Laera and Brinkgreve, 2005).

For the remaining layers (fill, silty sand and gravel 1b, sandy silt, silty sand and gravel 2a, sandy silt & clay, silty sand and gravel 2b, silty sand and gravel 3a, silty sand and gravel 3b), the visco-elastic constitutive model has been used for both static and dynamic calculations. Moreover, Free Field and Compliant base boundary conditions require columns of soil with drained behavior near the model boundaries. Thus, drained soil columns with the visco-elastic constitutive model are considered in order to stabilize the later boundaries.

5.8.1 Calibration of UBC3D-PLM model

The UBC3D-PLM model, described in paragraph 2.2.1, has been used in order to properly model the evolution of the excess pore pressures and capture the onset of liquefaction. Table 5.9 summarizes the model input parameters.

Table 5.9 Parameters of the UBC3D-PLM model.

Parameter	Symbol	Unit
Peak friction angle	φ'_p	$^\circ$
Friction angle at constant volume	φ'_{cv}	$^\circ$
Effective cohesion	c'	kN/m^2
Elastic bulk modulus number	k_B^e	-
Elastic shear modulus number	k_G^e	-

Plastic shear modulus number	k_G^p	-
Rate of stress-dependency of elastic bulk modulus	me	-
Rate of stress-dependency of elastic shear modulus	ne	-
Rate of stress-dependency of plastic shear modulus	np	-
Failure ratio	R_f	-
Reference stress	p_{ref}	kN/m^2
Fitting parameters to adjust densification rule	f_{dens}	-
Fitting parameters to adjust post liquefaction behaviour	f_{Epost}	-
Corrected SPT blow counts	$(N_1)_{60}$	-

Relationships for these parameters can be elaborated according to Beaty and Byrne (2011), based on the $(N_1)_{60}$ values, for the generic calibration of the UBCSAND model (Version 904aR). These equations were revised for the UBC3D-PLM soil model by Makra (2013). A second parameters selection procedure was developed by Souliotis and Gerolymos (2016), which uses the relative density of the soil as input.

These methods have to be used to obtain initial model parameters. Then, the model should be calibrated to experimental element tests performed on the soil type of interest. A cyclic triaxial test or a cyclic direct simple shear test is the proper way to extract the parameters for the UBC3D-PLM model.

The cyclic direct simple shear test (CDSS) is the laboratory test that best simulates the stress state in seismic conditions, especially for liquefaction problems. During the cyclic direct simple shear test, a cylindrical or prismatic soil specimen of limited height is enclosed in a reinforced rubber membrane which prevents radial deformation, but allows the specimen to be deformed vertically and in simple shear.

The test can be performed in two steps. In the first step, the specimen (after saturation) is subjected to isotropic ($\sigma'_H = \sigma'_V$) or anisotropic ($\sigma'_H \neq \sigma'_V$) condition. During the second step, in drained or undrained condition, a horizontal cyclic load of predetermined amplitude, τ_{CYC} (which generally varies with harmonic law), is applied to the specimen for a predetermined number of cycles or until failure (Figure 5.32).

Therefore, the soil specimen is subjected to K_0-consolidation stress. Moreover, cyclic loading can be performed as either stress-controlled or strain-controlled and the specimen can be subjected to varying cyclic stress/strain levels.

$\sigma_{H,V}$ = HORIZONTAL/VERTICAL TOTAL STRESS
τ_{cyc} = CYCLIC SHEAR STRESS
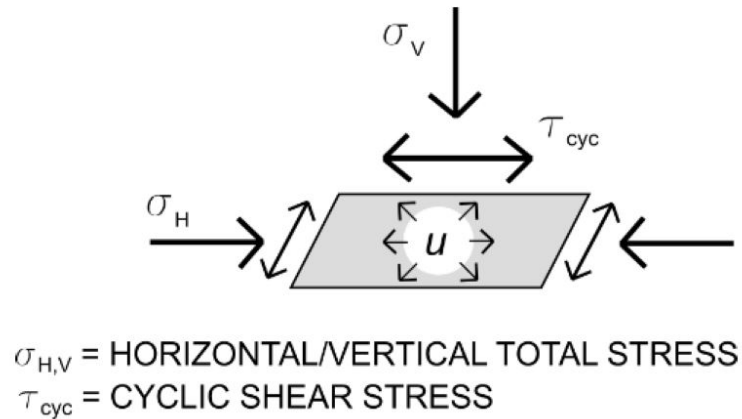
Figure 5.32 Simple shear cyclic loading conditions (From Cappellaro et al., 2017).

In this study, the parameters are based on N_{SPT} values (Makra, 2013). Then, the model has been calibrated to SPT-based liquefaction triggering curves (Boulanger and Idriss, 2014) by means of the simulation of cyclic direct simple shear tests (CDSS) using PLAXIS3D software. Indeed, CDSS tests are not available in the site under consideration.

The case history data (from Idriss and Boulanger, 2010) adjusted to the equivalent vertical effective stress of σ'_v=1 atm (~ 100 kPa) and to an earthquake of moment magnitude M=7.5 are reported in Figure 5.33 and compared with the SPT-based procedures from Youd et al. (2001) and Idriss and Boulanger (2010).
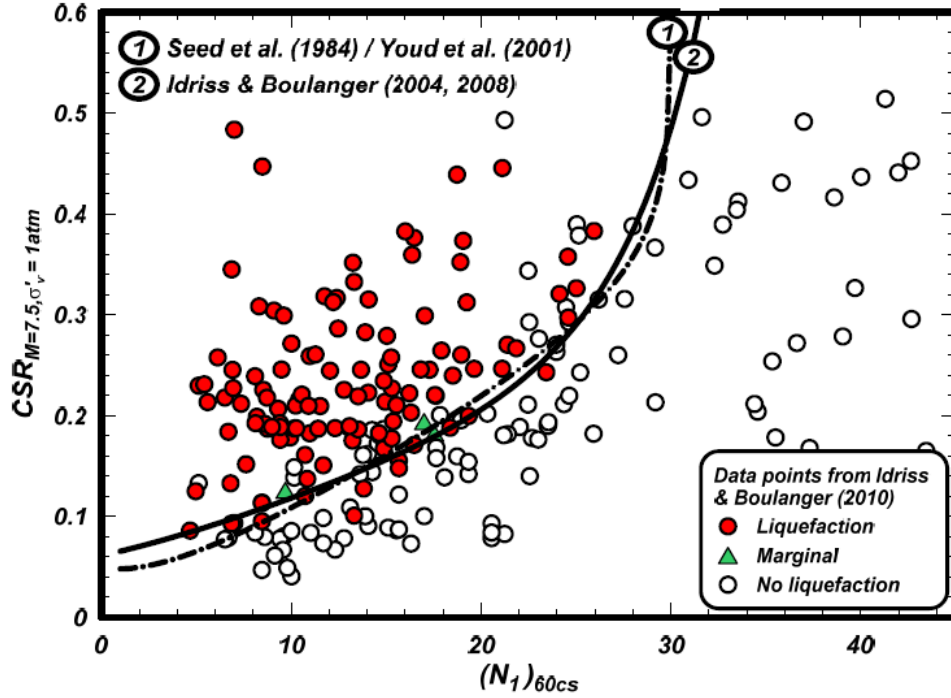
Figure 5.33 SPT-based liquefaction triggering curves with a database of case histories (From Boulanger and Idriss, 2014).

The stiffness modulus factors $k_B{}^e$, $k_G{}^e$ and $k_G{}^p$, the indexes *me*, *ne* and *np,* and the failure ratio R_f have been estimated from the proposed equations for the generic initial calibration (Beaty and Byrne, 2011; Makra, 2013):

$$k_G^e = 21.7 \times 20(N_1)_{60}^{0.333} \tag{5.25}$$

$$k_B^e = 0.7 k_G^e \tag{5.26}$$

$$k_G^p = 0.003\ k_G^e (N_1)_{60}^2 + 100 \tag{5.27}$$

$$me = 0.5; \quad ne = 0.5; \quad np = 0.4 \tag{5.28}$$

$$R_f = 1.1((N_1)_{60})^{-0.15} \tag{5.29}$$

The water head has been imposed at the depth of 3 m. Therefore the fill layer (from 0 to 2 m) is not liquefiable. The silty sand and gravel 1a layer (from 2 to 9 m) has been modelled with $(N_1)_{60}$ equals to 7.35. Instead, the silty sand and gravel 1b layer (from 9.0 to 17.5 m) has not been considered liquefiable due to the high value of $(N_1)_{60}=34.86$.

The strength parameters of the primary yield surface φ'_p, φ'_{cv} and c' have been derived directly from the DSS test performed in S1C1 sample (retrieved at 7.0-7.4 m in S1 borehole).

The densification factor f_{dens} is a multiplier that controls the scaling of the plastic shear modulus factor during the secondary loading. The acceptable range is 0-1, a value below 1 means that the k_G^p becomes lower and the behavior softer. f_{Epost} is the parameter to adjust post-liquefaction behavior. Galavi et al. (2013) carried out a parametric study for the influence of the f_{Epost}. They showed that this parameter controls the plastic behavior of soil at the post liquefaction regime and the higher it is, less plastic strain is generated.

In this work, the fitting parameters have been obtained by means of the simulation of cyclic direct simple shear tests (CDSS) using PLAXIS3D software.

According to the Boulanger-Idriss triggering correlation, the value of $CSR_{M=7.5,\sigma'=1}=0.104$ has been obtained at $(N_1)_{60}=7.35$ (Figure 5.34).
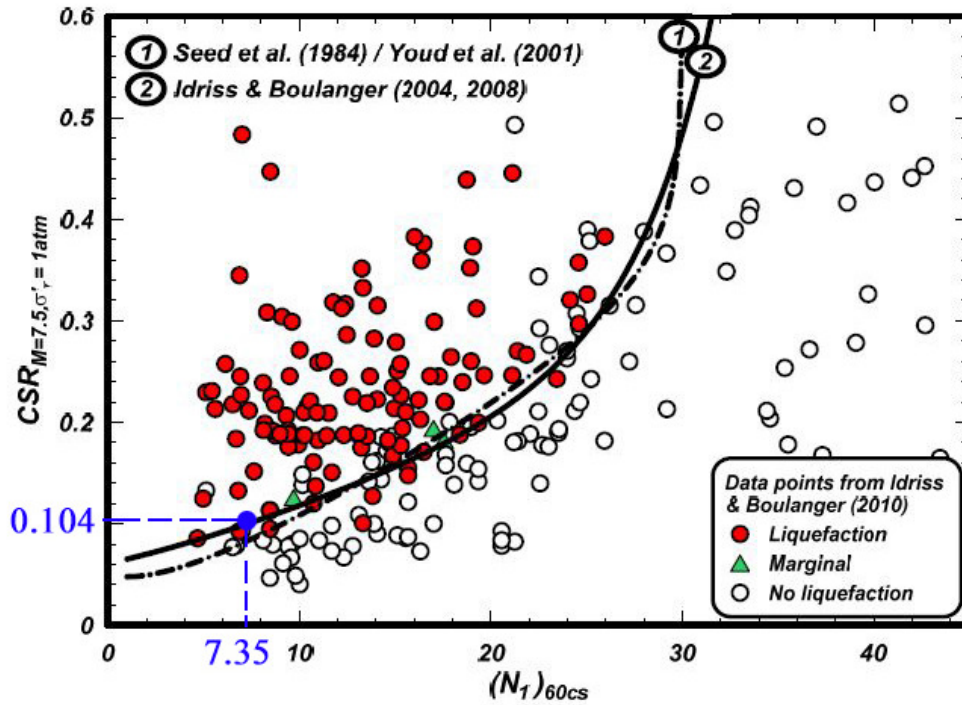
Figure 5.34 Value of $CSR_{M=7.5,\sigma'=1}$ obtained at $(N_1)_{60}$=7.35 (From Boulanger and Idriss, 2014; modified).

Moreover, the relation for the number of equivalent uniform stress cycles versus earthquake magnitude (Idriss and Boulanger, 2004) shows that an earthquake of moment magnitude of M=7.5 corresponds to a number of equivalent stress cycles of 15 (Figure 5.35).
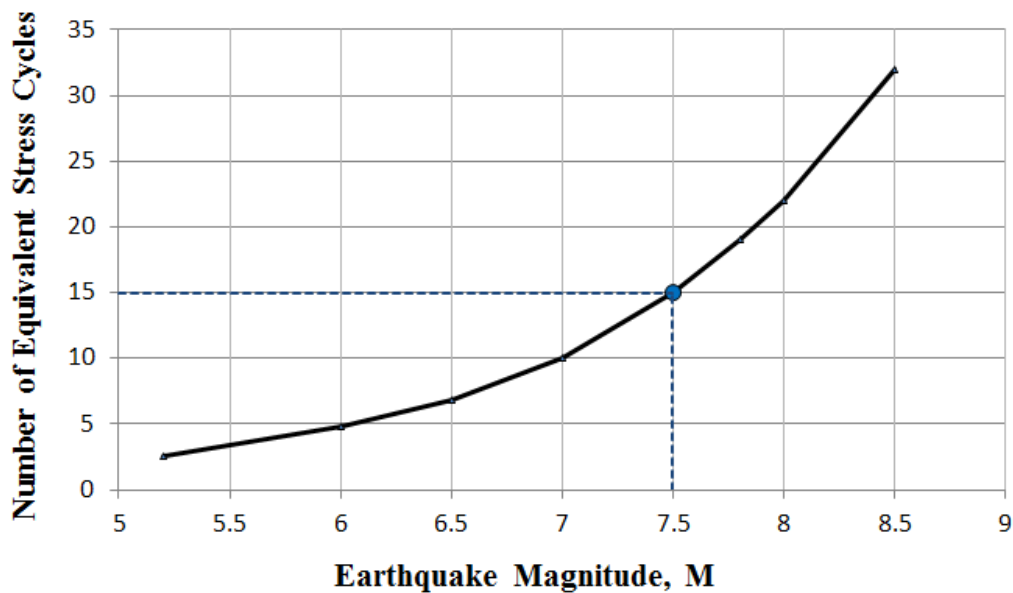
Figure 5.35 Number of equivalent stress cycles versus earthquake magnitude (From Idriss and Boulanger, 2004, redrawn).

The magnitude scaling factor, MSF, has been used to adjust the induced CSR during earthquake magnitude M to an equivalent CSR for an earthquake magnitude, M =7.5 (Idriss and Boulanger, 2004):

$$MSF = 6.9exp\left(\frac{-M}{4}\right) - 0.058 \leq 1.8 \tag{5.30}$$

These relations (Figure 5.35 and Equation 5.30) have been then used to derive the curve in Figure 5.36, where the CSR is reported against the number of cycles required to reach liquefaction (r_u=100%).
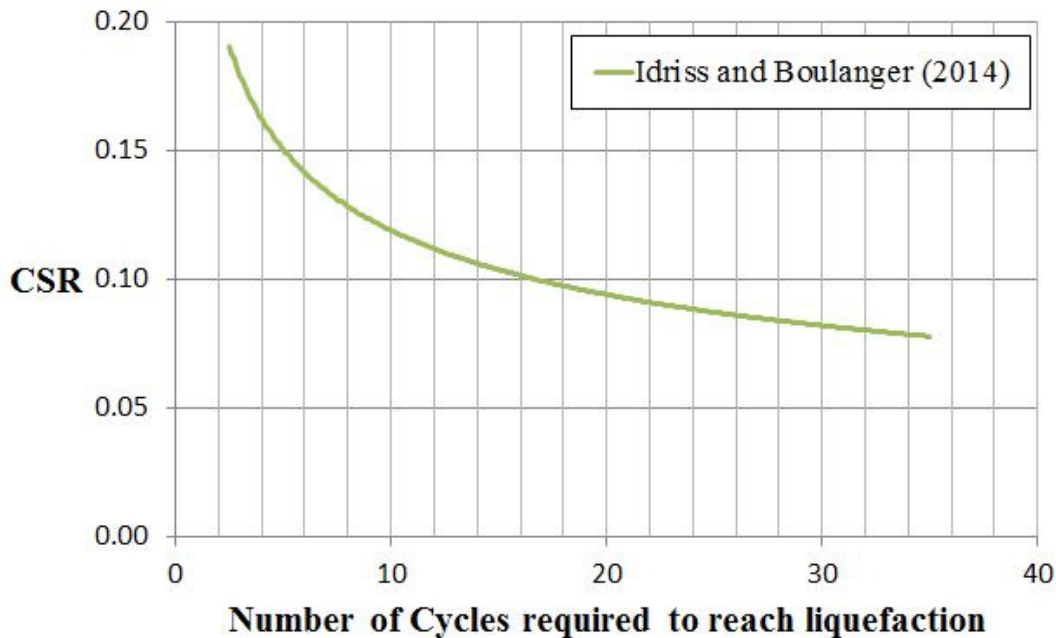
Figure 5.36 CSR versus the number of cycles required to reach liquefaction (r_u=100%) (From Idriss and Boulanger, 2004, redrawn).

Starting from the values derived according to the generic calibration of the UBC3D-PLM model (Makra, 2013), many direct cyclic shear tests have been simulated by varying the fitting parameters. The sample has been considered liquefied when the shear strain has reached the 3% (Idriss and Boulanger, 2004). The values of f_{dens} and f_{Epost} have been obtained when, considering a cyclic stress CSR=0.104, liquefaction has been achieved for a number of cycles equal to 15.

The conditions of the cyclic direct simple-shear stress tests are reported in Table 5.10, where K_0-value is the ratio of lateral stress over axial stress; $|\sigma_{yy}|$ is the absolute value of the initial vertical shear at which the sample is consolidated. In the case of K_0-consolidate test, the initial lateral stress is equal to $K_0\sigma_{yy}$; σ_{xy} is the initial static shear; the *number of cycles* is the number of total load cycles for the test; τ_{xy} is the applied shear stress amplitude.

Table 5.10 Conditions of the cyclic direct simple-shear stress tests.

Test Conditions	Symbol	Value/type
Type of test	-	Undrained
K_0-consolidate test	K_0-value	0.5
Initial Stress	$|\sigma_{yy}|$	100 kN/m^2
Number of cycles	-	100
Number of step per quarter cycle	-	50
Test control	-	Stress
Shear stress amplitude	τ_{xy}	10.4 kN/m^2

Liquefaction has been achieved for a number of cycles equal to 15 when f_{dens}=0.72 and f_{Epost}=0.02.

The CDSS test response in term of the shear stress (τ_{xy}) over the shear strain (γ_{xy}), excess water pore pressure (Δu) over the shear strain (γ_{xy}) and excess pore water pressure ratio (r_u) over cycles is reported in Figure 5.37.

(a)   (b)
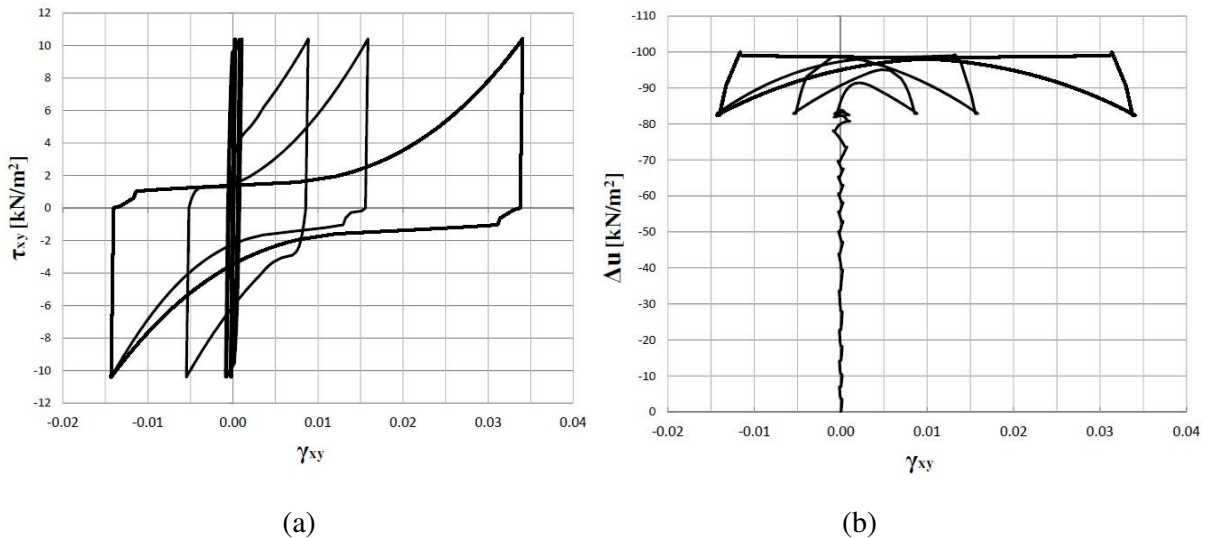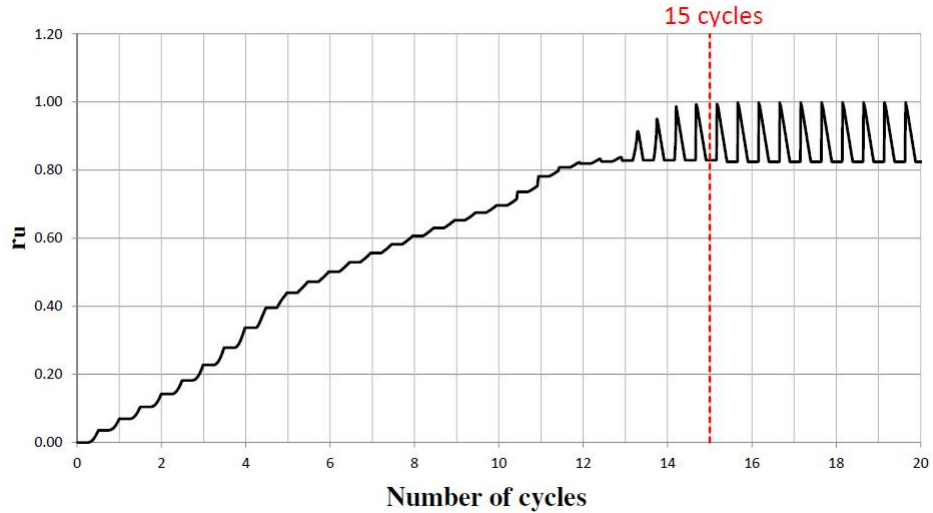
(c)

Figure 5.37 CDSS test response in term of: (a) shear stress (τ_{xy}) over shear strain (γ_{xy}), (b) excess water pore pressure (Δu) over shear strain (γ_{xy}) and (c) excess pore water pressure ratio (r_u) over cycles (CSR=0.104).

Then, direct cyclic shear tests have been simulated by varying the cyclic stress, CSR. The test conditions and the number of cycles needed to reach liquefaction for each test are reported in Table 5.11. Results obtained from all tests are reported in Appendix.

Table 5.11 Test conditions and the number of cycles needed to reach liquefaction.

Test	$|\sigma_{yy}|$	τ_{xy}	CSR	Number of cycles
1	100 kN/m^2	8.5 kN/m^2	0.085	27
2	100 kN/m^2	9.0 kN/m^2	0.090	23
3	100 kN/m^2	9.5 kN/m^2	0.095	20
4	100 kN/m^2	10.0 kN/m^2	0.100	17
5	100 kN/m^2	10.4 kN/m^2	0.104	15
6	100 kN/m^2	11.0 kN/m^2	0.110	13
7	100 kN/m^2	12.0 kN/m^2	0.120	11
8	100 kN/m^2	13.0 kN/m^2	0.130	9
9	100 kN/m^2	14.0 kN/m^2	0.140	7
10	100 kN/m^2	15.0 kN/m^2	0.150	6
11	100 kN/m^2	18.0 kN/m^2	0.180	4

Cyclic stress ratio as a function of the equivalent number of cycles in order to trigger liquefaction is reported in Figure 5.38. Comparison is given between the calibrated model and Idriss and Boulanger curve (2014). An optimum fitting has been obtained.
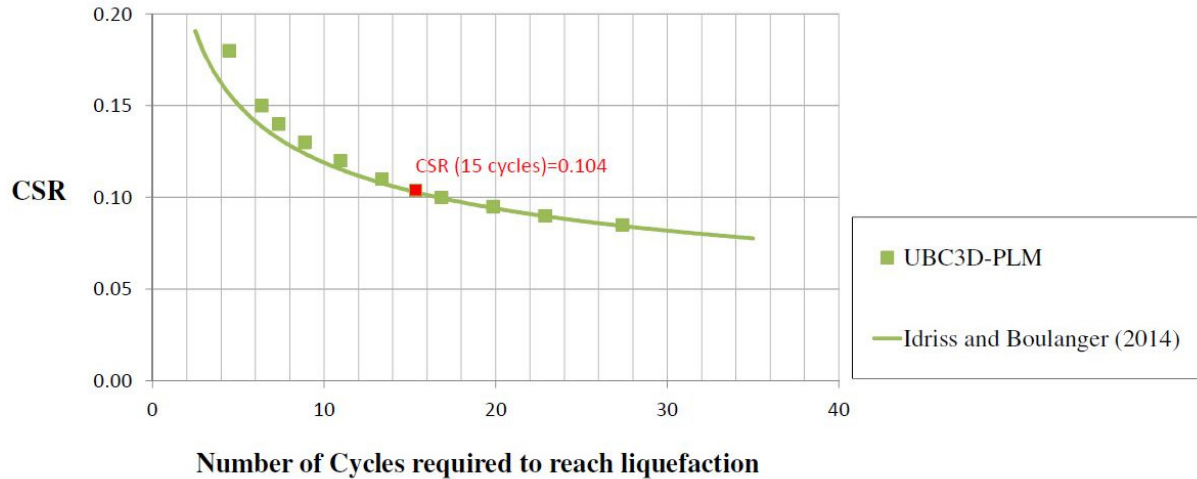
Figure 5.38 Comparison between the calibrated model and Idriss and Boulanger curve (2014).

The parameters of the calibrated UBC3D-PLM model are reported in Table 5.12.

Table 5.12 Parameters of the calibrated UBC3D-PLM model

Parameter	Unit	Silty Sand and Gravel 1a
γ_{unsat}	kN/m^3	16.7
γ_{sat}	kN/m^3	20.7
φ'_p	°	34
φ'_{cv}	°	30
c'	kN/m^2	1
k_B^e	-	590.6
k_G^e	-	843.8
k_G^p	-	236.8
me	-	0.5
ne	-	0.5
np	-	0.4
R_f	-	0.82
p_A	kN/m^2	100
f_{dens}	-	0.72
f_{Epost}	-	0.02
$(N_1)_{60}$	-	7.35

5.8.2 Results

The seismic behaviour of the soil-structure system on liquefiable soil has been analysed in terms of liquefaction potential, excess pore pressures (EPPs), accelerations, response spectra and displacements under the three different seismograms of the 1908 earthquake, described in detail in paragraph 5.4.1.

The excess pore pressure ratio in terms of vertical effective stress, $r_{u,\sigma'v}$, has been used to evaluate the liquefaction potential. It is defined by the following equation:

$$r_{u,\sigma'_v} = \frac{\sigma'_{v0} - \sigma'_v}{\sigma'_{vo}} = 1 - \frac{\sigma'_v}{\sigma'_{v0}} \tag{5.31}$$

where σ'_v is the current vertical effective stress during the dynamic calculation and σ'_{v0} is the initial effective vertical stress prior to the seismic motion. The soil can be considered liquefied when the $r_{u,\sigma'v}$ is equal to 1.

The excess pore pressure ratio in terms of vertical effective stress at the end of each earthquake is reported in Figure 5.39. The $r_{u,\sigma'v}$ reaches the value of 1 in the Silty Sand and Gravel 1a layer showing that the liquefaction occurs using as input the three 1908 seismograms.

(a)

(b)

122

(c)
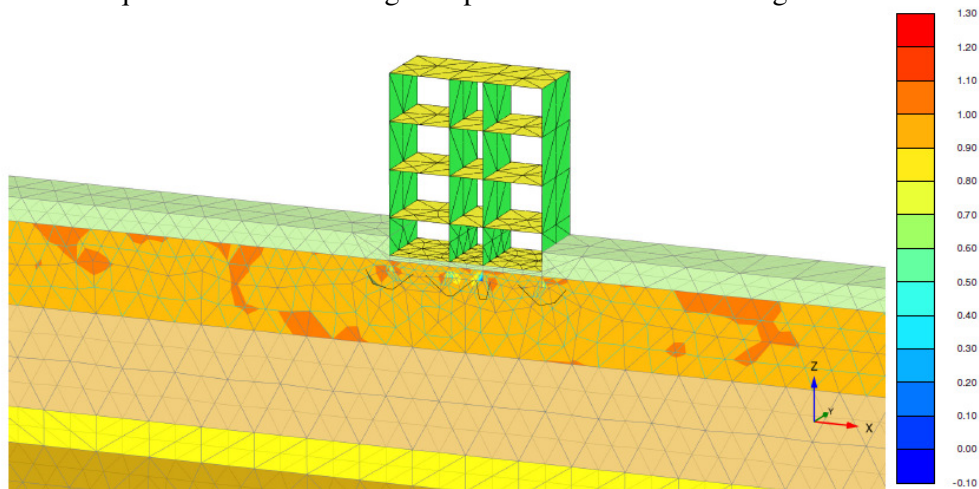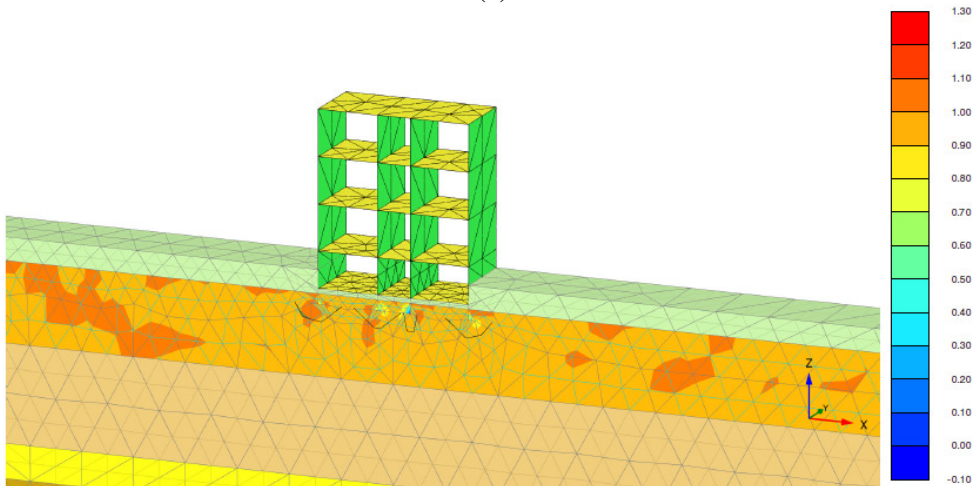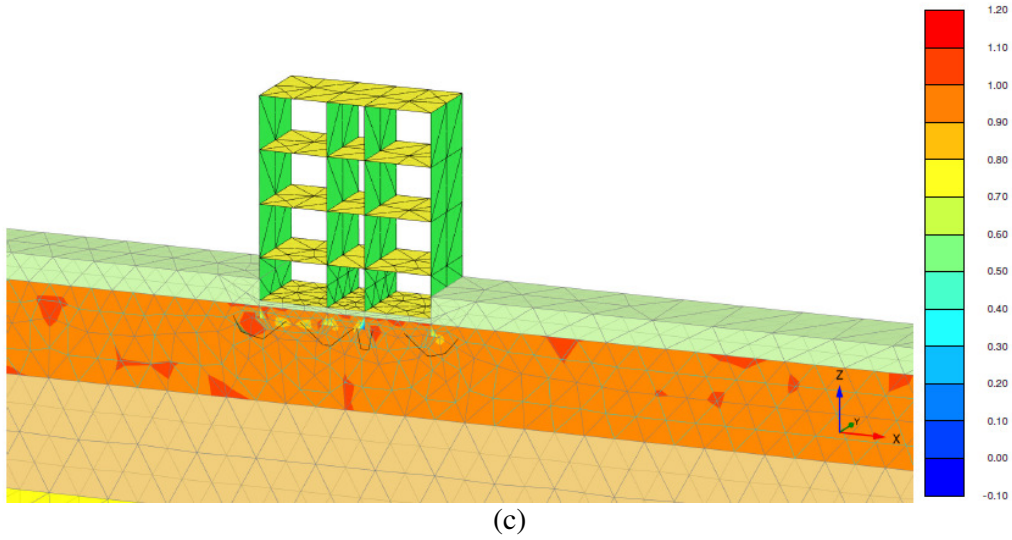
Figure 5.39 Excess pore pressure ratio in terms of vertical effective stress using: a) the Amoruso seismogram; b) the Tortorici seismogram; c) the DISS Messina Straits seismogram.

The state variable $r_{u,p'}$ gives similar information as $r_{u,\sigma'v}$ but, instead of the vertical effective stress, the mean effective stress is used:

$$r_{u,p'} = \frac{p'_0 - p'}{p'_o} = 1 - \frac{p'}{p'_0} \qquad (5.32)$$

where p' is the current mean effective stress during the dynamic calculation and p'$_0$ is the initial mean effective stress prior to the seismic motion.

The $r_{u,p'}$ and the excess pore water pressure time histories at the depth of 4.1 m are shown in Figure 5.40 for each of the three 1908 seismograms. When $r_{u,p'}$ equals 0.9, the soil has been considered in a liquefied state.

123

(a)

(b)

124
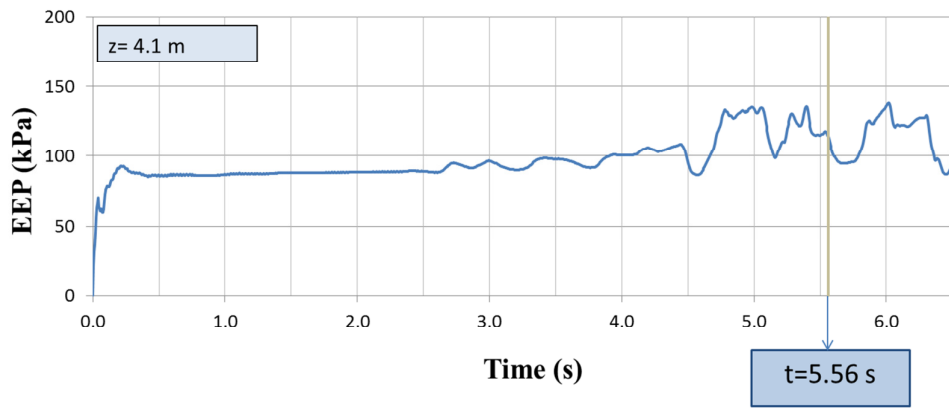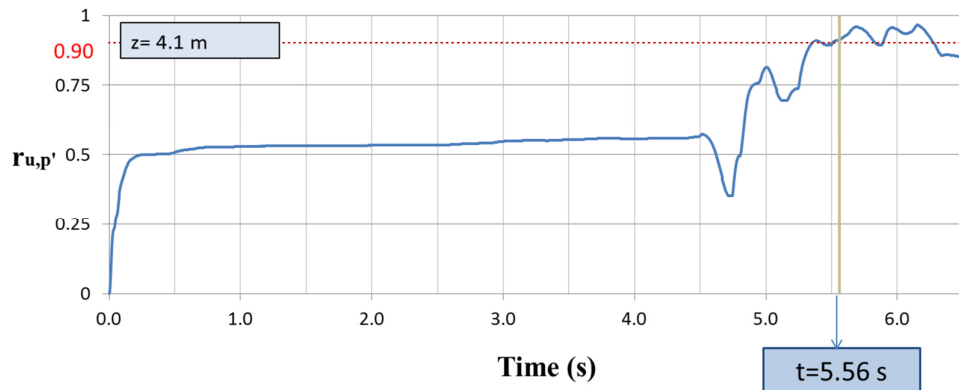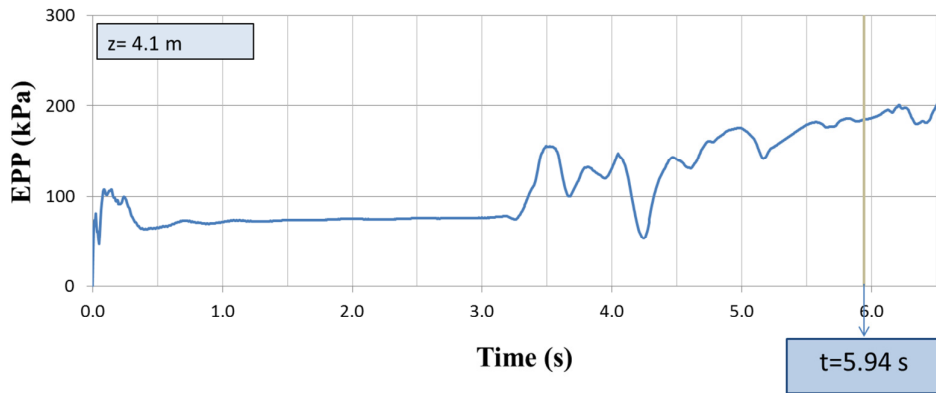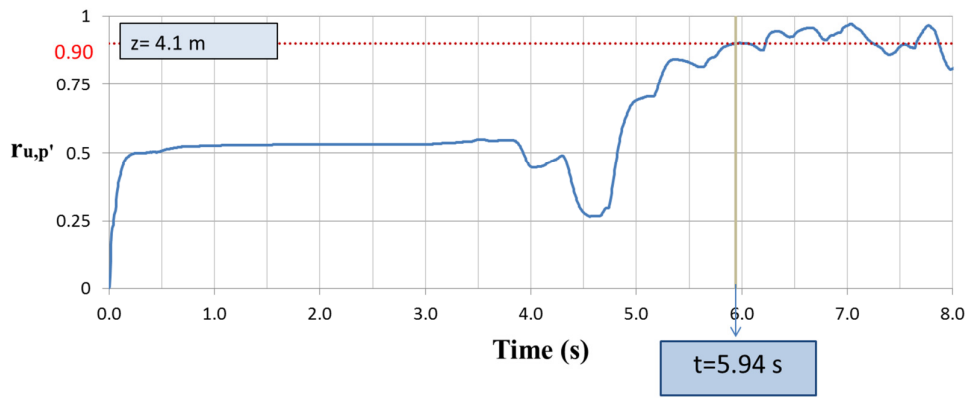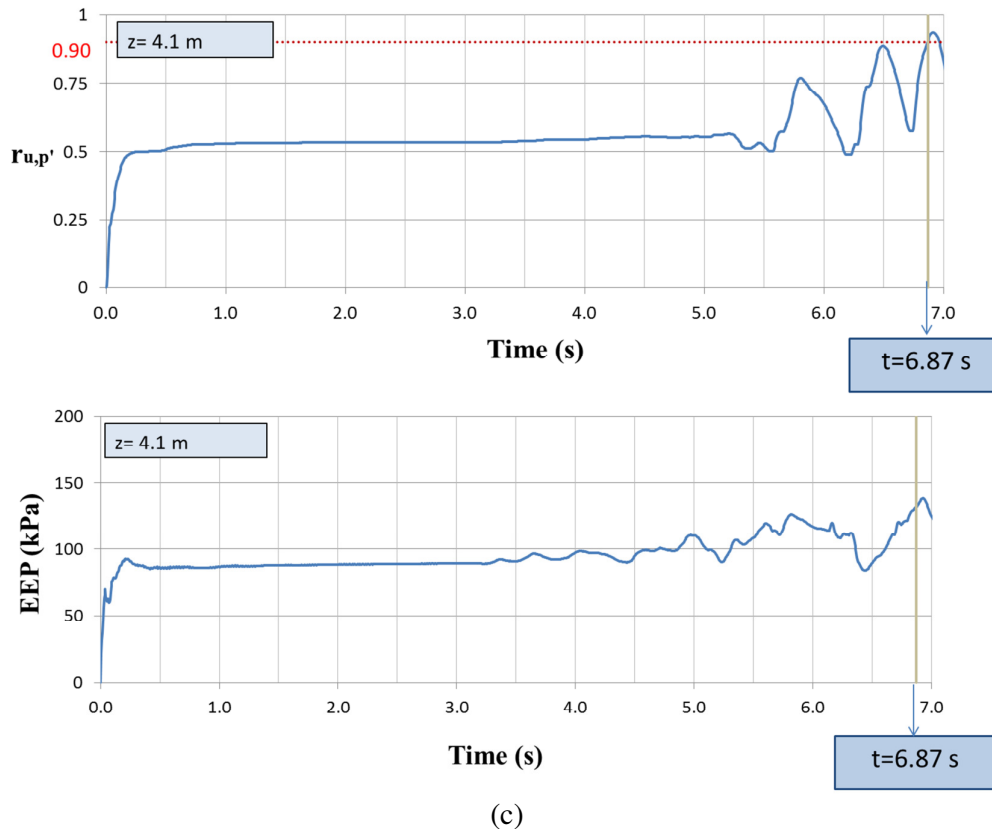
(c)

Figure 5.40 The $r_{u,p'}$ and the excess pore water pressure time histories using: a) the Amoruso seismogram; b) the Tortorici seismogram; c) the DISS Messina Straits seismogram.

Results show that at the depth of 4.1 m the dynamic times to reach liquefaction are equal to 5.56 s, 5.94 s and 6.87 s for Amoruso, Tortorici and DISS Messina Straits seismograms, respectively. Moreover, the rate of excess pore pressure buildup has been observed to change with time, being a function of the applied cyclic stress at the depth in question.

The $r_{u,p'}$ during the dynamic time at the depths of 5.3 m, 6.3 m and 7.1 m is shown in Figure 5.41 for the Amoruso seismogram, as an example. It is possible to observe that the time to reach liquefaction increases with depth, indicating that liquefaction occurs first near the surface.
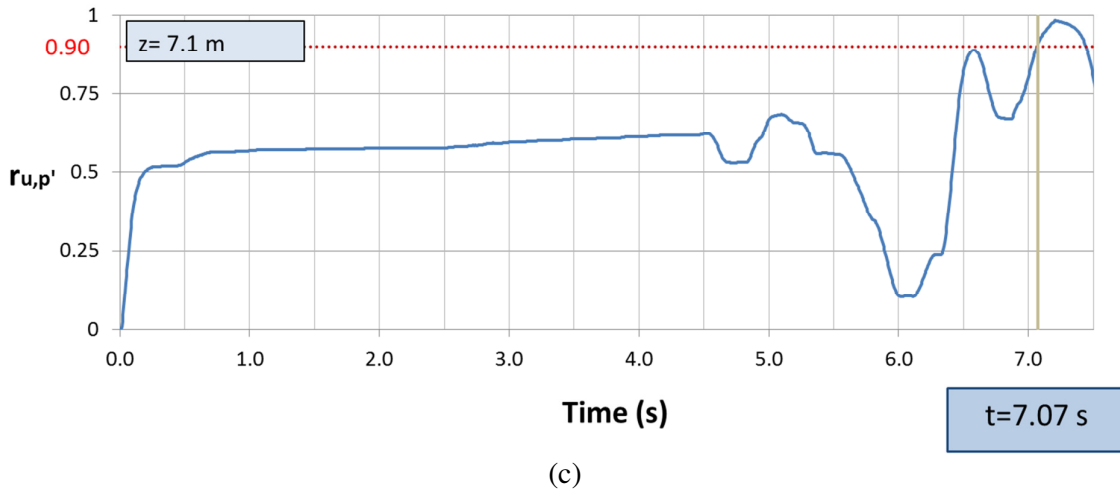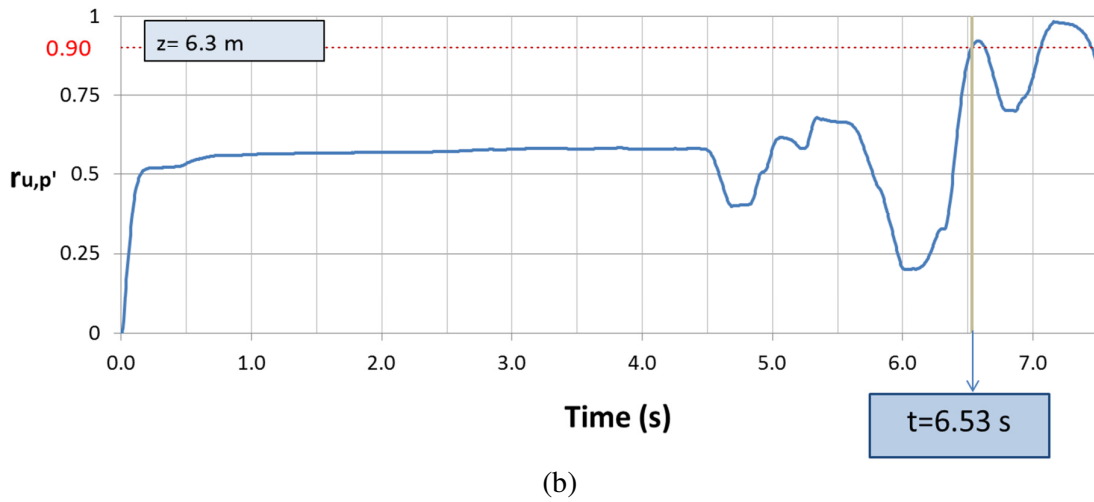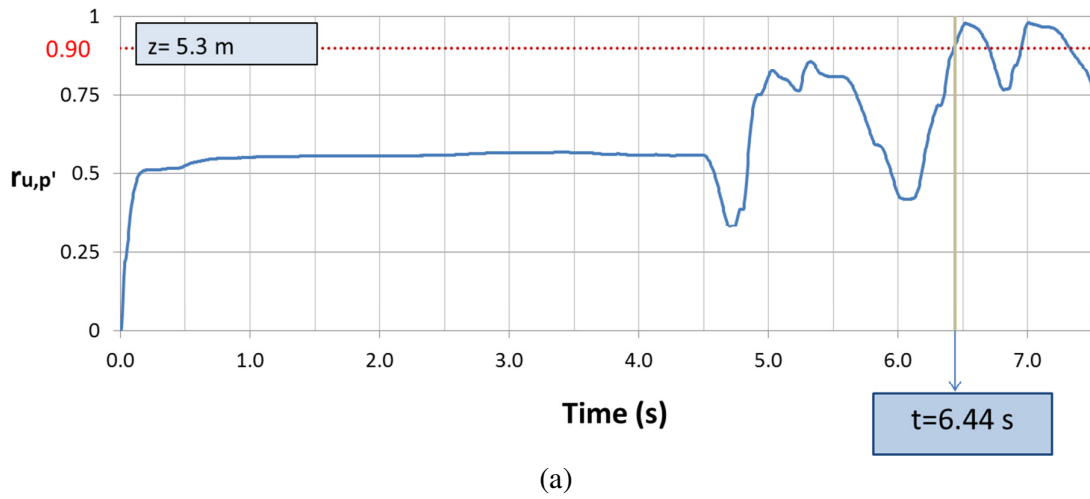
Figure 5.41 The $r_{u,p'}$ time histories at the depths of a) 5.3 m, b) 6.3 m and c) 7.1 m using as input the Amoruso seismogram.

126

Table 5.13 summarizes the dynamic times to reach liquefaction at different depths for the three 1908 seismograms, showing increasing values with depth. Furthermore, lower values are generally obtained considering DISS Messina Straits seismogram than those considering Tortorici seismogram. This is due to the fact that DISS Messina Straits has the maximum acceleration at 7 s, while Tortorici at 11 s. Finally, the lowest values have been derived from Amoruso seismogram that has high accelerations already at the time of 5 seconds.

Table 5.13 Dynamic times to reach liquefaction at different depths: a) the Amoruso seismogram; b) the Tortorici seismogram; c) the DISS Messina Straits seismogram.

Stress Point	Depth [m]	Time [s] (a)	Time [s] (b)	Time [s] (c)
A	4.1	5.56	5.94	6.87
B	5.3	6.44	7.84	6.90
C	6.3	6.53	9.35	7.36
D	7.1	7.07	11.45	7.45

The SSI condition considering the presence of liquefiable layer (silty sand and gravel 1a-from 2 to 9 m) has been compared with the results obtained without considering the liquefaction phenomenon (partly shown in paragraph 5.7). The acceleration time histories at the depth of 1.6 m (underground floor level) and 5.1 m (about in the middle of the liquefiable layer) are shown in Figures 5.42-5.44 for each seismogram of the 1908 earthquake. The acceleration profiles with depth are reported in Figure 5.45. Surface maximum accelerations and soil amplification factors, R, are summarized in Table 5.14.
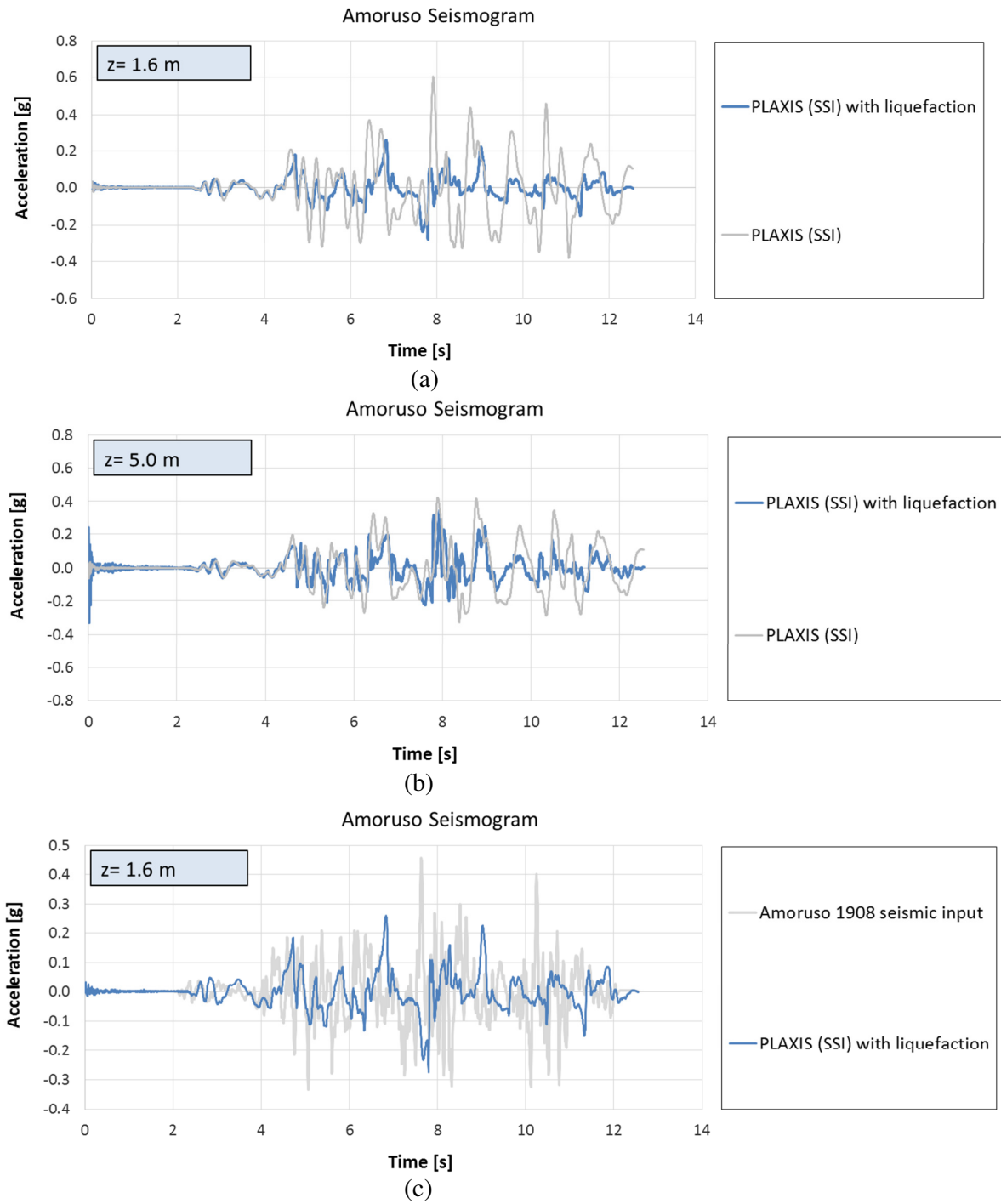
Figure 5.42 Acceleration time histories at the depth of: a)1.6 m and b) 5.1 m using as input the 1908 Amoruso seismogram. It is reported in Figure c) as a comparison with the results.

Tortorici Seismogram

z= 1.6 m

PLAXIS (SSI) with liquefaction

PLAXIS (SSI)

(a)

Tortorici Seismogram

z= 5.0 m

PLAXIS (SSI) with liquefaction

PLAXIS (SSI)

(b)

Tortorici Seismogram

z= 1.6 m

Tortorici 1908 seismic input

PLAXIS (SSI) with liquefaction
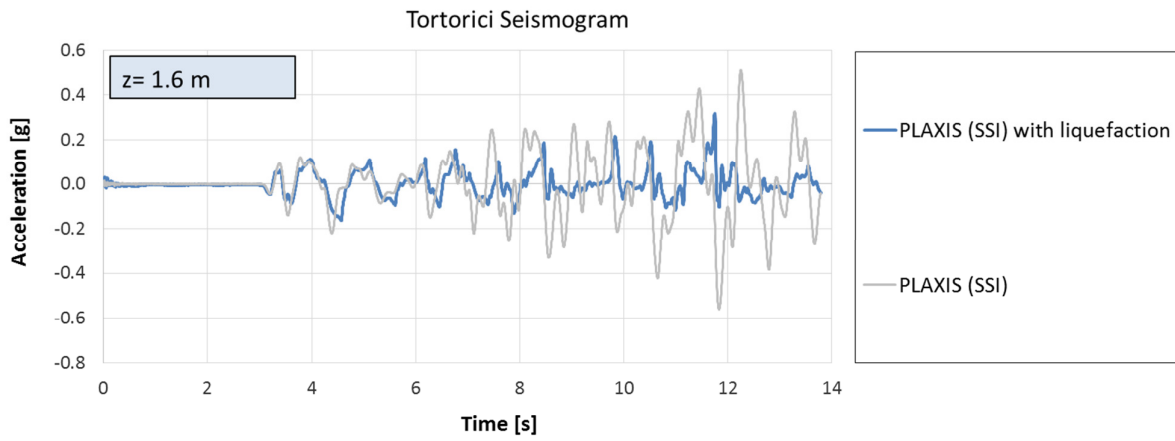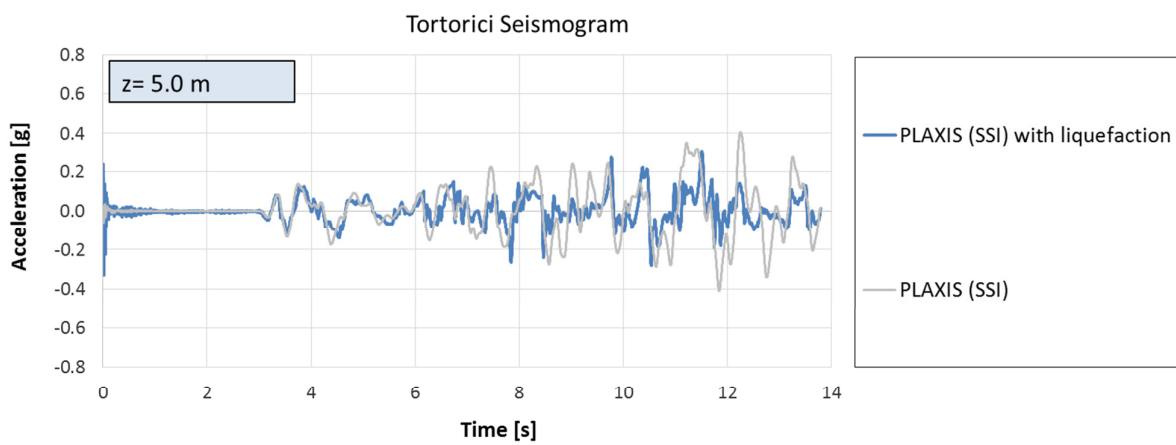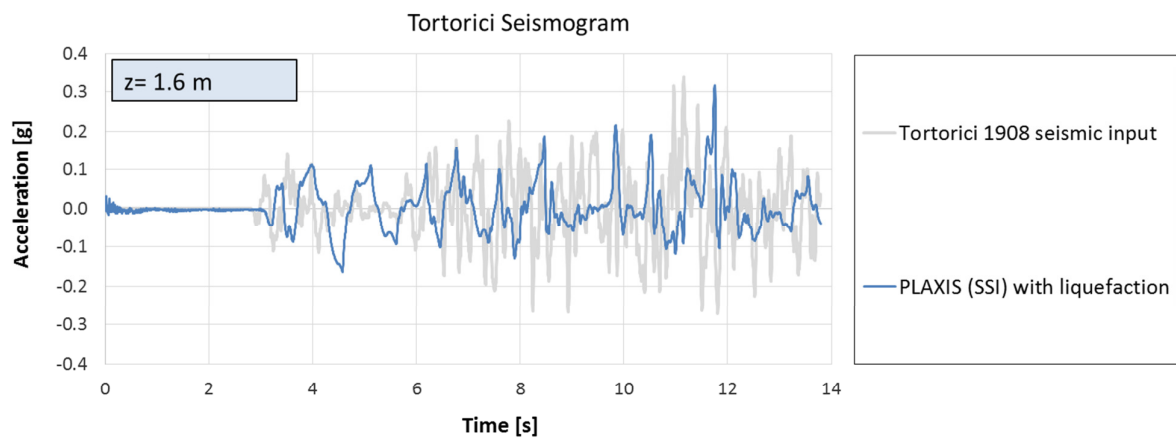
(c)

Figure 5.43 Acceleration time histories at the depth of: a)1.6 m and b) 5.1 m using as input the 1908 Tortorici seismogram. It is reported in Figure c) as a comparison with the results.
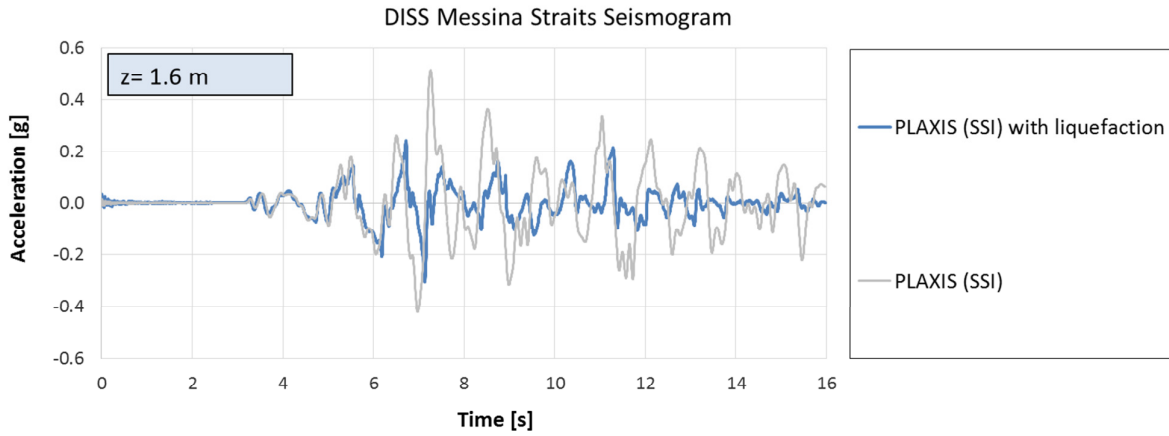
(a)
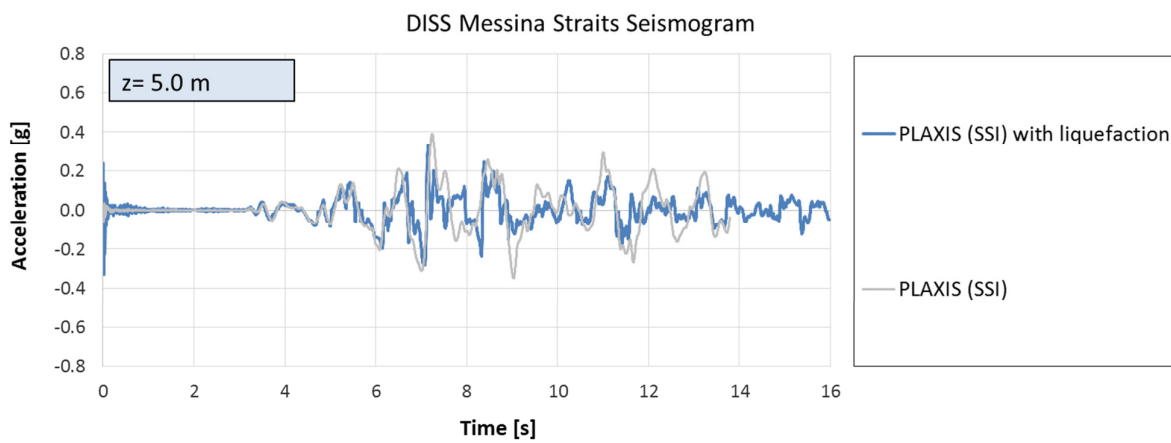
(b)
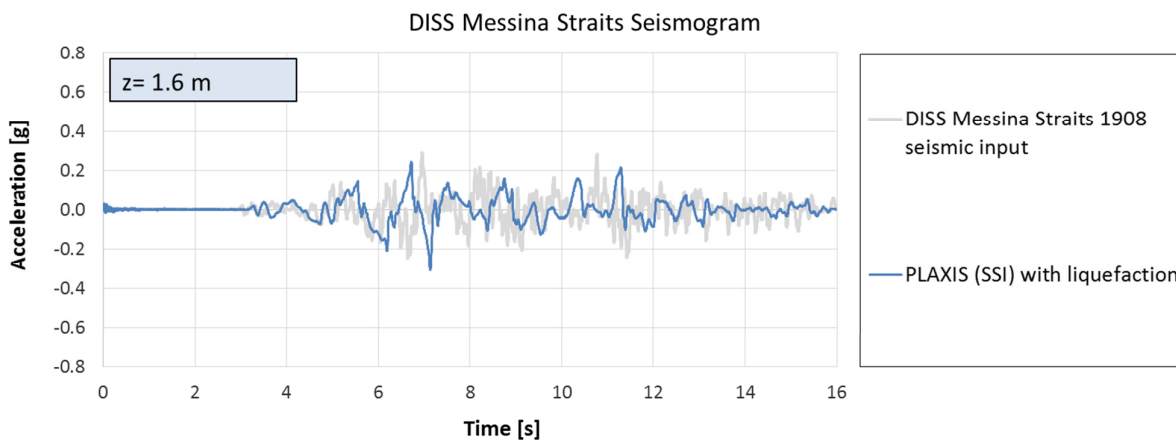
(c)

Figure 5.44 Acceleration time histories at the depth of: a)1.6 m and b) 5.1 m using as input the 1908 DISS Messina Straits seismogram. It is reported in Figure c) as a comparison with the results.
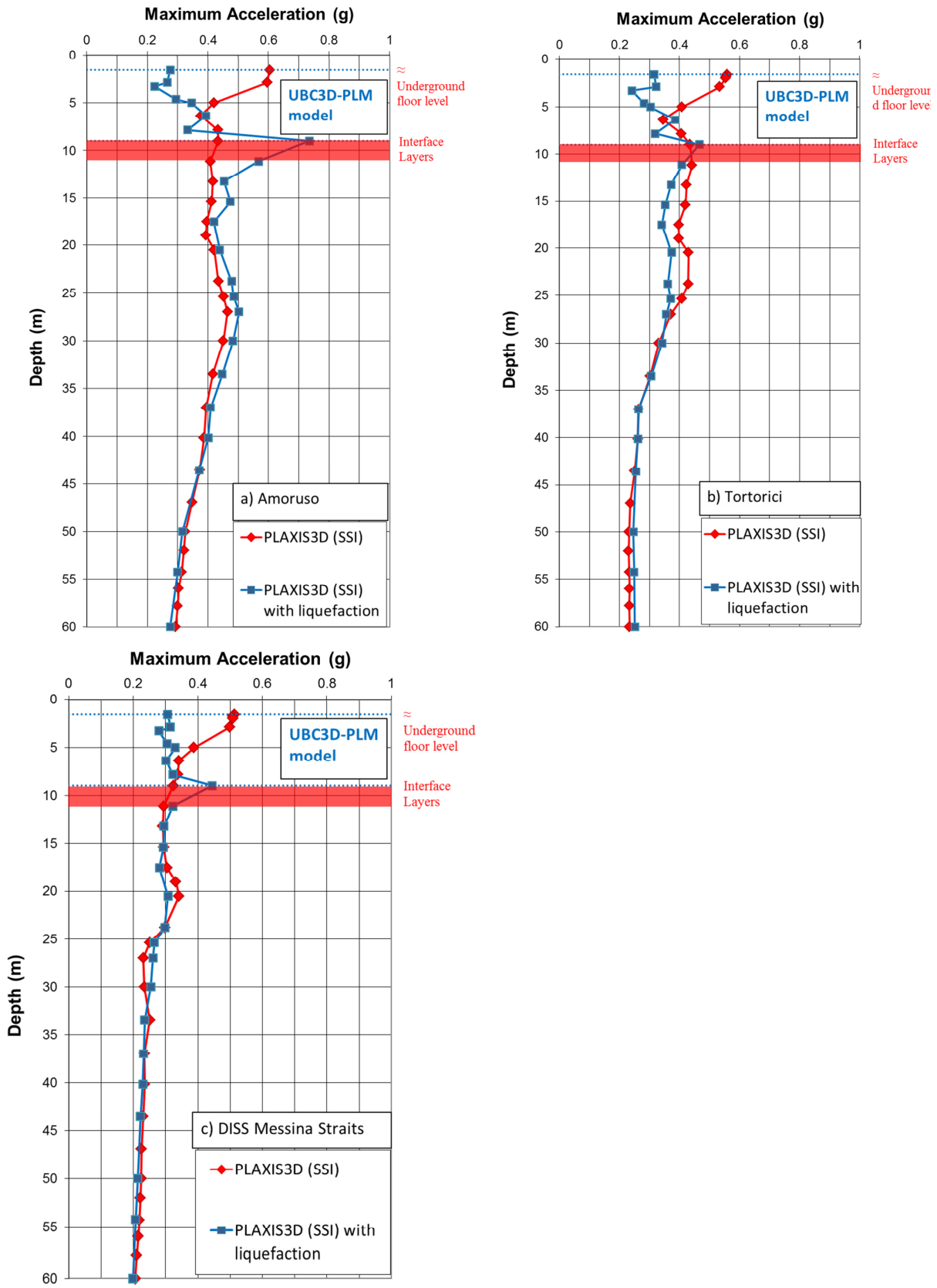
Figure 5.45 Maximum accelerations with depth considering and not considering the liquefaction phenomenon using: a) the Amoruso seismogram; b) the Tortorici seismogram; c) the DISS Messina Straits seismogram.

Table 5.14 Values of surface maximum accelerations and soil amplification factors considering (SSI) and not considering the liquefaction (SSI$_{liqu.}$) using: a) the Amoruso seismogram; b) the Tortorici seismogram; c) the DISS Messina Straits seismogram.

	SSI, a)	SSI$_{liqu}$, a)	SSI, b)	SSI$_{liqu}$, b)	SSI, c)	SSI$_{liqu}$, c)
PGA$_{input}$	0.456 g	0.456 g	0.337 g	0.337 g	0.293 g	0.293 g
PGA$_{output}$	0.604 g	0.276 g	0.558 g	0.316 g	0.513 g	0.306 g
R= PGA$_{output}$ / PGA$_{input}$	1.324	0.605	1.656	0.938	1.751	1.044

The accelerations shown in Figures 5.42-5.45 are in good agreement with the previous consideration, demonstrating that liquefaction has occurred fist near the surface and worked its way downward. In fact the acceleration values generally increase with depth in the liquefied layer. The lowest value occurs at about 3 meters where the water head has been imposed.

In Table 5.14, the parametric study demonstrates that higher PGA of the input motion corresponds to a greater demagnification on the surface.

It is possible to observe that liquefaction causes a large reduction in acceleration amplitude from 2-9 m in comparison to the case without liquefaction, resulting in beneficial effects. Indeed, the liquefaction leads to a reduction in soil stiffness (and resistance), consequently, the liquefied layer develops larger nonlinear strains and acts as a filter. The reduction in stiffness provides the isolation of the building that can be called "natural seismic isolation".

However, before the liquefaction triggering the structure can be subjected to shaking damages. Moreover, Bouckovalas et al. (2016) demonstrated that liquefaction can sometime cause a soil amplification in lower frequencies. They showed that a minimum liquefied layer thickness is required in order to ensure seismic isolation effects, while for thinner layers attenuation becomes marginal or may even turn into amplification.

At the depth of 9 m, it is possible to notice an increase in acceleration. Indeed, the interface between liquefied and non-liquefied layers develops a strong stiffness contrast. In fact, the soil stiffness during

liquefaction becomes nearly zero. Therefore, the interface between the liquefied and non-liquefied layers is an area of high stiffness contrast.

Similar considerations can be found in terms of response spectra at the depths of 1.6 m and 5.0 m for each seismogram (Figures 5.46-5.48). It is possible to notice a large reduction in spectral accelerations compared to those obtained without considering liquefaction.

For the period of the structure under consideration, the spectral accelerations of 0.32 g, 0.38 g and 0.45 g have been obtained using Amoruso (Figures 5.46 (a)), Tortorici (Figures 5.47 (a)) and DISS Messina Straits seismograms (Figures 5.48 (a)), respectively. Results again show the natural seismic isolation due to liquefaction.

(a)

(b)
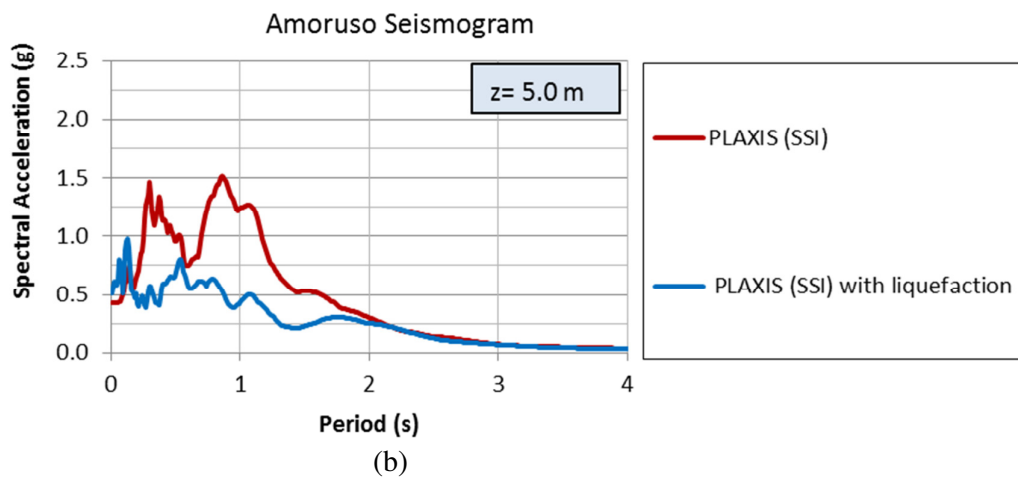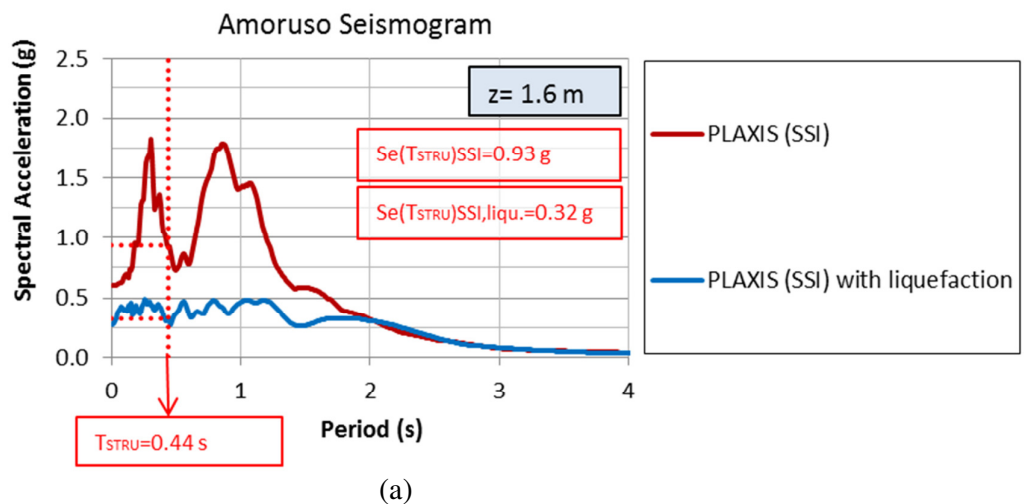
Figure 5.46 Response spectra at the depths of 1.6 m and 5.0 m obtained using Amoruso seismogram considering and not considering the liquefaction phenomenon.
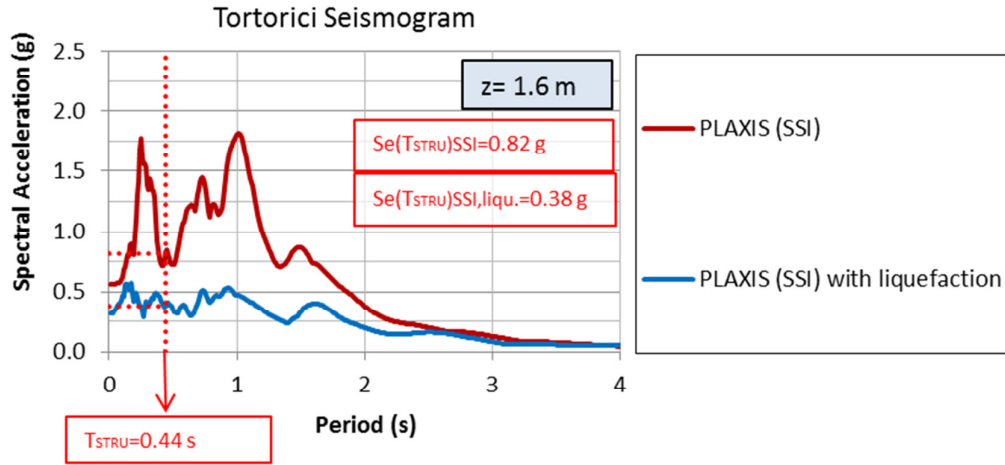
(a)
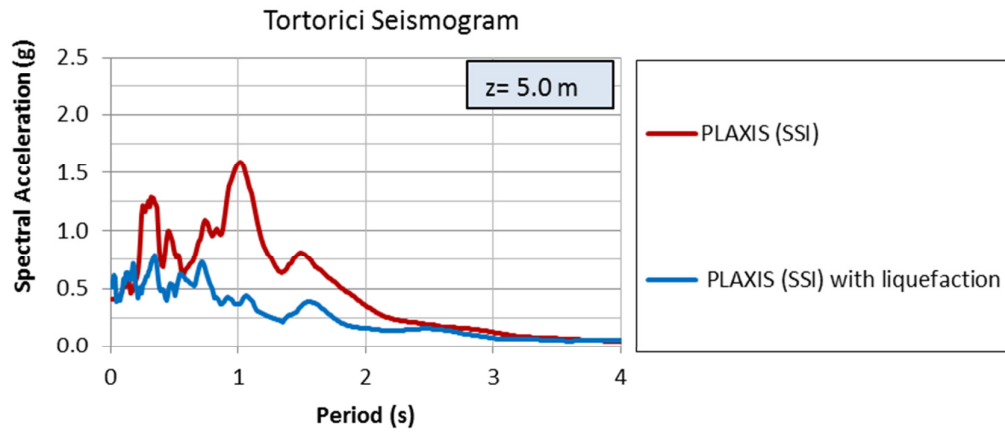
(b)

Figure 5.47 Response spectra at the depths of 1.6 m and 5.0 m obtained using Tortorici seismogram considering and not considering the liquefaction phenomenon.
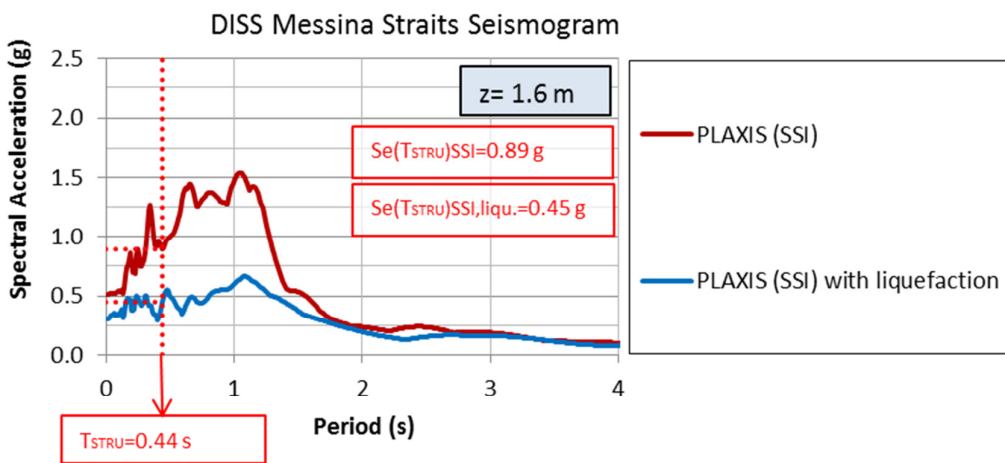
(a)
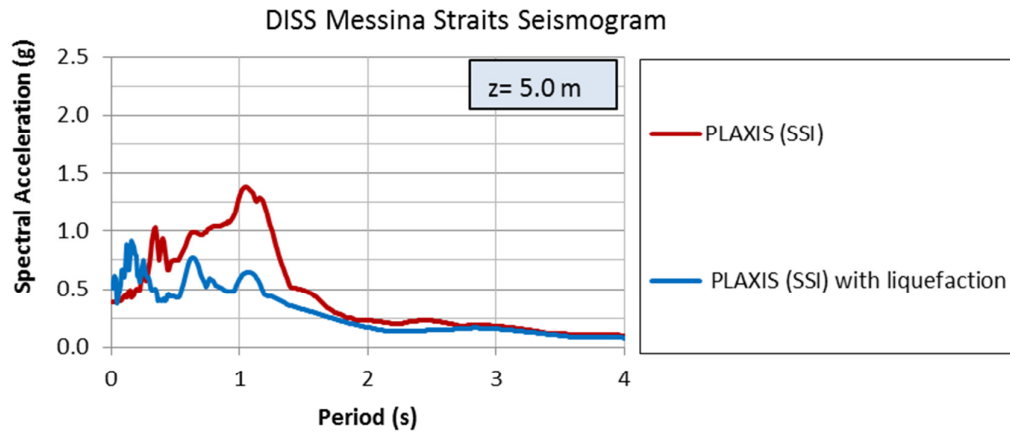
(b)

Figure 5.48 Response spectra at the depths of 1.6 m and 5.0 m obtained using DISS Messina Straits seismogram considering and not considering the liquefaction phenomenon.

When the soil deposit liquefies, the change in stiffness involves in a change in the natural frequency of the soil. Therefore, the results have been also investigated in term of amplification functions (Figure 5.49). In general, it is possible to observe that A(f) peaks move towards lower frequencies considering the liquefaction phenomenon.

(a)

(b)

di

(c)
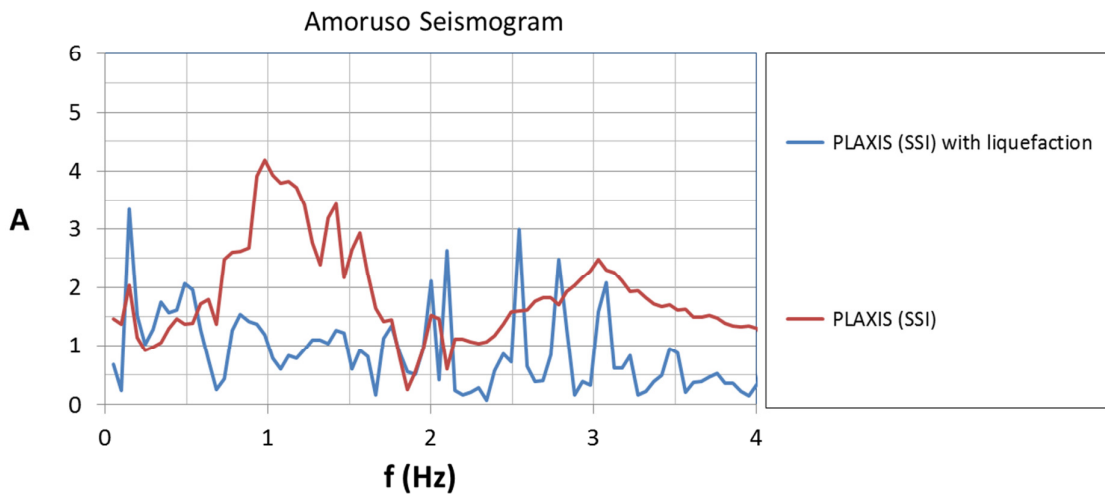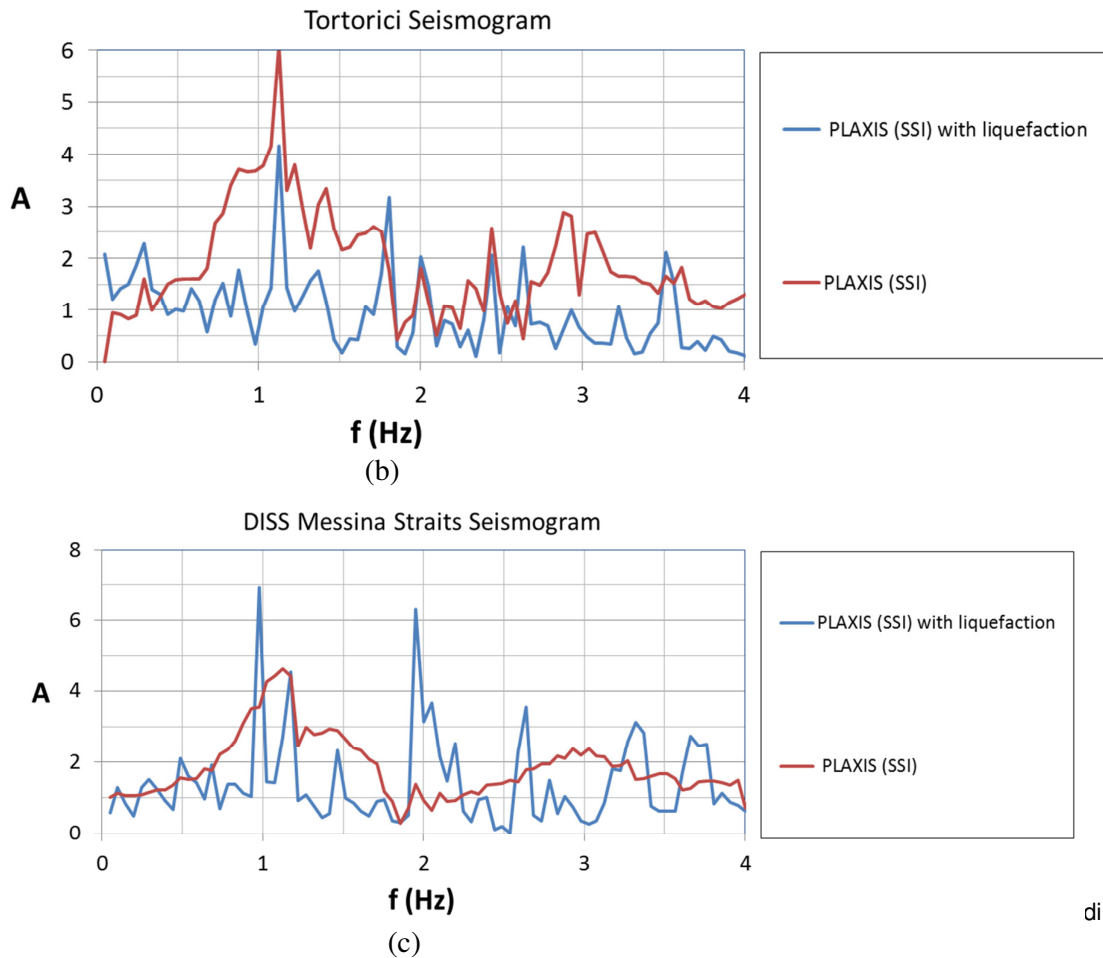
Figure 5.49 Amplification functions obtained using: a) the Amoruso seismogram; b) the Tortorici seismogram; c) the DISS Messina Straits seismogram, considering and not considering the liquefaction phenomenon.

The liquefaction phenomenon is usually accompanied by a large amount of ground surface settlements. The onset of liquefaction beneath shallow foundation can lead to permanent deformations of the building that can affect his operability.

The FE deformed meshes obtained at the end of the dynamic phase are given in Figure 5.50 for each seismogram. It is possible to notice that there two different types of displacements: settlements underneath the building and heave displacements next to the building.
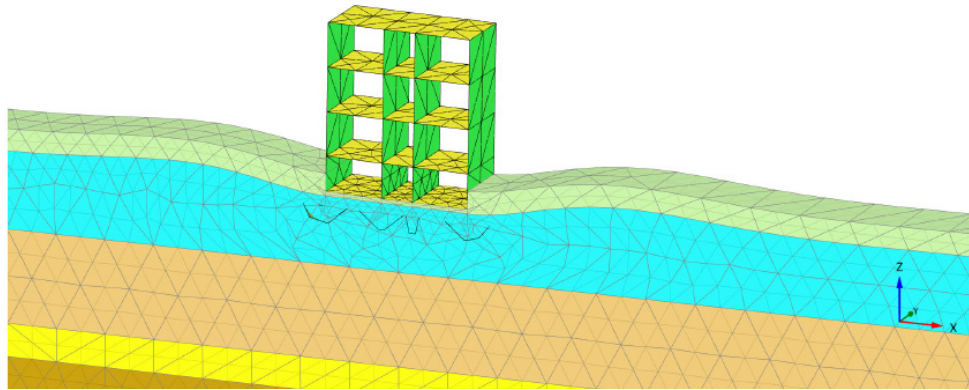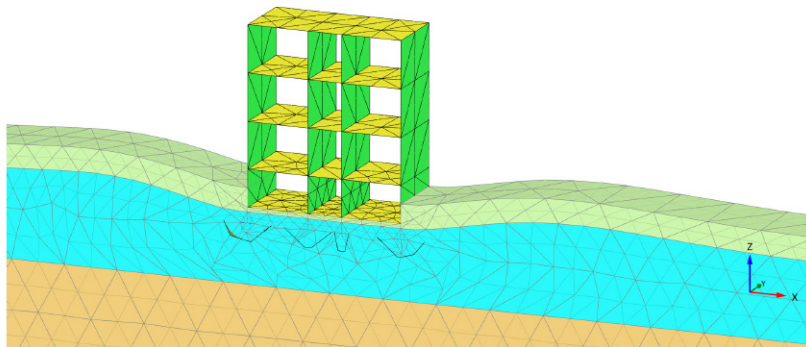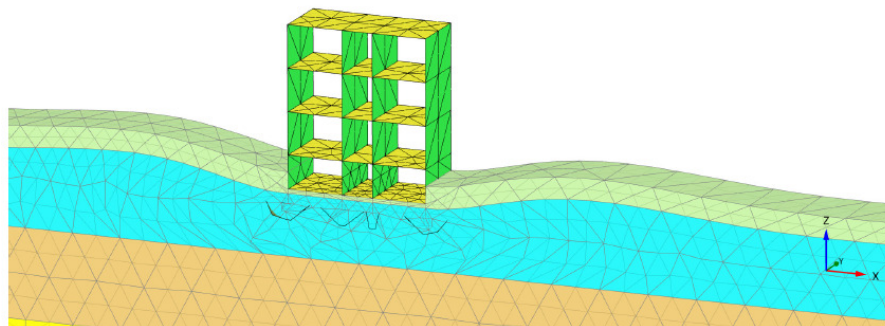
Figure 5.50 Deformed mesh (scaled up 5 times) at the end of the dynamic phase using: a) the Amoruso seismogram; b) the Tortorici seismogram; c) the DISS Messina Straits seismogram considering the liquefaction phenomenon.

Figure 5.51 presents the vertical displacements, u_z, at the end of the dynamic phase for each seismogram. According to the coordinate axis specified in PLAXIS3D, positive displacement stands for heaving of the soil and negative displacement stands for settlement of the soil. Results show that liquefaction-induced settlements under the structure are larger than those observed in free field condition.

(a)

(b)

(c)
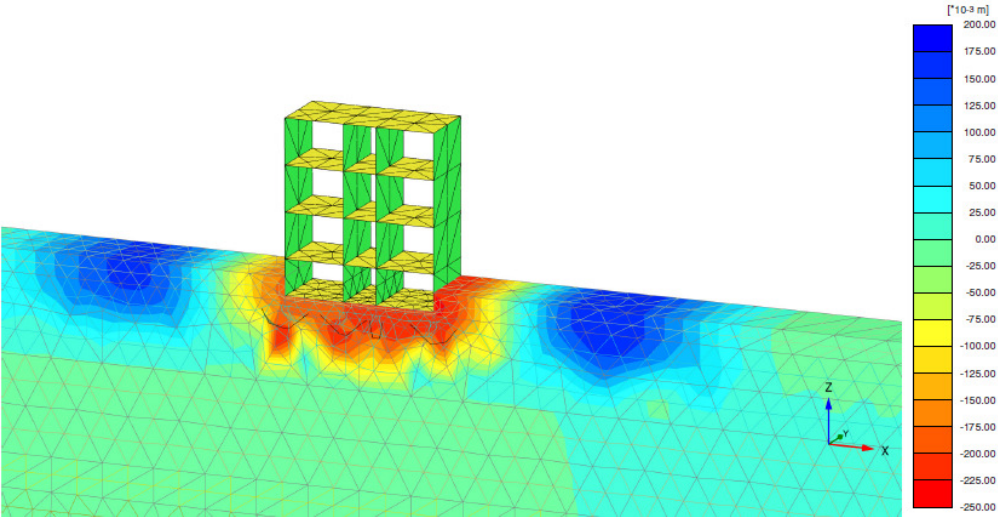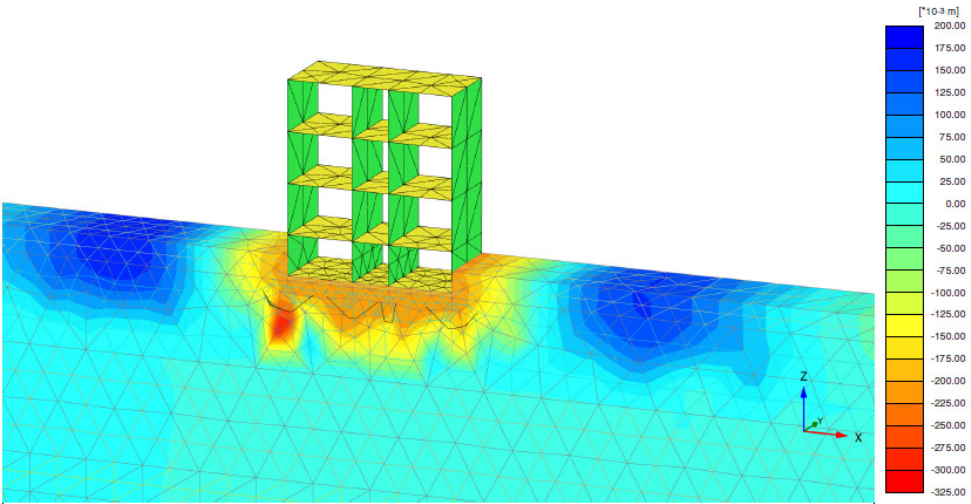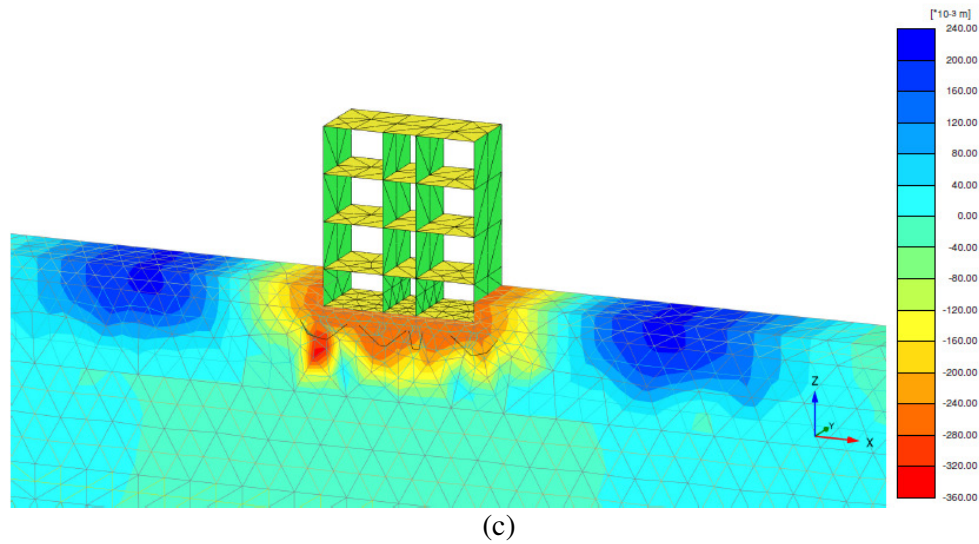
Figure 5.51 Vertical displacements at the end of the dynamic phase using: a) the Amoruso seismogram; b) the Tortorici seismogram; c) the DISS Messina Straits seismogram considering the liquefaction phenomenon.

The SSI condition considering the presence of liquefiable layer has been compared with the results obtained without considering the liquefaction phenomenon in terms of settlements (positive displacements) for different points selected along an alignment under the central part of the structure. Figure 5.52-5.54 show the vertical displacements at the depths of 1.6 m, 2.9 m, 5.0 m and 7.9 m for each seismogram.

(a)

139
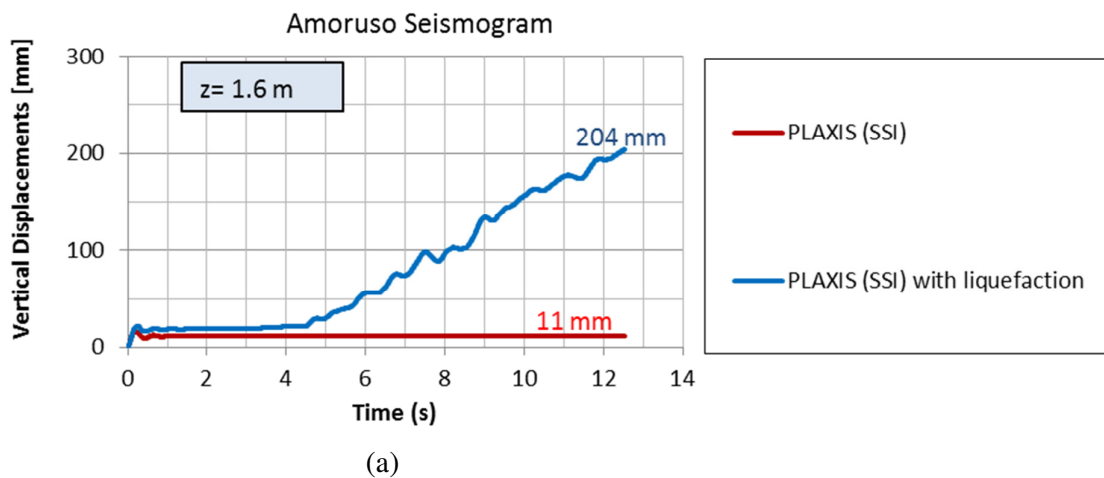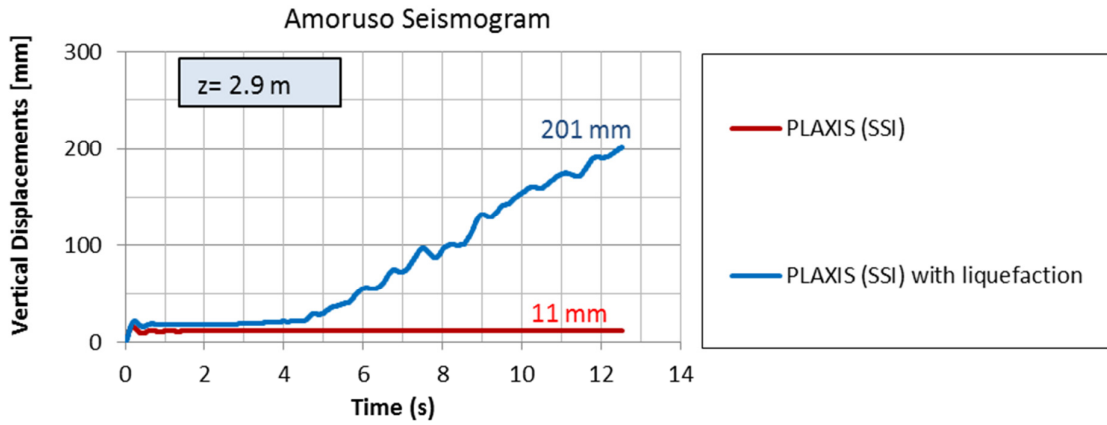
(b)
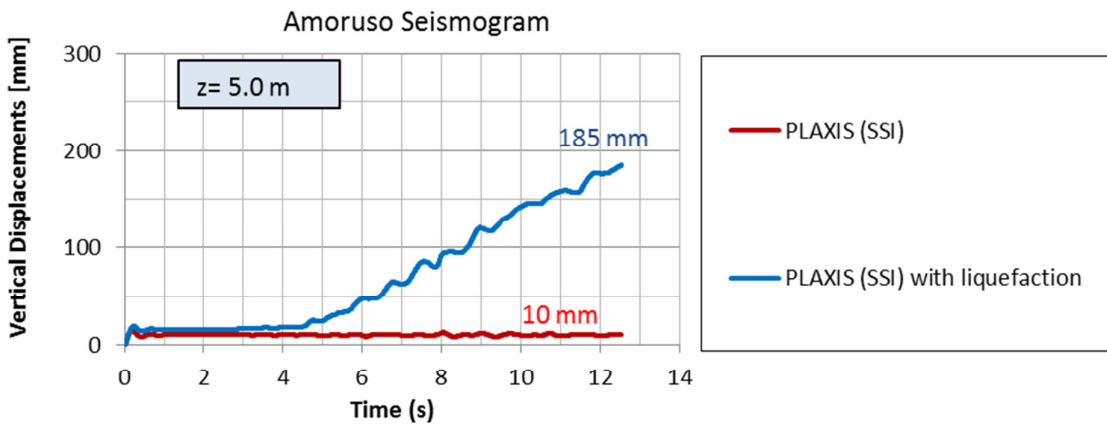
(c)
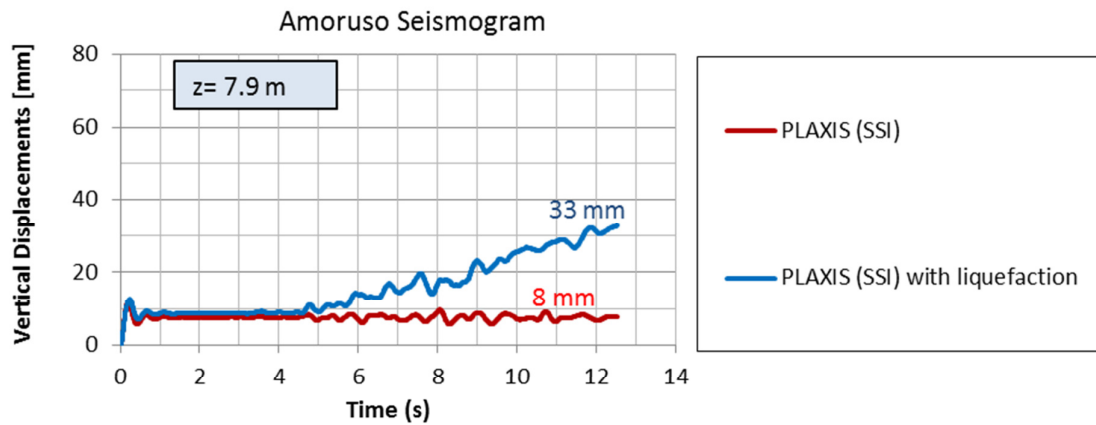
(d)

Figure 5.52 Vertical displacements at the depths of 1.6 m, 2.9 m, 5.0 m and 7.9 m using as input Amoruso seismogram.

(a)

(b)

(c)

141
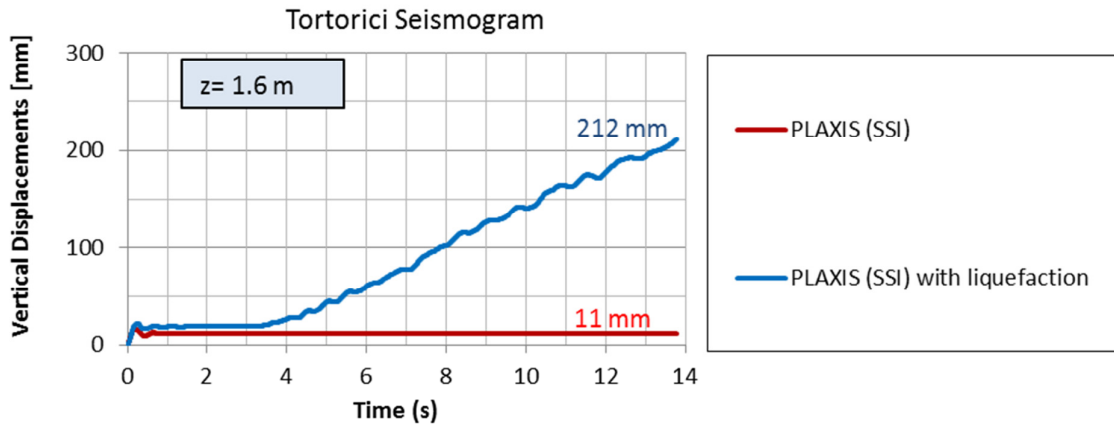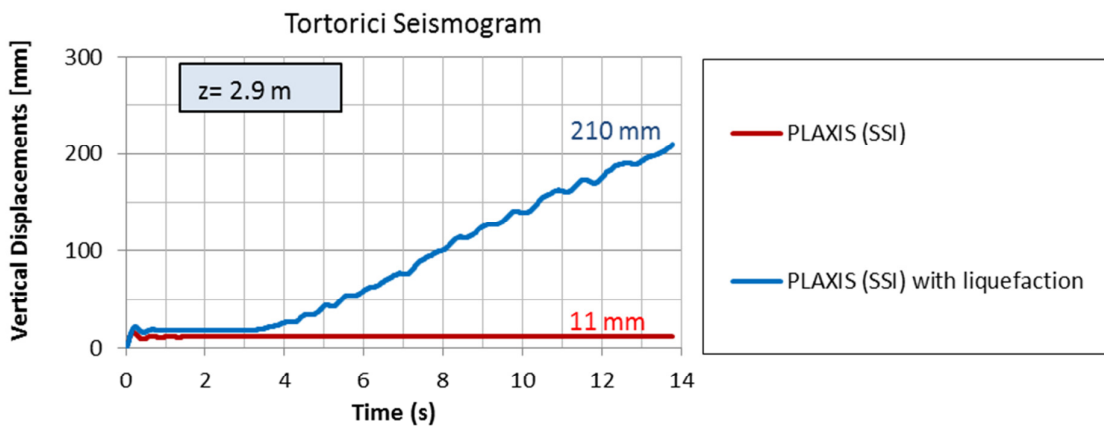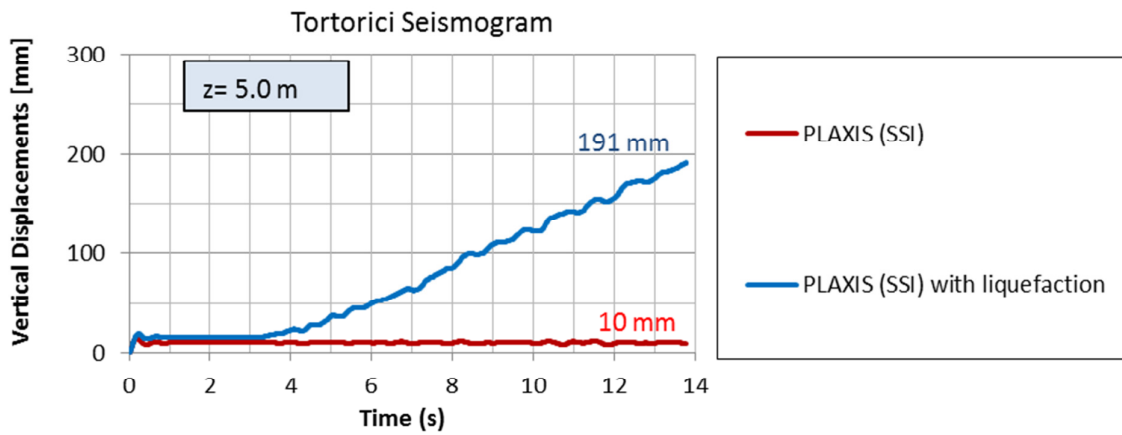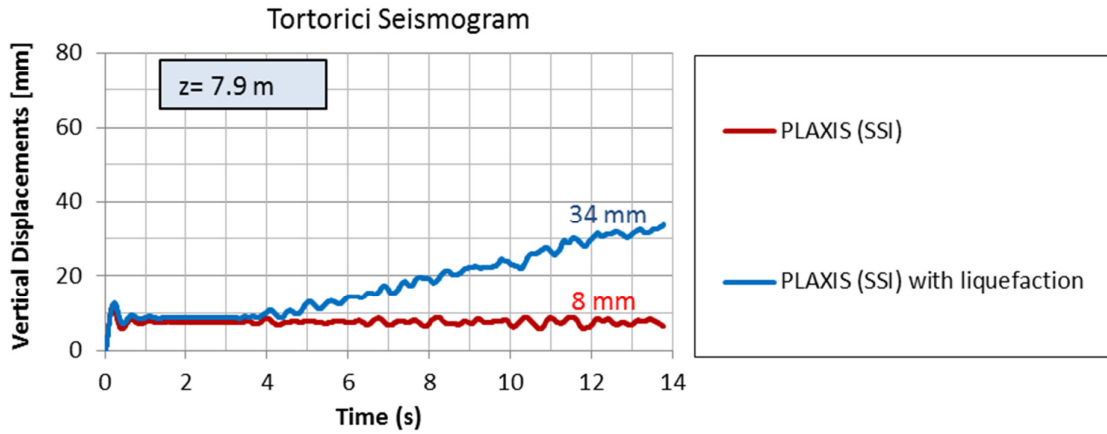
(d)

Figure 5.53 Vertical displacements at the depths of 1.6 m, 2.9 m, 5.0 m and 7.9 m using as input Tortorici seismogram.
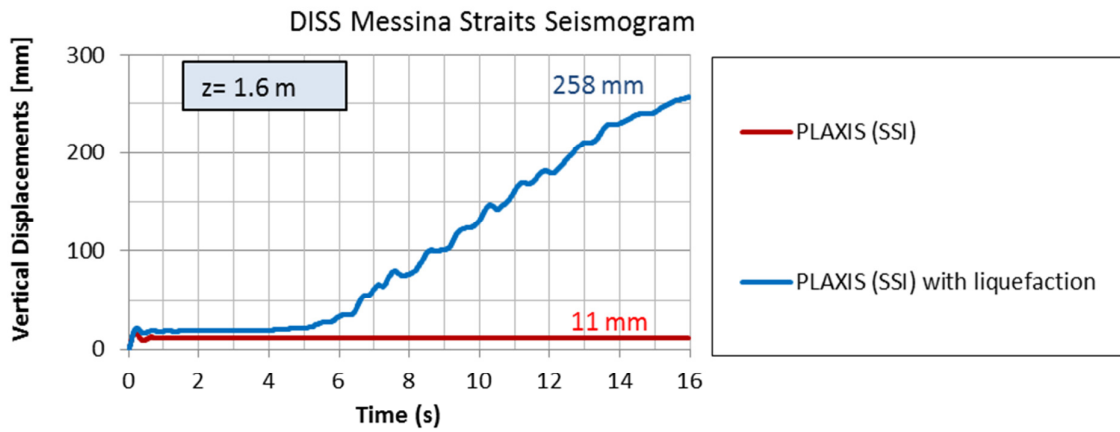
(a)
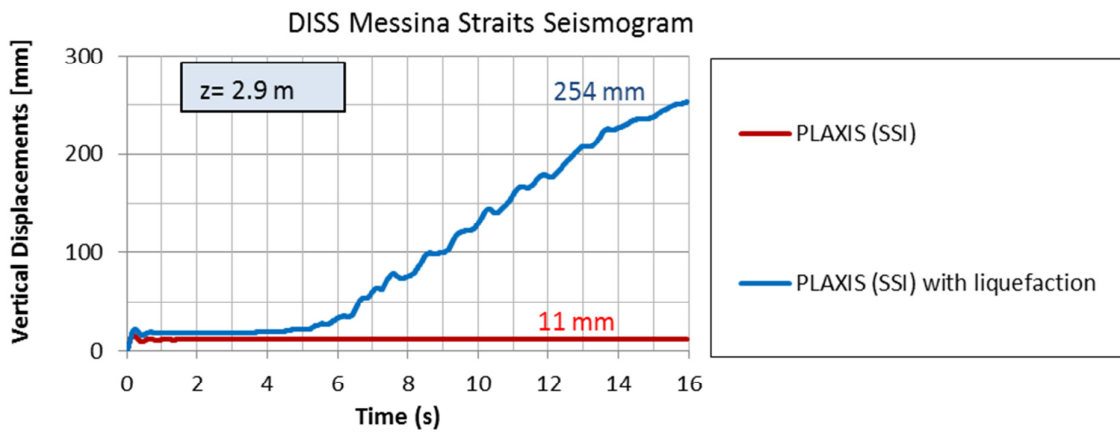
(b)
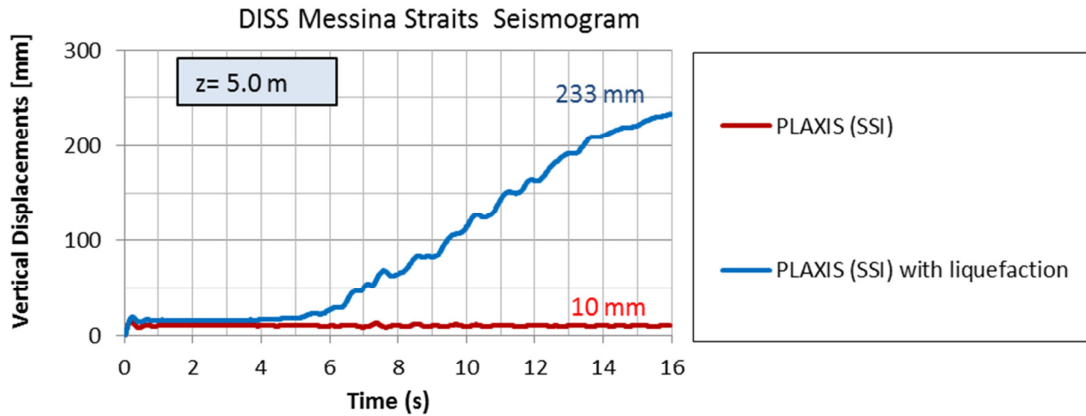
(c)
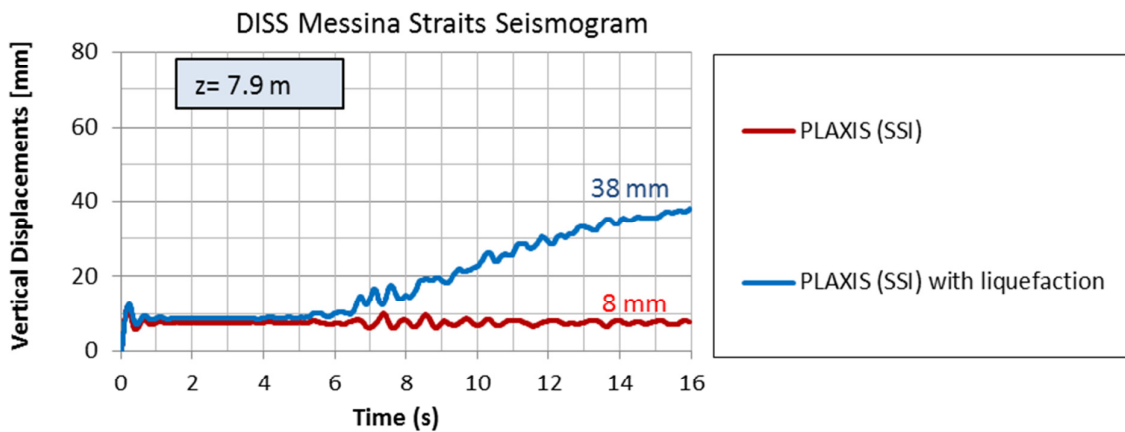
(d)

Figure 5.54 Vertical displacements at the depths of 1.6 m, 2.9 m, 5.0 m and 7.9 m using as input DISS Messina Straits seismogram.

Figures 5.52-5.54 show instantaneous settlements of 11 mm at the beginning of the dynamic phase without considering the liquefaction phenomenon. Moreover, vertical displacements do not vary significantly with depth and assume the same values for each accelerogram.

In the SSI condition considering the presence of liquefiable layer, the same instantaneous settlements occur at the beginning of the dynamic phase. However, after a dynamic time of 4-6 s, they raise significantly with increasing time. Indeed, the settlements are affected by the onset of liquefaction of the silty sand and gravel 1a layer.

At the end of the dynamic phase, settlements of 204 mm, 212 mm and 258 mm occur for the Amoruso (Figure 5.52 (a)), Tortorici (Figure 5.53 (a)) and DISS Messina Straits (Figure 5.54 (a))

seismograms, respectively. Results show that the duration of earthquake has a direct impact on soil liquefaction and its effects, being equals to 12.5 s for Amoruso seismogram, 13.8 s for Tortorici seismogram and 16.0 s for DISS Messina Straits seismogram. The parametric study demonstrates that higher duration of the input motion corresponds to greater settlements.

Moreover, considering the Amouso seismogram, as an example, it is possible to observe that the vertical displacements vary significantly with depth, being equal to 201 mm at the depth of 2.9 m (Figure 5.52 (b)), 185 mm at the depth of 5.0 m (Figure 5.52 (c)) and 33 mm at the depth of 7.9 m (Figure 5.52 (d)). The same consideration can be derived for Tortorici (Figure 5.53 (b), Figure 5.53 (c), Figure 5.53 (d)) and DISS Messina Straits seismograms (Figure 5.54 (b), Figure 5.54 (c), Figure 5.54 (d)). The results in terms of displacements are in good agreement with the previous consideration in terms of accelerations, demonstrating again that liquefaction has occurred fist near the surface and worked its way downward.

Therefore, according to the results, liquefaction and its consequences are directly affected by the amplitude, frequency content and duration of the earthquake.

Finally, heave displacements (negative) for different points selected along an alignment located 8 m far from the structure are reported in Figure 5.55, for Amoruso seismogram as an example.

Instantaneous displacements occur at the beginning of the dynamic phase. However, after a dynamic time of about 4.5 s, they raise significantly with increasing time, being affected by the onset of liquefaction.

It is possible to notice that the vertical displacements vary significantly with depth, being equal to -60 mm at the surface, -29 mm at the depth of 5.0 m and -18 mm at the depth of 7.9 m.

These heave displacements are the consequence of the undrained dynamic analyses. Indeed, the soil tends to heave where there is not the influence of the structure being the volumetric change

prevented. The results show that the drainage condition has a direct impact on soil liquefaction and

its consequences.
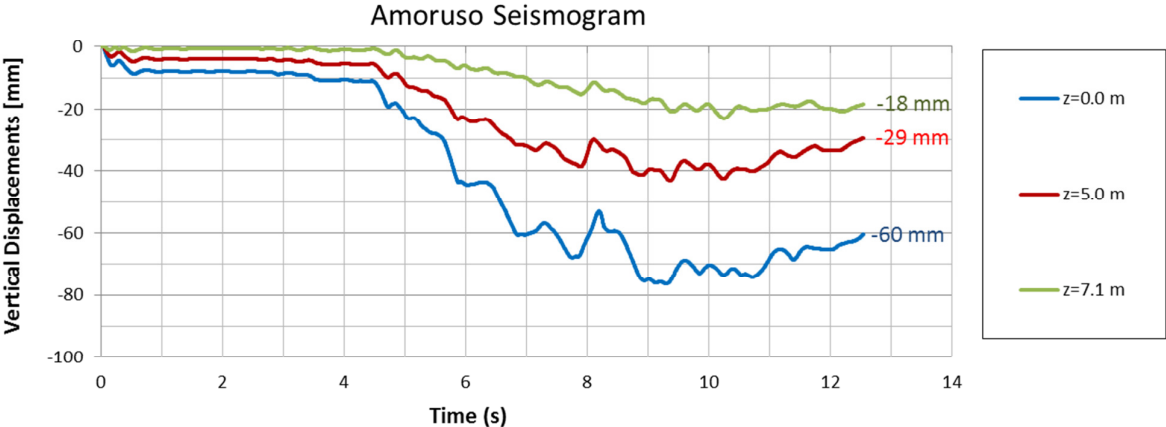
Figure 5.55 Heave displacements at the surface and at the depths of 5.0 m and 7.1 m using as input Amoruso seismogram.

6. Design of a Biaxial Laminar Shear Box for 1g shaking table test

6. 1 New laminar shear box at L.E.D.A.

Based on the large flexible laminar shear box developed by Ueng et al. (2006), a new laminar shear box has been designed at the Laboratory of Earthquake engineering and Dynamic Analysis (L.E.D.A.) of "Kore" University, Enna (Sicily, Italy), for 1g shaking table tests.

The most important facility of the laboratory is an array of two identical 6-DOF 4.0m x 4.0m shaking tables. It is possible to use the tables both separately and simultaneously in order to simulate the effects of earthquakes (Navarra et al. 2015).

The 2D laminar box has been developed to monitor liquefaction under two dimensional shaking on a shaking table at L.E.D.A.. Figure 6.1 shows the external and internal views of L.E.D.A. building. Figures 6.2 and 6.3 report some views of the shaking tables system, while the features for the configuration of single table are summarized in Table 6.1. For increasing the flexibility of the box wall, laminar system has been applied. A laminar shear box, during liquefaction, has least undesirable effect in the real behaviour of the model (Bojadjieva et al. 2015; Sesov, 2003).

The laminar box is rectangular in cross section and consists of 16 layers. Each layer is composed of two frames: an inner frame and an outer frame. The inner frame has an internal dimension of 2570 mm by 2310 mm, while the outer frame has an internal dimension of 2744 mm by 2770 mm. Each frame is made from hollow aluminum profiles with 30 x 80 mm^2 section and 2 mm thickness. Aluminum is chosen in order to reduce the inertial effect of the frame on the soil during shaking. Considering the box filled of saturated sand, the correction factor (Equation 3.1) is equal to 0.998. The isometric view of the inner and outer frames is shown in the Figure 6.4.

(a)

(b)

Figure 6.1 Laboratory of Earthquake Engineering and Dynamic Analysis (L.E.D.A.) of "Kore" University of Enna (Sicily, Italy): (a) external view; (b) internal view (Navarra et al., 2015).
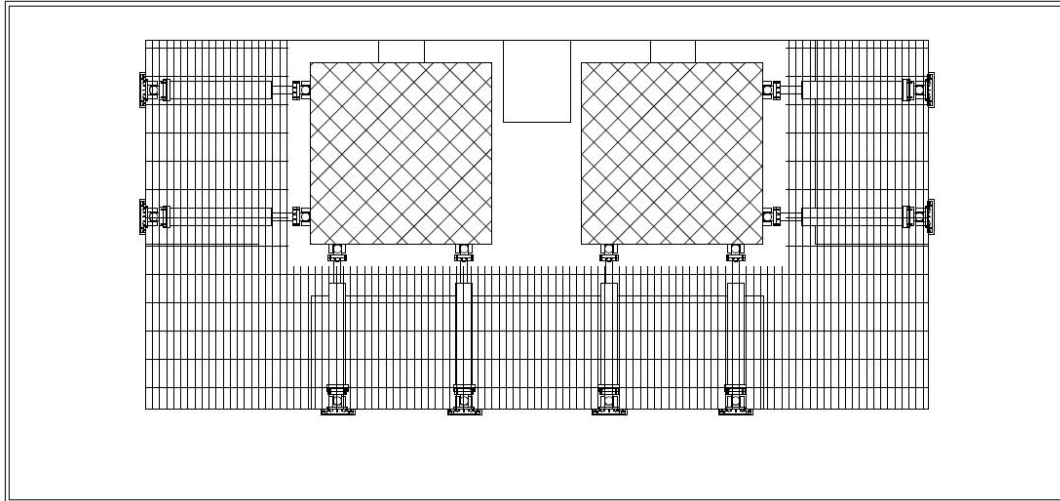
Figure 6.2 Plan view of the shaking tables system (Navarra et al., 2015)

Figure 6.3 Photographic view of the shaking tables system (Navarra et al., 2015).

Table 6.1. Features of LEDA shaking tables (Navarra et al. 2015).

Feature	Single Table
Dimensions [m]	4.0 x 4.0
DOF	6
Payload [t]	60
Max Frequency [Hz]	60
Stroke (horizontal axes) [mm]	± 400
Stroke (vertical axis) [mm]	± 250
Velocity (horizontal axes) [mm/s]	±2200
Velocity (vertical axis) [mm/s]	±1500
Acceleration (horizontal axes) [g]	±1.50
Acceleration (vert. axis) [g]	±1.00
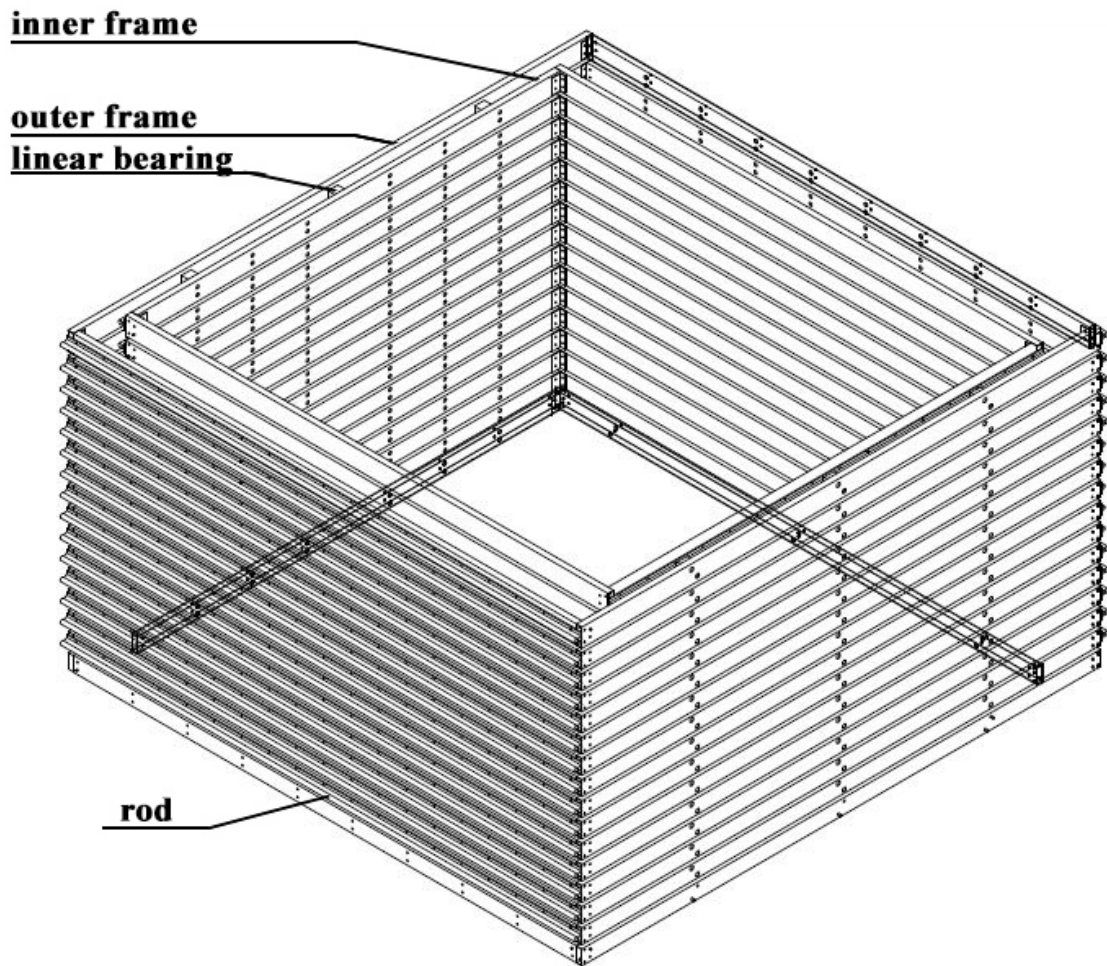
Figure 6.4 Isometric view of the inner and outer frames.

Each internal frame is supported independently by means of rods on a series of linear bearings connected to the external frame, while each external frame is supported independently by means of rods on a series of linear bearings connected to the surrounding rigid steel walls.

The isometric view of the rigid steel walls is shown in the Figure 6.5.
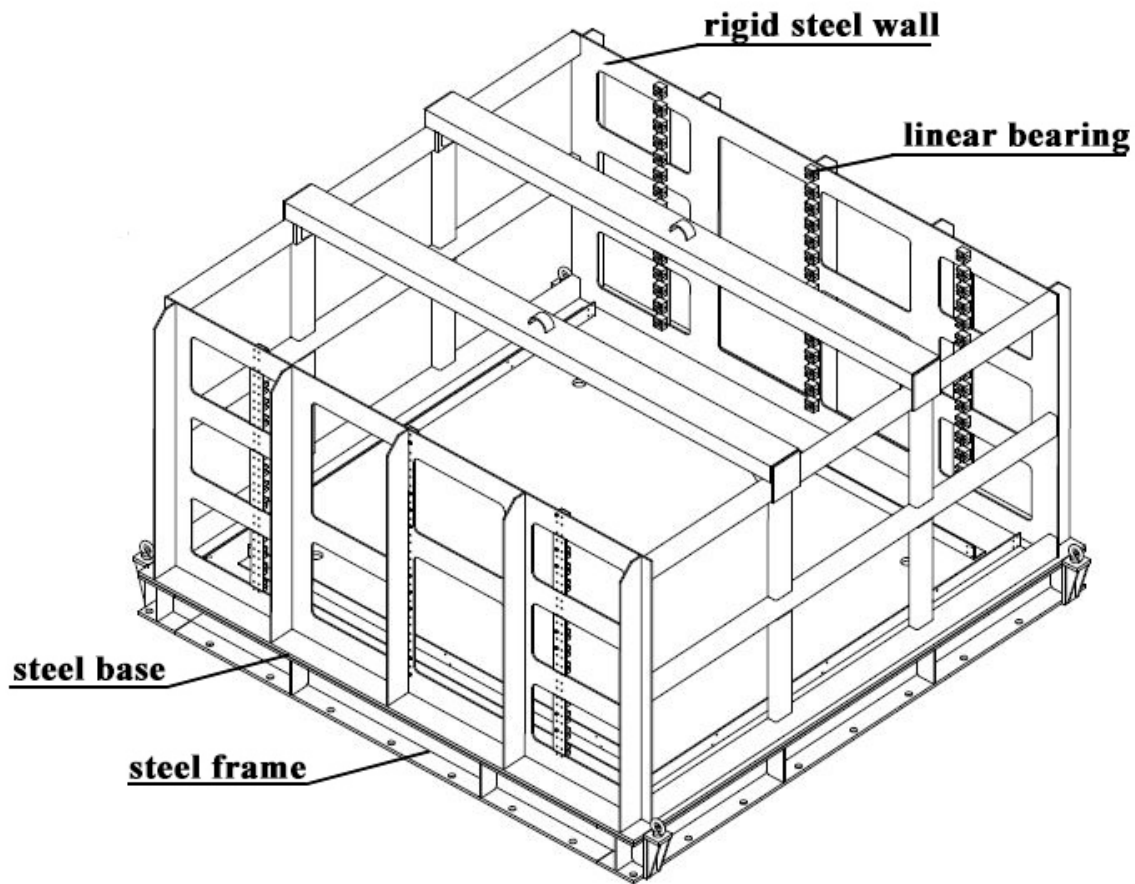
Figure 6.5 Isometric view of the rigid steel walls.

Linear bearings allow a maximum displacement of ± 150 mm in the two horizontal directions with almost negligible friction. Thanks to this arrangement, the external frames can move in the x direction and, at the same time, the internal frames can move in the y direction. This design has several advantages: the weight of each frame is transferred to the surrounding rigid steel walls; the effects of inertia and friction do not accumulate along the depth; each frame can move independently without torsion; the horizontal cross section remain horizontal (strain similarity).

Between the layers, there is a 20 mm gap making the total height of 1600 mm. The lowest layer is fixed on a steel base with 3274 mm x 3276 mm x 20 mm dimensions. To reinforce the base, a steel

frame is installed between the base and the shaking table. A drainage system is added on a steel base. It consists of water tubes and four valves. The plan view of the steel frame is shown in the Figure 6.6.
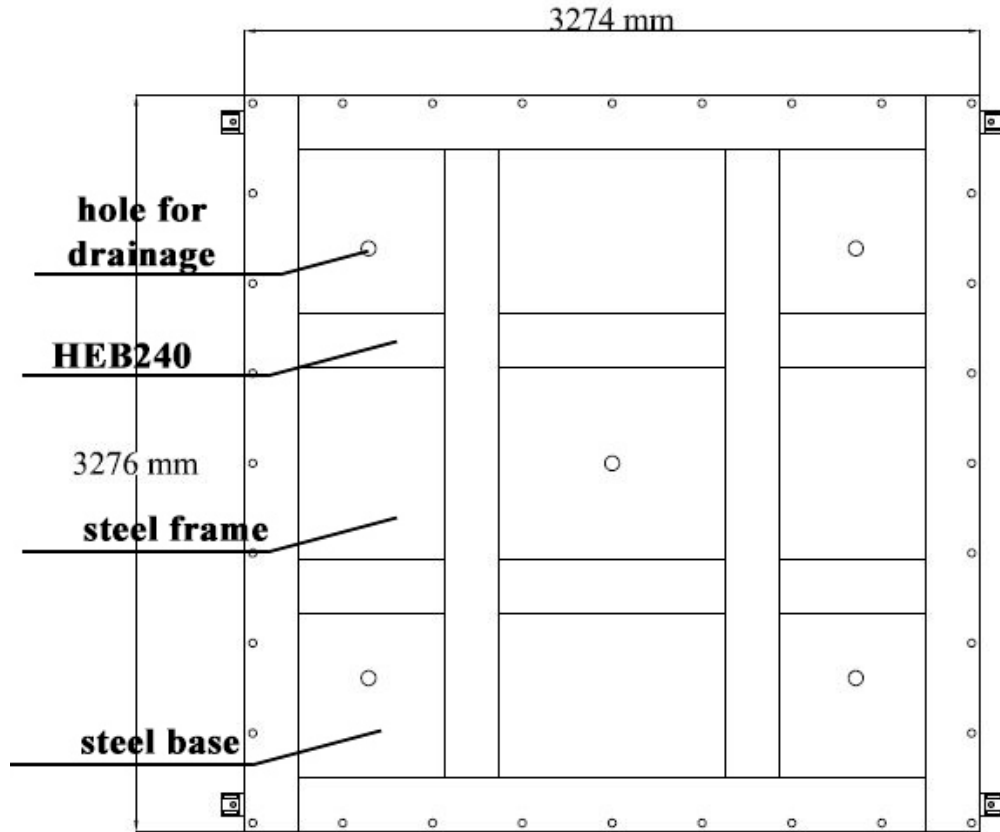
Figure 6.6 Plan view of the steel frame.

During the shaking, to improve the shear stress transition from the steel base to the soil, a thin layer of gravels will be placed on the base. Moreover, a 2 mm thick rubber membrane with high elasticity will be attached inside the box to provide the water tightness and to protect the external mechanism from soil penetration.

The main components of the laminar shear box are reported in Table 6.2.The plan view and the profile views of the laminar box are shown in the Figure 6.7 and 6.8, respectively.

Table 6.2 Components of the laminar shear box.

Component	Property	Value
Inner frame	Mass	12.07 kg
	Internal Dimensions	2570 x 2310 mm^2

	Number	16
	Height	80 mm
Outer frame	Mass	12.53 kg
	Internal Dimensions	2744 x 2770 mm²
	Number	16
	Height	80 mm
Rod (inner frame)	Length	2370 mm
	Diameter	19 mm
	Number	30
Rod (outer frame)	Length	2804 mm
	Diameter	19 mm
	Number	30
Linear bearing	Number	180
Gap between frames	Dimension	20 mm
Steel base	Mass	1682.89 kg
	Dimensions	3274 x 3276 mm²
	Height	20 mm
Steel walls	Total mass	592.94 kg
Steel frame	Total mass	1359.83 kg
Total mass of the laminar box		4033.27 kg

(a)

(d)   (b)

(c)
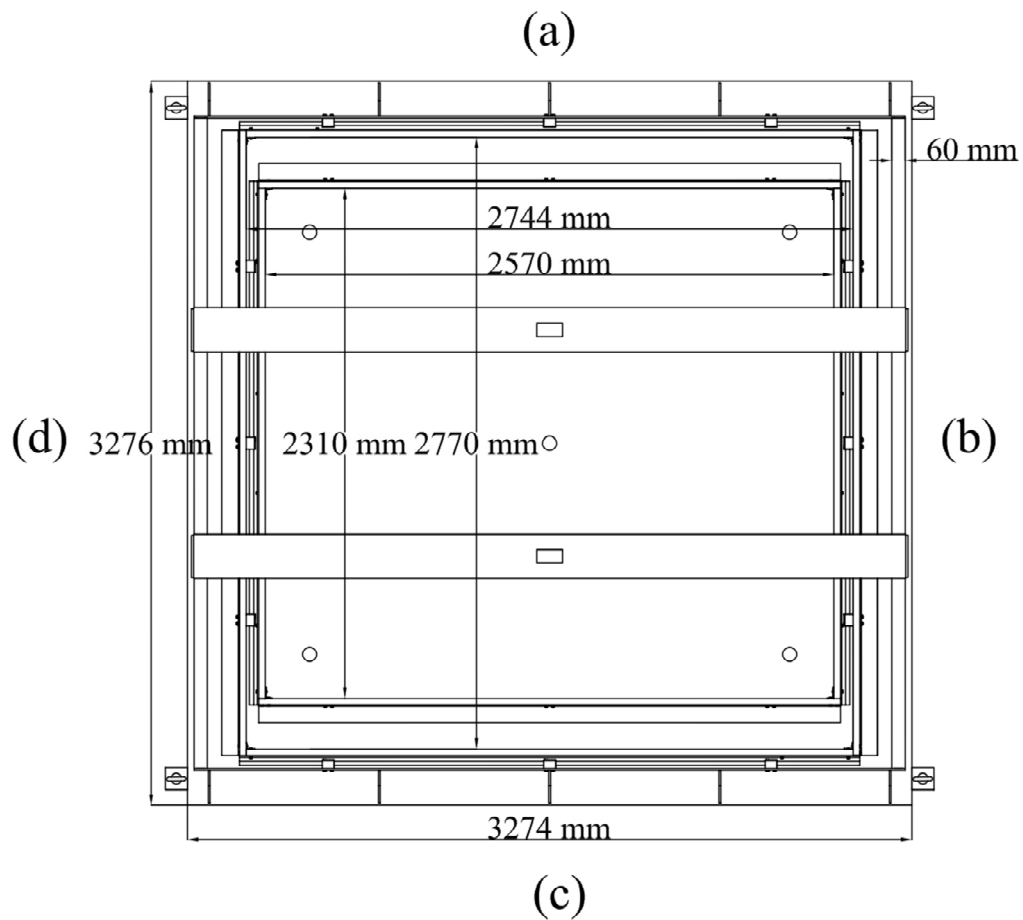
Figure 6.7 Plan view of the laminar shear box.

152
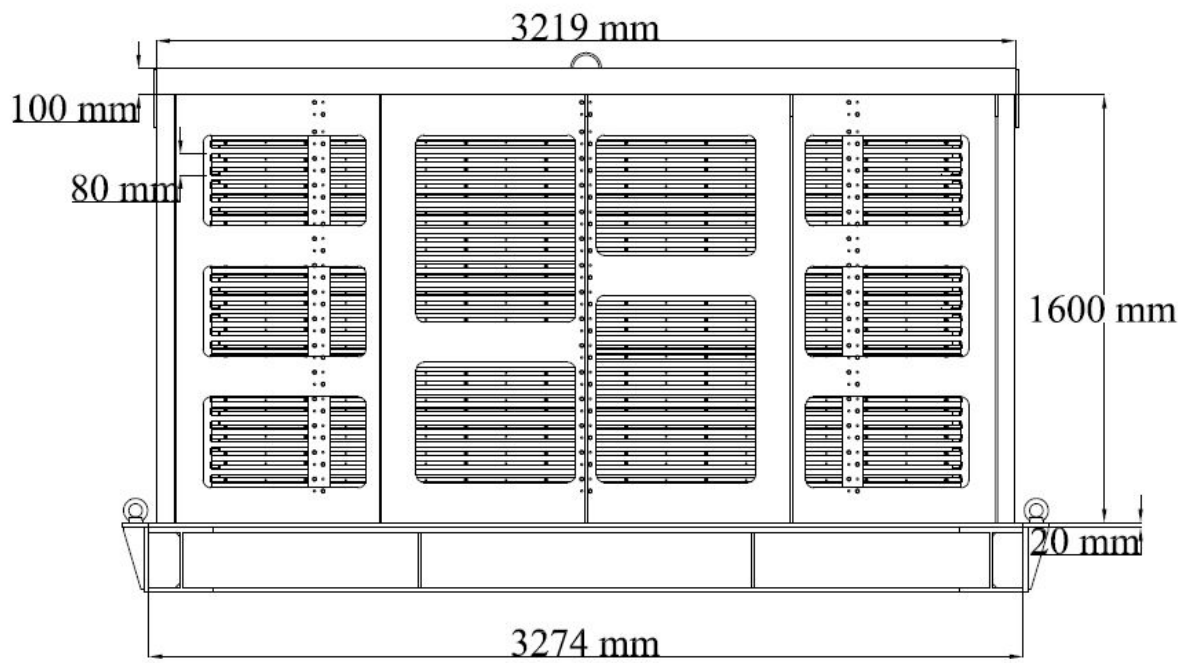
(a)
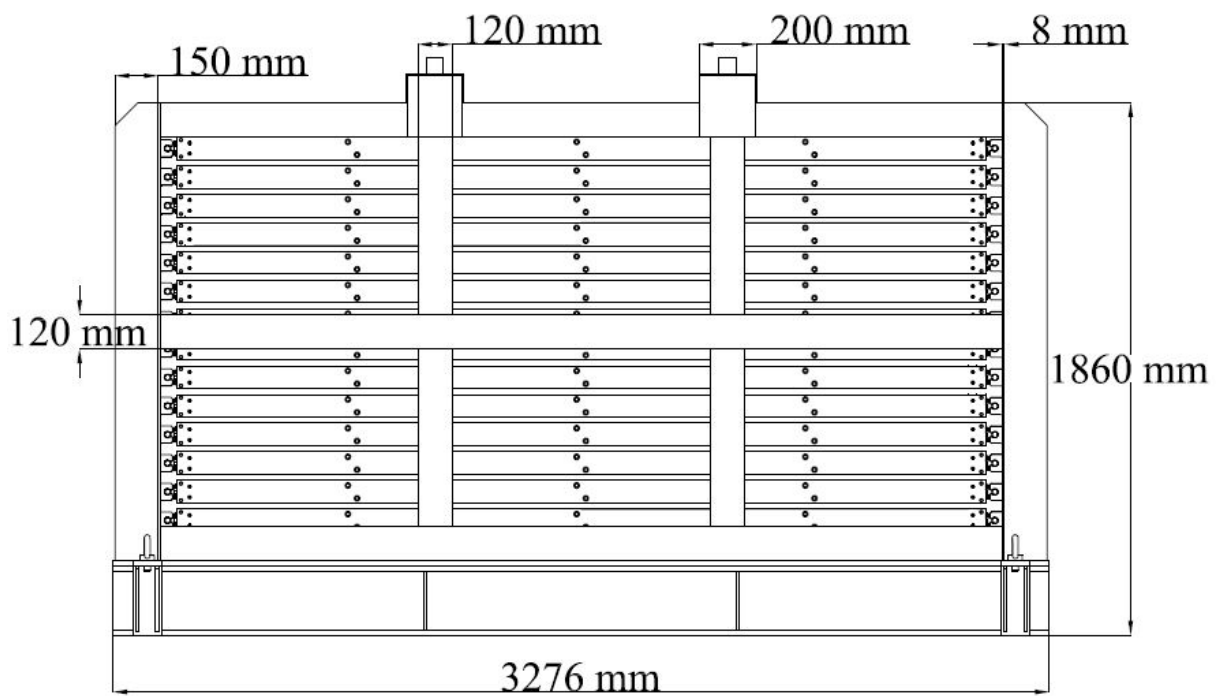
(b)
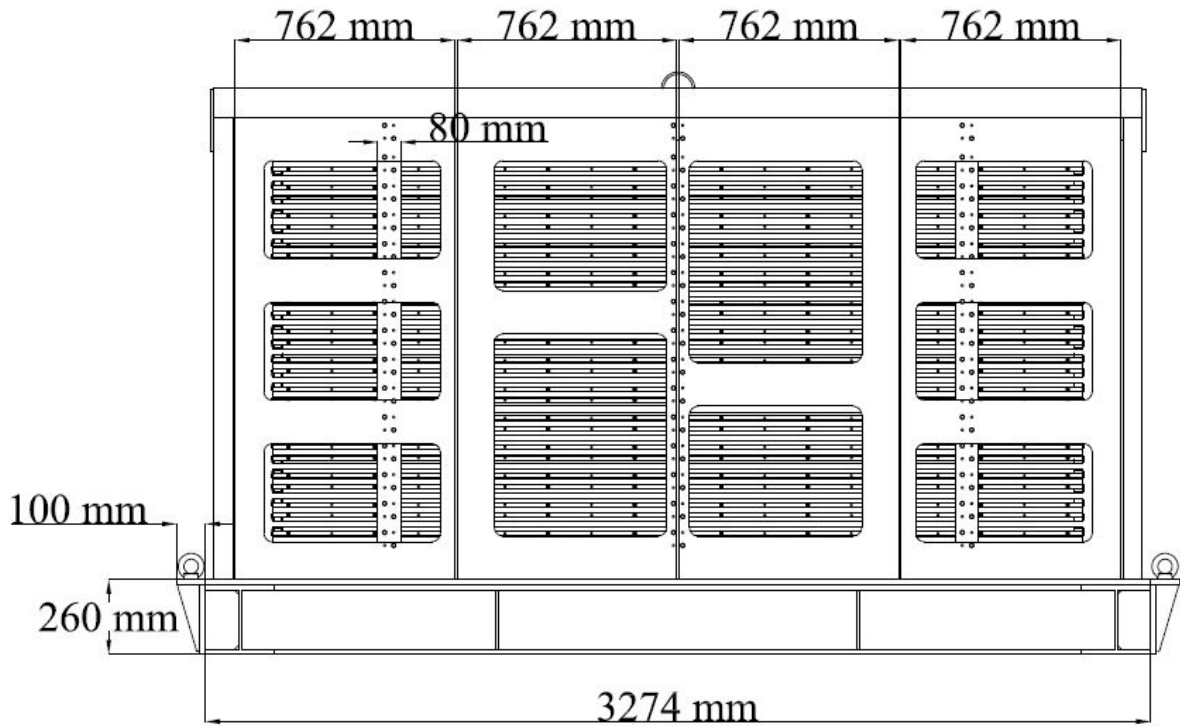
(c)
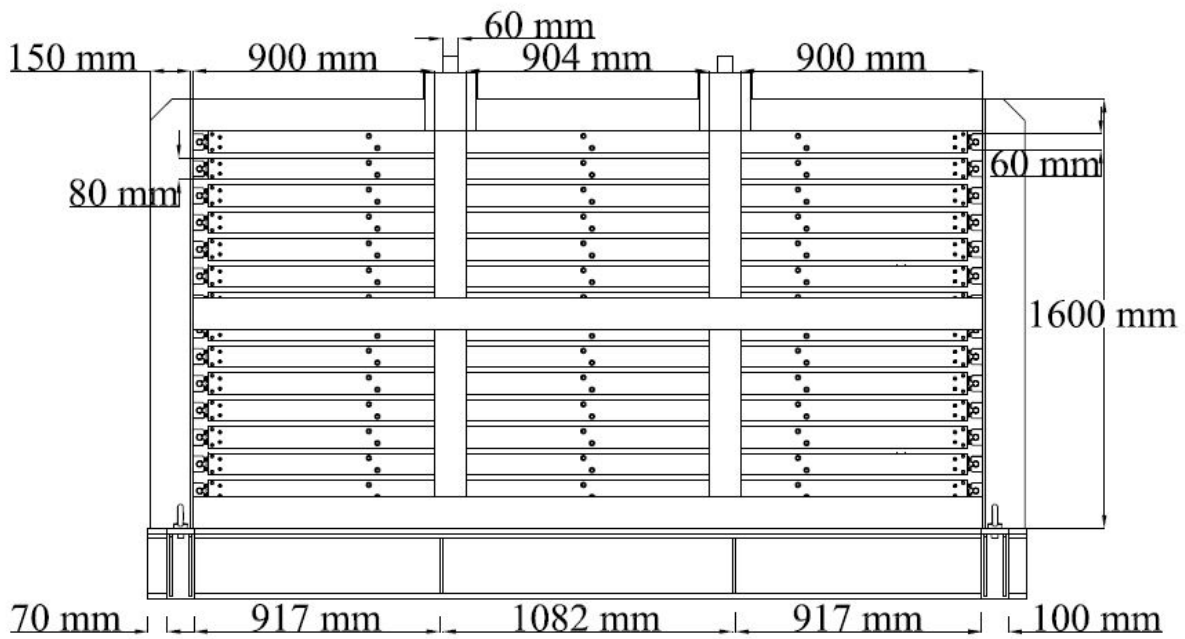
(d)

Figure 6.8 Profile views of the laminar shear box.

The isometric and 3D views are illustrated in Figure 6.9. The laminar shear box at the Laboratory of

Earthquake engineering and Dynamic Analysis (L.E.D.A.) is shown in Figure 6.10.

154
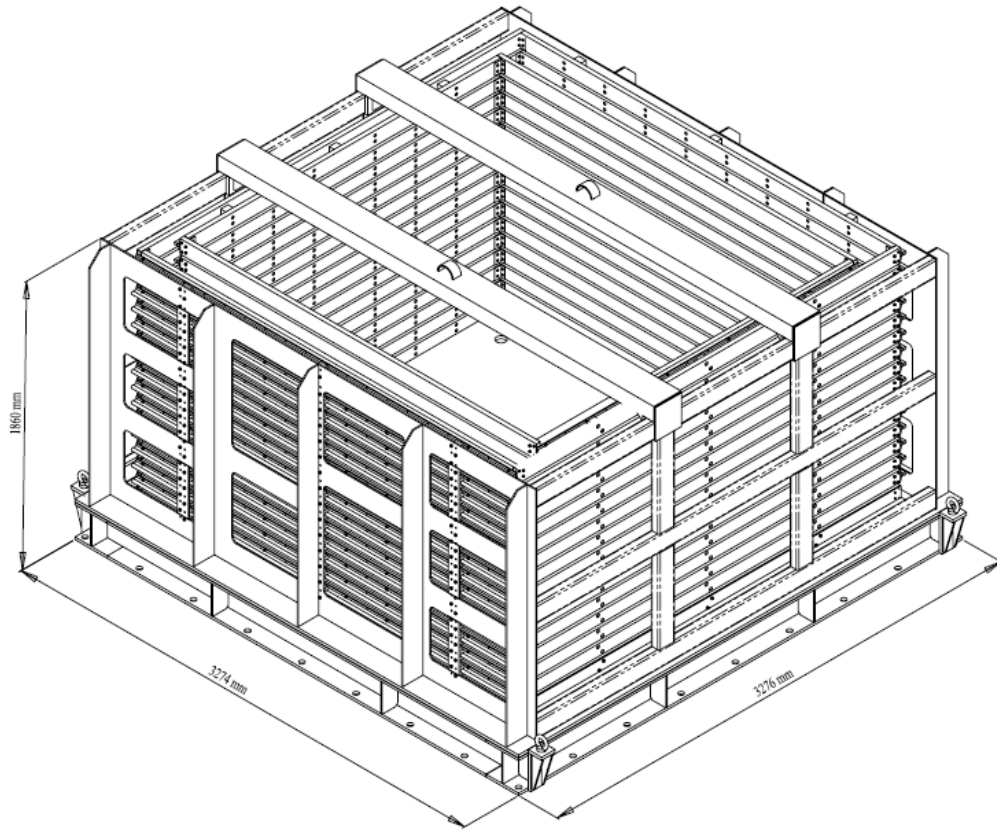
(a)
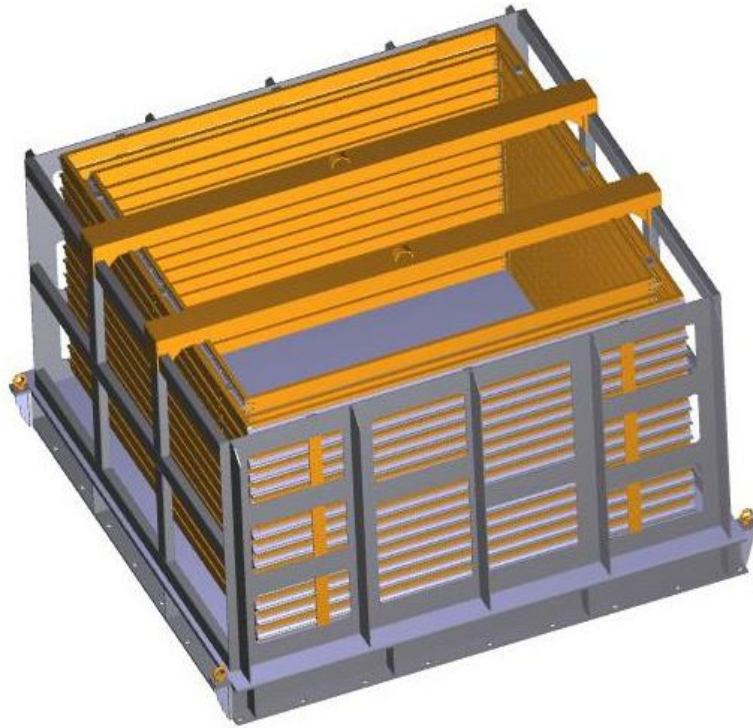
(b)

Figure 6.9 The isometric (a) and 3D (b) views of the laminar shear box.

(a)

(b)

Figure 6.10 Laminar shear box at the Laboratory of Earthquake engineering and Dynamic Analysis (L.E.D.A.).

6.2 Model preparation and instrumentation

The liquefiable soil deposit will be placed inside the laminar box using the raining method in order to achieve uniform density. The raining method allows to control the uniformity and the density of a large sand specimen. The saturation of a specimen by introducing water into the dry sand is unreliable and unachievable. Therefore, a membrane will be attached inside the box and dry sand will be poured into water in the laminar box.

Ueng et al. (2006) designed a special pluviator for preparing the sand specimen inside a shear box with internal size of 1880 x 1880 x 1520 mm^3. The pluviator (Figure 6.11) is composed of the following components: a container for the needed volume of sand, which is perforated with 40 mm diameter holes; a motor-driven perforated plate, which is exchangeable for various hole diameters to control the rate of pluviation and in turn the density of the specimen; a diffuser comprised of four layers of the No. 4 sieves with spacing of 70 mm to obtain a uniform deposit.
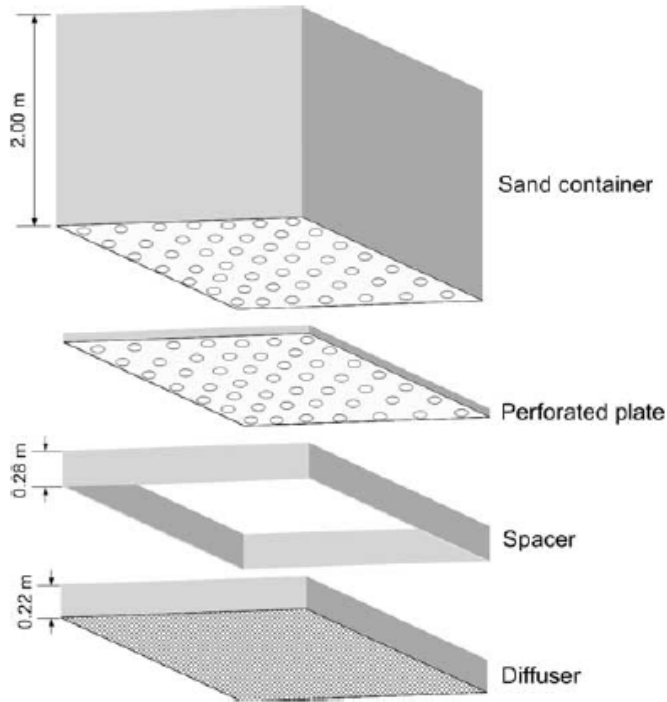
Figure 6.11 Pluviator for specimen preparation (Ueng et al., 2006).

Carvalho et al. (2010) designed a horizontally travelling pluviator to prepare a dry sand deposit for a box 2.00 m long by 0.75 m wide and 1.75 m high. It consists of a steel frame and a small container travelling in two rails at the top of the frame, moved by a motor driver (Figure 6.12).

Figure 6.12 Schematic view of the pluviation equipment setup (Carvalho et al., 2010).

The saturated sand can be placed inside the laminar box also using the hydraulic fill deposition (Whitman, 1984; Ecemis, 2013; Thevanayagam et al., 2009). It involves the following steps: (1) the membrane is placed inside the box and filled with water to a precalculated depth; (2) soil and water mixture is pumped by a slurry pump into the laminar box; (3) at the same time, a water pump is used to return back the excess water from the laminar box. The system is adjusted in order to maintain a precalculated height of water above the sand surface inside the laminar box, like the natural alluvial deposition of sand in rivers or lakes (Figure 6.13). Ecemis (2003) applied this technique to fill a laminar box with internal dimension of 1.6 x 0.38 x 1.5 m^3. The deposition process took about 9 h. Therefore, it would require days to fill the laminar shear box at L.E.D.A. For this reason, in this case, the raining method is preferred over hydraulic fill deposition for preparing the sand specimen.
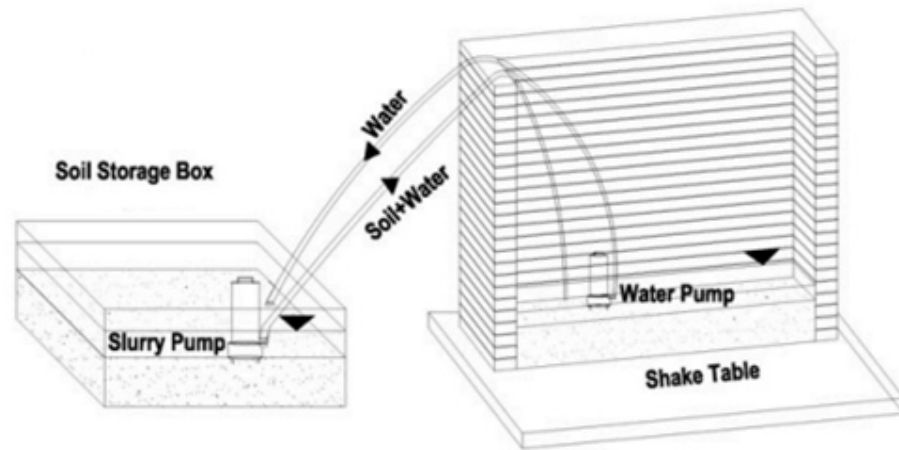
(a)
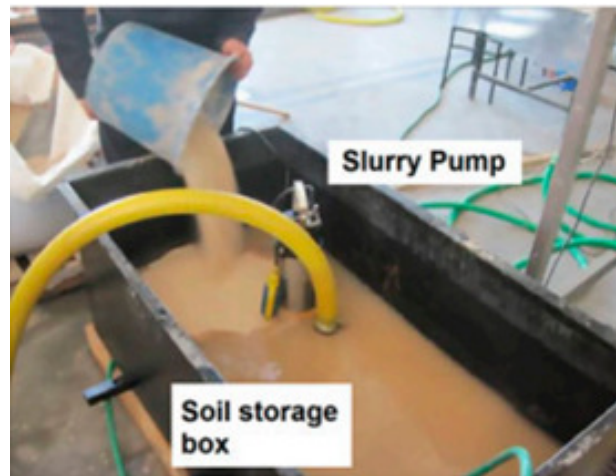
(b)

Figure 6.13 Hydraulic filling: (a) schematic view and (b) sample preparation (Ecemis, 2003).

The sand for investigating the liquefaction phenomena has to be rounded or sub rounded in shape, poorly graded and its grain distribution curve should fit into the boundaries given by Terzaghi et al. (1996) for high susceptibility sands to liquefaction. The grain size distribution curves of standard sands are reported in Figure 6.14.
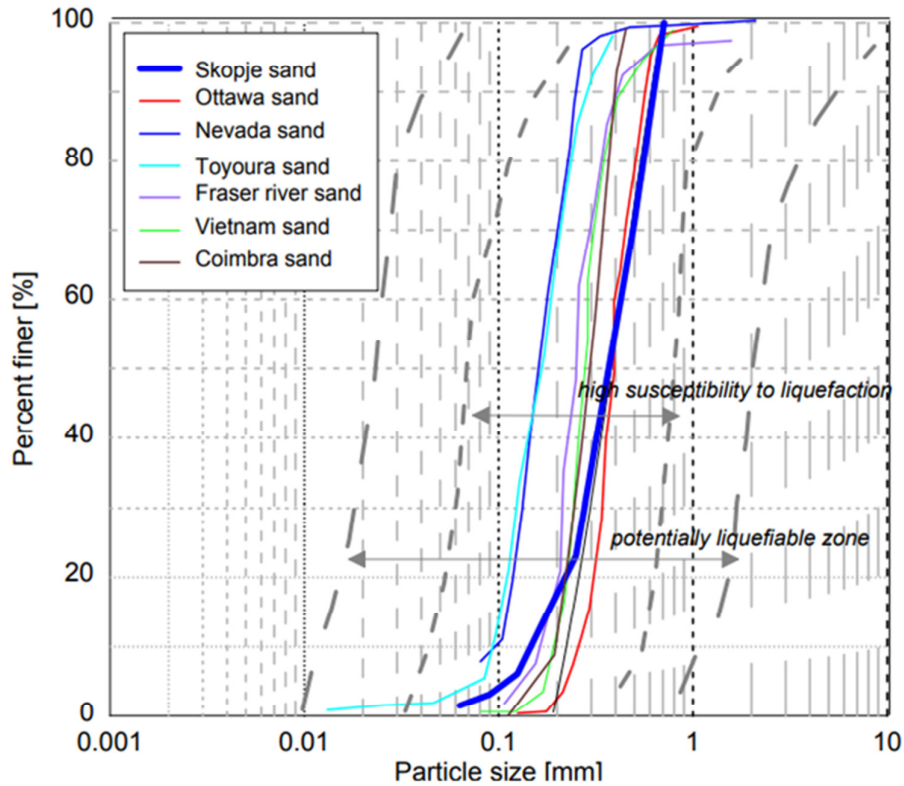
Figure 6.14 Grain size distribution curves of standard sands for investigating the liquefaction phenomena (From Bojadjieva et al., 2015).

The soil specimen will be made of a commercial sand from Catania area (Italy). The physical properties of the sand are reported in Table 6.3. They have been derived from the standard sands for investigating the liquefaction phenomena (Bojadjieva et al., 2015; Carvalho et al., 2010; Ecemis, 2013; Motamed and Towhata, 2010; Özener et al. 2008; Sadrekarimi and Ghalandarzadeh, 2005; Thevanayagam et al., 2009; Ueng et al., 2006; 2010; Yao et al., 2004; Zeghal et al., 2018).

Table 6.3 Physical properties of the commercial Catania sand.

Property	Value
Specific Gravity, G_s	2.65
D_{60} [mm]	0.25
D_{30} [mm]	0.20
D_{10} [mm]	0.15
e_{max}	0.85
e_{min}	0.65
Uniformity Coefficient, U	1.67
Curvature Coefficient, C	1.07

A total of twelve single axis MEMS accelerometers and twelve linear position transducers will be used to monitor the response of the model in term of accelerations and displacements at different depths. They will be placed on the external and internal frames for the x and y directions, respectively.

The instrumentation that will be installed inside the soil includes three submersible biaxial sensors for monitoring the accelerations in both x and y directions and six small-sized pore pressure transducer for measuring the pore pressures during the tests. These sensors will be placed inside the laminar box before the filling.

Discussion and conclusions

Liquefaction is one of the major reasons for damage during an earthquake. The phenomenon occurs as a result of build-up of pore pressure and hence a reduction of soil strength. A better understanding of this phenomenon is of relevant interest in geotechnical earthquake engineering. Liquefaction studies involve several approaches and procedures: laboratory cyclic tests, stress-based simplified procedures, numerical modelling, reduced-scale model tests and full-scale field tests.

Liquefaction potential can be evaluated using the stress-based simplified procedure originally developed by Seed and Idriss (1971). It compares the earthquake-induced cyclic stress ratios (CSR) with the cyclic resistance ratios (CRR) of the soil. One of the parameters to be evaluated is the stress reduction coefficient (r_d) as a parameter describing the ratio of cyclic stress for a flexible soil column to the cyclic stress for a rigid soil column.

In this work, new variations of r_d with depth have been obtained from equivalent-linear site response analyses performed on different profiles representative of eastern coastal plain of Catania area. To evaluate the soil profiles and the geotechnical characteristics, in situ and laboratory tests were performed. Two different charts were determined analytically using a seismogram of 1818 and three seismograms of 1693 with PGA of 0.3g and 0.5g as input motions. The dashed range represents the range of r_d values and the dashed line represents the recommended values of r_d from the surface to a depth of 30 m.

Average values can be approximated by Equations (4.4), (4.5), (4.6.1), (4.6.2), (4.6.3), (4.7.1), (4.7.2), (4.7.3). Comparing the relationships obtained in this study to the relationships previously proposed by Iwasaki, Liao and Whitman and Robertson and Wride, it is possible to notice that the values of r_d obtained here are lower. This work is useful for the potential liquefaction evaluation in Catania area because the new r_d relationships are more responsive to soil type examined.

Liquefaction triggering can be evaluated by means of simplified procedure or through advanced constitutive models. However, the complex interaction between the soil skeleton and the water makes this task extremely demanding and challenging. Moreover, the uncertainties associated to the soil behaviour are accompanied by the need to consider the dynamic soil-structure interaction effects in order to evaluate the overall behaviour. Due to the complexity of the phenomenon, the analysis of the soil-structure interaction on liquefiable soil has been treated in steps starting from free field conditions and considering gradually more complex configurations.

In this study, the soil-structure interaction analysis on liquefiable soil of a strategic building located in the city of Messina (Sicily, Italy) have been investigated by means of PLAXIS3D software (Bentley Systems). The 1908 Messina earthquake, that was the strongest seismic event of the 20th century in Italy, has been chosen as a scenario earthquake. It caused severe ground shaking, liquefaction phenomena and also a local tsunami. A parametric study with three different seismograms of the 1908 earthquake has been carried out. The Amoruso seismogram has a PGA of 0.456 g. The Tortorici seismogram has been scaled to the value of 0.337 g corresponding to a return period of 950 years (Class IV, public buildings of strategic importance) in the current Italian seismic code NTC(2018). The third seismogram, DISS Messina Straits, has a PGA of 0.293 g.

In order to validate the three-dimensional finite element model and to evaluate the influence of stratigraphic effects in the seismic response of the soil, simpler 1D free-field soil analyses have been carried out using the linear equivalent codes STRATA and EERA. The values of the shear modulus, G, and the damping ratio, ξ, evaluated by 1-D linear equivalent codes, have been inserted in the 3D finite element code. Results show high values of the soil amplification factors, R, and greater than the amplification value provided by Italian technical code NTC (2018). Moreover, results in time and frequency domains obtained by EERA, STRATA and PLAXIS3D are in good agreement.

The free field site responses have been compared with the full-coupled system analyses in order to investigate how the DSSI modifies the free-field motion and the design accelerations. The main conclusions of the study are as follows.

(1) A comparison between the alignment under the structure and the free field condition usually shows that the presence of the structure generates a beneficial effect. However, results demonstrate that the interaction can sometimes be detrimental inducing a higher amplification at the ground surface. In fact, the soil amplification factor for the SSI alignment is much greater than that achieved for the FF condition using the DISS Messina Straits seismogram.

(2) Considering the period of the structure under consideration, spectral accelerations obtained for the SSI alignment are lower than those found for the FF condition using as inputs the Amoruso and Tortorici seismograms.

(3) For T_{STRU}=0.44 s, the NTC(2018) spectrum is more conservative in comparison with the spectral acceleration obtained using the Tortorici seismogram (scaled to the value of 0.337 g corresponding to a return period of 950 years in the current Italian seismic code). Therefore, in this specific case, the NTC(2018) ensures to operate safely.

(4) Adopting the DISS Messina Straits seismogram, the presence of the structure leads to a designed acceleration greater than that required in the FF condition due to the second less important period T=0.65 s in the SSI alignment.

(5) Considering the Amoruso and DISS Messina Straits seismograms, the main resulting frequencies are far from the frequency of the structure; instead, using the Tortorici seismogram, A(f) peaks move towards greater frequencies in the full-coupled analysis. In the latter case, taking into account the SSI has a positive effect because the first resulting frequency for FF condition is close to the frequency of the structure.

164

In both cases, the second predominant frequencies of the input motions are very near to the first resulting frequencies.

(6) The results obtained using the DISS Messina Straits seismogram show a different trend mainly due to the predominant frequencies of the input motion. In this case, the first fundamental input frequency is close to the first resulting frequencies. Moreover, the presence of the structure causes a shift and an increase of the amplification values toward the second predominant frequency of the input motions.

The numerical modeling of soil liquefaction is a cornerstone of liquefaction studies. Constitutive models have to be able to describe the main aspects of the soil cyclic response. PLAXIS3D adopts the UBC3D-PLM model to simulate the seismic response of liquefiable soils. The model utilizes isotropic and simplified kinematic hardening rules for primary and secondary yield surface, to take into account the effects of soil densification and to predict a smooth transition into the liquefied state during undrained cyclic loading.

For the generic and initial calibration of the UBC3D-PLM model, the input parameters have been obtained according to the relationships proposed by Beaty and Byrne (2011), revised by Makra (2013), based on the $(N_1)_{60}$ values. Then, the model has been calibrated to SPT-based liquefaction triggering curves (Boulanger and Idriss, 2014) by means of the simulation of cyclic direct simple shear tests (CDSS) using PLAXIS3D software. The values of the fitting parameters f_{dens} and f_{Epost} have been obtained when, considering a cyclic stress CSR=0.104, liquefaction has been achieved for a number of cycles equal to 15. Direct cyclic shear tests have been simulated by varying the cyclic stress, CSR, showing an optimum fitting between the calibrated model and Idriss and Boulanger curve (2014).

The seismic behaviour of the soil-structure system on liquefiable soil has been analysed in terms of liquefaction potential, excess pore pressures (EPPs), accelerations, response spectra, amplification functions and displacements. Moreover, the SSI condition considering the presence of liquefiable layer has been compared with the results obtained without considering the liquefaction phenomenon. The main considerations can be summarized as follows.

(7) The excess pore pressure ratio in terms of vertical effective stress $r_{u,\sigma'v}$ can been used to evaluate the liquefaction potential, showing that the liquefaction occurs for all of the three 1908 seismograms.

(8) Liquefaction is strongly affected by the amplitude and the durations of the input motions. Indeed, the dynamic times to reach liquefaction with depth are generally lower considering DISS Messina Straits seismogram than those considering Tortorici seismogram. This is due to the fact that DISS Messina Straits has the maximum acceleration at 7 s, while Tortorici at 11 s. Instead, the lowest values have been derived from Amoruso seismogram that has high accelerations already at the time of 5 seconds.

(9) The time to reach liquefaction increases with depth, indicating that liquefaction occurs first near the surface. This is supported and confirmed by the fact that the acceleration values increase with depth in the liquefied layer. The lowest value occurs at about 3 meters where the water head has been imposed.

(10) The parametric study shows that higher PGA of the input motion corresponds to a greater demagnification on the surface. This finding demonstrates that the PGA is a critical parameter in liquefaction studies.

(11) Liquefaction causes a large reduction in acceleration amplitude in comparison to the case without liquefaction, resulting in beneficial effects. Indeed, the liquefaction leads a reduction in soil

stiffness (and resistance) that, acting as a filter, provides the "natural seismic isolation" of the building.

(12) The interface between the liquefied layer and non-liquefied layer develops a strong stiffness contrast that can produce an increase in terms of accelerations.

(13) It is possible to observe a strong reduction of the spectral accelerations compared to those obtained without considering liquefaction due to the natural seismic isolation provided by the onset of the liquefaction.

(14) When the soil deposit liquefies, the change in stiffness involves in a change in the natural frequency of the soil. In general, it is possible to notice that A(f) peaks move towards lower frequencies considering the liquefaction phenomenon.

(15) Two different types of displacements can be identified: settlements underneath the building and heave displacements next to the building. The latter are the consequence of the undrained dynamic analyses. Indeed, the soil tends to heave where there is not the influence of the structure being the volumetric change prevented.

(16) Considering the presence of liquefiable layer, instantaneous settlements occur at the beginning of the dynamic phase. However, after a dynamic time of 4-6 s, they raise significantly with increasing time, being affected by the onset of liquefaction.

(17) The parametric study demonstrates that higher duration of the input motion corresponds to greater settlements.

(18) The vertical displacements vary significantly with depth. This finding in terms of displacements is in good agreement with the previous consideration in terms of accelerations, demonstrating again that liquefaction has occurred fist near the surface and worked its way downward.

According to the results, liquefaction and its consequences are directly and strongly affected by the amplitude, duration of the earthquake, frequency content and drainage condition. The reduction in stiffness provides the isolation of the building that can be called "natural seismic isolation". However, complete liquefaction does not occur instantly and therefore the building can be subjected to shaking prior to liquefaction. Moreover, the liquefaction phenomenon is accompanied by a large amount of ground surface settlements that can affect the operability of the building.

Numerical modeling is essential to understand the basic processes occurring in soil during dynamic loading. Liquefaction damage during earthquakes, for example, can be prevented if the performance of liquefiable soils and its interaction with structures can be accurately predicted. Therefore, for a better understanding and to provide the data for verification of the analyses and modeling of soil responses under earthquake loading, a new large-scale shear box on a shaking table has been developed.

The design process of the laminar box system at L.E.D.A. of "Kore" University (Sicily, Italy) has been presented. It has been described along its various components, properties and design advantages. The new laminar shear box will be placed on a 6-DOF 4.0m x 4.0m shaking table for use in liquefaction studies.

BIBLIOGRAFY

Abate G., Massimino M. R. (2016) Dynamic soil–structure interaction analysis by experimental and numerical modelling, Riv Ital Geotecn, 50(2):44–70.

Adachi T., Iwai S., Yasui M., Sato, Y. (1992) Settlement and inclination of reinforced concrete buildings in Dagupan City due to liquefaction during the 1990 Philippine earthquake, Earthquake Engineering, Tenth World Conference, Rotterdam, Holland. pp. 147-152.

Alaie R., Chenari R. J. (2018) Design and Performance of a Single Axis Shake Table and a Laminar Soil Container. Civil Engineering Journal, Vol. 4, No.6.

Amini R., Barari A., Haddad A. (2019) Insight into the post-liquefaction behavior of skirted foundations, 7 Conference ICEGE 2019 - International Conference on Earthquake Geotechnical Engineering, Rome, Italy, 17-20 June 2019.

Amorosi A., Boldini D., Di Lernia A. (2016) Seismic ground response at Lotung: Hysteretic elasto-plastic-based 3D analyses. Soil Dynam. Earthq. Eng. 85, 44–61.

Arroyo M., Di Mariano A., Monaco P., Devincenzi M., Pérez N. (2008) SDMT-based deep excavation design. Geotechnical and Geophysical Site Characterization, 3rd International Conference on Site Characterization, Huang & Mayne (eds), Taylor & Francis Group, p. 967-973. Taiwan: Taipei

Baratta M. (1901) I Terremoti d'Italia. Saggio di storia, Geografia e Bibliografia Sismica Italiana Con 136 Sismocartogrammi; Arnaldo Forni Editore, Rome, Itali.

Bardet J.P., Ichii K., Lin C. H. (2000) EERA: a computer program for equivalent-linear earthquake site response analyses of layered soil deposits, user manual, University of Southern California, 40 pp.

Beaty M., Byrne P.M. (1998) An effective stress model for predicting liquefaction behavior of sand. Geotechnical earthquake engineering and soil dynamics III.

Beaty M.H., Byrne P.M. (2011) UBCSAND constitutive model, Version 904aR, UBCSAND Constitutive model on Itasca UDM Web Site, pp. 69.

Benz T. (2006) Small-Strain Stiffness of Soils and its numerical consequences. PhD Thesis. University of Stuttgart.

Benz T., Vermeer P.A., Schwab R. (2009) A small-strain overlay model. International Journal for Numerical and Analytical Methods in Geomechanics, 33(1), 25–44.

Bhatnagar S., Kumari S., Sawant V. A. (2016) Numerical Analysis of Earth Embankment Resting on Liquefiable Soil and Remedial Measures, International Journal of Geomechanics, Vol. 16, Issue 1: 04015029.

Bhattacharya S., Lombardi D., Dihoru L., Dietz M. S., Crewe A. J.; Taylor. C. A. (2012) Model Container Design for Soil-Structure Interaction Studies. M.N. Fardis and Z.T. Rakicevic (eds.) Role

of Seismic Testing Facilities in Performance-Based Earthquake Engineering: SERIES Workshop, Geotech, Geological and Earthquake Engrg. 22, Springer Science+Business Media B.V.

Biondi G., Massimino M. R., Maugeri M. (2015) Experimental study in the shaking table of the input motion characteristics in the dynamic SSI of a SDOF model. Bulletin Earthq. Eng., vol. XIII, no.6, 1835-1869.

Bojadjieva J., Sesov V., Edip K. (2015) Experimental Setup for Sand Liquefaction Studies on Shaking Table. 6th International Conference on Earthquake Geotechnical Engineering, 1-4 November, Christchurch, New Zealand.

Bonaccorso R., Grasso S., Lo Giudice E., Maugeri M. (2005) Cavities and hypogeal structures of the historical part of the City of Catania. Adv. Earthq. Eng., 14, 197–223.

Bouckovalas G., Tsiapas Y.Z., Theocharis A.I., Chaloulos Y.K. (2016) Ground response at liquefied sites: seismic isolation or amplification? Soil Dynamic sand Earthquake Engineering 91 329–339.

Boulanger R.W., Idriss I.M. (2014) CPT and SPT Based Liquefaction Triggering Procedures; Report No. UCD/CGM-14/01; Center for Geotechnical Modeling, Department of Civil and Environmental Engineering, College of Engineering, University of California: Davis, CA, USA.

Boulanger R.W., Ziotopoulou K. (2013) Formulation of a sand plasticity plane-strain model for Earthquake engineering applications. Soil dynamicas and Earthquake engineering, 53 (2013) 254–267. http://dx.doi.org/10.1016/j.soildyn.2013.07.006

Cappellaro C., Cubrinovski M., Chiaro G., Stringer M.E., Bray J.D., Riemer, M.F. (2017) Undrained cyclic direct simple shear testing of Christchurch sandy soils. Proc. 20th NZGS Geotechnical Symposium. Eds. GJ Alexander & CY Chin, Napier.

Caruso S., Ferraro A., Grasso S., Massimino M.R. (2016) Site Response Analysis in eastern Sicily based on direct and indirect Vs measurements. In Proceedings of the 1st IMEKO TC4 International Workshop on Metrology for Geotechnics, Benevento, Italy, 17–18 March 2016; pp. 115–120. ISBN 978-929900750-1.

Carvalho A. T., Bile Serra J., Oliveira F., Morais P., Ribeiro A. R., Santos Pereira C. (2010) Design of experimental setup for 1 g seismic load tests on anchored retaining walls. Springman S, Laue J, Seward L (eds) Physical modelling in geotechnics, Taylor and Francis Group, London.

Castelli F., Cavallaro A., Ferraro A., Grasso S., Lentini V., Massimino M.R. (2018a) Static and dynamic properties of soils in Catania (Italy). Ann. Geophys. , 61, SE221, doi:10.4401/ag-7706.

Castelli F., Cavallaro A., Ferraro A., Grasso S., Lentini V., Massimino M.R. (2018b) Dynamic characterisation of a test site in Messina (Italy). Ann Geophys. 61(2):222.

Castelli F., Cavallaro A., Grasso S, Lentini V. (2019) Undrained Cyclic Laboratory Behaviour of Sandy Soils. Geosciences 2019, 9(12), 512. https://doi.org/10.3390/geosciences9120512.

Castelli F., Cavallaro A., Grasso S. (2016a) SDMT soil testing for the local site response analysis. In Proceedings of the 1st IMEKO TC4 International Workshop on Metrology for Geotechnics, Benevento, Italy, 17–18 March 2016; pp. 143–148.

Castelli F., Grasso S., Lentini V., Massimino M.R. (2016b) In situ measurements for evaluating liquefaction potential under cyclic loading. In Proceedings of the 1st 1MEKO TC4 International Workshop on Metrology for Geotechnics, Benevento, Italy, 17–18 March 2016; pp. 79–84.

Castelli F., Grasso S., Lentini V., Sammito M.S.V. (2021) Effects of Soil-Foundation Interaction on the Seismic Response of a Cooling Tower by 3D-FEM Analysis. Geosciences, 11, 200. https://doi.org/10.3390/geosciences11050200

Cetin K.O., Seed R.B. (2004) Nonlinear shear mass participation factor (r_d) for cyclic shear stress ratio evaluation. Soil Dyn. Earthq. Eng., 24, 103–113, doi:10.1016/j.soildyn.2003.10.008.

Chen C. H., Ueng, T. S. (2011) Dynamic responses of model pile in saturated sand in shaking table tests. 5th International Conference on Earthquake Geotechnical Engineering, Santiago, Chile.

Comerci V., Vittori E., Blumetti A. M., Brustia E., Di Manna P., Guerrieri L., Lucarini M., Serva L. (2015) Environmental effects of the December 28, 1908, Southern Calabria–Messina (Southern Italy) earthquake, Natural Hazards 76(3 (2015)):1849-1891.

Cox C., Mayne P. (2015) Soil stiffness constitutive model parameters for geotechnical problems: A dilatometer testing approach. Third International Conference on Flat Dilatometer, Rome, Italy.

Crewe A. W., Lings M. L., Taylor C.A., Yeung A. K., Andrighetto R. (1995) Development of a large shear-stack for resting dry sand and simple direct foundations on a shaking table. Proceedings of 5th SECED conference on European seismic design practice, Chester, Balkema.

Cubrinovski M. (2013) Liquefaction-Induced Damage in The2010-2011 Christchurch (New Zealand) Earthquakes, Seventh International Conference on Case Histories in Geotechnical Engineering, Apr 29th - May 4th, Missouri.

Da Fonseca A. V., Millen M., Gomez-Martinez F., Romão X., et al. (2017) State of the art review of numerical modelling strategies to simulate liquefaction-induced structural damage and of uncertain/random factors on the behaviour of liquefiable soils. Liquefact Project, Version 1.0, October 2017.

Dar A. R. (1993) Development of flexible shear-stack for shaking table of geotechnical problems. PhD thesis, University of Bristol, Bristol.

Dashti S., Bray J.D. (2013) Numerical simulation of building response on liquefiable sand, J Geotech Geoenviron Eng., 139(8):1235–1249, https://doi.org/10.1061/(ASCE)GT.1943-5606.0000853.

Deghoul L., Gabi S., Hamrouni A. (2020) The influence of the soil constitutive models on the seismic analysis of pile-supported wharf structures with batter piles in cut-slope rock dike. Studia Geotech. Mech., 42, 191–209.

Del Giudice F. (1858) Terremoti avvenuti nel Regno delle due Sicilie nel 1857. Annali Civili del Regno delle due Sicilie nel 1857.

Dixit J., Dewaikar D.M., Jangrid, J.S. (2012) Assessment of liquefaction potential index for Mumbai City. Nat. Hazards Earth Sci. Syst., 12, 2759–2768.

Duncan J., Chang C. Y. (1970) Non linear analysis of stress and strain in soil. Journal of Soil Mech. Fdns Div., ASCE, Vol. 96, No. SM 5, pp. 1629-1653.

Ecemis N. (2013) Simulation of seismic liquefaction: 1-g model testing system and shaking table tests. European Journal of Environmental and Civil Engineering, 17(10).

Ferraro A., Grasso S., Massimino M.R. (2018) Site effects evaluation in Catania (Italy) by means of 1-D numerical analysis. Ann. Geophys., 61.

Fishman K. L., Mander J. B., Richards Jr. R. (1995) Laboratory study of seismic free-field response of sand. Soil Dynamics and Earthquake Engineering, 14:33-43, 19957.

Galavi V., Petalas A., Brinkgreve R.B.J. (2013) Finite element modelling of seismic liquefaction in soils. Geotechnical Engineering Journal of the SEAGS & AGSSEA Vol. 44 No.3 September 2013 ISSN 0046-5828.

Galli P., Meloni F. (1993) Nuovo catalogo nazionale dei processi di liquefazione avvenuti in occasione dei terremoti storici in Italia. Quat. Ital. J. Quat. Sci., 6, 271–292.

Gargano, C. (1994) Carta geologica di Messina e del settore nord-orientale dei Monti Peloritani (Sicilia NE), scala 1:25.000. Direttore del rilevamento: F. Lentini. S.El.Ca., Firenze.

Gibson A. (1996) Physical Scale Modeling of Geotechnical Structures at One-G, Ph.D. Dissertation, California Inst. of Tech., Pasadena.

Golesorkhi R. (1989) Factor Influencing the Computational Determination of Earthquake-Induced Shear Stressed in Sandy Soils. Ph.D. Thesis, University of California, Berkeley, CA, USA.

Grasso S., Laurenzano G., Maugeri M., Priolo E. (2005) Seismic response in Catania by different methodologies. Adv. Earthq. Eng., 14, 63–79.

Grasso S., Maugeri M. (2012) The Seismic Microzonation of the City of Catania (Italy) for the Etna Scenario Earthquake (M=6.2) of February 20, 1818. Earthquake Spectra, Vol. 28 (2): 573-594. https://doi.org/10.1193/1.4000013

Grasso S., Maugeri M. (2008) The Seismic Dilatometer Marchetti Test (SDMT) for Evaluating Liquefaction Potential under Cyclic Loading. In Proc. IV Geotechnical Earthquake Engineering and Soil Dynamic; Sacramento, USA, May 18-22, 2008. Geotechnical Earthquake Engineering and Soil Dynamics IV GSP 181 © 2008 ASCE, Geo Institute, ISBN 978-0-7844-0975-6, 15 p.

Grasso S., Maugeri M. (2009) The Seismic Microzonation of the City of Catania (Italy) for the Maximum Expected Scenario Earthquake of January 11, 1693. Soil Dynamics and Earthquake Engineering, 29 (6): 953-962. https://doi.org/10.1016/j.soildyn.2008.11.006.

Grasso S., Maugeri M. (2014) Seismic Microzonation Studies for the City of Ragusa (Italy). Soil Dynamics and Earthquake Engineering. ISSN: 0267-7261. Vol. 56, 86–97.

Grasso S., Massimino M.R., Sammito M.S.V. (2021) New Stress Reduction Factor for Evaluating Soil Liquefaction in the Coastal Area of Catania (Italy). Geosciences, 11, 12. https://doi.org/10.3390/geosciences11010012

Guidoboni E., Ferrari G., Mariotti D., Comastri A., Tarabusi G., Sgattoni G., Valensise G. (2018) CFTI5Med. Catalogue of Strong Earthquakes in Italy (461 B.C.-1997) and Mediterranean Area (760 B.C.-1500). INGV. https://doi.org/10.6092/ingv.it-cfti5

Guidoboni E., Ferrari G., Tarabusi G., Sgattoni G., Comastri A., Mariotti D., Ciuccarelli C., Bianchi M.G., Valensise G. (2019) CFTI5Med, the new release of the catalogue of strong earthquakes in Italy and in Mediterranean area. Scientific Data 6, Article number: 80. http://doi.org/10.1038/s41597-019-0091-9.

Hardin B. O., Drnevich V. P. (1972) Shear modulus and damping ratio: measurement and parameter effects. J Soil Mech Found Div 800 98(6):603–624.

Hashash Y., Park D. (2002) Viscous damping formulation and high frequency motion propagation in non-linear site response analysis. Soil dynamic earthquake engineering, 22 (7), 611-624.

Hushmand B., Scott R.F., Crouse C.B. (1988) Centrifuge liquefaction tests in a laminar box. Geotechnique, 38(2):253-262.

Idriss I.M. (1999) An update to the Seed-Idriss simplified procedure for evaluating liquefaction potential. In Proceedings of the TRB Workshop on New Approaches to Liquefaction, Washington, DC, USA, 10 January 1999.

Idriss I.M., Boulanger R.W. (2004) Semi-empirical procedures for evaluating liquefaction potential during earthquakes. In Proceedings of the 11th IC SDEE/3rd ICEGE Proceedings, Berkeley, CA, USA, 7–9 January 2004; Volume 1, pp. 32–56, doi:10.1016/j.soildyn.2004.11.023.

Idriss I.M., Boulanger R.W. (2010) SPT-based liquefaction triggering rocedures (Report UCD/CGM-10/02) Davis, CA: Center for Geotechnical Modeling, Department of Civil and Environmental Engineering, University of California.

Ishihara K. (1977) Simple method of analysis for liquefaction of sand deposits during earthquakes. Soils Found., 17, 1–17, doi:10.3208/sandf1972.17.3_1.

Itasca (2017) FLAC, Fast Lagrangian Analysis of Continua, Itasca Consulting Group, Inc. (www.itascach.com/flac).

Iwasaki, T.(1986) Soil liquefaction studies in Japan: State-of-the-art. Soil Dyn Earthquake Engng., 5, 2–68, doi:10.1016/0267-7261(86)90024-2.

Iwasaki T., Tatsuoka F., Tokida K., Yasuda S. (1978) A practical method for assessing soil liquefaction potential based on case studies at various sites in Japan. In Proceedings of the 2nd Int Conf on Microzonation for Safer Construction, Research and Application, San Francisco, CA, USA, 26 November–1 December 1978, Volume 1, pp. 885–896.

Iwasaki T., Tokida K., Tatsuoka F., Watanabe S., Yasuda, S., Sato H. (1982) Microzonation for soil liquefaction potential using simplified methods. In Proceedings of the 3rd International Conference on Microzonation, Seattle, WA, USA, June 28-July 1, 1982; pp. 1319–1330.

Joyner W.B., Chen, A.T.F. (1975) Calculation of non linear ground response in earthquake. Bulletin of Seismological Society of America, 65, 1315-1336.

Kanibir A., Ulusay R., Aydan Ö. (2006) Assessment of liquefaction and lateral spreading on the shore of Lake Sapanca during the Kocaeli (Turkey) earthquake, Eng Geol 83(4):307–331

Karimi Z., Dashti, S. (2016) Seismic performance of shallow founded structures on liquefiable ground: validation of numerical simulations using centrifuge experiments. Journal of Geotechnical Geoenvironment Engineering 142(6): 13 pp.

Kavazanjian E., Andrade J., Arulmoli K.A., Atwater B.F., Christian J.T., Green R., Kramer S.L., Mejia L., Mitchell J.K., Rathje E., et al. (2016). State of the Art and Practice in the Assessment of Earthquake-Induced Soil Liquefaction and Its Consequences, Washington, DC: The National Academies Press.

Kim H.S., Kim M., Baise L.G., Kim B. (2020) Local and regional evaluation of liquefaction potential index and liquefaction severity number for liquefaction-induced sand boils in Pohang, South Korea. Soil Dyn. Earthq. Eng., 106459, doi:10.1016/j.soildyn.2020.106459.

Kishida T., Boulanger R.W., Abrahamson N.A., Driller M.W., Wehling T.M. (2009a) Site effects for the Sacramento-San Joaquin Delta. Earthq. Spectra, 25, 301–322, doi:10.1193/1.3111087.

Kishida T., Boulanger R.W., Abrahamson N.A., Driller M.W., Wehling T.M. (2009b) Seismic response of levees in Sacramento-San Joaquin Delta. Earthq. Spectra, 25, 557–582, doi:10.1193/1.3157259.

Kiyota T., Ikeda T., Konagai K., Shiga M. (2017) Geotechnical Damage Caused by the 2016 Kumamoto Earthquake, Japan, International Journal of Geoengineering Case Histories, Vol. 4, Issue 2, p.78-95.

Kokusho T., Yoshida Y. (1997) SPT N-value and S-wave velocity for gravely soils with different grain size distribution. Soils Found., 37, 105–113.

Kondner R., Zelasko J. (1961) A hyperbolic stress-strain formulation of sands. Proceedings of the 2nd Conference on Soil Mechanics and Foundation Engineering.

Kottke A..R., Rathje E.M. (2008) Technical Manual for Strata. PEER Report. Pacific Earthquake. Engineering Research Center College of Engineering. University of California, Berkeley.

Kramer, S. L. (1996). Geotechnical Earthquake Engineering. Prentice Hall, 1 edition, ISBN: 0133749436.

Kramer S. L., Elgamal A. W. (2001). Modeling soil liquefaction hazards for performance-based earthquake engineering, PEER Report 2001/13.

Kuhlemeyer R.L., Lysmer J. (1973) Finite element method accurancy for wave propagation problems. Journal of soil mechanics and foundation devision, 99 (5): 421-427.

Laera A., Brinkgreve R.B.J. (2015) Site response analysis and liquefaction evaluation. Delft University of Technology & Plaxis BV, Delft, The Netherlands.

Lasley S.J., Green R.A., Rodriguez-Marek A. (2016) New stress reduction coefficient relationship for liquefaction triggering analyses. J. Geotech. Geoenvironmental Eng., 142, 06016013, doi:10.1061/(asce)gt.1943-5606.0001530.

Laurenzano G., Priolo E., Klinc P., Vuan, A. (2004) Near fault earthquake scenarios for the February 20, 1818 M = 6.2 "Catanese" event. In Proceedings of the Fourth International Conference on Computer Simulation in Risk Analysis and Hazard Mitigation: "Risk Analysis 2004", Rhodes, Greece, 27–29 September 2004; pp. 81–91.

Liao S.S.C., Whitman R.V. (1986) Overburden Correction Factor for SPT in Sands. J. Geotech. Eng., 112, 373–377, doi:10.1061/(ASCE)0733-9410(1986)112:3(373).

Madabhushi S. P. G., Butler G., Schofield, A. N. (1998) Design of an Equivalent Shear Beam (ESB) container for use on the US Army. Kimura, Takemura (eds) Centrifuge, Balkema, Rotterdam.

Madabhushi S.P.G., Schofield A.N., Zeng, X. (1992) Complementary shear stresses in dynamic centrifuge modelling. Technical Report under preparation, CUED.

Makra A. (2013) Evaluation of the UBC3D-PLM constitutive model for prediction of earthquake induced liquefaction on embankment dams, MSc Thesis, TU Delft.

Marchetti S. (1982) Detection of liquefiable sand layers by means of quasi-static penetration test. In Proceedings of the 2nd European Symp. on Penetration Testing, Amsterdam, Netherlands, 24–27 May 1982; Volume 2, pp. 689–695.

Marcuson, W. F., III. (1978) Definition of terms related to liquefaction, J. Geotech. Engrg. Div., ASCE, 104(9), pp. 1197–1200, 1978.

Masing G. (1926) Eigenspannungen und Verfestigung beim Messing. In Proceedings of the 2nd International Congress on Applied Mechanics, Zurich, Switzerland, 12–17 September, 1926; pp. 332–335.

Massimino M.R., Abate G., Corsico S., Grasso S., Motta E. (2018) Dynamic behaviour of coupled soil-structure systems by means of FEM analysis for the seismic risk mitigation of INGV building in Catania (Italy). Ann. Geophys. 61(2):SE216.

Massimino M. R., Abate G., Grasso S., Pitilakis, D. (2019) Some aspects of DSSI in the dynamic response of fully-coupled soil-structure system, Riv Ital Geotecn.

Maugeri M. (2005) Seismic Prevention of Damage: A Case Study in a Mediterranean City. M. Maugeri Editor. WIT Press, Southampton (UK) ISBN: 1-84564-004-7. ISSN: 1361-617X

Maugeri M., Grasso S. (2013) Liquefaction potential evaluation at Catania Harbour (Italy). Wit Trans Built Environ., 1, 69–81. doi:10.2495/ERES130061.

Maurer B.W., Green R.A., Cubrinovski M., Brendon A., Bradley B.A. (2014) Evaluation of the liquefaction potential index for assessing liquefaction hazard in Christchurch, New Zealand. J. Geotech. Geoenviron. Eng., 140, 04014032, doi:10.1061/(asce)gt.1943-5606.0001117.

Mercalli G. (1883) I terremoti storici italiani. Geologia d'Italia, part III, Vulcani e fenomeni vulcanici in Italia, Vallardi Editore, Milan, Italy.

Mohsan M., Kiyota T., Munoz H., Nihahaj M., Katagiri T. (2018) Fabrication and Performance of laminar soil box with rigid soil box for liquefaction study. Bulletin of ERS, No. 51.

Monaco P., Marchetti S. (2004) Evaluation of the coefficient of subgrade reaction for design of multi-propped diaphragm walls from DMT moduli. Proc. ISC-2 on Geotech. and Geophys. Site Charact., 993-1002.

Monaco P., Marchetti S., Totani G., Calabrese M. (2005) Sand liquefiability assessment by Flat Dilatometer Test (DMT). In Proceedings of the XVI ICSMGE, Osaka, Japan, 12–16 September 2005; Volume 4, pp. 2693–2697.

Motamed R., Towhata I. (2010) Mitigation measures for pile groups behind quay walls subjected to lateral flow of liquefied soil: Shake table model tests. Soil Dynamics and Earthquake Engineering, 30 (2010): 1043-1060.

NASEM-National Academies of Sciences, Engineering, and Medicine (2016). State of the Art and Practice in the Assessment of Earth-quake-Induced soil Liquefaction and Its Consequences; The National Academies Press: Washington, DC, USA, 2016, doi:1017226/23474.

Navarra G., Lo Iacono F., Oliva M., Tesoriere G. (2015) A new research facility: The Laboratory of Earthquake engineering and Dynamic Analysis (L.E.D.A.). Proc. of XXII Congresso - Associazione Italiana di Meccanica Teorica e Applicata - AIMETA 2015, ISBN 978-88-97752-55-4, 297-306, Genoa, Italy, September 14-17.

Ng C. W. W., Li X. S., Van Laak P. A., Hou D. Y. J. (2004) Centrifuge modeling of loose fill embankment subjected to uni-axial and bi-axial earthquakes. Soil Dynamics and Earthquake Engineering; 24(4):305e18.

NTC (2018) D.M. New Technical Standards for Buildings, 2018. Available online: https://www.gazzettaufficiale.it/eli/gu/2018/02/20/42/so/8/sg/pdf

Ohta Y., Goto N. (1978) Empirical Shear Wave Velocity Equations in Terms of Characteristic Soil Indexes. Earthq. Eng. Struct. Dyn., 6, 167–187, doi:10.1002/eqe.4290060205.

Open system for earthquake engineering simulation (OpenSees) (2017). Pacific Earthquake Engineering Research Center, University of California, Berkeley, CA. Available from: http://opensees.berkeley.edu.

Orense R. P. (2011) Soil liquefaction during the 2010 Darfield and 1990 Luzon Earthquakes: A comparative study. Proceedings of the Ninth Pacific Conference on Earthquake Engineering Building an Earthquake-Resilient Society 14-16 April, 2011, Auckland, New Zealand.

Özener P. T., Özaydin K., Berilgen M. (2008) Numerical and Physical Modeling of Liquefaction Mechanisms in Layered Sands. Proceedings of Geotechnical Earthquake Engineering and Soil Dynamics IV, 18-22 May, California.

Pamuk A., Gallagher P. M., Zimmie, T. F. (2007) Remediation of piled foundations against lateral spreading by passive site stabilization technique. Soil Dyn Earthq Eng 27:864–874.

Pappalardo G., Punturo R., Mineo S., Ortolano G., Castelli F. (2016) Engineering geological and petrographic characterization of migmatites belonging to the Calabria-Peloritani orogen (Southern Italy). Rock Mechanics and Rock Engineering, Vol. 49, no.4, pp.1143-1160, DOI 10.1007/s00603-015-0808-9.

Petalas A., Galavi V. (2013) PLAXIS liquefaction model UBC3D-PLM. PLAXIS Knowledge Base.

Pino P., D'Amico S., Orecchio B., Presti D., Scolaro S., Torre A., Neri G. (2018) Integration of geological and geophysical data for re-evaluation of local seismic hazard and geological structure: the case study of Rometta, Sicily (Italy). Ann Geophy 61(2):SE227.

PLAXIS3D (2020), Reference Manual, Last Updated: September 01, 2020. Available online: https://communities.bentley.com

PLAXIS3D (2018a), Material models Manual. Available online: https://communities.bentley.com/products/geotech-analysis/w/plaxissoilvision-wiki/50826/manuals-archive---plaxis

PLAXIS3D (2018b), Scientific Manual. Available online: https://communities.bentley.com/products/geotech-analysis/w/plaxissoilvision-wiki/50826/manuals-archive---plaxis

Prasad S. K., Towhata I., Chandradhara G. P., Nanjunaswamy P. (2004) Shaking table tests in earthquake geotechnical engineering. Current Science, 87(10): 1398-1404.

Puebla H., Byrne M., Phillips P. (1997) Analysis of canlex liquefaction embankments prototype and centrifuge models. Canadian Geotechnical Journal, 34: 641-657.

RMS Special Report (2008) The 1908 Messina Earthquake: 100-Year Retrospective.

Robertson P.K., Wride C.E. (1997) Cyclic Liquefaction and its Evaluation Based on the SPT and CPT. Proc., NCEER Workshop on Evaluation of Liquefaction Resistance of Soils, National Center for Earthquake Engineering Research, State University of New York at Buffalo, Technical Report No. NCEER-97-0022, December, pp 41 – 88, 1997.

Rowe P. W. (1962) The stress-dilatancy relation for static equilibrium of an assembly of particles in contact, Proc. R. Soc., 269 A: 500-527, 1962.

Sadrekarimi A., Ghalandarzadeh A. (2005) Evaluation of gravel drains and compacted sand piles in mitigating liquefaction. Ground Improvement 9, No. 3: 91-104.

Saha R., Sumanta, H., Dutta, S. C. (2015) Influence of dynamic soil-pile raft-structure interaction: an experimental approach. Earthquake Eng. & Eng. Vib., 14: 625-645 DOI: 10.1007.

Santos J.A., Correia A. G. (2001) Reference threshold shear strain of soil. Its application to obtain a unique strain-dependent shear modulus curve for soil, 15th International Conference on Soil Mechanics and Geotechnical Engineering, 2001.

Sarlak A., Saeedmonir H., Gheyretmand C. (2017) Numerical and experimental study of soil-structure interaction in structures resting on loose soil using laminar shear box. International Journal of Engineering-Transactions B: Applications, Vol. 30, No. 11, 1654-1663.

Schanz T., Vermeer P. A. (1997) On the Stiffness of Sands. Proc. Symp. Pre-failure Deformation Behaviour of Geomaterials, ICE, London: 383-387

Schanz T., Vermeer P.A., Bonnier P.G. (1999) The Hardening Soil model : formulation and verification. In: Proceedings Plaxis Symposium ''Beyond 2000 in Computational Geotechnics, Amsterdam, Balkema, p. 281–96.

Seed H.B., Idriss I.M. (1971) Simplified procedure for evaluating soil liquefaction potential. J. Soil Mech. Found. Div., 97, 1249–1273.

Sesov V. (2003) Dynamic behaviour of potentially nonstable layers and application of a model for decreasing the seismic risk of liquefaction occurrence, PhD Thesis, University Ss. Cyril and Methodius-Skopje, Macedonia.

Seylabi E.E., Jeong C., Dashti S., Hushmand A., Taciroglu E. (2018) Seismic response of buried reservoir structures: a comparison of numerical simulations with centrifuge experiments. Soil Dyn. Earthq. Eng., 109, 89–101.

Soga K. (1998) Soil liquefaction effects observed in the Kobe earthquake of 1995. Proceedings of the Institution Of Civil Engineers-Geotechnical Engineering, 131(1):34–51.

Souliotis C., Gerolymos N. (2016). Seismic Effective Stress Analysis of Quay Wall in Liquefiable Soil: The Case History of Kobe. International Journal of Geomate, 10(2), 1770-1775.

Surarak C., Likitlersuang S., Wanatowski D., Balasubramaniam A., Oh E., Guan H. (2012) Stiffness and strength parameters for hardening soil model of soft and stiff Bangkok clays. Soils and Foundations, 52 (4), pp. 682-697.

Takahashi A., Takemura J., Suzuki A., Kusakabe, O. (2001) Development and performance of an active type shear box in a centrifuge. International Journal of Physical Modelling in Geotechnics, 1(2):1-17

Terzaghi K., Peck R., Mesri G. (1996). Soil mechanics in Engineering Practise. 3ª ed., New York, John Wiley & Sons Inc, USA.

Teymur B., Madabhushi S. P. G. (2003) Experimental study of boundary effects in dynamic centrifuge modelling, Géotechnique, 53(7):655-63.

Thevanayagam S., Kanagalingam T., Reinhorn A., Tharmenddhira R., Dobry R., Pitman M., Abdoun T., Elgamal A., Zeghal M., Ecemis N., El Shamy U. (2009) Laminar Box System for 1-g Physical Modeling of Liquefaction and Lateral Spreading. Geotechnical testing Journal, Vol. 32, No. 5.

Tsegaye A. (2010) Plaxis liquefaction model. Report no. 1. PLAXIS knowledge base.

Turan A., Hinchberger, S., El Naggar, H. (2013) Seismic soil–structure interaction in buildings on stiff clay with embedded basement stories. Canadian Geotechnical Journal, Vol. 50, No. 3, pp. 858-873.

Ueng T. S., Wang M. H., Chen M. H., Chen C.H., Peng, L.H. (2006) A large Biaxial Shear Box for Shaking Table Test on Saturated Sand. Geotechnical testing Journal, Vol. 19, No. 1.

Ueng T.S., Wu C.W., Cheng H.W., Chen C.H. (2010) Settlement of saturated clean sand deposits in shaking table tests. Soil Dynamics and Earthquake Engineering 30, 50-60.

Vakili K.N., Barciago T., Lavason A.A., Schanz J. (2013) A practical approach to constitutive models for the analysis of geotechnical problems. The 3rd International Conference on Computational Geomechanics (ComGeo III), vol. 1, Krakow, Poland.

Vannucchi G., Crespellani T., Facciorusso J., Ghinelli A., Madiani G., Puliti A., Renzi S. (2012) Soil liquefaction phenomena observed in recent seismic events in Emilia-Romagna Region, Italy, Ingegneria Sismica, no. 2-3, Special issue Emilia-Romagna Earthquake, pp. 20-30.

Verdugo R. (2015) Liquefaction Observed During the 2010 Chile Earthquake, Perspectives on Earthquake Geotechnical Engineering, GGEE, Vol. 37, pp 365-390.

Verdugo R., González J. (2015) Liquefaction-induced ground damages during the 2010 Chile earthquake. Soil Dyn Earthq Eng 79:280–295. https://doi.org/10.1016/j.soildyn.2015.04.016

Vermeer P.A. (2001) On single anchored retaining walls. Plaxis Bulletin 10.

Whitman, R.V. (1984) Experiments with earthquake ground motion simulation. Proc. Application of Centrifuge Modelling to Geotechnical Design: 282–299. Rotterdam

Yao S., Kobayaski K., Yoshida N., Hiroshi M. (2004) Interactive behaviour of soil-pile-superstructure system in transient state to liquefaction by means of large shake table tests. Soil Dynamics and Earthquake Engineering 24, 397-409.

Yokota K., Imai T., Konno M. (1981) Dynamic Deformation Characteristics of Soils Determined by Laboratory Tests. OYO Tec. Rep. 3, pp. 13 – 37.

Yoshida Y., Motonori I. (1988) Empirical Formulas of SPT Blow-Counts for Gravelly Soils. In Proceedings of ISOPT-1, Orlando, FL, USA, 20–24 March 1988; pp. 381–387, doi:10.1007/s11069-017-2744-3.

Youd T.L., Idriss I.M., Andrus R.D., Arango I., Castro G., Christian J.T., Dobry R., Finn W.D.L., Harder L.F., Hynes M.E., et al. (2001) Liquefaction Resistance of Soils: Summary Report from the 1996 NCEER and 1998 NCEER/NSF Workshops on Evaluation of Liquefaction Resistance of Soils. J. Geotech. Geoenviron. Eng., 127, 817–833.

Zayed M., Luo L., Kim K., McCarteney J. S., Elgamal, A. (2017) Development and performance of a laminar container for seismic centrifuge modeling. Proc. 3rd International Conference on Performance-Based Design in Earthquake Geotechnical Engineering, Vancouver, BC, Canada, July.

Zeghal M., El Shafee O., Abdoun T. (2018) Analysis of soil liquefaction using centrifuge tests of a site subjected to biaxial shaking. Soil Dynam Earthq Eng, 114:229–41.

Zeng X., Schofield A.N. (1996) Design and performance of an equivalent-shear-beam container for earthquake centrifuge modelling. Geotecnique, 46(1), 83-102.

Table captions

Table 2.1 Level of liquefaction severity Iwasaki et al. (1982).

Table 3.1. Examples of laminar shear boxes**.**

Table 4.1 Experimental sites and tests used to obtain new r_d relationships in Catania area.

Table 5.1 Index properties for the study area.

Table 5.2 Strength parameters for the study area.

Table 5.3 Soil model for site response analyses.

Table 5.4 Values of the shear modulus, G, and the damping ratio, ξ, assigned to each layers using as input the three 1908 seismograms.

Table 5.5 Values of the Rayleigh coefficients assigned to each layers using as input the three 1908 seismograms.

Table 5.6 Values of the surface maximum accelerations and soil amplification factors R obtained by EERA, STRATA and PLAXIS3D.

Table 5.7 Input parameters for the Silty Sand and Gravel 1a and Sandy Silt and Clay layers.

Table 5.8 Values of surface maximum accelerations and soil amplification factors for FF and SSI conditions using: a) the Amoruso seismogram; b) the Tortorici seismogram; c) the DISS Messina Straits seismogram.

Table 5.9 Parameters of the UBC3D-PLM model.

Table 5.10 Conditions of the cyclic direct simple-shear stress tests.

Table 5.11 Test conditions and the number of cycles needed to reach liquefaction.

Table 5.12 Parameters of the calibrated UBC3D-PLM model.

Table 5.13 Dynamic times to reach liquefaction at different depths: a) the Amoruso seismogram; b) the Tortorici seismogram; c) the DISS Messina Straits seismogram.

Figure captions

Figure 2.1 3D soil elements (10-node tetrahedrons) (From PLAXIS 3D, 2020).

Figure 2.2 Hyperbolic stress-strain relation in primary loading for a standard triaxial test (From Schanz et al., 1999).

Figure 2.3 Total yield contour of the Hardening Soil Model in the principal stress space for cohesionless soil (From PLAXIS3D, 2018a; modified).

Figure 2.4 Definition of $E_{oed}{}^{ref}$ in oedometer test results (From PLAXIS3D, 2018a).

Figure 2.5 Variation of the yield locus with various values of the hardening parameter γ_p in p'-q space. (From PLAXIS3D, 2018a).

Figure 2.6 Plot of mobilized dilatancy angle ψ_m and mobilized friction angle φ_m (From PLAXIS3D, 2018a).

Figure 2.7 Secant and tangent shear modulus curves (From PLAXIS3D, 2018a).

Figure 2.8 Hysteretic material behaviour (From PLAXIS3D, 2018a).

Figure 2.9 Yield surfaces in p'-q space (From Galavi et al. 2013).

Figure 2.10 Modified Rowe's flow rule as used in UBC3D-PLM model (From PLAXIS3D, 2018a).

Figure 2.11 Liquefaction-induced bearing capacity failures of the Kawagishi-cho apartment buildings following the 1964 Niigata earthquake (From Kramer, 1996).

Figure 2.12 Settlement and tilting of buildings following the 1990 Luzon earthquake (From Orense, 2011).

Figure 2.13 Damages to the road infrastructure and railroads system after the 1999 Kocaeli earthquake (From Verdugo and González, 2015).

Figure 2.14 Differential settlement of a 6 storey reinforced concrete building in the city of Christchurch (From Cubrinovski, 2014).

Figure 2.15 Liquefaction-induced damage to levee along Akitsukawa-River (From Kiyota et al., 2017).

Figure 2.16 Liquefaction evidences observed immediately after the earthquake (From Vannucchi et al., 2012).

Figure 2.17 Range of values of r_d for different soil profiles (From Seed and Idriss, 1971; modified).

Figure 5.19. Values of $\gamma_{0.7}$ obtained from RCT and CLTST carried out on (a) sample S1C1 (retrieved at 7-7.4 m in S1 borehole) and (b) S3C4 (retrieved at 27-27.5 m in S3 borehole).

Figure 5.20. Comparison of maximum accelerations with depth obtained by means of PLAXIS3D using the HSsmall and linear visco-elastic constitutive models.

Figure 5.21. Comparison of the response spectrum at the surface obtained by means of PLAXIS3D using the HSsmall and linear visco-elastic constitutive models.

Figure 5.22 Maximum accelerations and stress reduction factor with depth obtained from site response analysis using as input the Amoruso seismogram (PGA=0.456g).

Figure 5.23 (a) $(N_1)_{60}$ test results versus depth; (b) $CRR_{7.24}$ from SPT date.

Figure 5.24 Liquefaction potential values obtained from SPT date.

Figure 5.25 Coupled soil-structure system.

Figure 5.26 Maximum accelerations with depth along SSI and FF alignments using: a) the Amoruso seismogram; b) the Tortorici seismogram; c) the DISS Messina Straits seismogram.

Figure 5.27 Results at the surface in term of spectral accelerations using: a) the Amoruso seismogram; b) the Tortorici seismogram; c) the DISS Messina Straits seismogram.

Figure 5.28 Amplification functions obtained as the ratio between the Fourier Spectra at the top and at the bottom of the structure.

Figure 5.29 Amplification functions for FF and SSI conditions using: a) the Amoruso seismogram; b) the Tortorici seismogram; c) the DISS Messina Straits seismogram.

Figure 5.30 Deformed mesh (scaled up 50 times) at the end of the dynamic phase using DISS Messina Straits seismic input.

Figure 5.31 Total displacements at the end of the dynamic phase using DISS Messina Straits seismic input.

Figure 5.32 Simple shear cyclic loading conditions (From Cappellaro et al., 2017).

Appendix-Results of CDSS tests simulated by PLAXIS3D

TEST 1

Test Conditions	Symbol	Value/type
Type of test	-	Undrained
K_0-consolidate test	$K_0\text{-}value$	0.5
Initial Stress	$|\sigma_{yy}|$	100 kN/m^2
Number of cycles	-	100
Number of step per quarter cycle	-	50
Test control	-	Stress
Shear stress amplitude	τ_{xy}	8.5 kN/m^2

(a)　　　　　　　　　　　　　　　(b)

(c)

Figure 1 CDSS test response in term of: (a) shear stress (τ_{xy}) over shear strain (γ_{xy}), (b) excess water pore pressure (Δu) over shear strain (γ_{xy}) and (c) excess pore water pressure ratio (r_u) over cycles (CSR=0.085).

TEST 2

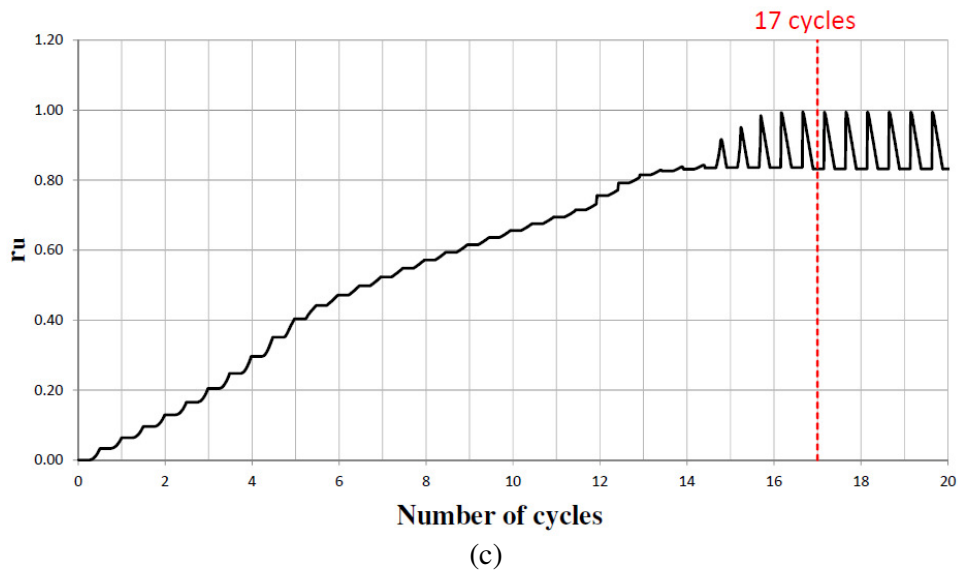| Test Conditions	Symbol	Value/type
Type of test	-	Undrained
K_0-consolidate test	$K_0\text{-}value$	0.5
Initial Stress	$|\sigma_{yy}|$	100 kN/m²
Number of cycles	-	100
Number of step per quarter cycle	-	50
Test control	-	Stress
Shear stress amplitude	τ_{xy}	9 kN/m²

(a)

(b)

(c)

Figure 2 CDSS test response in term of: (a) shear stress (τ_{xy}) over shear strain (γ_{xy}), (b) excess water pore pressure (Δu) over shear strain (γ_{xy}) and (c) excess pore water pressure ratio (r_u) over cycles (CSR=0.090).

TEST 3

Test Conditions	Symbol	Value/type
Type of test	-	Undrained
K_0-consolidate test	$K_0\text{-}value$	0.5
Initial Stress	$|\sigma_{yy}|$	100 kN/m^2
Number of cycles	-	100
Number of step per quarter cycle	-	50
Test control	-	Stress
Shear stress amplitude	τ_{xy}	9.5 kN/m^2

(a)

(b)

(c)

Figure 3 CDSS test response in term of: (a) shear stress (τ_{xy}) over shear strain (γ_{xy}), (b) excess water pore pressure (Δu) over shear strain (γ_{xy}) and (c) excess pore water pressure ratio (r_u) over cycles (CSR=0.095).
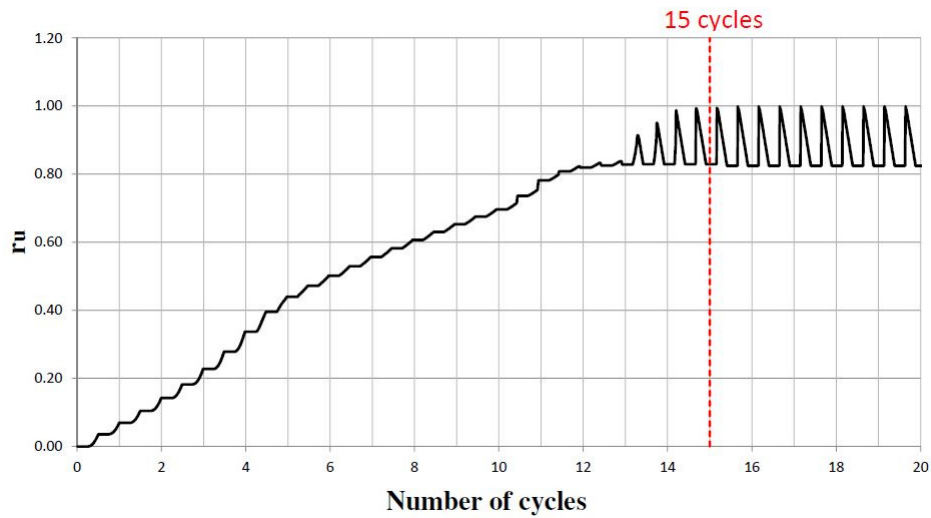
TEST 4

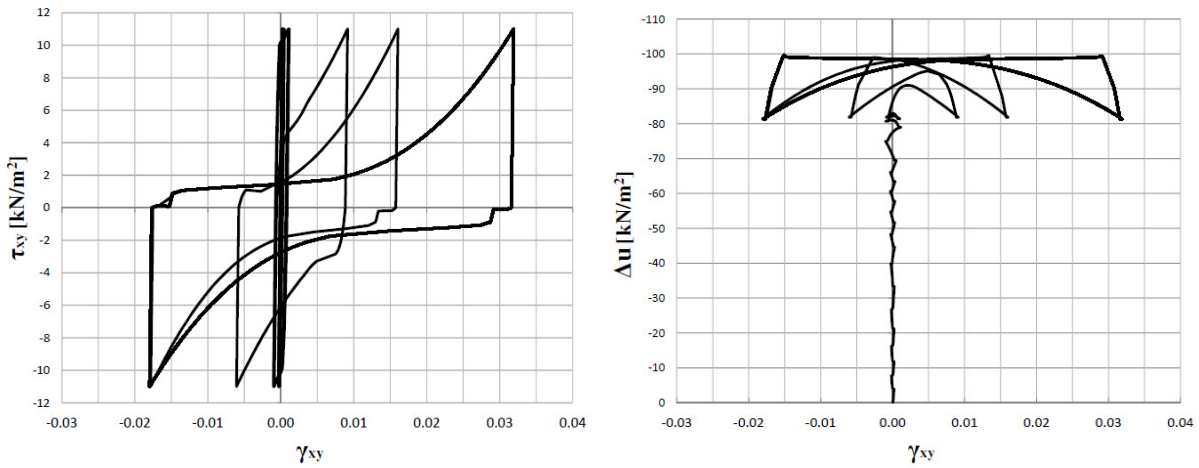| Test Conditions	Symbol	Value/type
Type of test	-	Undrained
K_0-consolidate test	$K_0\text{-}value$	0.5
Initial Stress	$|\sigma_{yy}|$	100 kN/m^2
Number of cycles	-	100
Number of step per quarter cycle	-	50
Test control	-	Stress
Shear stress amplitude	τ_{xy}	10 kN/m^2

(a)

(b)

(c)

Figure 4 CDSS test response in term of: (a) shear stress (τ_{xy}) over shear strain (γ_{xy}), (b) excess water pore pressure (Δu) over shear strain (γ_{xy}) and (c) excess pore water pressure ratio (r_u) over cycles (CSR=0.100).
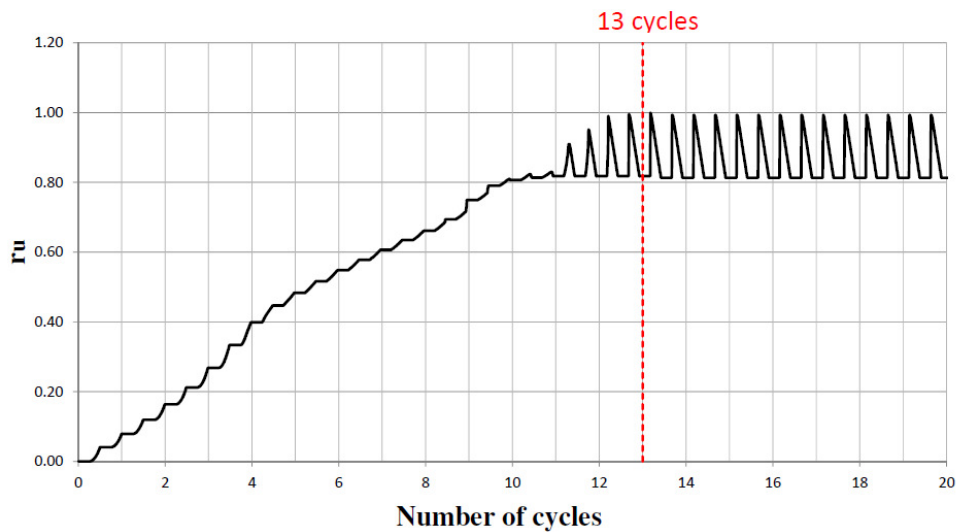
TEST 5

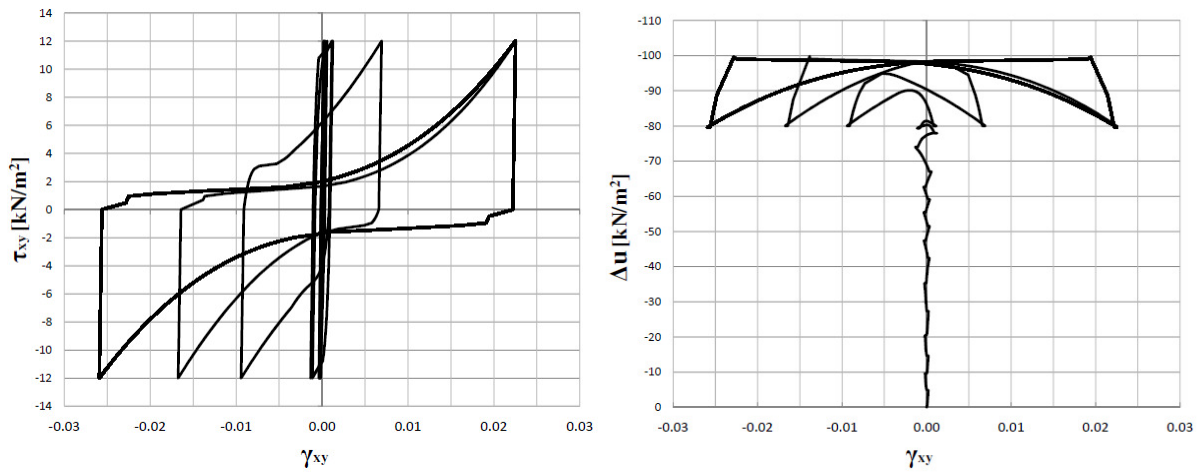| Test Conditions	Symbol	Value/type
Type of test	-	Undrained
K_0-consolidate test	$K_0\text{-}value$	0.5
Initial Stress	$|\sigma_{yy}|$	100 kN/m^2
Number of cycles	-	100
Number of step per quarter cycle	-	50
Test control	-	Stress
Shear stress amplitude	τ_{xy}	10.4 kN/m^2

(a)

(b)

(c)

Figure 5 CDSS test response in term of: (a) shear stress (τ_{xy}) over shear strain (γ_{xy}), (b) excess water pore pressure (Δu) over shear strain (γ_{xy}) and (c) excess pore water pressure ratio (r_u) over cycles (CSR=0.104).
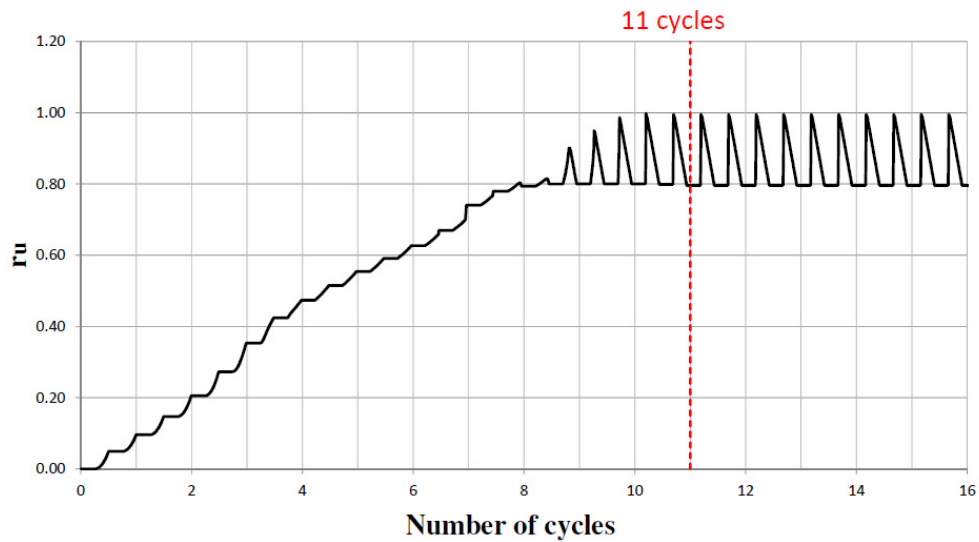
TEST 6

Test Conditions	Symbol	Value/type
Type of test	-	Undrained
K_0-consolidate test	$K_0\text{-}value$	0.5
Initial Stress	$|\sigma_{yy}|$	100 kN/m^2
Number of cycles	-	100
Number of step per quarter cycle	-	50
Test control	-	Stress
Shear stress amplitude	τ_{xy}	11 kN/m^2

(a)

(b)
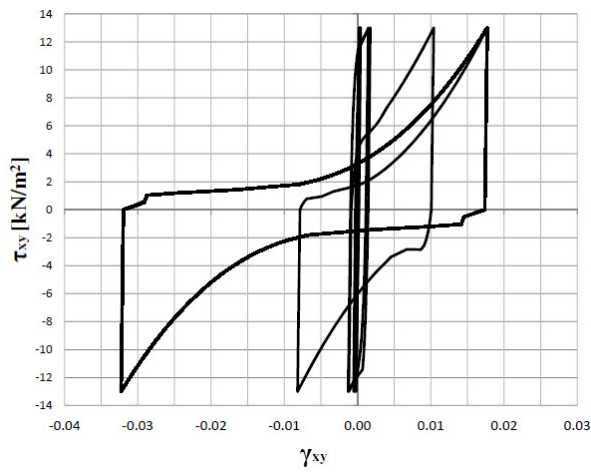
(c)

Figure 6 CDSS test response in term of: (a) shear stress (τ_{xy}) over shear strain (γ_{xy}), (b) excess water pore pressure (Δu) over shear strain (γ_{xy}) and (c) excess pore water pressure ratio (r_u) over cycles (CSR=0.110).

TEST 7

Test Conditions	Symbol	Value/type
Type of test	-	Undrained
K_0-consolidate test	$K_0\text{-}value$	0.5
Initial Stress	$|\sigma_{yy}|$	100 kN/m²
Number of cycles	-	100
Number of step per quarter cycle	-	50
Test control	-	Stress
Shear stress amplitude	τ_{xy}	12 kN/m²

(a)

(b)

(c)

Figure 7 CDSS test response in term of: (a) shear stress (τ_{xy}) over shear strain (γ_{xy}), (b) excess water pore pressure (Δu) over shear strain (γ_{xy}) and (c) excess pore water pressure ratio (r_u) over cycles (CSR=0.120).
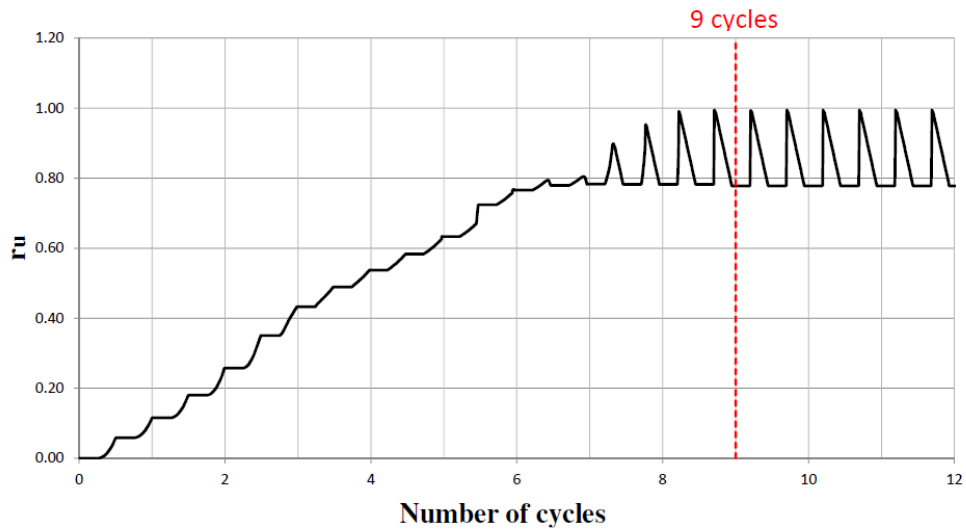
TEST 8

Test Conditions	Symbol	Value/type
Type of test	-	Undrained
K_0-consolidate test	$K_0\text{-value}$	0.5
Initial Stress	$|\sigma_{yy}|$	100 kN/m^2
Number of cycles	-	100
Number of step per quarter cycle	-	50
Test control	-	Stress
Shear stress amplitude	τ_{xy}	13 kN/m^2

(a)

(b)
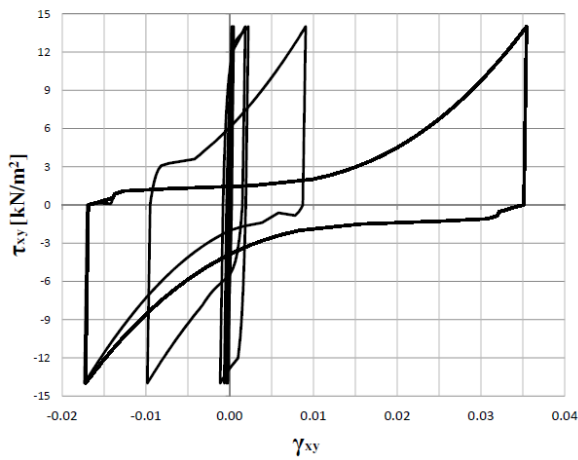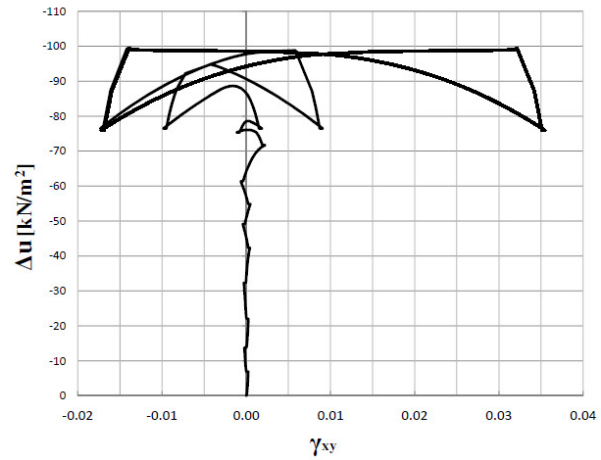
(c)

Figure 8 CDSS test response in term of: (a) shear stress (τ_{xy}) over shear strain (γ_{xy}), (b) excess water pore pressure (Δu) over shear strain (γ_{xy}) and (c) excess pore water pressure ratio (r_u) over cycles (CSR=0.130).
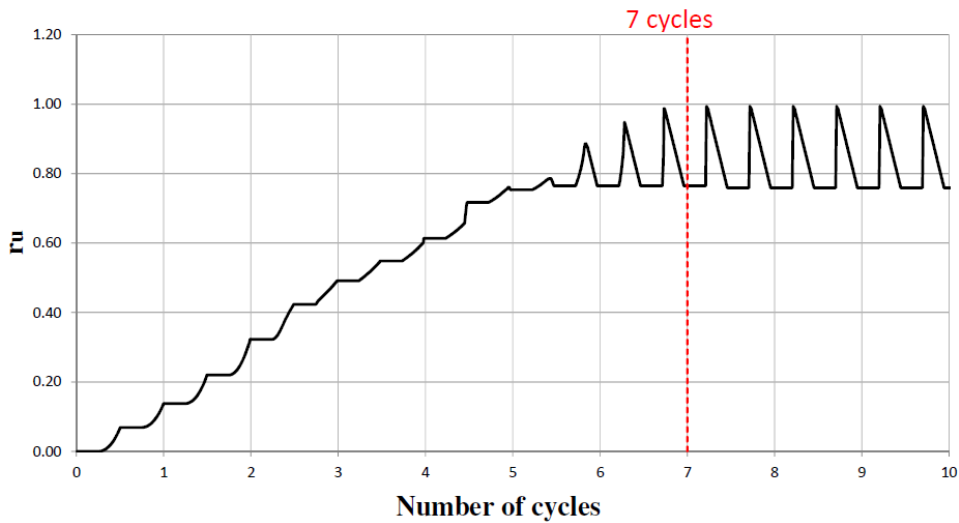
TEST 9

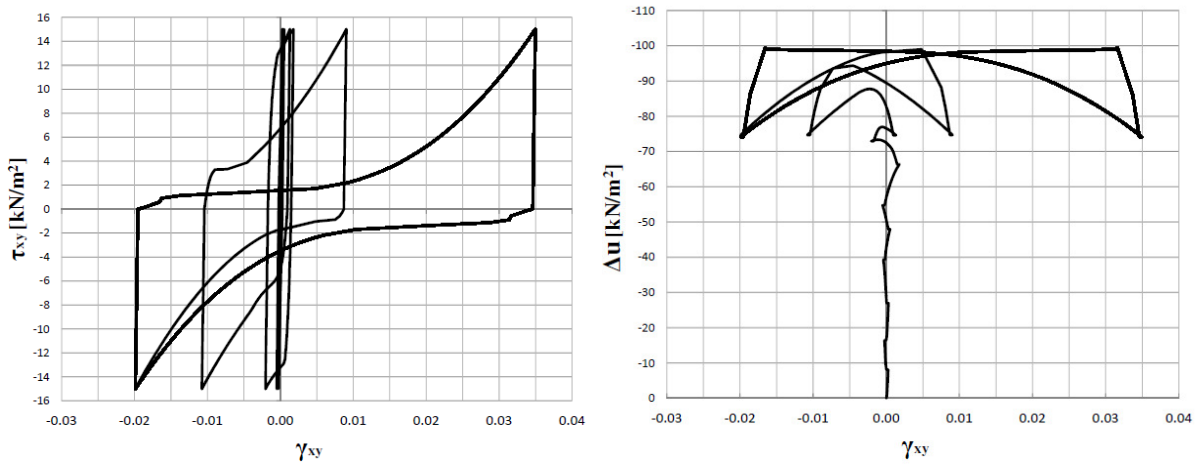| Test Conditions	Symbol	Value/type
Type of test	-	Undrained
K_0-consolidate test	$K_0\text{-}value$	0.5
Initial Stress	$|\sigma_{yy}|$	100 kN/m^2
Number of cycles	-	100
Number of step per quarter cycle	-	50
Test control	-	Stress
Shear stress amplitude	τ_{xy}	14 kN/m^2

(a)

(b)

(c)

Figure 9 CDSS test response in term of: (a) shear stress (τ_{xy}) over shear strain (γ_{xy}), (b) excess water pore pressure (Δu) over shear strain (γ_{xy}) and (c) excess pore water pressure ratio (r_u) over cycles (CSR=0.140).
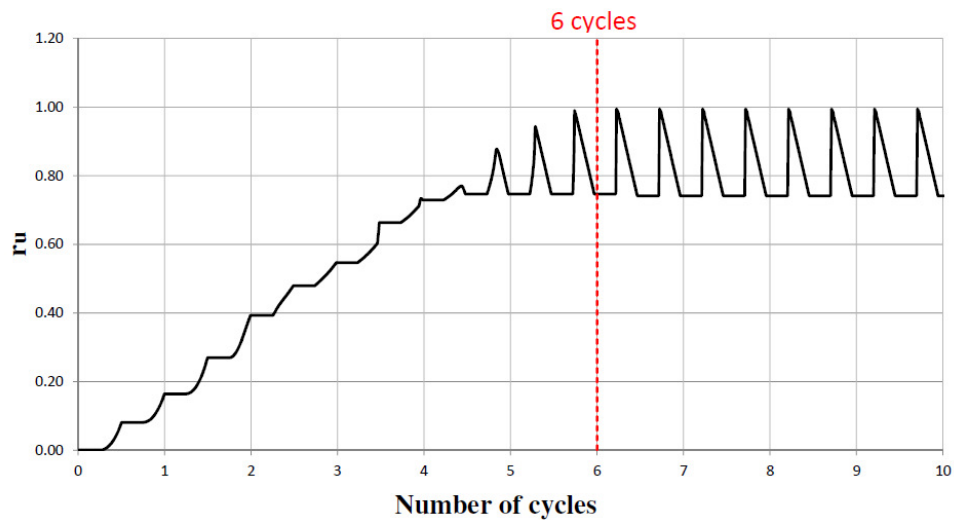
TEST 10

Test Conditions	Symbol	Value/type
Type of test	-	Undrained
K_0-consolidate test	$K_0\text{-}value$	0.5
Initial Stress	$|\sigma_{yy}|$	100 kN/m^2
Number of cycles	-	100
Number of step per quarter cycle	-	50
Test control	-	Stress
Shear stress amplitude	τ_{xy}	15 kN/m^2

(a)

(b)

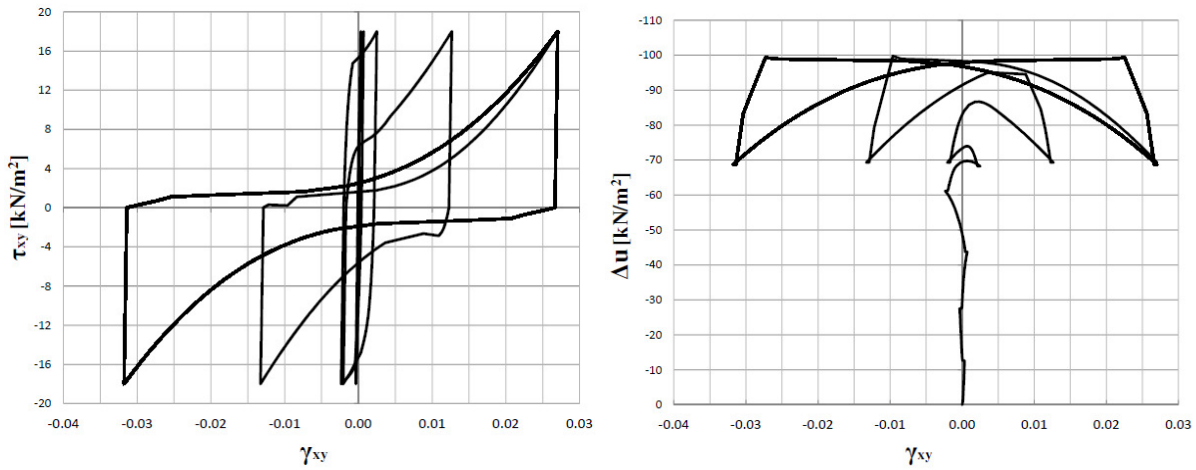(c)

Figure 10 CDSS test response in term of: (a) shear stress (τ_{xy}) over shear strain (γ_{xy}), (b) excess water pore pressure (Δu) over shear strain (γ_{xy}) and (c) excess pore water pressure ratio (r_u) over cycles (CSR=0.150).
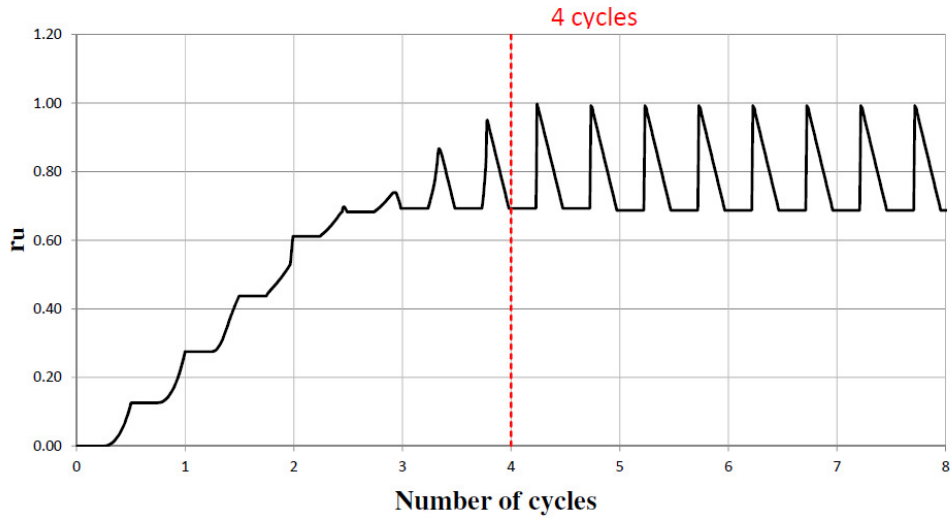
TEST 11

Test Conditions	Symbol	Value/type
Type of test	-	Undrained
K_0-consolidate test	$K_0\text{-}value$	0.5
Initial Stress	$|\sigma_{yy}|$	100 kN/m^2
Number of cycles	-	100
Number of step per quarter cycle	-	50
Test control	-	Stress
Shear stress amplitude	τ_{xy}	18 kN/m^2

(a)

(b)

(c)

Figure 11 CDSS test response in term of: (a) shear stress (τ_{xy}) over shear strain (γ_{xy}), (b) excess water pore pressure (Δu) over shear strain (γ_{xy}) and (c) excess pore water pressure ratio (r_u) over cycles (CSR=0.180).

201